

Biochemical and cellular studies of the KDM6 sub-family of JmjC histone lysine demethylases



Kate Dunne
Brasenose College, University of Oxford

Michaelmas Term 2018

A thesis submitted to the board of the Faculty of Physical Sciences of the University of Oxford in partial fulfilment of the requirements for the degree of Doctor of Philosophy

Abstract

The JmjC domain containing histone lysine demethylases (JmjC-KDMs) are a family of epigenetic enzymes which regulate gene expression by catalysing demethylation of $^{\varepsilon}N$-terminal lysines on histone tails. KDM6A and KDM6B catalyse demethylation of histone H3 trimethyllysine (H3K27Me3) on the tail of histone H3, activating gene expression. The KDM6 family have various roles in development and disease, including in hypoxic disease states such as cancer and atherosclerosis. The aim of this project was to evaluate KDM6 activity in the context of cellular hypoxia, both in terms of reduced oxygen availability and alterations to the metabolic milieu. Efforts were made to establish a phenotypic cellular assay for atherosclerosis, a hypoxic disease state in which epigenetic regulation of macrophage functions, including by KDM6B, plays a central role.

Expression and purification of recombinant KDM6A was undertaken, but low or no catalytic activity was observed, likely due to aggregation. Production of fusion-protein cleaved KDM6B resulted in inactive enzyme which was found to contain DNA contamination. Endonuclease treatment and heparin affinity purification restored KDM6B activity, indicating a catalytically inactivating interaction between KDM6B and contaminating DNA.

The oxygen sensitivity of several JmjC-KDMs has been demonstrated.[1,2] The oxygen dependence of KDM6B against global H3K27Me3 was assessed in HeLa and COS-7 cells. A graded response of KDM6B activity to oxygen concentrations (0.1-21%) was observed in both cell lines, indicating KDM6B activity can be modulated by oxygen availability in a physiologically relevant manner.

Hypoxia impacts cellular metabolism, and leads to increased cellular concentration of tricarboxylic acid cycle intermediates (TCAI).[3–7] Inhibition of various 2OG oxygenases by TCAI and related metabolites has been reported, and may contribute to reduction of activity seen in hypoxia.[8–10] An AlphaScreen inhibition assay was used to evaluate KDM6B inhibition by 17 TCAI, with D-2HG, L-2HG and succinate identified as the most potent inhibitors (IC_{50} values of 9.7, 15, 20 and 20 μM). An orthogonal MALDI-MS assay validated potent inhibition by succinate, L-2HG and D-2HG. Cell permeable esters of TCAI were evaluated using the KDM6B immunofluorescence assay, but no strong cellular inhibition was observed, possibly due to saturating cellular 2OG conditions.

Lipid-droplet filled foam cells make up the expanding core of an atherosclerotic plaque.[11] Hypoxia was shown to stimulate foam cell formation using a cellular phenotypic assay. Inhibition of foam cell formation by small molecule inhibitors, including those of JmjC-KDMs, were evaluated but no modulation of foam cell formation was observed, in part due to the small dynamic range of the assay.

The work described in this thesis demonstrates that KDM6B activity is reduced both by reduced oxygen availability in cells, and by TCAI inhibition *in vitro*. This may have important implications for gene regulation in the context of hypoxic disease states, where both reduced oxygen availability and dysregulation of metabolism occur.

Abstract References

1. Hancock, R. L., Masson, N., Dunne, K., Flashman, E. & Kawamura, A. The Activity of JmjC Histone Lysine Demethylase KDM4A is Highly Sensitive to Oxygen Concentrations. *ACS Chem. Biol.* **12,** 1011–1019 (2017).
2. Hancock, R. L., Dunne, K., Walport, L. J., Flashman, E. & Kawamura, A. Epigenetic regulation by histone demethylases in hypoxia. *Epigenomics* 1–21 (2015). doi:10.2217/epi.15.24
3. Czibik, G., Steeples, V., Yavari, A. & Ashrafian, H. Citric acid cycle intermediates in cardioprotection. *Circ. Cardiovasc. Genet.* **7,** 711–9 (2014).
4. Cerebral metabolism in hypoxic hypoxia. II. Citric acid cycle intermediates and associated amino acids. *Brain Res.* **86,** 45–54 (1975).
5. Hochachka, P. W., Owen, T. G., Allen, J. F. & Whittow, G. C. Multiple end products of anaerobiosis in diving vertebrates. *Comp. Biochem. Physiol. B.* **50,** 17–22 (1975).
6. J.Folbergrova, B.Ljunggren, K.Norberg, B. K. S. Influence of complete ischemia on glycolytic metabolites, citric acid cycle intermediates, and associated amino acids in the rat cerebral cortex. *Brain Res.* **80,** 265–279 (1974).
7. Intlekofer, A. M. *et al.* Hypoxia Induces Production of L-2-Hydroxyglutarate. *Cell Metab.* **22,** 304–11 (2015).
8. Tarhonskaya, H. *et al.* Studies on the Interaction of the Histone Demethylase KDM5B with Tricarboxylic Acid Cycle Intermediates. *J. Mol. Biol.* **429,** 2895–2906 (2017).
9. Chowdhury, R. *et al.* The oncometabolite 2-hydroxyglutarate inhibits histone lysine demethylases. *EMBO Rep.* **12,** 463–469 (2011).
10. Hewitson, K. S. *et al.* Structural and Mechanistic Studies on the Inhibition of the Hypoxia-inducible Transcription Factor Hydroxylases by Tricarboxylic Acid Cycle Intermediates. *J. Biol. Chem.* **282,** 3293–3301 (2007).
11. Ross, R. Atherosclerosis--an inflammatory disease. *N. Engl. J. Med.* **340,** 115–26 (1999).

Contents

Abstract i
Abstract References ii
Contents iv
Abbreviations vii
Acknowledgments xiii
Chapter 1: Introduction 1
1.1 Epigenetics arises from DNA packing within cells 1
1.2 Mechanisms of epigenetic gene regulation 2
1.3 The 2-oxoglutarate dependent oxygenase enzymes 8
1.4 JmjC histone demethylases 11
1.5 The KDM6 sub-family of JmjC histone demethylases 13
1.6 The role of KDM6 mediated gene regulation in development 15
1.7 The role of KDM6 mediated gene regulation in disease 17
1.8 Hypoxia and the hypoxic response 18
1.9 Hypoxia induces alteration of epigenetic marks 21
1.10 Histone methylation and hypoxia 23
1.11 Thesis objectives 27
1.12 References 29
Chapter 2 –Establishment of biochemical assays to assess KDM6A and KDM6B activity and inhibition 48
2.1 Introduction 48
2.2. Expression and purification of KDM6A constructs BR71, BR281 and BR242 51
2.3 Batch-to-batch variability of KDM6A activity assessed by MALDI-MS 59
2.4 Dynamic light scattering assessment of BR71 JK reveals aggregation 60
2.5 Expression and purification of KDM6B 61
2.6 Assessment of KDM6B activity by MALDI-MS activity assay 62
2.7 Kinetic characterisation of KDM6B by MALDI-MS 63
2.8 Alternate assays for the evaluation of KDM6 demethylase activity 65
2.9 Purification of cleaved KDM6B for use in FDH assays 66
2.10 Endonuclease treatment of contaminated KDM6B restores catalytic activity 76
2.11 Purification of KDM6B P2 via heparin affinity chromatography removes contamination and restores activity 79
2.12 Efforts towards establishment of an KDM6B binding assays 82
2.13 Discussion 86
2.14 References 90
Chapter 3: Studies of the cellular oxygen dependence of KDM6B activity 93

3.1 Introduction 93
3.2 Establishment of a cellular immunofluorescence activity assay 100
3.3 Selection of transfected cells based on nuclear FLAG fluorescence intensity 102
3.4 Establishment of an optimal transfection protocol for KDM6A/B/C in HeLa 104
3.5 Evaluation of cellular demethylase activity of KDM6A/C in HeLa cells 108
3.6 Effect of transfection window duration on transfection efficiency 109
3.7 Evaluation of oxygen-dependence of cellular KDM6B activity in HeLa 111
3.8 Evaluation of the effect of normoxic transfection window on oxygen-dependence of cellular KDM6B activity 113
3.9 Identification of unusual HeLa morphology 117
3.10 Evaluation of cellular KDM6A/B/C activity in COS-7 cells 119
3.11 Establishment of an optimal transfection protocol for KDM6AB in COS-7 122
3.12 Evaluation of oxygen-dependence of cellular KDM6B activity in COS-7 123
3.13 Discussion 125
3.13 References 129
Chapter 4. Inhibition of KDM6B activity by tricarboxylic acid intermediates 135
4.1 Introduction 135
4.2 AlphaScreen™ inhibition assay 138
4.2.2 Screening of TCAI by KDM6B AlphaScreen™ inhibition assay 139
4.3 Evaluation of TCAI inhibitors using a MALDI-MS inhibition assay 144
4.4 Efforts towards establishment of alternate KDM6B activity assays 147
4.5 Cellular inhibition studies 149
4.6 Discussion 152
4.7 References 159
Chapter 5: Efforts towards a phenotypic cellular assay of foam cell formation 162
5.1 Introduction 162
5.2 Techniques for the evaluation of foam cell formation 166
5.3 Evaluation of THP-1 and RAW 264.7 cell lines for use in the foam cell formation assay 166
5.4 Treatment of RAW 264.7 with oxLDL and acLDL produces a lipid droplet filled macrophage phenotype 169
5.5 Optimisation of fluorescence microscopy image acquisition method 172
5.6 Establishment of an imaging analysis pipeline 174
5.7 acLDL treatment induces lipid droplet accumulation in RAW 264.7 in a concentration-dependent manner 175
5.8 Hypoxia enhances foam cell formation in RAW 264.7 cells 176
5.9 Evaluation of treatment with small molecule inhibitors on acLDL induced foam cell formation in normoxia 182
5.10 Statistical analysis reveals small dynamic range of foam cell assay 184

5.11 Discussion 189
References 193
Chapter 6: Summary and Conclusions 200
6.1 References 208
Chapter 7: Materials and Methods 213
General methods 213
Procedures relating to *in vitro* experiments 213
In vitro assays 222
Procedures relating to cellular experiments 227
References 234
Appendix 1: HPLC-MS analysis of H3K27Me3 peptide for use in *in vitro* assays 236
Appendix 2: NMR analysis of H3K27Me3 peptide used for *in vitro* assays 237
Appendix 3: Recombinant KDM6B construct JMJC3A-C031 238
Appendix 4: Protein LC-MS analysis of His-tagged KDM6B JMJC3A-C031 239
Appendix 5: Protein LC-MS analysis of cleaved KDM6B JMJC3A-C031 240
Appendix 6: Supplementary AlphaScreen IC_{50} curves 241
Appendix 7: Dissolved oxygen calibration curve 243
Appendix 8: Summary of reported substrates and functions of human 2OG oxygenases 244
References 245

Abbreviations

2HG	2-Hydroxyglutarate
2OG	2-Oxoglutarate
2TY	2-Tryptone Yeast Extract
5hmC	5-Hydroxmethylcytosine
5mC	5-Methylcytosine
acLDL	acetylated LDL
AID	Activation induced deaminase
ApoE	apolipoprotein E
APS	Ammonium persulphate
ARID	AT-rich interaction domain
ATCC	American Type Culture Collection
ATP	Adenosine Triphosphate
BER	base excision repair
CAD	C-terminal transactivation domain
CHCA	α-cyano-4-hydroxycinnamic acid
CI	Confidence Interval
CODD	C-terminal oxygen dependent degradation domain
Da	Dalton (mass unit)
DAPI	4',6-Diamidino-2-phenylindole
DIC	diisopropylcarbodiimide
DLS	Dynamic light scattering
DLS	Dynamic light scattering
dm	Dimethyl
DMEM	Dulbecco's Modified Eagle Medium

DMF	dimethyl formamide
DMSO	Dimethyl sulfoxide
DNA	Deoxyribonucleic Acid
DNMT	DNA Methyltransferase
Dox	Doxycycline
DSBH	Double Stranded Beta Helix
DTT	Dithiothreitol
E. coli	Escherichia coli
EDTA	Ethylenediaminetetracetic acid
EPO	erythropoietin
ESC	Embyonic stem cells
FBS	Foetal Bovine Serum
FDH	formaldehyde dehydrogenase
FH	fumarate hydratase
FH	fumarate hydratase
FIH	Factor Inhibiting HIF
Fmoc	Fluorenylmethyloxycarbonyl
FOXY	fluorescent oxygen detecting electrode
FPLC	Fast Protein Liquid Chromatography
FPLC	fast protein liquid chromatography
FTO	fat mass and obesity associated protein
H3	Histone 3
HAT	histone acetyltransferases
HDAC	Histone Deacetylase
HeLa	Henrietta Lacks' Human Cervical Cancer Cell Line

HEPES	4-(2-hydroxyethyl)-1-piperazineethanesulfonic acid
HIF	Hypoxia Inducible Factor
HPLC	High pressure liquid chromatography
ICP-MS	Inductively coupled plasma mass spectrometry
IDH	Isocitrate Dehydrogenase
IDH	isocitrate dehydrogenase
IF	Immunofluorescence
IMAC	immobilised metal affinity chromatography
IOX1	5-Carboxy-8-hydroxyquinoline
IPTG	Isopropyl β-D-1-thiogalactopyranoside
JmjC-KDM	JumonjiC- Domain Containing KDM
KDM	Histone Lysine Demethylase
KMT	lysine methyltransferase
LB	Lysogeny Broth
LC	Liquid Chromatography
LDHA	lactate dehydrogenase A
LDL	low denisty lipoprotein
LDPCMW	lipid droplets per cell mean per well
LPS	Lipopolysaccaride
LSD	Lysine Specific Demethylase
LSD1	Lysine-specific histone demethylase 1A
MALDI-TOF	Matrix-Assisted Laser Desorption Ionisation Time of Flight
MAT2A	Methionine adenosyltransferase 2A
MES	2-(N-morpholino)ethanesulfonic acid hydrate

MFC	Mass Flow Controller
MIP	Maximum intensity projection
MMS	methyl methanesulfonate
MNNG	N-methyl-N'-nitro-N-nitrosoguanidine
MS	Mass Spectrometry
MUT	Catalytically Inactive Mutant
MW	Molecular Weight
NAD	nicotinamide adenine dinucleotide
NEC	No enzyme control
NF- κβ	nuclear factor-κβ
NMR	Nuclear magnetic resonance
NODD	N-terminal oxygen dependent degradation domain
NOG	N-oxalylglycine
oxLDL	oxidised LDL
PAGE	Polyacrylamide Gel Electrophoresis
PAMP	pathogen-associated molecular patterns
PBS	Phosphate Buffered Saline
PCR	Polymerase Chain Reaction
PHD	Plant Homeodomain
PHD2	Prolyl Hydroxylase Domain 2
PMA	phorbol 12-myristate 13-acetate
PMSF	Phenylmethylsulfonyl fluoride
PRMT	Protein Arginine Methyltransferase
PRMT	protein arginine methyltransferases
pVHL	von Hippel–Lindau tumour suppressor protein

RNA	Ribonucleic Acid
RPMI	Roswell Park Memorial Institute Medium
RT-qPCR	Quantitative Reverse Transcription PCR
SAA	serum amyloid A
SAM	S-adenosyl methionine
sd	Standard Deviation
SD	succinate dehydrogenase
SDH	succinate dehydrogenase
SDS	Sodium Dodecyl Sulfate
SEC	size exclusion chromatography
sem	Standard Error of the Mean
SGC	structural genomics consortium
SOC	Super Optimal Broth with Catabolite Repression
SR-A	Scavenger Receptor A
TCA	tricarboxylic acid
TCAI	TCA cyle intermediates
TED	tris(carboxymethyl)ethylene diamine
TEMED	N,N,N',N'-Tetramethyl-Ethane-1,2-Diamine
TET	Ten-Eleven Translocation Enzyme
TEV	tobacco etch virus
TFA	Trifluoroacetic Acid
tKDM4A	truncated recombinant KDM4A1-359
TNF-α	tumour necrosis factor α
TPR	tetratricopeptide repeat
TR:DNA	Transfection reagent: DNA ratio

Tris	Tris(hydroxymethyl)aminomethane
TRX	Thioredoxin
UV	Ultraviolet
UV-Vis	Ultraviolet-visible
WT	Wild Type

Acknowledgments

Firstly, I would like to thank Dr Akane Kawamura and Dr Emily Flashman for their supervision and support throughout my D.Phil. I could not have asked for better supervisors. Thanks also to Professor Chris Schofield for his encouragement and enthusiasm. I am grateful to the British Heart Foundation CRE for providing funding and to Professor Angie Russell and Professor Shoumo Bhattacharya for this amazing opportunity.

A number of people have contributed directly to the work in this thesis. I am particularly indebted to Dr Rebecca Hancock, Dr Anthony Tumber, Dr Jan Kristensen, Alex Brooks and Grasilda Zenkeviciute for materials, protocols and experimental assistance. Thanks also to H. Manso Jubier, Dr Adam Hardy and Wendy Sobey for keeping the lab running smoothly.

An enormous number of people in the CJS/AK/EF groups have been both excellent colleagues and friends during my D.Phil. Particular thanks for technical advice and useful discussions go to Dr Rebecca Hancock, Joanna Bonnici, Leah Taylor-Kearney, Dr Richard Hopkinson, Gareth Langley, Dr Tom McAllister, Yijia Zhang and Dr Hanna Tarhonskaya. Many others have provided a lovely working environment: thank you Ollie, Grace, Cyrille, David, Hilal, Joan, John-Paul, Martine, Rachel, Bhaskar, and everyone I am bound to have missed.

Finally, thank you to my wonderful parents, and awesome sister Emma.

Declaration

The work described in this report is entirely my own, except where I have either acknowledged help from a named person or given reference to a published source.

Signed: Date:

Chapter 1: Introduction

1.1 Epigenetics arises from DNA packing within cells

Genetic information is encoded in deoxyribonucleic acid (DNA), which is transcribed and translated, yielding proteins. The type, combination and abundance of proteins in a cell result in a unique cellular phenotype and function. Although all cells contain the same DNA, not all DNA is translated at once; cellular phenotypes arise from differential protein expression.

The level and activity of a given protein in a cell are controlled by mechanisms involved in transcription, such as transcription factors and epigenetic regulation, and translation, such as alternative splicing and post translational modification.[1]

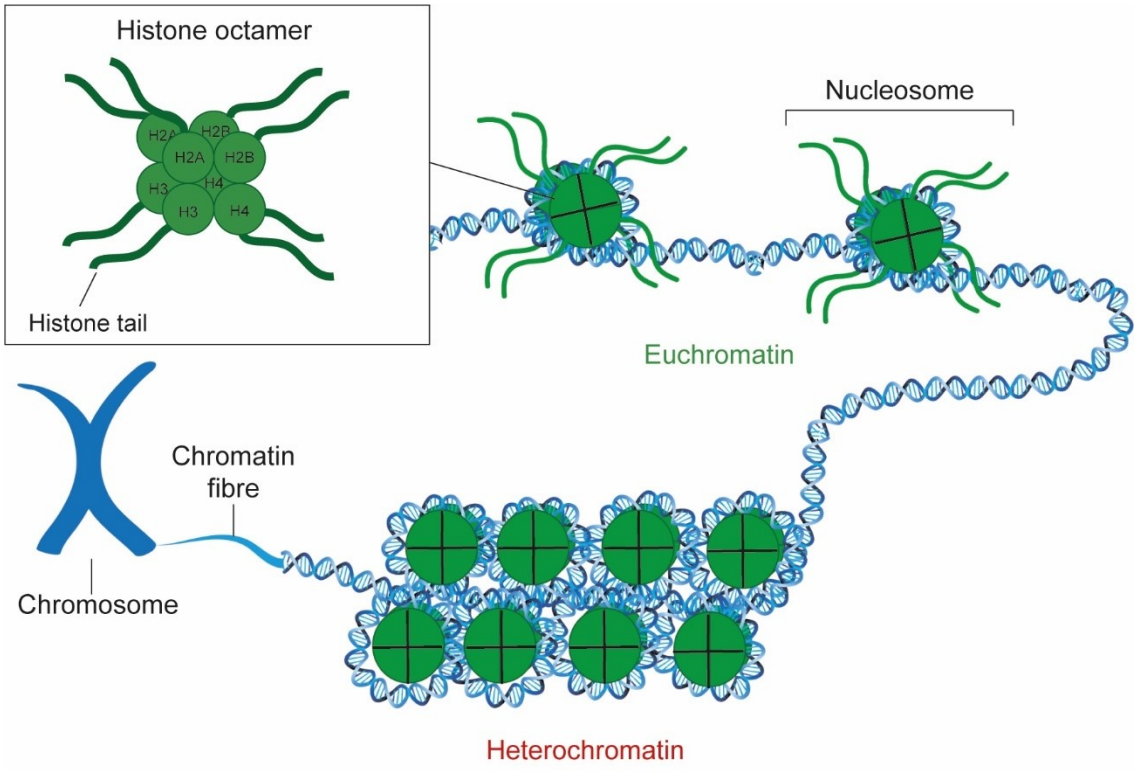


Figure 1.1 – Schematic representation of DNA packing within cells. *Histone subunits consist of a globular domain and an unstructured tail. These subunits form octamers consisting of four H3/H4 and H2A/H2B histone heterodimers. DNA (blue) is wound around these histone octamers (green), like thread around a bobbin, forming nucleosomes. These nucleosomes pack together forming chromatin, which can take an open form, euchromatin, or a closed form heterochromatin. Packing of chromatin yields increasingly ordered chromatin fibres, resulting in the organisation of DNA into chromosomes.*

Epigenetic control of gene expression arises due to the packing of this DNA within cells, with each cell containing around 2 meters of DNA (Figure 1.1). Negatively charged DNA is wound around an octamer of histone proteins which form a positively charged globular protein known as a histone. Four histone subunits H2A, H2B, H3, and H4 are combined in H2A/H2B and H3/H4 heterodimers to form histone octamers.[2,3] Each subunit has an unstructured N-terminal tail which projects out from the nucleosome. Though these tails have no ordered structure, their presence is required for stability.[4–6] Nucleosomes are stable; their formation is energetically favourable due to the cumulative binding interactions between DNA and histone proteins.[6] Nucleosomes pack together to form chromatin. Chromatin can take an open form, euchromatin, which allows access of the transcriptional machinery to DNA, or a closed form, heterochromatin, where the DNA is inaccessible (Figure 1.1). Dynamic covalent modifications to DNA and the unstructured N-terminal tails of histones modulate gene expression by altering chromatin structure and accessibility of the transcriptional machinery to DNA. This forms the basis of epigenetic gene regulation.

1.2 Mechanisms of epigenetic gene regulation

1.2.1 DNA methylation

Methylation of DNA occurs at the C5 position of cytosine residues in cytosine-guanine (CG) dinucleotide sequences, often referred to as CpG. CpG methylation is associated with transcriptional repression via two mechanisms. Firstly, methylation at specific CpG-containing sequences may prevent recognition and/or binding to DNA of transcription factors. For example, CpG methylation has been shown to block binding of hypoxia-inducible factor 1 (HIF-1), and induction of erythropoietin transcription under hypoxic conditions.[7] Secondly, other DNA binding factors may preferentially bind to methylated DNA, preventing transcription by blocking transcription factor access or recruiting

transcriptional co-repressors.[8] Repression of gene transcription by DNA methylation is important in X-inactivation which limits the expression of most X-chromosome genes to those from only one X chromosome in females.[9] Similarly, DNA methylation contributes to silencing of one parental allele of a given gene, known as genomic imprinting.[9] DNA methylation is established and maintained by DNA methyltransferases 1, 3A, and 3B (DNMT1, DNMT3A, DNAMT3B) (Figure 1.2). (The fourth member of the family DNMT2, shows no *in vivo* activity and little *in vitro* activity.)[8] DNA methylation can also arise from exposure to exogenous methylating agents including methyl methanesulfonate (MMS) and N-methyl-N'-nitro-N-nitrosoguanidine (MNNG), though this occurs randomly and is potentially carcinogenic.[10,11]

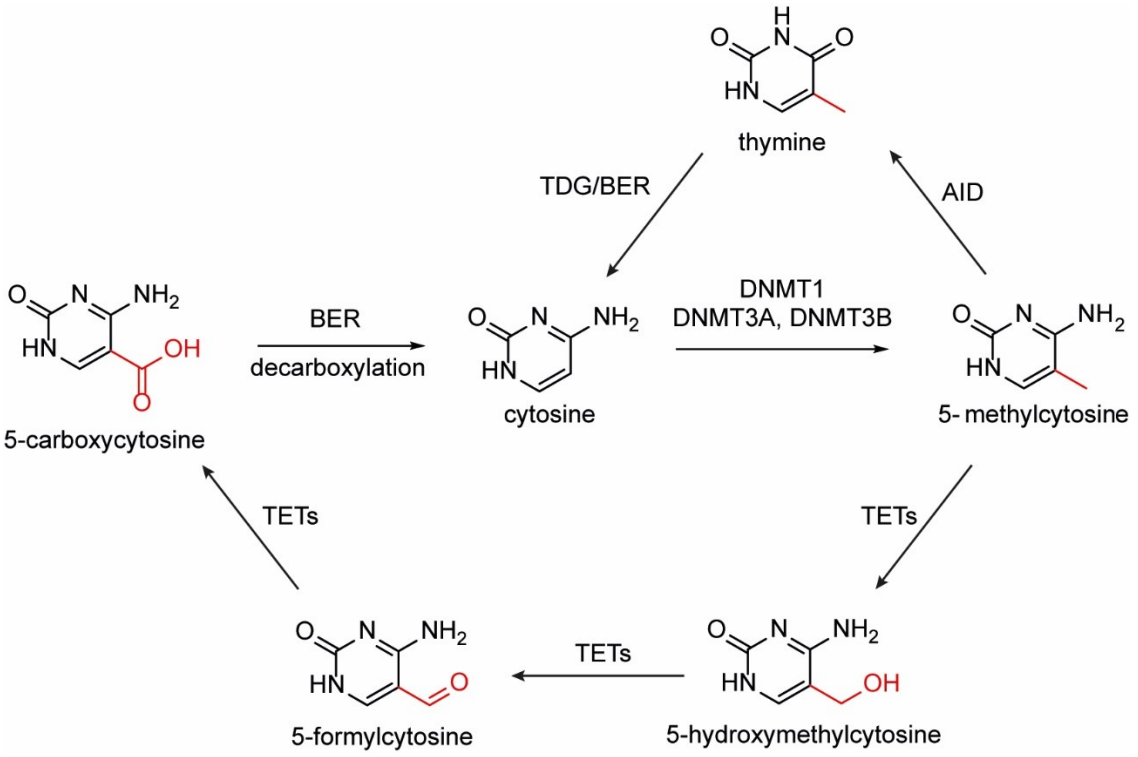


Figure 1.2 – Enzymatic regulation of cytosine methylation. *Methylation of cytosine is catalysed by DNMT enzymes. Cytosine demethylation is catalysed via successive oxidations by the Ten-Eleven-Translocation (TET) enzymes; proceeding via 5-hydroxymethylcytosine, 5-formylcytosine and 5-carboxymethylcytosine which either undergoes decarboxylation, or is removed and replaced via base excision repair (BER), in both cases to yield cytosine. Modifications to cytosine highlighted in red. Demethylation of cytosine can also occur via an alternative pathway whereby 5mC is converted to thymine by activation induced deaminase (AID) and replaced via BER.*

Passive DNA demethylation can occur when DNMT enzymes fail to maintain DNA methylation during DNA replication.[12] Alternatively, active DNA demethylation is catalysed by the Ten-Eleven-Translocation enzymes (TET) which successively oxidise 5-methyl-cytosine (5mC) to 5-hydroxy, 5-formyl to 5-carboxycytosine which then undergoes spontaneous decarboxylation to give cytosine, or is replaced via base excision repair (BER).[13] Demethylation of cytosine can also occur via an alternative pathway whereby 5mC is converted to thymine by activation induced deaminase (AID), and replaced via BER but the significance of this is questionable due to low enzymatic conversion observed *in vitro*.[14]

1.2.2 Histone modifications

Histone modifications allow highly dynamic and specific spatiotemporal control of gene regulation. Histone tail modifications, known as histone marks, are written, read and removed by histone modifying proteins and/or complexes known as readers, writers and erasers respectively. Aberrant behaviour or expression of these histone modifiers can cause alterations of gene expression leading to disease.[1]

Various post-translational modifications are found on histone tails, including methylation, acetylation, phosphorylation and ubiquitination (Figure 1.3). Other histone marks such as crotonylation and hydroxylation have also been proposed, but as yet their role in gene regulation is not well established.[15,16] These histone modifications occur at lysine, arginine, threonine, tyrosine and serine residues.[15] Each histone modification may be activating or repressive with respect to gene expression depending on which histone subunit and residue is modified, the modification, the degree of modification (in the case of methylation) and the combination of multiple modifications. This complexity and cross talk between modifications and transcriptional outcome is referred to as the histone code.[17]

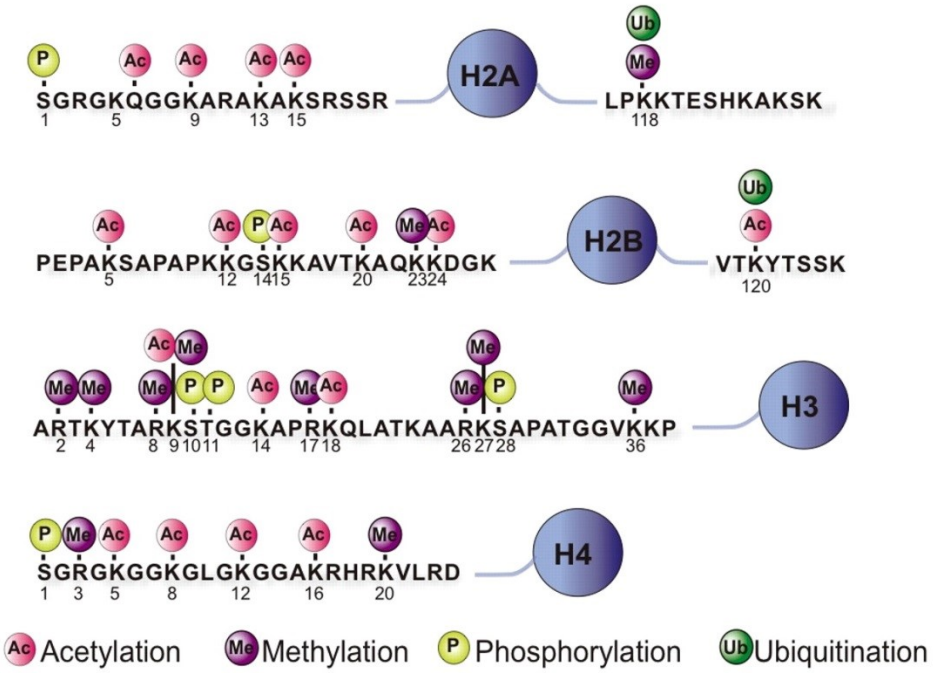


***Figure 1.3 – Post-translational modifications of the N-terminal histone tails**. Various post-translational modifications are involved in epigenetic regulation of gene expression. The most well-characterised modifications are methylation, ubiquitination, phosphorylation and acetylation. Location of common modifications found on histone protein, and their modified residues indicated above. Reproduced with permission from Kato et al.*[18]

Acetylation is one of the most studied histone modifications and occurs on lysine residues. Lysine acetylation results in transcriptional activation as the acetyl group neutralises the positively charged lysine, reducing the binding interaction with negatively charged DNA and consequently opening the chromatin structure.[19] Additionally, histone acetylation facilitates the binding of transcription factors, many of which contain a bromodomain which specifically interacts with the acetylated histone.[20] Histone acetylation is written and erased by histone acetyltransferases (HATs) and histone deacetylases (HDACs) respectively.[21,22]

Histone phosphorylation occurs on serine, tyrosine and threonine residues, and is associated with both repression and activation. As with other proteins, phosphorylation of histone residues is likely to induce large structural changes. Histone phosphorylation is written and erased by kinases and phosphatases.[23] Whilst histone phosphorylation is less

extensively characterised compared with histone acetylation and histone methylation, it is known to have important roles in cell cycle regulation and DNA damage repair.[15,24]

Histone methylation occurs on lysine and arginine residues. Lysine residues may be mono-, di- or tri-methylated at the ε nitrogen, whereas arginine residues may be mono- or di- methylated at the ω nitrogen.[25] Unlike acetylation and phosphorylation, histone methylation does not alter the charge of the histone protein. Instead it alters the steric and hydrophobic properties of the histone, changing its affinity for proteins and creating binding sites for certain specific protein domains such as plant homeodomain or chromodomain.[26] Nevertheless, histone methylation state alters both compaction of chromatin and binding of protein complexes. Histone methylation is associated with activation and repression depending on the location, degree and combination of concurrent epigenetic marks. For example, H3K4Me3 is associated with transcriptional activation, whereas H3K27Me3 is associated with transcriptional repression. The combination of both marks renders repression of gene expression.[27–29]

Athough not recognised as such until 2007, methylation is a dynamic histone modification deposited and removed by enzyme catalysis. Three enzyme families have been identified which catalyse transfer of methyl groups from S-adenosyl methionine (SAM) to histones. Histone lysines are methylated by SET-domain containing proteins and DOT-1-like proteins (classified as lysine methyltransferases, KMTs), whilst protein arginine methyltransferases (PRMTs) methylate histone arginines.[30] Histone methylation was thought to be irreversible, due to early experiments showing that bulk histone and methylation turnover rates were the same.[31,32] However, the first histone demethylase, Lysine-specific histone demethylase 1A (LSD1) a member of the flavin-dependent monoamine oxidase family, was discovered in 2004.[33] Following this, the JmjC domain–containing histone demethylase (JmjC-KDM) family was discovered, which contains

more than 20 histone demethylases. Reversibility of all histone methylation states (mono-, di-, and trimethylation) at almost all major histone methylation modified sites has now been demonstrated,[30] including recent reports of an H3K79 demethylase.[34] The JmjC-KDMs are members of the 2-oxoglutarate dependent oxygenase (2OG oxygenase) superfamily of enzymes.

1.3 The 2-oxoglutarate dependent oxygenase enzymes

The 2OG oxygenase enzymes are a large superfamily, consisting of over 60 members, that are involved in a diverse range of biological roles including chromatin/transcription factor modification, collagen biosynthesis, lipid metabolism and nucleic acid repair (Appendix 8, Table A8).[35] These enzymes catalyse a wide range of reactions in mammals, plants and bacteria (Figure 1.4).[36]

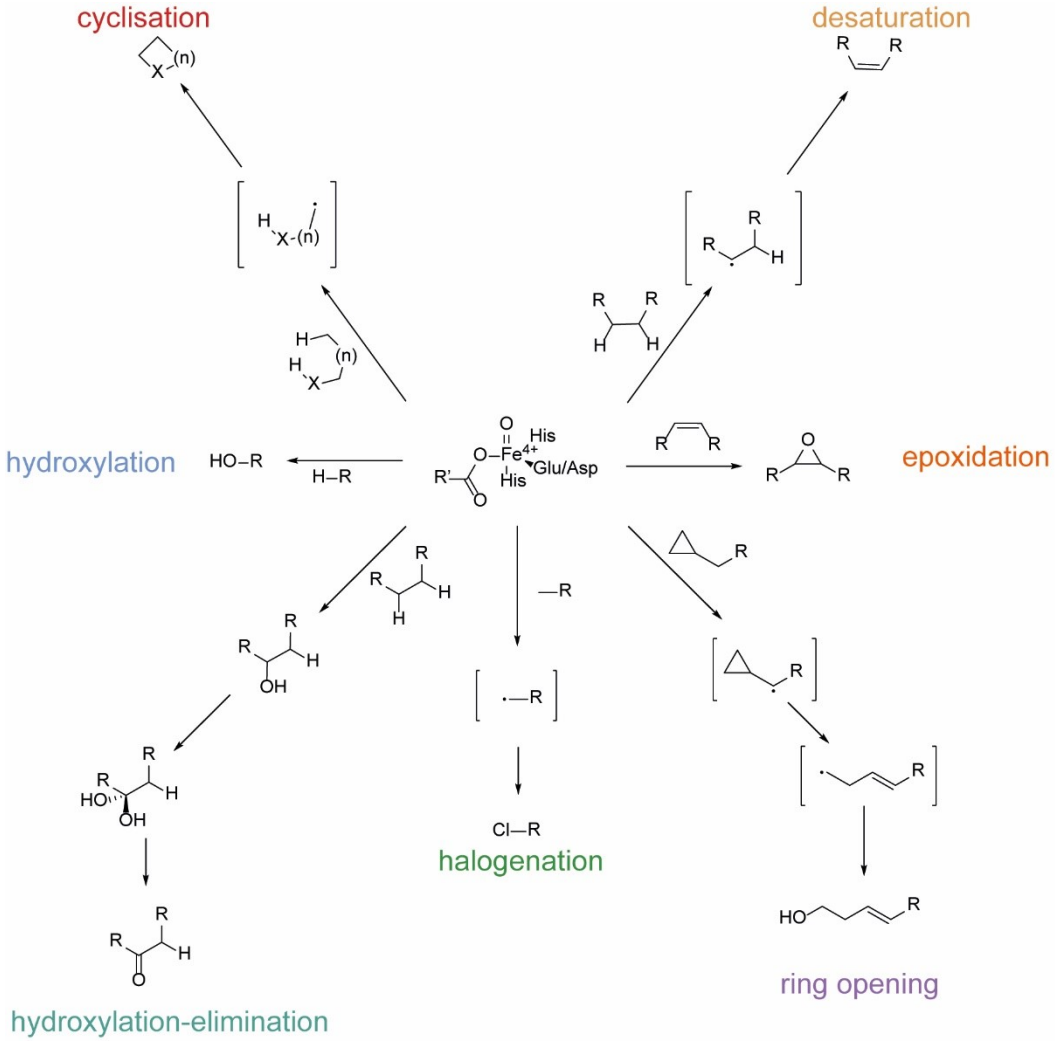


Figure 1.4 – Range of reactions catalysed by members of the 2OG oxygenase superfamily of enzymes. *Adapted from Clifton et al with permission from Elsevier.[36] R' – CH2CH2CO2-, R – Alkyl group, X – nitrogen, oxygen. The highly reactive oxo-Fe4+ species (centre) abstracts a proton from the substrate. Halogenation, epimerisation, desaturation and ring cyclisation arise from abstraction or re-arrangement of the carbon radical formed, whilst hydroxylation occurs via subsequent donation of a hydroxyl group from the Fe3+ centre. (Full 2OG oxygenase mechanism Figure 1.6.)*

In almost all cases 2OG oxygenases couple the two-electron oxidation of substrate to the oxidative decarboxylation of 2OG to give succinate and carbon dioxide.[37] All identified

2OG oxygenases use Fe^{2+} as a cofactor, and some, such as the HIF hydroxylases and collagen prolyl-4 hydroxylase require ascorbate for optimal activity.[38–40] Though the role of ascorbate in catalysis is not known, it has been proposed to be involved in maintenance of the Fe^{2+} oxidation state.[39]

Crystallographic studies have revealed a conserved structure across the 2OG oxygenases consisting of a double-stranded β-helix fold (DSBH) 'jelly roll'. Within the DSBH Fe^{2+} is chelated by a His-X-Asp/Glu...His triad motif via the histidine lone pairs and glutamate or aspartate carboxyl group (Figure 1.5).[36,41] The 2OG oxygenase family is divided in to sub-families of enzymes which includes the prolyl hydroxylases, collagen prolyl hydroxylases, nucleotide hydroxylases, small-molecule hydroxylases and JmjC-KDMs.[42] 2OG-binding residues and substrate-binding residues vary across the different sub-families. Additional domains, such as substrate binding 'reader' domains, confer functionality and specificity to the various families.

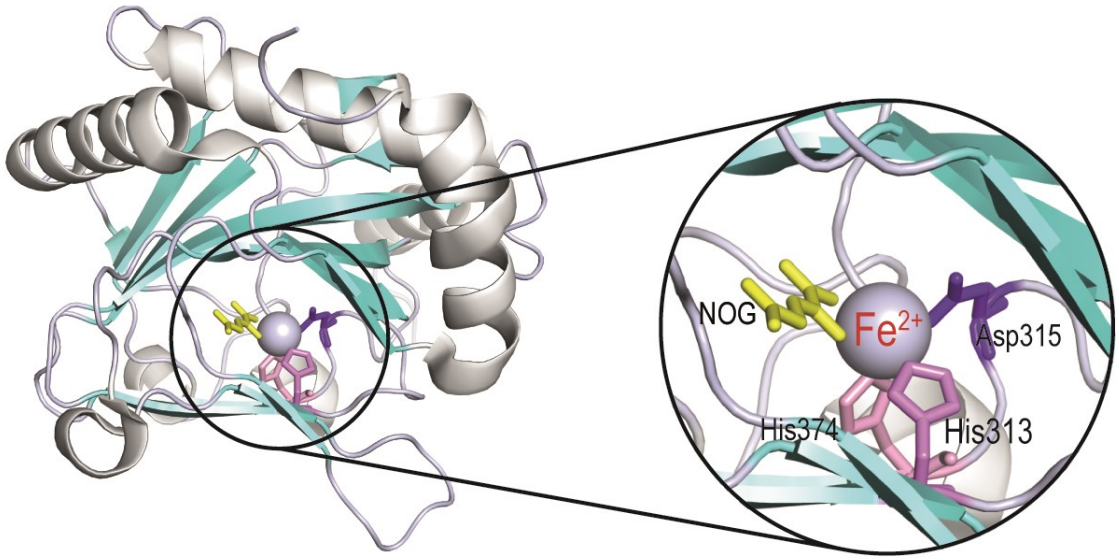


Figure 1.5 *Ribbon representation of a representative 2OG oxygenase, PHD2 (PDB ID: 3HQR), showing double-stranded β-helix (teal) and α-helices (grey). Stick representation of active site His-X-Asp/Glu-Xn-His Fe^{2+} binding motif residues (magenta, pink, purple) common to this class of enzymes. N-oxalylglycine (NOG), an inhibitory 2OG analogue is shown bound in the 2OG binding site of these enzymes (yellow).*

Structural and spectroscopic observations of Enz.Fe(II).2OG.substrate complexes and kinetic investigations indicate that catalysis by the 2OG oxygenases conforms to a consensus mechanism.36,41 Fe^{2+} is held in octahedral geometry within the His-X-Asp/Glu...His triad motif (Figure 1.6). 2OG binds to Fe^{2+} via its ketol and carboxylate oxygens, displacing two water molecules. The 5-carboxylate of 2OG is usually bound to the side-chain of a basic residue (Arg/Lys). Binding of the primary substrate at the active site weakens the interaction between Fe^{2+} and the final coordinated water molecule (Figure 1.6) (II).

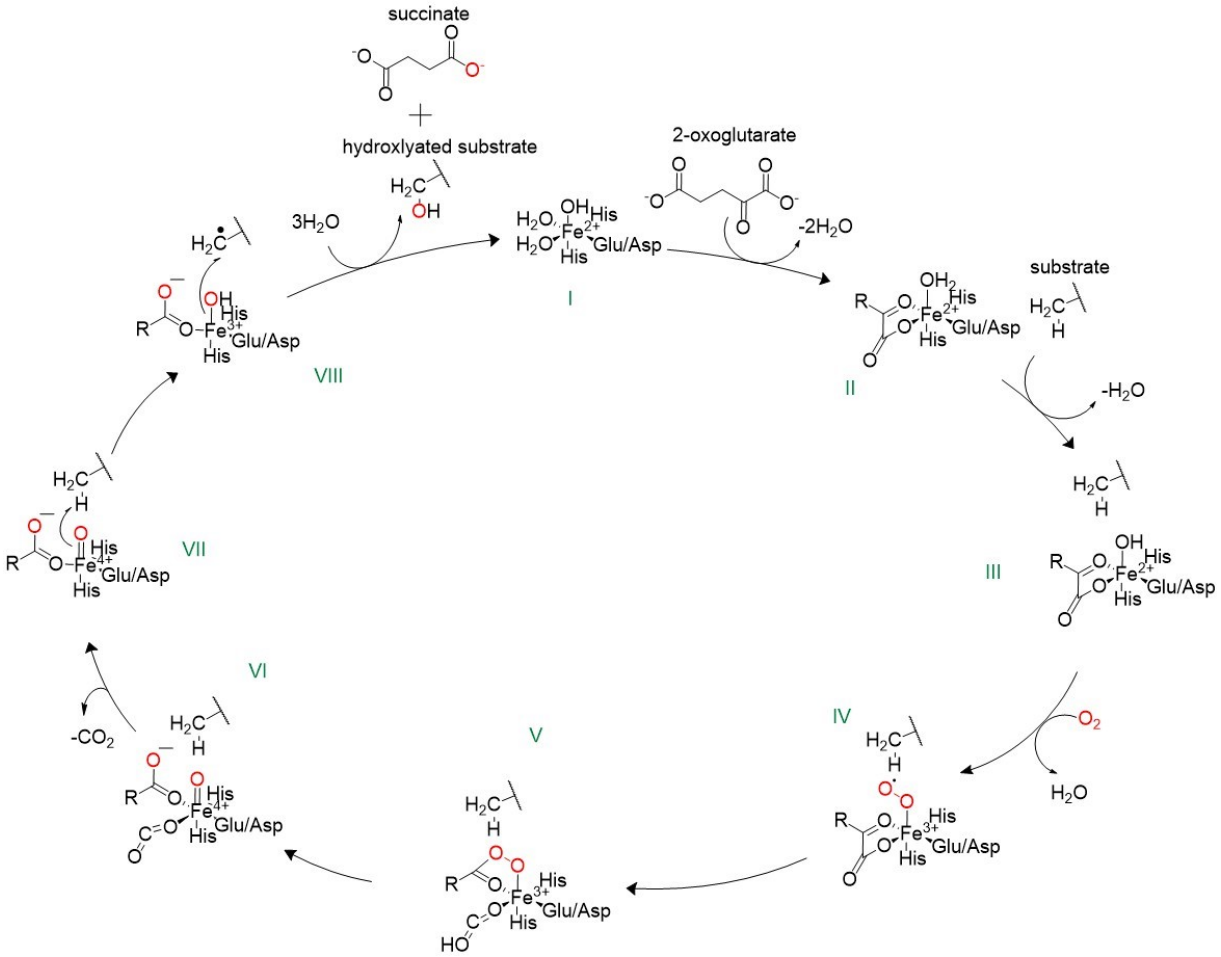


Figure 1.6 2OG oxygenase consensus mechanism. *2OG binding to Fe^{2+} displaces two water molecules (II). Substrate binding weakens binding of the final water molecule (III), allowing binding of oxygen and displacement of water (IV). Oxidation of 2OG results in the formation of succinate and carbon dioxide, and a highly reactive Fe^{4+}-oxo species (V-VII). The Fe^{4+}-oxo species then abstracts a proton from the prime substrate (VII), forming a hydroxyl-Fe^{3+} species which is transferred to the radical substrate carbon, resulting in hydroxylation of substrate (VII-VIII). Oxygen atoms derived from O_2 shown in red.*

This allows binding of oxygen and subsequent oxidation of 2OG, resulting in the formation of succinate, CO2 and a highly reactive oxo-Fe^{4+} species (as observed by Ultraviolet–visible (UV-Vis), electron paramagnetic resonance and Raman spectroscopy) (Figure 1.6) (V-VII).[43,44] The oxo-Fe4+ species abstracts a proton from the prime substrate, forming a hydroxyl-Fe^{3+} species which is then transferred to the resulting radical substrate carbon (Figure 1.6) (VIII-IX). In the case of histone demethylation, spontaneous collapse of the hemiaminal intermediate formed results in demethylation. Other reactions including halogenation, epimerisation, desaturation and ring cyclisation arise from abstraction or re-arrangement of the carbon radical.[37]

1.4 JmjC histone demethylases

The JmjC-KDMs are 2OG oxygenases which catalyse demethylation of *N*(Ɛ)-methyl lysines on histone tails. JmjC-KDM structure differs slightly from other 2OG oxygenases in that within the JmjC domain, the basic 2OG coordinating residue is located on the 4^{th} β strand, whilst in other 2OG oxygenases this is located on the eighth β strand.[45] Despite this differences in structure, JmjC-KDMs appear to share the consensus 2OG oxygenase mechanism. *N*(ε)-methyl lysine undergoes JmjC-KDM catalysed hydroxylation, and spontaneous collapse of the hemiaminal produces the de-methylated lysine (Figure 1.7). In addition to the catalytic JmjC domain, many JmjC-KDMs also have "reader" domains which act to target the catalytic domains to the correct substrate. These domains include DNA binding and recognition domains such as AT-rich interaction domain (ARID) and CXXC,[46] chromatin reader domains such as bromodomains and substrate binding domains such as planthomeo or Tudor domains.[47]

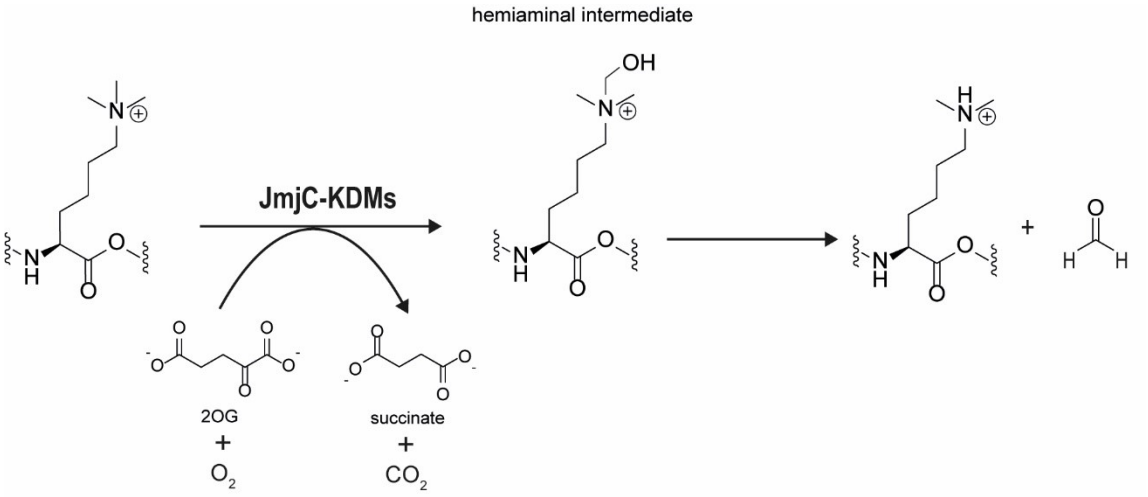


Figure 1.7 JmjC-KDM catalysed demethylation of N(ε)-methylated lysine on histone tails. *JmjC-KDMs catalyse hydroxylation of the N(ε) methyl lysine forming a hemiaminal intermediate which rapidly collapses to release formaldehyde and the demethylated substrate.*

Though over 30 2OG oxygenases have been identified with JmjC domains, not all catalyse histone lysine demethylation, and a number of JmjC-KDMs have also been shown to catalyse arginine demethylation.[48,49] The JmjC-KDMs are divided in to sub-families based on their sequence identity and substrate specificity, with one largely belying the other. Many studies have characterised the substrate specificity of JmjC-KDMs both *in vitro* and in cells (Table 1.1).

JmjC-KDM	H3K4			H3K9			H3K27			H3K36			H3K79			H4K20			H1.4K26			Refs.
	1	2	3	1	2	3	1	2	3	1	2	3	1	2	3	1	2	3	1	2	3	
KDM2A										■	■											34,50,51
KDM2B			■							■	■			■	■							
KDM3A				■	■																	52–56
KDM3B				■	■																	
KDM3C				■	■																	
KDM4A					■	■		■	■		■	■								■	■	53,57–63
KDM4B					■	■			■		■	■								■	■	
KDM4C					■	■		■	■		■	■								■	■	
KDM4D					■	■														■	■	
KDM4E					■	■		■	■													
KDM5A		■	■																			64–68
KDM5B		■	■																			
KDM5C		■	■																			
KDM5D		■	■																			
KDM6A								■	■													63,69–74
KDM6B								■	■													
KDM6C								■	■													
KDM7A				■	■		■	■														75–79
KDM7B							■	■									■					
PHF2					■	■																
KDM8											■	■										80–82
MINA53						■																
NO66	■	■	■								■	■										

Table 1.1 Substrate specificity of JmjC-KDMs to date. *Green – Activity demonstrated in vitro and in cells. Grey - Activity demonstrated in vitro only. Yellow - Assignment as histone demethylase is controversial.*

1.5 The KDM6 sub-family of JmjC histone demethylases

The KDM6 sub-family of JmjC histone demethylases consists of KDM6A, KDM6B and KDM6C (also known as UTX, JMJD3, UTY respectively). KDM6A and KDM6B were first identified as specific H3K27Me3 histone demethylases by a number of groups in 2007.[70–73] It was previously thought that KDM6C was inactive. However, work by Walport *et al*. demonstrated KDM6C catalysed demethylation H3K27Me3 peptides *in vitro*, albeit at vastly reduced levels of activity compared with KDM6A and KDM6B.[74]

KDM6B also catalyses demethylation of methylarginine, though the biological consequences of this are yet to be elucidated.[49] Methylation status is a key regulator of gene transcription, with H3K27Me3 marking transcriptionally inactive genes. Both KDM6A and KDM6B catalyse demethylation of H3K27Me3, resolving chromatin to an active transcriptional state.

Domain structure is largely conserved within the KDM6 sub-family (Figure 1.8). Each enzyme has a C-terminal catalytic JmjC domain and a zinc-binding domain, also known as the 'GATA-like' domain, which is essential to substrate binding. The zinc-binding domain is inserted within a helical domain, and is flanked by alpha helices. The helical and JmjC domains pack together via hydrophobic interactions.[83,84] Both KDM6A and KDM6C also contain N-terminal tetratricopeptide repeat (TPR) domains, although the function of these domains is unknown, and they are not required for catalytic activity.[63] TPR domains are present in a range of functionally unrelated proteins and usually mediate protein-protein interactions within multi-protein complexes.[85]

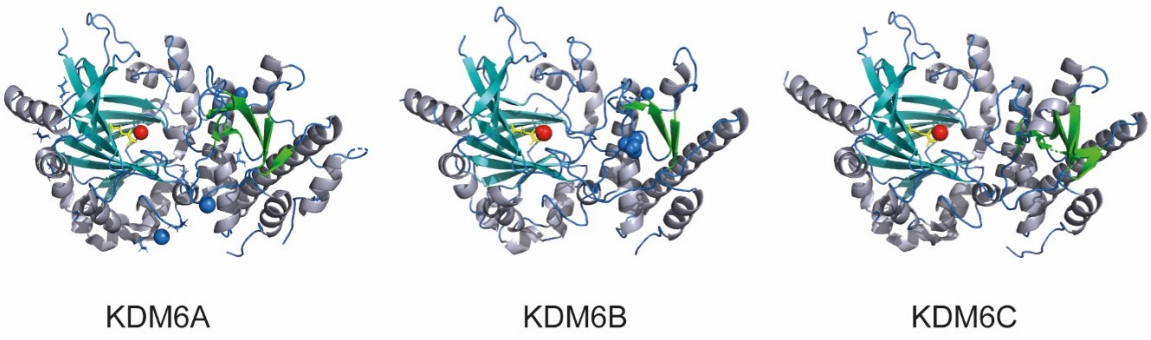


Figure 1.8 KDM6A/B/C crystal structures reveal conserved structure within the catalytic region. *Views from KDM6A/B/C crystal structures (visualised using pyMOL PDB ID: 3AVR, 2XUE and 3ZLI respectively). β-helix fold shown in teal. Loop shown in blue. Helical region shown in grey. Zinc binding domain shown in green. NOG shown in yellow. Fe^{2+} centre shown in red. Zinc shown in blue.*

KDM6A and KDM6B have no activity towards other methylated H3 lysine residues such as H3K4, H3K9, H3K36 or H4K20.[63,69,73,83,86] Within histone peptides, the amino acid sequences directly surrounding H3K9 and H3K27 are very similar and include identical

‘‘A-R-Kme-S’’ motifs. Substrate specificity for KDM6A arises from substrate binding at both the catalytic domain and the zinc-binding domain. Structural studies by Sengoku *et al* revealed that the catalytic JmjC domain binds H3 residues 25–33, recognizing H3R26, H3A29, and H3P30 in a sequence-specific manner, whilst H3K27Me3 binds in the catalytic pocket and the zinc-binding domain binds residues 17–21 of H3.[83] Recent studies by Jones *et al* demonstrated a similar mode of substrate binding in KDM6B.[84] Although KDM6A and KDM6B differ in primary sequence within the H3L20 binding pocket of the zinc binding domains, where two histidines in KDM6A have been replaced by a glutamate and a tyrosine, peptide binding within this region is similar.[84] Specific residues in both binding regions of the substrate are essential to catalytic activity, explaining both observed specificity and the requirement for the zinc-binding domain.[83]

1.6 The role of KDM6 mediated gene regulation in development

Histone lysine methylation is a stable modification, well-suited to maintain gene expression patterns and cell identity during development and differentiation. The transformation of a single cell to a multicellular organism is achieved through differentiation. Spatio-temporal regulation of gene expression under epigenetic control yields a range of specialised cell lineages from initially totipotent stem cells. The JmjC-KDMs regulate development by maintaining or removing histone lysine methylation states which repress or activate gene expression, such as H3K27Me3 or H3K4Me3, respectively.[87] Bivalent histone modifications, where both activating and repressive modifications occur together, are said to be ‘poised’ for transcription, and represent an important regulatory mechanisms in development.[29]

Both KDM6A and KDM6B are essential to normal embryonic development, tissue-specific differentiation and organogenesis.[88,89] In humans, constitutional KDM6A mutations have been identified as a cause of Kabuki syndrome.[90] Homozygous deletion of

KDM6A causes embryonic lethality in mice, *Caenorhabditis elegans* and *Dropsophila melanogaster* in a sex-specific manner.[91] KDM6B deletion causes embryonic and postnatal lethality in mice.[92,93] However, time of death and the precise phenotype of KDM6B knockout mice are dependent on the gene dosage and gene deletion strategy used to generate knockout mice, consistent with the role of KDM6B regulation in the development of multiple tissue/organ systems.[94,95] KDM6A and KDM6B have key roles in cardiovascular and neural development. H3K27Me3 levels decrease in many neural-specific genes during differentiation.[96,97] KDM6B is upregulated during differentiation of embryonic stem cells (ESC) to neuronal lineages,[96] and overexpression of KDM6B in neural progenitor cells lead to expression of neuronal genes.[98] KDM6A is essential for retinoic acid induced neural differentiation in an ESC model.[99] Both KDM6A and KDM6B null ESC's have reduced capacity for cardiac lineage commitment.[100,101] Murine KDM6A deficiency leads to embryonic lethality and severe cardiac defects concurrent with reduced expression of cardiac genes.[101] KDM6B also regulates lung development. Deletion and ablation studies resulted in defective lung development, shown to be mediated by downregulation of developmental genes, accounting for perinatal mortality observed in both studies. [92,93]

KDM6A, KDM6B and KDM6C are all known to have histone demethylase independent roles in gene regulation.[102] Many of the studies conducted investigated the effect of KDM6 deletion on development, which could detect effects unrelated to KDM6 catalytic activity. A number of studies have addressed this issue. A study by Jiang *et al* demonstrated that catalytic activity of KDM6A was required for rescue of KDM6B knockout in endoderm differentiation.[103] A recent study by Chung *et al* demonstrated that KDM6B catalytic activity was required for normal development of bovine embryos. In the study H3K27Me3 levels were correlated with KDM6B knockdown, and this

correlation was recapitulated by small molecule KDM6B inhibition using the small molecule inhibitor GSK-J4.[104] Correlation between H3K27Me3 changes and KDM6A/B knockout suggests that KDM6 histone demethylases regulate development by catalytic removal of repressive H3K27Me3 marks resulting in gene expression, although histone demethylase independent regulation by the KDM6s is also significant.[89,105]

1.7 The role of KDM6 mediated gene regulation in disease

Both KDM6A and KDM6B have roles in disease including cancer and inflammation.[88,89] KDM6A has been identified as a bona-fide tumour suppressor gene; both deletions and loss-of-function mutations have been identified in multiple cancer types including multiple myeloma, oesophageal and renal cancer.[106,107] Similarly, KDM6B has also been identified as a tumour suppressor, regulating oncogenic stress induced senescence through gene promoter demethylation.[108] However, KDM6B expression is upregulated in a number of cancers including lymphoblastic leukemia and hodgkins lymphoma, where it is associated with upregulation of oncogenes.[109,110] Interestingly KDM6B has been shown to up-regulate estrogen receptor expression in plueral mesothelioma in response to hypoxia.[111] Inhibition of KDM6B by the small molecule inhibitor GSK-J4 results in slowed cell growth in a number of cancer cell types,[109,112,113] indicating the potential of KDM6B inhibition in cancer therapeutics.

KDM6B has been extensively linked to inflammatory gene regulation, especially with regard to regulation of macrophage phenotypes and inflammatory mediator expression.[114] KDM6B has a key role in the regulation of pro- and anti-inflammatory macrophage phenotypes. KDM6B expression is up-regulated in response to inflammatory stimulators such as serum amyloid A (SAA) and lipopolysaccharide (LPS).[115,116] KDM6B mediated expression of inflammatory genes via reduction of repressive H3K27Me3 marks has been demonstration for many inflammatory genes.[70,115,117,118] Consistent with these

observations, inhibition of KDM6B using the small molecule inhibitor GSK-J4 reduced the pro-inflammatory macrophage response.[118] KDM6B has roles in various conditions related to inflammation and immune cell/macrophage phenotypes including infection and sepsis,[70,119] autoimmune conditions,[120,121] neurodegenerative disease and atherosclerosis.[122–126]

Considering the role of KDM6 JmjC-KDM mediated gene regulation in many disease areas, pharmacological inhibition of these enzymes presents an exciting avenue for therapeutic intervention. However, as KDM6 JmjC-KDMs regulate a vast array of cellular processes, it is likely that inhibitors targeting KDM6 would result in any number of off-target effects, as underscored by the oncogenic effect of KDM6A loss of function mutations.[106,107] However, this issue is not unique within therapeutics targeting epigenetic pathways, and various strategies to allow cell or tissue-specific dosing of inhibitors are being developed.[127]

1.8 Hypoxia and the hypoxic response

Oxygen makes up 21% of the air we breathe, but this concentration drops as oxygen is transported within the body and diffuses within tissues. Perfusion of different tissues is variable, and accordingly, the concentration of oxygen in different tissues also varies from approximately 3-14%.[128] Oxygen is essential for eukaryotic cellular respiration, and cells cannot survive for prolonged periods without it. Abnormally low oxygen levels (generally considered to be <2% oxygen),[132] are termed ‘hypoxia’, and can disrupt normal cellular processes. Hypoxia has an essential regulatory role in normal development. Insults to the normal gestational oxygen conditions, both hypoxic and hyperoxic, lead to morphological defects,[129–131] and oxygen tension has been shown to regulate differentiation potential in various embryonic and induced stem cell models.[133]

Hypoxia is known to have a pathophysiological role in a number of diseases including cancer, cardiovascular disease and inflammation.[134] Hypoxia is characteristic of various cardiovascular disease states including ischaemic diseases such as myocardial infarction and stroke,[135] but also conditions including atherosclerosis and anaemia.[136,137] Hypoxia contributes to inflammation due to conversion of regulatory networks involved in both the hypoxic response and inflammatory gene regulation, for example the nuclear factor-κβ (NF- κβ) pathway.[130] Tumour hypoxia arises due to insufficient vascularisation, and is associated with resistance to cancer therapies.[138] Tumour hypoxia leads to activation of the HIF-mediated hypoxic response (see below), and a shift in metabolism from oxidative phosphorylation to glycolysis known as the 'Warburg effect' - a recognized hallmark of cancer.[139]

The reaction of an organism to reduced oxygen availability is termed the hypoxic response. The hypoxic response encompasses both physiological and molecular responses - so-called 'Huffing and HIF-ing' as described by Guillemin *et al*.[140] The chronic hypoxic response is mediated by HIF, a transcription factor which activates the transcription of hundreds of genes involved in hypoxic responses including production of erythropoietin (EPO), angiogenesis, inflammation and metabolism, amongst numerous other processes.[138,141,142] The HIF-mediated hypoxic response has been well characterised over the past two decades; recent reviews include those by Kaelin and Ratcliffe, Myllyharju and Semenza.[138,142–144] HIF consists of two subunits: HIF-α and HIF-β. Dimerisation of the subunits is required for binding and transcription of the hypoxia controlled genes. HIF-β is expressed constitutively, and on binding to HIF-α enables translocation of the complex to the nucleus. HIF-α has three isoforms, HIF-1α, HIF-2α and HIF-3α, although only HIF-1α and HIF-2α levels are dependent on oxygen availability.[145] Both the cellular

levels of HIF-α and its transcriptional activity are regulated via posttranslational modifications, the deposition of which is regulated by changes in oxygen concentration.

In normoxia, hydroxylation of HIF-1/2α is catalysed by four enzymes, known as the the HIF hydroxylases. These enzymes consist of prolyl hydroxylases, prolyl hydroxylase domain 1-3 (PHD1-3) and an asparaginyl hydroxylase, factor inhibiting HIF (FIH). The PHDs catalyse hydroxylation of one or two prolyl residues in HIF-1/2α within the C-terminal oxygen dependent degradation domain (CODD) and the N-terminal oxygen dependent degradation domain (NODD). This allows binding of the von Hippel–Lindau tumour suppressor protein (pVHL) and ubiquitin ligase, resulting in HIF-1/2α degradation via the proteasome (Figure 1.9). FIH catalyses hydroxylation of an asparaginyl residue within the C-terminal transactivation domain (CAD) of HIF-1/2α, preventing interaction with the transcriptional co-activator p300/CBP and consequently preventing transcription of hypoxic genes (Figure 1.9).[138] Interestingly, these enzymes also belong to the 2OG oxygenase family, and have an absolute requirement for oxygen. Kinetic characterisation of the PHD enzymes has revealed that their activity is highly sensitive to oxygen concentration, with $K_M(O_2)$ values between 230 μM-1.7mM.[43,146–148] In contrast, FIH does not appear to be as sensitive to oxygen as the PHDs; its $K_M(O_2)$ value is reported to be lower at 90–150 μM compared with the PHDs,[149,150] and CAD hydroxylation is maintained in clear cell renal cell carcinoma RCC4 cells exposed to an environment of 0.25% oxygen.[148] Calibration curves allow conversion of percentage oxygen (%) to micromolar concentration of dissolved oxygen concentration. These curves were generated using a fluorescent oxygen detecting electrode (FOXY) to determine the concentration of buffer solutions equilibrated under atmospheres of known percentage oxygen. For instance, calibration curves determined by Hancock *et al,* (Appendix 7),

show that dissolved oxygen concentration is proportional to percentage oxygen in with the relationship O_2 concentration (μM) = 9.026*(O_2%).[189]

In hypoxia, the activity of the PHD HIF hydroxylases is reduced, and HIF levels are stabilised, resulting in HIF-mediated expression of hypoxia associated genes. The PHD HIF hydroxylases are cellular oxygen sensors that provide a direct link between oxygen concentration and regulation of the hypoxic response pathway.

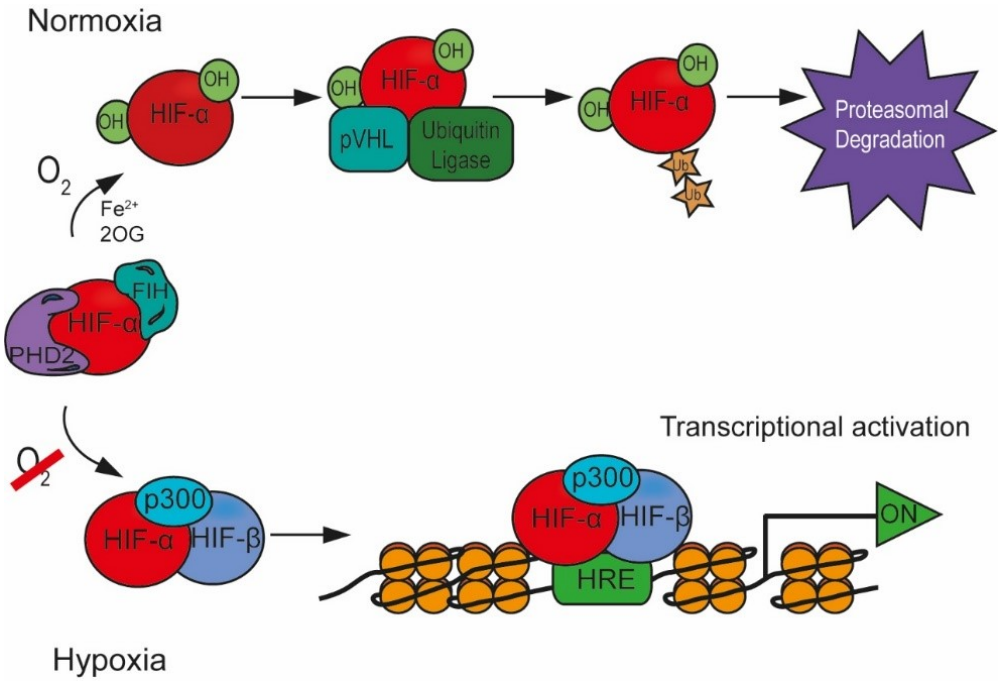


Figure 1.9 The HIF-mediated hypoxic response. *In normoxia, HIF hydroxylases, e.g PHD2 and FIH, catalyse hydroxylation the HIF-α subunit, targeting HIF-α for ubiquitination and degradation by the proteasome. In hypoxia, the activity of the HIF hydroxylases is reduced and HIF-α is not degraded. HIF-α translocates into the nucleus, binding to the HIFβ subunit and the p300 coactivator. The HIF-p300 complex then binds to hypoxia response elements (HREs) at gene promoter regions, activating the transcriptional hypoxic response. Figure adapted from Hancock et al with permission from Future Medicine.*[134]

1.9 Hypoxia induces alteration of epigenetic marks

HIF binds to the DNA sequences of its target genes in the context of a complex chromatin structure. Hypoxia has been shown to alter both epigenetic marks and the activity and expression of epigenetic modifiers. Alterations to epigenetic marks can arise due to changes in the expression of epigenetic modifiers, many of which are HIF-target genes. It

has been hypothesised that long-term HIF-mediated changes are orchestrated via epigenetic regulation. The activity of epigenetic modifiers may also be altered in hypoxia, leading to changes in epigenetic marks. Further, several epigenetic modifiers activate HIF either by direct interaction, or by interaction with components of the hypoxic response pathway.[151,152]

Various studies have demonstrated that hypermethylation of DNA at the promotors of HIF target genes prevents HIF binding.[153–156] Analysis of the DNA methylation profiles of over 3,000 tumour samples in The Cancer Genome Atlas by Thienpont *et al*, revealed that DNA hypermethylation is strongly associated with tumour hypoxia.[157] Hypermethylation has been associated with hypoxic loss of TET activity,[157,158] and HIF-dependent elevation of DNMT levels[159]. Conversely, global hypomethylation in hypoxia has been related to upregulation of TET enzymes resulting in 5mC demethylation,[159] and to upregulation of Methionine adenosyltransferase 2A (MAT2A) a protein which is involved in homeostasis of the methyl donor S-adenosylmethionine (SAM).[160] Additionally, hypoxic down-regulation of DNMT1 and DNMT3A in colorectal cancer cells was also reported.[161]

Though global changes to histone acetylation levels have been reported in hypoxia,[162] the effect of HATs and HDACs on HIF regulation are better characterised. Around 40% of HIF target genes are dependent on HIF's association with the HAT p300 or CBP, both of which are HATs.[163] HDAC7 has been found to enhance transcriptional activity within this complex,[164] and HDAC1 and HDAC3 also regulate HIF-1α stability and transcriptional activity.[165] Activity of HDAC1 and HDAC2 was found to be increased in hypoxia via increased phosphorylation of the enzymes by the protein kinase CK2 (the activity of which is itself increased in hypoxia), resulting in downregulation of pVHL and HIF activation (although levels of histone acetylation were not assessed). HDAC inhibition

has been shown to block tumour angiogenesis,[166] and reduce ischemia-reperfusion injury by reduction of HIF activity and gene expression.[167]

1.10 Histone methylation and hypoxia

Global and gene-specific alterations to histone methylation patterns have been reported in hypoxia across a wide range of cell lines, and hypoxia-induced gene specific histone methylation changes have been shown to result in alterations to gene expression (Table 1.2).

Cell line	% O_2	Changes to global methylation	Gene locus and change in expression levels	Altered methylation status at promoter	Reference
A549	NS	H3K9me2 ↗ H3K9me3 ↗	--	--	[168]
Fetal lung type II	2.0	H3K9me2 ↗	SP-A ↗	H3K9me2 ↗	[169]
A549, HOS, HEK293	0.5	H3K9me2 ↗	MLH1 ↘, DHFR ↘	H3K9me2 ↗	[170]
Hepa1-6	0.2	H3K4me2 ↗ H3K4me3 ↗ H3K79me2 ↗ H3K27me3 ↘	AFP ↘, ALB ↘	H3K9me2 ↗ H3K27me2 ↗	[171]
		H3K9me2 ↘ H3K4me1 ↗	EGR1 ↗	H3K9me2 ↘, H3K27me2 ↘	
HepG2	0.1-5	H3K4me2 ↗ H3K4me3 ↗ H3K9me2 ↗ H3K36me3 ↗	--	--	[172]
BEAS-2B, A549	1.0	H3K4me3 ↗	--	--	[173]
RAW264.7		H3K9me2 ↗ H3K9me3 ↗ H3K36me3 ↗	CCL2 ↘, CCR1 ↘, CCR5 ↘	H3K9me2 ↗ H3K9me3 ↗	[174]
RKO NIH 3T3		H3K9me3 ↗	PP2A ↘	H3K9me3 ↗	[175]
McA-RH7777	1.0 or 5.0	H3K9me3 ↗	--	--	[176]
IMR-90	<0.5	ND	INK4a does not change	H3K27me3 ↗ H3K4me3 ↗	[177]
RKO	<0.1	ND	APAK ↘	H3K9me3 ↗	[178]
MCF-7 RKO	0.01	ND	BRCA1 ↘ RAD51 ↘	H3K4me1/2/3↘	[179]
HeLa	0.5	None observed	MCP1 ↘	H3K4me3 ↗ H3K9me2 ↗	[180]
Human adipocyte-derived stem cells	0.5	H3K4me3 ↗ H3K9me2 ↗ H3K27me3 ↗	Various (>10 genes)	Various	[181]
RKO cells	0.1 or 2.0	H3K9me3 ↗ H3K36me3 ↗	HIF-1A	H3K9me3 ↗	[182]
hPDCs	NS	--	BMP-2	H3K27me3 ↗	[183]

Table 1.2 Hypoxia leads to changes in histone lysine methylation. *Both global and gene specific changes to histone lysine methylation, (gain (↗) and loss (↘)) with associated changes in gene expression, have been observed in cells exposed to hypoxia. NS = not stated, ND = not determined. Table adapted and updated with permission of Future Medicine Ltd from Hancock et al.*[184]

Alterations to cellular levels of both histone demethylases and histone methyltransferases has been reported in hypoxia. Hypoxia-induced H3K9me2 increase was correlated with an increase in histone methyltransferase G9a protein in murine ESCs.[170,185] A recent publication by Casciello *et al*, linked this increase to G9a protein stabilisation, mediated through reduced PHD2 catalysed proline hydroxylation of G9a in hypoxia, resulting in reduced ubiquitination by pVHL and proteasomal degradation.[186]

As with other 2OG oxygenases including the PHDs and TET families, JmjC-KDMs utilise oxygen in their catalysis. There has been increasing interest in kinetic characterisation of 2OG oxygenases with regards to their oxygen sensitivity. $K_M(O_2)$ values have been determined for a number of 2OG oxygenases, with a number of enzymes showing high sensitivity to oxygen concentration in a physiologically relevant oxygen concentration range.[184] Differential oxygen sensitivity has been demonstrated for the KDM4 sub-family of histone demethylases.[187–189] Biochemical characterisation of KDM4A and KDM4E demonstrated a high level of oxygen sensitivity *in vitro*.[188,189] Pre-steady state results for KDM4E show that the rate of reaction of the enzyme:Fe(II):2OG:substrate complex with O_2 is relatively slow, as observed for PHD2.[188] Immunofluorescence experiments in U2OS cells conditionally overexpressing KDM4A showed that the cellular activity of KDM4A against its primary substrate, H3K9me3, displayed a graded response to oxygen concentrations, in line with the *in vitro* result.[189] Differential sensitivity to hypoxia of overexpressed KDM3A and KDM4B in HeLa cells incubated at 0.2% oxygen was demonstrated by Beyer *et al*.[194] KDM4B catalysed demethylation of H3K9me3 was attenuated in hypoxia, while the activity of KDM3A was maintained.[194] Differential reduction of JmjC-KDM activity may result in an array of histone methylation changes which are dependent on the degree of hypoxia.

Various studies have shown upregulation of a sub-set of JmjC-KDMs including KDM3A, KDM4B, KDM4C, KDM5B, KDM5C and KDM6B in hypoxia (Table 1.3). KDM3A, KDM4B, KDM4C, KDM5Band KDM5C are HIF-1α target genes,[190] whilst KDM6B is upregulated via both HIF-2α and HIF-2α.[191,192] Besides these, other JmjC-KDMs are upregulated in hypoxia in an apparently HIF-independent manner. Adding an additional layer of complexity, several JmjC-KDMs, including KDM6B, bind to and activate HIF (Table 1.3).

	Hypoxic induction	HIF induction	HIF binding/ cooperation	References
KDM2A/FBXL11/JHDM1A	+			193
KDM2B/FBXL10/JHDM1B	+			193
KDM3A/JMJD1A	+	+	+	193–199
KDM3B/JMJD1B	+			193
KDM3C/JMJD1C	+			193
HR				
KDM4A/JMJD2A				
KDM4B/JMJD2B	+	+		193,194,196,197,200,201
KDM4C/JMJD2C	+	+	+	193,194,196,202
KDM4D/JMJD2D				
KDM4A/JMJD2E				
KDM5A/JARID1A/RBP2	+			193
KDM5B/JARID1B/PLU1	+	+		179,193,203
KDM5C/JARID1C/SMCX	+	+		193
KDM5D/JARID1D/SMCY	+			193
KDM6A/UTX	+			193
KDM6B/JMJD3	+	+	+	191,193,204
KDM7A/KIAA1718	+			193
KDM7B/PHF8	+			193,205
PHF2	+			193

Table 1.3. *Hypoxia leads to increased JmjC-KDM expression, in both a HIF-dependent and HIF-independent manner. Several JmjC-KDMs also bind to and/or activate HIF. Table adapted and updated with permission of Future Medicine Ltd from Hancock et al.*[184]

It has been proposed that the upregulation of KDMs acts as a compensatory mechanism whereby increased levels of these enzymes compensate for their reduced activity in depleted oxygen conditions.[193,194] Studies by Hancock *et al* demonstrated hypoxic inhibition of overexpressed KDM4A in U2OS, whilst Lee *et al* reported hypoxic

inhibition of overexpressed KDM4A, KDM4C, KDM6B and to a lesser extent KDM5B in hADSC.[181] Together these studies suggest that overexpression may not be able to entirely overcome the reduction of activity in hypoxia, depending on the individual oxygen sensitivity of the JmjC-KDM in question.

Hypoxia is a pathophysiological stimulus spanning many diseases. Increasing evidence indicates that this is, at least in part, due to aberrant epigenetic regulation arising from alterations to HIF-associated gene regulation or the direct effect of reduced oxygen availability on the network of proteins mediating epigenetic regulation. The studies described above demonstrate the complex relationship(s) between hypoxia, HIF and epigenetic regulation of gene expression. The effect of hypoxia on epigenetic marks seems to be highly context specific (Table 1.2), indicating the outcome of hypoxia is dependent on a number of factors including the cell type, genomic targets and the activity and balance of epigenetic modifiers present in a given cellular environment.

1.11 Thesis objectives

The KDM6 sub-family of JmjC histone demethylases have important roles in development and disease. Reduced oxygen availability is a feature of both development and several of these diseases including cancer, inflammation and cardiovascular disease. The HIF-mediated hypoxic response stimulates up-regulation of histone demethylases including KDM6B, whereas recent studies have demonstrated that the activity of various 2OG oxygenases including JmjC histone demethylases is differentially limited by oxygen availability. In addition, hypoxia is known to alter the metabolic milieu, resulting in changes to cellular TCA cycle intermediate concentrations (see Chapter 4, Section 4.1). The relationship between hypoxia, HIF and JmjC-KDM mediated gene regulation is likely to be complex, and will have important implications for transcriptional outcome. A deeper understanding of the activity of these enzymes in physiologically relevant

conditions is desirable, particularly in the context of hypoxic disease states. Atherosclerosis, a chronic inflammatory condition, is a hypoxic disease state. Epigenetic regulation of macrophage functions, including by KDM6B, plays a central role in the pathogenesis of this disease.

The aims of the work described in this thesis were to evaluate KDM6 activity in the context of cellular hypoxia, both in terms of reduced oxygen availability and alterations to the metabolic milieu. Answers to the following questions were sought:

- What is the oxygen sensitivity of KDM6A and KDM6B *in vitro*? (Chapter 2)
- Does oxygen availability affect cellular KDM6B activity, and if so is this in line with *in vitro* oxygen sensitivity? (Chapter 3)
- How do hypoxically induced changes to metabolism, i.e. concentration of the TCA cycle intermediates affect KDM6B activity *in vitro* and in cells? (Chapter 4)
- How does hypoxia affect cellular models of atherosclerosis, an epigenetically regulated hypoxic disease state? (Chapter 5)
- Does JmjC-KDM inhibition modulate foam cell formation, the primary pathogenic pathway in atherosclerosis? (Chapter 5)

1.12 References

1. Berger, S. L., Kouzarides, T., Shiekhattar, R. & Shilatifard, A. An operational definition of epigenetics. *Genes Dev* **23,** 781–783 (2009).
2. Luger, K., Mader, A. W., Richmond, R. K., Sargent, D. F. & Richmond, T. J. Crystal structure of the nucleosome core particle at 2.8 A resolution. *Nature* **389,** 251–260 (1997).
3. Arents, G., Burlingame, R. W., Wang, B. C., Love, W. E. & Moudrianakis, E. N. The nucleosomal core histone octamer at 3.1 A resolution: a tripartite protein assembly and a left-handed superhelix. *Proc. Natl. Acad. Sci. U. S. A.* **88,** 10148–52 (1991).
4. Gao, M. *et al.* Histone H3 and H4 N-terminal tails in nucleosome arrays at cellular concentrations probed by magic angle spinning NMR spectroscopy. *J. Am. Chem. Soc.* **135,** 15278–81 (2013).
5. Saikusa, K. *et al.* Gas-phase structure of the histone multimers characterized by ion mobility mass spectrometry and molecular dynamics simulation. *Anal. Chem.* **85,** 4165–71 (2013).
6. Iwasaki, W. *et al.* Contribution of histone N-terminal tails to the structure and stability of nucleosomes. *FEBS Open Bio* **3,** 363–9 (2013).
7. Rössler, J. *et al.* Hypoxia-induced erythropoietin expression in human neuroblastoma requires a methylation free HIF-1 binding site. *J. Cell. Biochem.* **93,** 153–161 (2004).
8. Klose, R. J. & Bird, A. P. Genomic DNA methylation: the mark and its mediators. *Trends Biochem. Sci.* **31,** 89–97 (2006).
9. Paulsen, M. & Ferguson-Smith, A. C. DNA methylation in genomic imprinting, development, and disease. *J. Pathol.* **195,** 97–110 (2001).
10. Lundin, C. *et al.* Methyl methanesulfonate (MMS) produces heat-labile DNA damage but no detectable in vivo DNA double-strand breaks. *Nucleic Acids Res.* **33,** 3799–3811 (2005).
11. Lingens, F., Haerlin, R. & Sussmuth, R. Mechanism of mutagenesis by N-methyl-N'-nitro-N-nitrosoguanidine (MNNG). Methylation of nucleic acids by N-

trideuteriomethyl-N'-nitro-N-nitrosoguanidine (D3-MNNG) in the presence of cysteine and in cells of Escherichia coli. *FEBS Lett.* **13,** 241–242 (1971).

12. Moore, L. D., Le, T. & Fan, G. DNA methylation and its basic function. *Neuropsychopharmacology* **38,** 23–38 (2013).

13. He, Y.-F. *et al.* Tet-mediated formation of 5-carboxylcytosine and its excision by TDG in mammalian DNA. *Science* **333,** 1303–7 (2011).

14. Nabel, C. S. *et al.* AID/APOBEC deaminases disfavor modified cytosines implicated in DNA demethylation. *Nat. Chem. Biol.* **8,** 751–758 (2012).

15. Bannister, A. J. & Kouzarides, T. Regulation of chromatin by histone modifications. *Cell Res.* **21,** 381–395 (2011).

16. Tan, M. *et al.* Identification of 67 histone marks and histone lysine crotonylation as a new type of histone modification. *Cell* **146,** 1016–28 (2011).

17. Strahl, B. D. & Allis, C. D. The language of covalent histone modifications. *Nature* **403,** 41–45 (2000).

18. Kato, S., Inoue, K. & Youn, M.-Y. Emergence of the osteo-epigenome in bone biology. *IBMS Bonekey* **7,** 314–324 (2010).

19. Strahl, B. D. & Allis, C. D. The language of covalent histone modifications. *Nature* **403,** 41–5 (2000).

20. Arrowsmith, C. H., Bountra, C., Fish, P. V, Lee, K. & Schapira, M. Epigenetic protein families: a new frontier for drug discovery. *Nat Rev Drug Discov* **11,** 384–400 (2012).

21. Kuo, M.-H. & Allis, C. D. Roles of histone acetyltransferases and deacetylases in gene regulation. *BioEssays* **20,** 615–626 (1998).

22. Khan, S. N. & Khan, A. U. Role of histone acetylation in cell physiology and diseases: An update. *Clin. Chim. Acta* **411,** 1401–1411 (2010).

23. Rossetto, D., Avvakumov, N. & Côté, J. Histone phosphorylation: a chromatin modification involved in diverse nuclear events. *Epigenetics* **7,** 1098–108 (2012).

24. Banerjee, T. & Chakravarti, D. A peek into the complex realm of histone phosphorylation. *Mol. Cell. Biol.* **31,** 4858–73 (2011).

25. Di Lorenzo, A. & Bedford, M. T. Histone arginine methylation. *FEBS Lett.* **585,** 2024–31 (2011).

26. Simon, M. D. *et al.* The Site-Specific Installation of Methyl-Lysine Analogs into Recombinant Histones. *Cell* **128,** 1003–1012 (2007).

27. Santos-Rosa, H. *et al.* Active genes are tri-methylated at K4 of histone H3. *Nature* **419,** 407–11 (2002).

28. Swigut, T. & Wysocka, J. H3K27 Demethylases, at Long Last. *Cell* **131,** 29–32 (2007).

29. Voigt, P., Tee, W.-W. & Reinberg, D. A double take on bivalent promoters. *Genes Dev.* **27,** 1318–38 (2013).

30. Greer, E. L. & Shi, Y. Histone methylation: a dynamic mark in health, disease and inheritance. *Nat. Rev. Genet.* **13,** 343–57 (2012).

31. Byvoet, P., Shepherd, G. R., Hardin, J. M. & Noland, B. J. The distribution and turnover of labeled methyl groups in histone fractions of cultured mammalian cells. *Arch. Biochem. Biophys.* **148,** 558–67 (1972).

32. Thomas, G., Lange, H. W. & Hempel, K. [Relative stability of lysine-bound methyl groups in arginie-rich histones and their subfrations in Ehrlich ascites tumor cells in vitro]. *Hoppe. Seylers. Z. Physiol. Chem.* **353,** 1423–8 (1972).

33. Shi, Y. *et al.* Histone Demethylation Mediated by the Nuclear Amine Oxidase Homolog LSD1. *Cell* **119,** 941–953 (2004).

34. Seo, S. B. *et al.* KDM2B is a histone H3K79 demethylase and induces transcriptional repression via SIRT1-mediated chromatin silencing. *bioRxiv* 228379 (2017). doi:10.1101/228379

35. Loenarz, C. & Schofield, C. J. Expanding chemical biology of 2-oxoglutarate oxygenases. *Nat. Chem. Biol.* **4,** 152–6 (2008).

36. Clifton, I. J. *et al.* Structural studies on 2-oxoglutarate oxygenases and related double-stranded β-helix fold proteins. *J. Inorg. Biochem.* **100,** 644–669 (2006).

37. Martinez, S. & Hausinger, R. P. Catalytic Mechanisms of Fe(II)- and 2-Oxoglutarate-dependent Oxygenases. *J. Biol. Chem.* **290,** 20702–11 (2015).

38. Flashman, E., Davies, S. L., Yeoh, K. K. & Schofield, C. J. Investigating the

dependence of the hypoxia-inducible factor hydroxylases (factor inhibiting HIF and prolyl hydroxylase domain 2) on ascorbate and other reducing agents. *Biochem. J.* **427,** (2010).

39. Knowles, H. J., Raval, R. R., Harris, A. L. & Ratcliffe, P. J. Effect of Ascorbate on the Activity of Hypoxia-inducible Factor in Cancer Cells. *Cancer Res.* **63,** (2003).

40. De Jong, L., Albracht, S. P. J. & Kemp, A. Prolyl 4-hydroxylase activity in relation to the oxidation state of enzyme-bound iron: The role of ascorbate in peptidyl proline hydroxylation. *Biochim. Biophys. Acta - Protein Struct. Mol. Enzymol.* **704,** 326–332 (1982).

41. Aik, W., McDonough, M. A., Thalhammer, A., Chowdhury, R. & Schofield, C. J. Role of the jelly-roll fold in substrate binding by 2-oxoglutarate oxygenases. *Curr Opin Struct Biol* **22,** 691–700 (2012).

42. Johansson, C. *et al.* The roles of Jumonji-type oxygenases in human disease. *Epigenomics* **6,** 89–120 (2014).

43. Flashman, E. *et al.* Evidence for the slow reaction of hypoxia-inducible factor prolyl hydroxylase 2 with oxygen. *FEBS J* **277,** 4089–4099 (2010).

44. Hoffart, L. M., Barr, E. W., Guyer, R. B., Bollinger, J. M. & Krebs, C. Direct spectroscopic detection of a C-H-cleaving high-spin Fe(IV) complex in a prolyl-4-hydroxylase. *Proc. Natl. Acad. Sci.* **103,** 14738–14743 (2006).

45. McDonough, M. A., Loenarz, C., Chowdhury, R., Clifton, I. J. & Schofield, C. J. Structural studies on human 2-oxoglutarate dependent oxygenases. *Curr. Opin. Struct. Biol.* **20,** 659–672 (2010).

46. Tu, S. *et al.* The ARID domain of the H3K4 demethylase RBP2 binds to a DNA CCGCCC motif. *Nat. Struct. Mol. Biol.* **15,** 419–421 (2008).

47. Yu, L. *et al.* Structural insights into a novel histone demethylase PHF8. *Cell Res.* **20,** 166–73 (2010).

48. Chang, B., Chen, Y., Zhao, Y. & Bruick, R. K. JMJD6 is a histone arginine demethylase. *Science* **318,** 444–7 (2007).

49. Walport, L. J. *et al.* Arginine demethylation is catalysed by a subset of JmjC histone lysine demethylases. *Nat. Commun.* **7,** 11974 (2016).

50. Tsukada, Y. *et al.* Histone demethylation by a family of JmjC domain-containing proteins. *Nature* **439,** 811–816 (2005).

51. Tzatsos, A., Pfau, R., Kampranis, S. C. & Tsichlis, P. N. Ndy1/KDM2B immortalizes mouse embryonic fibroblasts by repressing the Ink4a/Arf locus. *Proc. Natl. Acad. Sci.* **106,** 2641–2646 (2009).

52. Loh, Y.-H., Zhang, W., Chen, X., George, J. & Ng, H.-H. Jmjd1a and Jmjd2c histone H3 Lys 9 demethylases regulate self-renewal in embryonic stem cells. *Genes Dev.* **21,** 2545–57 (2007).

53. Klose, R. J. *et al.* The transcriptional repressor JHDM3A demethylates trimethyl histone H3 lysine 9 and lysine 36. *Nature* **442,** 312–6 (2006).

54. Kim, J.-Y. *et al.* KDM3B Is the H3K9 Demethylase Involved in Transcriptional Activation of lmo2 in Leukemia. *Mol. Cell. Biol.* **32,** 2917–2933 (2012).

55. Kim, S.-M. *et al.* Regulation of mouse steroidogenesis by WHISTLE and JMJD1C through histone methylation balance. *Nucleic Acids Res.* **38,** 6389–403 (2010).

56. Liu, L. *et al.* Hairless is a histone H3K9 demethylase. *FASEB J.* **28,** 1534–1542 (2014).

57. Fodor, B. D. *et al.* Jmjd2b antagonizes H3K9 trimethylation at pericentric heterochromatin in mammalian cells. *Genes Dev.* **20,** 1557–62 (2006).

58. Cloos, P. A. C. *et al.* The putative oncogene GASC1 demethylates tri- and dimethylated lysine 9 on histone H3. *Nature* **442,** 307–11 (2006).

59. Whetstine, J. R. *et al.* Reversal of histone lysine trimethylation by the JMJD2 family of histone demethylases. *Cell* **125,** 467–81 (2006).

60. Chen, Z. *et al.* Structural insights into histone demethylation by JMJD2 family members. *Cell* **125,** 691–702 (2006).

61. Shin, S. & Janknecht, R. Diversity within the JMJD2 histone demethylase family. *Biochem. Biophys. Res. Commun.* **353,** 973–977 (2007).

62. Trojer, P. *et al.* Dynamic Histone H1 Isotype 4 Methylation and Demethylation by Histone Lysine Methyltransferase G9a/KMT1C and the Jumonji Domain-containing JMJD2/KDM4 Proteins. *J. Biol. Chem.* **284,** 8395–405 (2009).

63. Williams, S. T. *et al.* Studies on the catalytic domains of multiple JmjC oxygenases

using peptide substrates. *Epigenetics* **9,** 1596–603 (2014).

64. Christensen, J. *et al.* RBP2 Belongs to a Family of Demethylases, Specific for Tri- and Dimethylated Lysine 4 on Histone 3. *Cell* **128,** 1063–1076 (2007).

65. Iwase, S. *et al.* The X-linked mental retardation gene SMCX/JARID1C defines a family of histone H3 lysine 4 demethylases. *Cell* **128,** 1077–88 (2007).

66. Eissenberg, J. C. *et al.* The trithorax-group gene in Drosophila little imaginal discs encodes a trimethylated histone H3 Lys4 demethylase. *Nat. Struct. Mol. Biol.* **14,** 344–346 (2007).

67. Lee, M. G., Norman, J., Shilatifard, A. & Shiekhattar, R. Physical and Functional Association of a Trimethyl H3K4 Demethylase and Ring6a/MBLR, a Polycomb-like Protein. *Cell* **128,** 877–887 (2007).

68. Blair, L. P., Cao, J., Zou, M. R., Sayegh, J. & Yan, Q. Epigenetic Regulation by Lysine Demethylase 5 (KDM5) Enzymes in Cancer. *Cancers (Basel).* **3,** 1383–404 (2011).

69. Agger, K. *et al.* UTX and JMJD3 are histone H3K27 demethylases involved in HOX gene regulation and development. *Nature* **449,** 731–734 (2007).

70. De Santa, F. *et al.* The histone H3 lysine-27 demethylase Jmjd3 links inflammation to inhibition of polycomb-mediated gene silencing. *Cell* **130,** 1083–94 (2007).

71. Lan, F. *et al.* A histone H3 lysine 27 demethylase regulates animal posterior development. *Nature* **449,** 689–94 (2007).

72. Lee, M. G. *et al.* Demethylation of H3K27 regulates polycomb recruitment and H2A ubiquitination. *Science* **318,** 447–50 (2007).

73. Hong, S. *et al.* Identification of JmjC domain-containing UTX and JMJD3 as histone H3 lysine 27 demethylases. *Proc. Natl. Acad. Sci. U. S. A.* **104,** 18439–44 (2007).

74. Walport, L. J. *et al.* Human UTY(KDM6C) is a male-specific Nϵ-methyl lysyl demethylase. *J. Biol. Chem.* **289,** 18302–13 (2014).

75. Loenarz, C. *et al.* PHF8, a gene associated with cleft lip/palate and mental retardation, encodes for an Nepsilon-dimethyl lysine demethylase. *Hum. Mol. Genet.* **19,** 217–22 (2010).

76. Huang, C. *et al.* Dual-specificity histone demethylase KIAA1718 (KDM7A) regulates neural differentiation through FGF4. *Cell Res.* **20,** 154–65 (2010).

77. Yokoyama, A. *et al.* KIAA1718 is a histone demethylase that erases repressive histone methyl marks. *Genes to Cells* **15,** no-no (2010).

78. Wen, H. *et al.* Recognition of histone H3K4 trimethylation by the plant homeodomain of PHF2 modulates histone demethylation. *J. Biol. Chem.* **285,** 9322–6 (2010).

79. Horton, J. R. *et al.* Enzymatic and structural insights for substrate specificity of a family of jumonji histone lysine demethylases. *Nat. Struct. Mol. Biol.* **17,** 38–43 (2010).

80. Sinha, K. M., Yasuda, H., Coombes, M. M., Dent, S. Y. R. & de Crombrugghe, B. Regulation of the osteoblast-specific transcription factor Osterix by NO66, a Jumonji family histone demethylase. *EMBO J.* **29,** 68–79 (2010).

81. Lu, Y. *et al.* Lung cancer-associated JmjC domain protein mdig suppresses formation of tri-methyl lysine 9 of histone H3. *Cell Cycle* **8,** 2101–9 (2009).

82. Hsia, D. A. *et al.* KDM8, a H3K36me2 histone demethylase that acts in the cyclin A1 coding region to regulate cancer cell proliferation. *Proc. Natl. Acad. Sci. U. S. A.* **107,** 9671–6 (2010).

83. Sengoku, T. & Yokoyama, S. Structural basis for histone H3 Lys 27 demethylation by UTX/KDM6A. *Genes Dev* **25,** 2266–2277 (2011).

84. Jones, S. E., Olsen, L. & Gajhede, M. Structural Basis of Histone Demethylase KDM6B Histone 3 Lysine 27 Specificity. *Biochemistry* acs.biochem.7b01152 (2017). doi:10.1021/acs.biochem.7b01152

85. Blatch, G. L. & Lässle, M. The tetratricopeptide repeat: a structural motif mediating protein-protein interactions. *BioEssays* **21,** 932–939 (1999).

86. Kristensen, J. B. L. *et al.* Enzyme kinetic studies of histone demethylases KDM4C and KDM6A: towards understanding selectivity of inhibitors targeting oncogenic histone demethylases. *FEBS Lett.* **585,** 1951–6 (2011).

87. Nottke, A., Colaiacovo, M. P. & Shi, Y. Developmental roles of the histone lysine demethylases. *Development* **136,** 879–889 (2009).

88. Burchfield, J. S., Li, Q., Wang, H. Y. & Wang, R.-F. JMJD3 as an epigenetic regulator in development and disease. *Int. J. Biochem. Cell Biol.* **67,** 148–157 (2015).

89. Van der Meulen, J., Speleman, F. & Van Vlierberghe, P. The H3K27me3 demethylase UTX in normal development and disease. *Epigenetics* **9,** 658–668 (2014).

90. Banka, S. *et al.* Novel KDM6A (UTX) mutations and a clinical and molecular review of the X-linked Kabuki syndrome (KS2). *Clin. Genet.* (2014). doi:10.1111/cge.12363

91. Welstead, G. G. *et al.* X-linked H3K27me3 demethylase Utx is required for embryonic development in a sex-specific manner. *Proc. Natl. Acad. Sci. U. S. A.* **109,** 13004–9 (2012).

92. Burgold, T. *et al.* The H3K27 demethylase JMJD3 is required for maintenance of the embryonic respiratory neuronal network, neonatal breathing, and survival. *Cell Rep.* **2,** 1244–58 (2012).

93. Li, Q. *et al.* Stage-dependent and locus-specific role of histone demethylase Jumonji D3 (JMJD3) in the embryonic stages of lung development. *PLoS Genet.* **10,** e1004524 (2014).

94. Li, Q. *et al.* Stage-dependent and locus-specific role of histone demethylase Jumonji D3 (JMJD3) in the embryonic stages of lung development. *PLoS Genet.* **10,** e1004524 (2014).

95. Satoh, T. *et al.* The Jmjd3-Irf4 axis regulates M2 macrophage polarization and host responses against helminth infection. *Nat. Immunol.* **11,** 936–44 (2010).

96. Burgold, T. *et al.* The histone H3 lysine 27-specific demethylase Jmjd3 is required for neural commitment. *PLoS One* **3,** e3034 (2008).

97. Boyer, L. A. *et al.* Polycomb complexes repress developmental regulators in murine embryonic stem cells. *Nature* **441,** 349–353 (2006).

98. Jepsen, K. *et al.* SMRT-mediated repression of an H3K27 demethylase in progression from neural stem cell to neuron. *Nature* **450,** 415–9 (2007).

99. Shahhoseini, M., Taghizadeh, Z., Hatami, M. & Baharvand, H. Retinoic acid

dependent histone 3 demethylation of the clustered HOX genes during neural differentiation of human embryonic stem cells. *Biochem. Cell Biol.* **91,** 116–22 (2013).

100. Ohtani, K. *et al.* Jmjd3 controls mesodermal and cardiovascular differentiation of embryonic stem cells. *Circ. Res.* **113,** 856–62 (2013).

101. Lee, S., Lee, J. W. & Lee, S.-K. UTX, a histone H3-lysine 27 demethylase, acts as a critical switch to activate the cardiac developmental program. *Dev. Cell* **22,** 25–37 (2012).

102. Shpargel, K. B., Sengoku, T., Yokoyama, S. & Magnuson, T. UTX and UTY demonstrate histone demethylase-independent function in mouse embryonic development. *PLoS Genet.* **8,** e1002964 (2012).

103. Jiang, W., Wang, J. & Zhang, Y. Histone H3K27me3 demethylases KDM6A and KDM6B modulate definitive endoderm differentiation from human ESCs by regulating WNT signaling pathway. *Cell Res.* **23,** 122–30 (2013).

104. Chung, N. *et al.* Active H3K27me3 demethylation by KDM6B is required for normal development of bovine preimplantation embryos. *Epigenetics* 01–20 (2017). doi:10.1080/15592294.2017.1403693

105. Burchfield, J. S., Li, Q., Wang, H. Y. & Wang, R.-F. JMJD3 as an epigenetic regulator in development and disease. *Int. J. Biochem. Cell Biol.* **67,** 148–157 (2015).

106. van Haaften, G. *et al.* Somatic mutations of the histone H3K27 demethylase gene UTX in human cancer. *Nat Genet* **41,** 521–523 (2009).

107. Kandoth, C. *et al.* Mutational landscape and significance across 12 major cancer types. *Nature* **502,** 333–339 (2013).

108. Agger, K. *et al.* The H3K27me3 demethylase JMJD3 contributes to the activation of the INK4A-ARF locus in response to oncogene- and stress-induced senescence. *Genes Dev.* **23,** 1171–6 (2009).

109. Ntziachristos, P. *et al.* Contrasting roles of histone 3 lysine 27 demethylases in acute lymphoblastic leukaemia. *Nature* **514,** 513–7 (2014).

110. Anderton, J. A. *et al.* The H3K27me3 demethylase, KDM6B, is induced by

Epstein–Barr virus and over-expressed in Hodgkin's Lymphoma. *Oncogene* **30,** 2037–2043 (2011).

111. Manente, A. G. *et al.* KDM6B histone demethylase is an epigenetic regulator of estrogen receptor β expression in human pleural mesothelioma. *Epigenomics* **8,** 1227–1238 (2016).

112. Wu, G. *et al.* The genomic landscape of diffuse intrinsic pontine glioma and pediatric non-brainstem high-grade glioma. *Nat. Genet.* **46,** 444–450 (2014).

113. Hashizume, R. *et al.* Pharmacologic inhibition of histone demethylation as a therapy for pediatric brainstem glioma. *Nat. Med.* **20,** 1394–6 (2014).

114. Salminen, A., Kaarniranta, K., Hiltunen, M. & Kauppinen, A. Histone demethylase Jumonji D3 (JMJD3/KDM6B) at the nexus of epigenetic regulation of inflammation and the aging process. *J. Mol. Med.* **92,** 1035–1043 (2014).

115. Yan, Q. *et al.* Jmjd3-mediated epigenetic regulation of inflammatory cytokine gene expression in serum amyloid A-stimulated macrophages. *Cell. Signal.* **26,** 1783–91 (2014).

116. De Santa, F. *et al.* Jmjd3 contributes to the control of gene expression in LPS-activated macrophages. *EMBO J.* **28,** 3341–52 (2009).

117. Das, N. D. *et al.* Gene networking and inflammatory pathway analysis in a JMJD3 knockdown human monocytic cell line. *Cell Biochem. Funct.* **30,** 224–32 (2012).

118. Kruidenier, L. *et al.* A selective jumonji H3K27 demethylase inhibitor modulates the proinflammatory macrophage response. *Nature* **488,** 404–8 (2012).

119. Das, N. D., Jung, K. H. & Chai, Y. G. The role of NF-kappaB and H3K27me3 demethylase, Jmjd3, on the anthrax lethal toxin tolerance of RAW 264.7 cells. *PLoS One* **5,** e9913 (2010).

120. Yin, H. *et al.* Histone demethylase JMJD3 regulates CD11a expression through changes in histone H3K27 tri-methylation levels in CD4+ T cells of patients with systemic lupus erythematosus. *Oncotarget* **8,** 48938–48947 (2017).

121. Liu, Z. *et al.* The histone H3 lysine-27 demethylase Jmjd3 plays a critical role in specific regulation of Th17 cell differentiation. *J. Mol. Cell Biol.* (2015). doi:10.1093/jmcb/mjv022

122. He, X.-B. *et al.* Vitamin C facilitates dopamine neuron differentiation in fetal midbrain through TET1- and JMJD3-dependent epigenetic control manner. *Stem Cells* **33,** 1320–32 (2015).

123. Holla, S. *et al.* MUSASHI-Mediated Expression of JMJD3, a H3K27me3 Demethylase, Is Involved in Foamy Macrophage Generation during Mycobacterial Infection. *PLoS Pathog.* **12,** e1005814 (2016).

124. Neele, A. E. *et al.* Macrophage Kdm6b controls the pro-fibrotic transcriptome signature of foam cells. *Epigenomics* **9,** 383–391 (2017).

125. Lee, H. Y. *et al.* Serum amyloid A stimulates macrophage foam cell formation via lectin-like oxidized low-density lipoprotein receptor 1 upregulation. *Biochem. Biophys. Res. Commun.* **433,** 18–23 (2013).

126. Fonseca, M. B., Nunes, A. F., Morgado, A. L., Solá, S. & Rodrigues, C. M. P. TAp63γ demethylation regulates protein stability and cellular distribution during neural stem cell differentiation. *PLoS One* **7,** e52417 (2012).

127. Campbell, R. M. & Tummino, P. J. Cancer epigenetics drug discovery and development: the challenge of hitting the mark. *J. Clin. Invest.* **124,** 64–9 (2014).

128. Carreau, A., Hafny-Rahbi, B. El, Matejuk, A., Grillon, C. & Kieda, C. Why is the partial oxygen pressure of human tissues a crucial parameter? Small molecules and hypoxia. *J. Cell. Mol. Med.* **15,** 1239–1253 (2011).

129. Patterson, A. J. & Zhang, L. Hypoxia and fetal heart development. *Curr Mol Med* **10,** 653–666 (2010).

130. Wang, Z., Huang, Z., Lu, G., Lin, L. & Ferrari, M. Hypoxia during pregnancy in rats leads to early morphological changes of atherosclerosis in adult offspring. *Am. J. Physiol. Heart Circ. Physiol.* **296,** H1321-8 (2009).

131. Balasubramaniam, V., Mervis, C. F., Maxey, A. M., Markham, N. E. & Abman, S. H. Hyperoxia reduces bone marrow, circulating, and lung endothelial progenitor cells in the developing lung: implications for the pathogenesis of bronchopulmonary dysplasia. *Am. J. Physiol. Cell. Mol. Physiol.* **292,** L1073–L1084 (2007).

132. Bertout, J. A., Patel, S. A. & Simon, M. C. The impact of O2 availability on human cancer. Nat. Rev. Cancer 8, 967–975 (2008).

133. Mohyeldin, A., Garzón-Muvdi, T. & Quiñones-Hinojosa, A. Oxygen in stem cell biology: a critical component of the stem cell niche. *Cell Stem Cell* **7,** 150–61 (2010).

134. Hancock, R. L., Dunne, K., Walport, L. J., Flashman, E. & Kawamura, A. Epigenetic regulation by histone demethylases in hypoxia. *Epigenomics* 1–21 (2015). doi:10.2217/epi.15.24

135. Giordano, F. J. Oxygen, oxidative stress, hypoxia, and heart failure. *J. Clin. Invest.* **115,** 500–8 (2005).

136. Hultén, L. M. & Levin, M. The role of hypoxia in atherosclerosis. *Curr. Opin. Lipidol.* **20,** 409–14 (2009).

137. Rose, N. R., McDonough, M. A., King, O. N., Kawamura, A. & Schofield, C. J. Inhibition of 2-oxoglutarate dependent oxygenases. *Chem Soc Rev* **40,** 4364–4397 (2011).

138. Semenza, G. L. Oxygen Sensing, Hypoxia-Inducible Factors, and Disease Pathophysiology. *Annu. Rev. Pathol. Mech. Dis.* **9,** 47–71 (2014).

139. WARBURG, O. On the origin of cancer cells. *Science* **123,** 309–14 (1956).

140. Guillemin, K. & Krasnow, M. A. The hypoxic response: huffing and HIFing. *Cell* **89,** 9–12 (1997).

141. Schofield, C. J. & Ratcliffe, P. J. Oxygen sensing by HIF hydroxylases. *Nat Rev Mol Cell Biol* **5,** 343–354 (2004).

142. Kaelin, W. G. & Ratcliffe, P. J. Oxygen Sensing by Metazoans: The Central Role of the HIF Hydroxylase Pathway. *Mol. Cell* **30,** 393–402 (2008).

143. Myllyharju, J. Prolyl 4-hydroxylases, master regulators of the hypoxia response. *Acta Physiol.* **208,** 148–165 (2013).

144. Semenza, G. L. Oxygen homeostasis. *Wiley Interdiscip. Rev. Syst. Biol. Med.* **2,** 336–61

145. Wang, G. L., Jiang, B. H., Rue, E. A. & Semenza, G. L. Hypoxia-inducible factor 1 is a basic-helix-loop-helix-PAS heterodimer regulated by cellular O2 tension. *Proc. Natl. Acad. Sci. U. S. A.* **92,** 5510–4 (1995).

146. Tarhonskaya, H. *et al.* Kinetic Investigations of the Role of Factor Inhibiting

Hypoxia-inducible Factor (FIH) as an Oxygen Sensor. *J. Biol. Chem.* **290,** 19726–42 (2015).

147. Ehrismann, D. *et al.* Studies on the activity of the hypoxia-inducible-factor hydroxylases using an oxygen consumption assay. *Biochem. J.* **401,** 227–34 (2007).

148. Hirsila, M., Koivunen, P., Gunzler, V., Kivirikko, K. I. & Myllyharju, J. Characterization of the human prolyl 4-hydroxylases that modify the hypoxia-inducible factor. *J Biol Chem* **278,** 30772–30780 (2003).

149. Ehrismann, D. *et al.* Studies on the activity of the hypoxia-inducible-factor hydroxylases using an oxygen consumption assay. *Biochem J* **401,** 227–234 (2007).

150. Koivunen, P., Hirsilä, M., Günzler, V., Kivirikko, K. I. & Myllyharju, J. Catalytic properties of the asparaginyl hydroxylase (FIH) in the oxygen sensing pathway are distinct from those of its prolyl 4-hydroxylases. *J. Biol. Chem.* **279,** 9899–904 (2004).

151. Guo, X. *et al.* Regulation of histone demethylase KDM6B by hypoxia-inducible factor-2. *Acta Biochim. Biophys. Sin. (Shanghai).* **47,** 106–113 (2015).

152. Pluemsampant, S., Safronova, O. S., Nakahama, K. & Morita, I. Protein kinase CK2 is a key activator of histone deacetylase in hypoxia-associated tumors. *Int. J. Cancer* **122,** 333–341 (2008).

153. Place, T. L. *et al.* Aberrant Promoter CpG Methylation Is a Mechanism for Impaired PHD3 Expression in a Diverse Set of Malignant Cells. *PLoS One* **6,** e14617 (2011).

154. Okami, J., Simeone, D. M. & Logsdon, C. D. Silencing of the Hypoxia-Inducible Cell Death Protein BNIP3 in Pancreatic Cancer. *Cancer Res.* **64,** 5338–5346 (2004).

155. Murai, M. *et al.* Aberrant DNA methylation associated with silencing BNIP3 gene expression in haematopoietic tumours. *Br. J. Cancer* **92,** 1165–1172 (2005).

156. Huang, K. T., Mikeska, T., Dobrovic, A. & Fox, S. B. DNA methylation analysis of the HIF-1α prolyl hydroxylase domain genes PHD1, PHD2, PHD3 and the factor inhibiting HIF gene FIH in invasive breast carcinomas. *Histopathology* **57,**

451–460 (2010).

157. Thienpont, B., Galle, E. & Lambrechts, D. TET enzymes as oxygen-dependent tumor suppressors: exciting new avenues for cancer management. *Epigenomics* **8,** 1445–1448 (2016).

158. Thienpont, B. *et al.* Tumour hypoxia causes DNA hypermethylation by reducing TET activity. *Nature* **537,** 63–68 (2016).

159. Watson, C. J. *et al.* Hypoxia-induced epigenetic modifications are associated with cardiac tissue fibrosis and the development of a myofibroblast-like phenotype. *Hum. Mol. Genet.* **23,** 2176–2188 (2014).

160. Liu, Q. *et al.* Hypoxia Induces Genomic DNA Demethylation through the Activation of HIF-1 and Transcriptional Upregulation of MAT2A in Hepatoma Cells. *Mol. Cancer Ther.* **10,** 1113–1123 (2011).

161. Skowronski, K., Dubey, S., Rodenhiser, D. & Coomber, B. Ischemia dysregulates DNA methyltransferases and p16INK4a methylation in human colorectal cancer cells. *Epigenetics* **5,** 547–56 (2010).

162. POLJAKOVÁ, J. *et al.* Hypoxia-mediated histone acetylation and expression of N-myc transcription factor dictate aggressiveness of neuroblastoma cells. *Oncol. Rep.* **31,** 1928–1934 (2014).

163. Delvecchio, M., Gaucher, J., Aguilar-Gurrieri, C., Ortega, E. & Panne, D. Structure of the p300 catalytic core and implications for chromatin targeting and HAT regulation. *Nat. Struct. Mol. Biol.* **20,** 1040–1046 (2013).

164. Kato, H., Tamamizu-Kato, S. & Shibasaki, F. Histone Deacetylase 7 Associates with Hypoxia-inducible Factor 1 and Increases Transcriptional Activity. *J. Biol. Chem.* **279,** 41966–41974 (2004).

165. Kim, S.-H. *et al.* Regulation of the HIF-1alpha stability by histone deacetylases. *Oncol. Rep.* **17,** 647–51 (2007).

166. Ellis, L., Hammers, H. & Pili, R. Targeting tumor angiogenesis with histone deacetylase inhibitors. *Cancer Lett.* **280,** 145–153 (2009).

167. Granger, A. *et al.* Histone deacetylase inhibition reduces myocardial ischemia-reperfusion injury in mice. *FASEB J.* **22,** 3549–60 (2008).

168. Costa, M. *et al.* Nickel carcinogenesis: epigenetics and hypoxia signaling. *Mutat Res* **592,** 79–88 (2005).

169. Islam, K. N. & Mendelson, C. R. Permissive effects of oxygen on cyclic AMP and interleukin-1 stimulation of surfactant protein A gene expression are mediated by epigenetic mechanisms. *Mol Cell Biol* **26,** 2901–2912 (2006).

170. Chen, H., Yan, Y., Davidson, T. L., Shinkai, Y. & Costa, M. Hypoxic stress induces dimethylated histone H3 lysine 9 through histone methyltransferase G9a in mammalian cells. *Cancer Res* **66,** 9009–9016 (2006).

171. Johnson, A. B., Denko, N. & Barton, M. C. Hypoxia induces a novel signature of chromatin modifications and global repression of transcription. *Mutat Res* **640,** 174–179 (2008).

172. Xia, X. *et al.* Integrative analysis of HIF binding and transactivation reveals its role in maintaining histone methylation homeostasis. *Proc. Natl. Acad. Sci.* **106,** 4260–4265 (2009).

173. Zhou, X. *et al.* Hypoxia induces trimethylated H3 lysine 4 by inhibition of JARID1A demethylase. *Cancer Res.* **70,** 4214–21 (2010).

174. Tausendschön, M., Dehne, N. & Brüne, B. Hypoxia causes epigenetic gene regulation in macrophages by attenuating Jumonji histone demethylase activity. *Cytokine* **53,** 256–262 (2011).

175. Olcina, M. M. *et al.* Replication stress and chromatin context link ATM activation to a role in DNA replication. *Mol. Cell* **52,** 758–66 (2013).

176. Osumek, J. E., Revesz, A., Morton, J. S., Davidge, S. T. & Hardy, D. B. Enhanced Trimethylation of Histone H3 Mediates Impaired Expression of Hepatic Glucose 6-Phosphatase Expression in Offspring From Rat Dams Exposed to Hypoxia During Pregnancy. *Reprod. Sci.* **21,** 112–121 (2014).

177. Chang, S. *et al.* Hypoxic reprograming of H3K27me3 and H3K4me3 at the INK4A locus. *FEBS Lett.* (2016). doi:10.1002/1873-3468.12375

178. Olcina, M. M. *et al.* H3K9me3 facilitates hypoxia-induced p53-dependent apoptosis through repression of APAK. *Oncogene* **35,** 793–9 (2016).

179. Lu, Y., Chu, A., Turker, M. S. & Glazer, P. M. Hypoxia-induced epigenetic

regulation and silencing of the BRCA1 promoter. *Mol. Cell. Biol.* **31,** 3339–50 (2011).

180. Safronova, O., Pluemsampant, S., Nakahama, K. & Morita, I. Regulation of chemokine gene expression by hypoxia via cooperative activation of NF-κB and histone deacetylase. *Int. J. Biochem. Cell Biol.* **41,** 2270–2280 (2009).

181. Lee, S. *et al.* Multi-dimensional histone methylations for coordinated regulation of gene expression under hypoxia. *Nucleic Acids Res.* **45,** 11643–11657 (2017).

182. Dobrynin, G. *et al.* KDM4A regulates HIF-1 levels through H3K9me3. *Sci. Rep.* **7,** 11094 (2017).

183. Yoon, D.-K. *et al.* The involvement of histone methylation in osteoblastic differentiation of human periosteum-derived cells cultured in vitro under hypoxic conditions. *Cell Biochem. Funct.* **35,** 441–452 (2017).

184. Hancock, R. L., Dunne, K., Walport, L. J., Flashman, E. & Kawamura, A. Epigenetic regulation by histone demethylases in hypoxia. *Epigenomics* **7,** 1–21 (2015).

185. Ueda, J. *et al.* The Hypoxia-Inducible Epigenetic Regulators Jmjd1a and G9a Provide a Mechanistic Link between Angiogenesis and Tumor Growth. *Mol. Cell. Biol.* **34,** 3702–3720 (2014).

186. Casciello, F. *et al.* G9a drives hypoxia-mediated gene repression for breast cancer cell survival and tumorigenesis. *Proc. Natl. Acad. Sci. U. S. A.* **114,** 7077–7082 (2017).

187. Cascella, B. & Mirica, L. M. Kinetic analysis of iron-dependent histone demethylases: α-ketoglutarate substrate inhibition and potential relevance to the regulation of histone demethylation in cancer cells. *Biochemistry* **51,** 8699–701 (2012).

188. Sanchez-Fernandez, E. M. *et al.* Investigations on the oxygen dependence of a 2-oxoglutarate histone demethylase. *Biochem J* **449,** 491–496 (2013).

189. Hancock, R. L., Masson, N., Dunne, K., Flashman, E. & Kawamura, A. The Activity of JmjC Histone Lysine Demethylase KDM4A is Highly Sensitive to Oxygen Concentrations. *ACS Chem. Biol.* **12,** 1011–1019 (2017).

190. Ponnaluri, V. K. C. *et al.* Hypoxia induced expression of histone lysine demethylases: implications in oxygen-dependent retinal neovascular diseases. *Biochem. Biophys. Res. Commun.* **415,** 373–7 (2011).

191. Guo, X. *et al.* Regulation of histone demethylase KDM6B by hypoxia-inducible factor-2α. *Acta Biochim. Biophys. Sin. (Shanghai).* (2014). doi:10.1093/abbs/gmu122

192. Lee, H. Y., Choi, K., Oh, H., Park, Y. K. & Park, H. HIF-1-Dependent Induction of Jumonji Domain-Containing Protein (JMJD) 3 under Hypoxic Conditions. *Mol Cells* **37,** 43–50 (2014).

193. Xia, X. *et al.* Integrative analysis of HIF binding and transactivation reveals its role in maintaining histone methylation homeostasis. *Proc. Natl. Acad. Sci. U. S. A.* **106,** 4260–5 (2009).

194. Beyer, S., Kristensen, M. M., Jensen, K. S., Johansen, J. V. & Staller, P. The histone demethylases JMJD1A and JMJD2B are transcriptional targets of hypoxia-inducible factor HIF. *J. Biol. Chem.* **283,** 36542–52 (2008).

195. Wellmann, S. *et al.* Hypoxia upregulates the histone demethylase JMJD1A via HIF-1. *Biochem. Biophys. Res. Commun.* **372,** 892–7 (2008).

196. Pollard, P. J. *et al.* Regulation of Jumonji-domain-containing histone demethylases by hypoxia-inducible factor (HIF)-1alpha. *Biochem J* **416,** 387–394 (2008).

197. Yang, J. *et al.* Role of hypoxia-inducible factors in epigenetic regulation via histone demethylases. *Ann. N. Y. Acad. Sci.* **1177,** 185–97 (2009).

198. Krieg, A. J. *et al.* Regulation of the histone demethylase JMJD1A by hypoxia-inducible factor 1 alpha enhances hypoxic gene expression and tumor growth. *Mol. Cell. Biol.* **30,** 344–53 (2010).

199. Mimura, I. *et al.* Dynamic change of chromatin conformation in response to hypoxia enhances the expression of GLUT3 (SLC2A3) by cooperative interaction of hypoxia-inducible factor 1 and KDM3A. *Mol. Cell. Biol.* **32,** 3018–32 (2012).

200. Fu, L. *et al.* HIF-1α-induced histone demethylase JMJD2B contributes to the malignant phenotype of colorectal cancer cells via an epigenetic mechanism. *Carcinogenesis* **33,** 1664–73 (2012).

201. Wilson, C. *et al.* The histone demethylase KDM4B regulates peritoneal seeding of ovarian cancer. *Oncogene* **36,** 2565–2576 (2017).

202. Luo, W., Chang, R., Zhong, J., Pandey, A. & Semenza, G. L. Histone demethylase JMJD2C is a coactivator for hypoxia-inducible factor 1 that is required for breast cancer progression. *Proc. Natl. Acad. Sci. U. S. A.* **109,** E3367-76 (2012).

203. Lee, H. Y., Yang, E. G. & Park, H. Hypoxia enhances the expression of prostate-specific antigen by modifying the quantity and catalytic activity of Jumonji C domain-containing histone demethylases. *Carcinogenesis* **34,** 2706–2715 (2013).

204. Lee, H.-Y., Choi, K., Oh, H., Park, Y.-K. & Park, H. HIF-1-dependent induction of Jumonji domain-containing protein (JMJD) 3 under hypoxic conditions. *Mol. Cells* **37,** 43–50 (2014).

205. Tong, D. *et al.* The HIF/PHF8/AR axis promotes prostate cancer progression. *Oncogenesis* **5,** e283 (2016).

Chapter 2 –Establishment of biochemical assays to assess KDM6A and KDM6B activity and inhibition

2.1 Introduction

The KDM6 sub-family of JmjC histone demethylases consists of KDM6A, KDM6B and KDM6C. KDM6A and KDM6B were first identified as specific H3K27Me3/2/1 histone demethylases by a number of groups in 2007.[1–4] It was previously thought that KDM6C was inactive. However, work by Walport *et al*. demonstrated KDM6C catalysed demethylation of H3K27Me3 peptides *in vitro*, albeit at vastly reduced levels of activity compared with KDM6A and KDM6B.[5] H3K27 methylation status is a key regulator of gene transcription, with H3K27Me3 marking transcriptionally inactive genes. Both KDM6A and KDM6B catalyse demethylation of H3K27Me3, resolving chromatin to an active transcriptional state.

This mechanism of gene regulation by KDM6A and KDM6B has important roles in development,[6–8] and diseases such as cancer and inflammation.[9,10] Consequently, there has been wide interest in the characterisation of these enzymes, and the development of small molecule inhibitors. A variety of methods have been utilised to study the activity and inhibition of histone demethylases. Discontinuous, or end-point, assay methods for JmjC-KDMs include MALDI-MS, AlphaScreen and radioactive ^{14}C-2OG turnover assays. The major disadvantage of discontinuous assay methods is that they provide only a snapshot of the reaction and so multiple experiments must be undertaken, for example to acquire a time course. Consequently, additional control experiments must be undertaken prior to kinetic characterisation and together this can make endpoint assays time and material expensive. Continuous assay methods include oxygen consumption,

2OG turnover and enzyme-coupled formaldehyde dehydrogenase assays. In these assays substrate consumption or product formation is monitored using fluorescence or colorimetric spectroscopy. This allows facile identification of the linear range of reaction and kinetic characterisation.

Each assay has its own limitations. Uncoupled 2OG turnover by JmjC histone demethylases can interfere with both oxygen consumption and 2OG turnover assays.[11] Additionally, radioactive 2OG turnover assays are especially cumbersome due the need to handle and dispose of radioactive waste. Enzyme coupled assays rely on the activity of the coupled enzyme being constant regardless of the reaction conditions, reaction components or presence of small molecule inhibitors. Control experiments must be conducted to ensure the reaction rate of the coupled enzyme does not become limited. Finally, whilst AlphaScreen (Chapter 4, Section 4.2) is an ideal assay for inhibitor characterisation, it is not suitable for determination of kinetic parameters because the binding capacity and proximity of the detection beads is limited. The limitations of each given assay must be carefully considered in experimental design. Similarly, determination of the kinetic parameters of the enzyme under investigation is essential to ensure that no factor, other than that under investigation, perturbs enzyme activity or it's detection.

KDM6A/B/C all contain a C-terminal catalytic JmjC domain and zinc-binding domain (Figure 2.1), both within the catalytic core region. The catalytic JmjC domain consists of a beta-barrel jellyroll within which catalytic Fe^{2+} is coordinated by two histidines and a glutamate residue. The zinc-binding domain, also known as the 'GATA-like' domain, is essential to substrate binding and is flanked by alpha helices. These two domains pack together via hydrophobic interactions, facilitating substrate binding. Both KDM6A and KDM6C also contain N-terminal tetratricopeptide repeat domains, although the function of these domains is unknown, and they are not required for catalytic activity.[12,13]

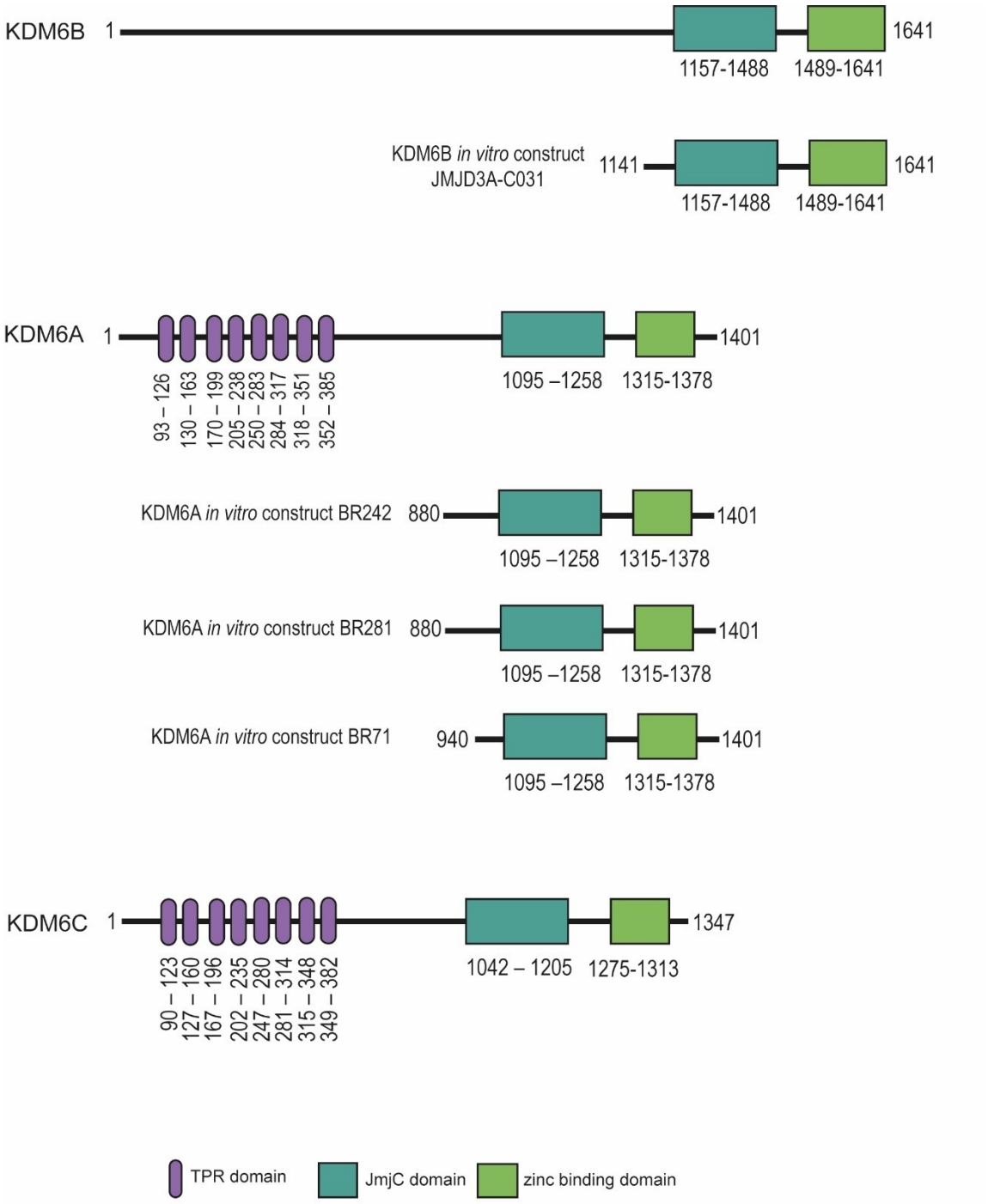


Figure 2.1 Domain organisation of the KDM6 subfamily of JmjC KDMs and truncated contructs used for in vitro studies. *Colour shading indicates structural elements present within KDM6 enzymes; TPR (purple), JmjC domain (teal) and zinc binding domain, also known as GATA-like domain (green). Numbering indicates residue number corresponding to boundaries of full-length enzyme and truncated constructs and position of domains.*

Highly pure, active recombinant enzyme is required for kinetic characterisation studies. The use of high purity recombinant enzyme eliminates the possibility that contaminating enzymes with potentially competing activities interfere with the assay, and also allows the

determination of kinetic parameters for which an accurate knowledge of protein concentration is required. Purification of KDM6A and KDM6B for use in crystallography and *in vitro* activity assays has been carried out by several groups. Constructs used for *in vitro* activity assays generally encompass the JmjC and helical domain, within which is a GATA-like binding domain. Expression of KDM6A and KDM6B has been reported via mammalian (293T)[1], insect (Sf9)[8] and bacterial (*E.coli*)[5,14,15] expression methods, with *E.Coli* expression the more commonly used method for production of protein used in *in vitro* assays. However, robust production of active recombinant KDM6A/B of high purity has been problematic within the group. Establishment of effective protein expression and purification methods will be essential to allow the development of activity and inhibition assays for KDM6A and KDM6B.

2.1.1 Chapter aims

The work in this Chapter describes efforts towards the expression, purification and kinetic characterisation of KDM6A and KDM6B.

Plasmid DNA encoding KDM6A constructs BR71, BR281, BR242 were kindly gifted by Jan Kristensen. Plasmid DNA encoding KDM6B, JMJD3-C031, was kindly gifted by the structural genomics consortium (SGC), University of Oxford. Samples of KDM6A BR71 for comparison experiments were purified by Jan Kristensen and Alex Brooks, as indicated below.

2.2. Expression and purification of KDM6A constructs BR71, BR281 and BR242

Plasmids encoding truncated *N*-His_6-tagged KDM6A, BR71, BR242 and BR281, were gifted to the group by Jan Kristensen (Gajhede/Olsen/Kastrup group, Department of Medicinal Chemistry, University of Copenhagen). These constructs comprise the JmjC- and zinc-binding/GATA domains, both of which are required for demethylase activity. These constructs express under a T7 promotor, and encode fusion protein tags to allow affinity purification and enhance solubility. Previous studies by Jan Kristen which

assessed the activity of KDM6A had demonstrated a lack of reproducibility in the production of pure, active enzyme. Therefore, expression and purification of all three constructs was undertaken to obtain pure and active enzyme for use in *in vitro* activity assays.

KDM6A construct	Vector	Tag	KDM6A residues
BR281	pET47b	*N*-His_6/*C*-S-tag	880-1401
BR242	pOPIN F	*N*-His_6	880-1401
BR71	pOPIN F	*N*-His_6	940-1401

Table 2.1 *Details of KDM6A constructs used for E.coli expression. Full length KDM6A 1-1401. All constructs encode JmjC domain (1095-1258) and zinc binding/GATA domain (1315-1378), no additional domains are present within the construct boundaries.*

Due to the abundance of rare codons in the construct sequences, expression was carried out in Rossetta2(DE3) pLysS or Rossetta2(DE3) *E.coli*, both of which carry a pRARE2 plasmid encoding tRNAs for seven rare codons. Small and large expressions were carried out in 2TY LB growth media using Isopropyl β-D-1-thiogalactopyranoside (IPTG) induction in addition to selection antibiotic (ampicillin, 50 μg/mL). Growth media was inoculated using a scrape from a glycerol stock of transformed cells, and incubated overnight at 37°C degrees. Aliquots (10mL) of resulting overnight culture were used to inoculate each litre of large scale growth media, which was then allowed to grow at 37°C until reaching O.D=1.0. The culture temperature was then reduced to 18°C, and expression was induced using IPTG. Culture was then incubated for 14-16 hours at 18°C. Cell pellets were collected by centrifugation and stored at -80°C. KDM6A was then purified from lysate via fast protein liquid chromatography (FPLC), as described below.

2.2.1 Purification of KDM6A BR281

Lysate was purified by Ni^{2+} immobilised metal affinity chromatography (IMAC) using a Histrap™ HP column (GE Healthcare). His-tagged protein was eluted with a gradient of 0-100% binding buffer containing 250mM imidazole (Figure 2.2, A). Eluted fractions were analysed by sodium dodecyl sulphate-polyacrylamide gel electrophoresis (SDS-PAGE) (5 µL of 1:1 fraction and 2x loading buffer per lane) (Figure 2.2). Selected fractions were combined and concentrated using a centrifugal protein concentrator (30kDa, Amicon®) before further purification by size exclusion chromatography (SEC) using a Superdex S200 300mL column (GE Healthcare).

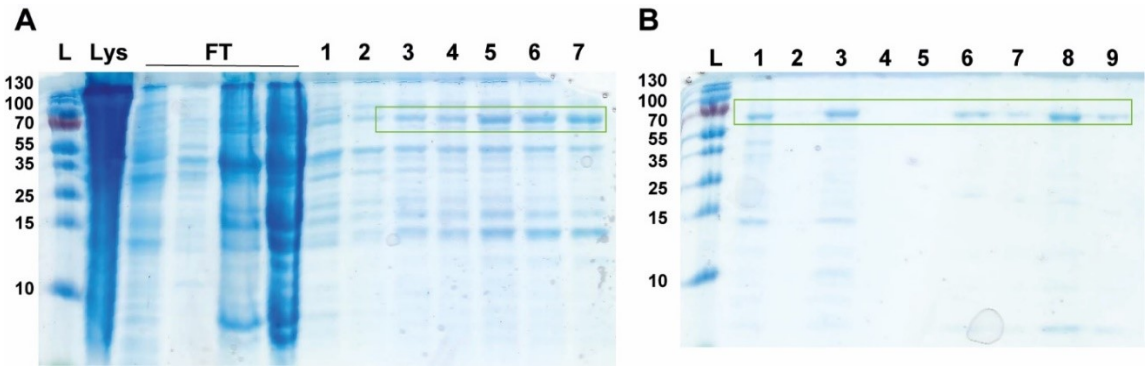
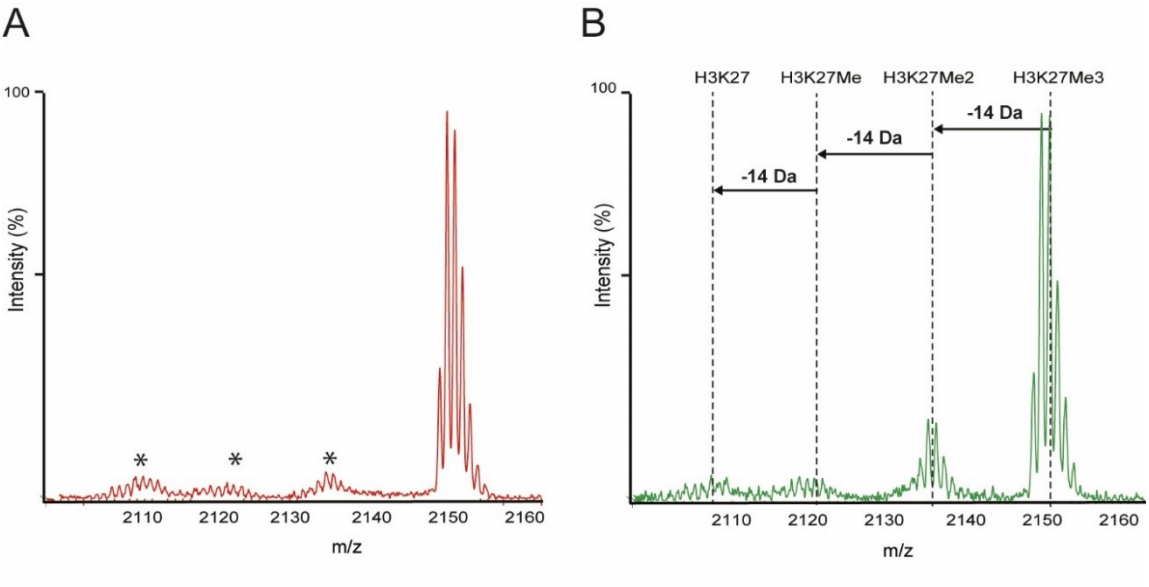


Figure 2.2. Purification of KDM6A BR281 by two step chromatography. SDS-PAGE gels from A. *IMAC purification using Histrap™ HP column.* ***B.*** *SEC purification using Superdex S200 300mL column.* ***L:*** *ladder,* ***Lys:*** *cell lysate, FT: unbound flow through,* ***No.****: numbered elution fractions. Green box indicates fractions combined for concentration. Gels show band corresponding to expected mass of N-His$_6$-KDM6A BR281 at 61 kDa.*

Although some low molecular weight impurities remained after SEC, BR281 of approximately 85% purity by SDS-PAGE analysis was acquired. Combined fractions were buffer exchanged to remove imidazole using a PD-10 desalting column (storage buffer 50mM 4-(2-hydroxyethyl)-1-piperazineethanesulfonic acid (HEPES), 300mM NaCl, 10% glycerol, pH7.5), then concentrated. Aliquots (3.11 mg/ml) were snap-frozen using liquid nitrogen and stored at -80°C.

2.2.2 Assessment of KDM6A BR281 demethylase activity by a MALDI-MS enzyme activity assay

The use of Matrix-assisted laser desorption/ionisation mass spectrometry (MALDI-MS) to evaluate activity of JmjC histone demethylases is well established.[14] MALDI-MS directly allows quantification of the relative abundance of substrate and product in the sample, and is ideally suited for use in kinetic characterisation. MALDI-MS is a mass spectrometry technique in which a matrix compound transfers energy from a laser strike to the sample resulting in ionisation. The mass of the ions is then determined according their time of flight. An advantage of MALDI-MS is that ionisation occurs almost entirely without fragmentation of the sample, reducing the complexity of analysis. In this assay, enzyme, cofactors and histone peptide are incubated and the reaction is quenched with methanol. The quenched reaction mixture is then mixed with a solution of matrix (α-cyano-4-hydroxycinnamic acid, (CHCA) and allowed to dry before analysis by MALDI-MS. Mono-, di- and tri-demethylated peptide products are identified as mass spectra peaks shifted -14, -28 and -42 Da relative to the substrate peptide (Figure 2.3). The percentage of a given methylation state, H3K27Me3 for instance, can be calculated from the relative intensities of these peaks. The percentage demethylation can be calculated by comparing H3K27Me3(%) in sample x with H3K27Me3(%) in a control sample. The H3K27Me3 peptide substrate initially contains around 10% of H3K27Me2/1/0 (see starred peaks in Figure 2.3, A), and so to account for this, change in percentage demethylation is normalised against the H3K27Me3 (%) in the no enzyme control sample (Figure 2.3, C).



C.

$$\text{Percentage H3K27Me3 (\%)} = \frac{(I_{H3K27Me3})}{I_{H3K27Me3}+I_{H3K27Me2}+I_{H3K27Me1}I_{H3K27}}$$

$$\text{Demethylation (\%)} = \frac{Control\ Me3\ (\%) - Sample\ Me3\ (\%)}{Control\ Me3\ (\%)}$$

Figure 2.3. Assessment of KDM6A activity by MALDI-MS. *KDM6A (2.5 µM), was incubated with H3K27Me3 21mer peptide (20 µM), Fe^{2+} (ferrous ammonium sulphate) (50 µM) and 2-oxoglutarate (100 µM) in 50mM HEPES 50mM NaCl pH7.5 at 37°C and quenched with methanol at each time point.* ***A, B MALDI-MS spectra of A, No enzyme control.*** *H3K27Me3 peptide incubated with Fe^{2+}, ascorbate and 2OG for 60 minutes.* ***B. KDM6B*** *incubated with H3K27Me3 peptide incubated with Fe^{2+}, ascorbate and 2OG for 60 minutes.* ***C.*** *Calculation of percentage H3K27Me3, calculation of percentage demethylation.*

KDM6A BR281 (2.5 µM), was incubated with H3K27Me3 21mer peptide (20 µM), Fe^{2+} (ferrous ammonium sulphate) (50 µM) and 2-oxoglutarate (100 µM) in 50mM HEPES 50mM NaCl pH7.5 at 37°C for 60 minutes before quenching. Increased intensity was seen at the MALDI-MS peak corresponding to H3K27Me2, (Figure 2.3, B), with percentage demethylation calculated to be 18%, indicating activity of KDM6A BR281 against H3K27Me3, albeit a low level of activity.

2.2.3 Purification of KDM6A BR71

BR71 was purified from 80 mL of lysate by Ni^{2+} IMAC using a Histrap™ HP column (GE Healthcare) (Figure 2.4, A), eluted with a gradient of 0-100% binding buffer containing 100mM imidazole. Eluted protein was then further purified by SEC but only one faint band corresponding KDM6A was present in the SDS-PAGE (5 µL of 1:1 fraction and 2x loading buffer per lane) (Figure 2.4 B). As the expression level was minimal using this construct, no further work was carried out for BR71.

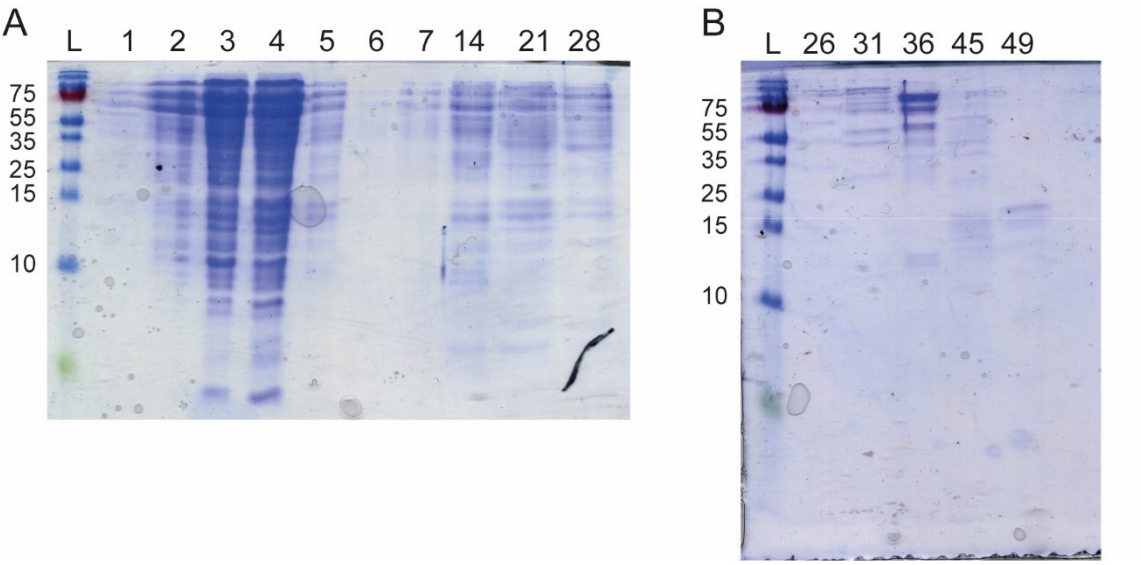


Figure 2.4. Purification of KDM6A BR71 by two step chromatography. SDS-PAGE gels from A. *IMAC purification using Histrap™ HP column. Fractions 3, 4 selected for concentration and SEC chromatography.* ***B.*** *SEC purification using Superdex S200 300mL column. No band corresponding to N-His_6-KDM6A BR71 expected mass present. Expected mass of N-His_6-KDM6A BR71 55 kDa.* ***L:*** *ladder,* ***No.****: numbered elution fractions*

2.2.4 Purification of KDM6A BR242 and assessment of activity by MALDI-MS

A key structural motif of 2OG oxygenases, including JmjC-KDMs, is a facial triad of two histidine residues and one carboxylate which coordinates the Fe^{2+} within the active site. Leaching of Ni^{2+} from chromatography resins during purification can be problematic as the Ni^{2+} can replace Fe^{2+} within the active site, resulting in loss of activity.[16] Studies by Krishnan et al. demonstrated Ni^{2+} 'contamination' of KDM4A and KDM4D during Ni^{2+} IMAC purification and consequent reduction in catalytic activity. Inductively coupled plasma mass spectrometry (ICP-MS) was used to quantify relative transition metal content of two KDM4D batches, the first purified by Ni^{2+} IMAC and the second by Strep-Tactin affinity chromatography which utilises an alternative affinity tag and circumvents the need for Ni^{2+} in purification. Comparison of the two batches demonstrated a twelve-fold increase in percentage nickel ion content in the batch purified using Ni^{2+} IMAC compared with Strep-Tactin purification. Since attempts to purify KDM6A BR281 using a Histrap^{TM} HP resin had failed to produce highly active enzyme, potentially in part due to Ni^{2+} contamination (see section 2.2.1). An alternative 'non-leaching' resin, Protino-Ni-TED was utilised instead for purification of BR242. This resin contains the chelating group (tris(carboxymethyl)ethylene diamine) (TED), which occupies five of the six available Ni^{2+}coordination sites. This results in tighter binding of Ni^{2+} and reduced leaching compared with other resins, such as Nickel Sepharose (GE healthcare) and TALON® (Qiagen), which occupy only four coordination sites.

Cell lysate was incubated with Protino-Ni-TED for 45 minutes at 4°C and which was then packed in to a gravity column and eluted with binding buffer containing 250 mM imidazole. Eluted fractions were concentrated and the buffer exchanged for a low salt buffer using a PD-10 column. Protein was loaded to a HiTrap Heparin HP column (as per section 2.11) and eluted with a 0-100% gradient of 50 mM HEPES, 1M NaCl 5%

glycerol pH 7.5. Combined fractions were concentrated as above and snap-frozen using liquid nitrogen and stored at -80°C.

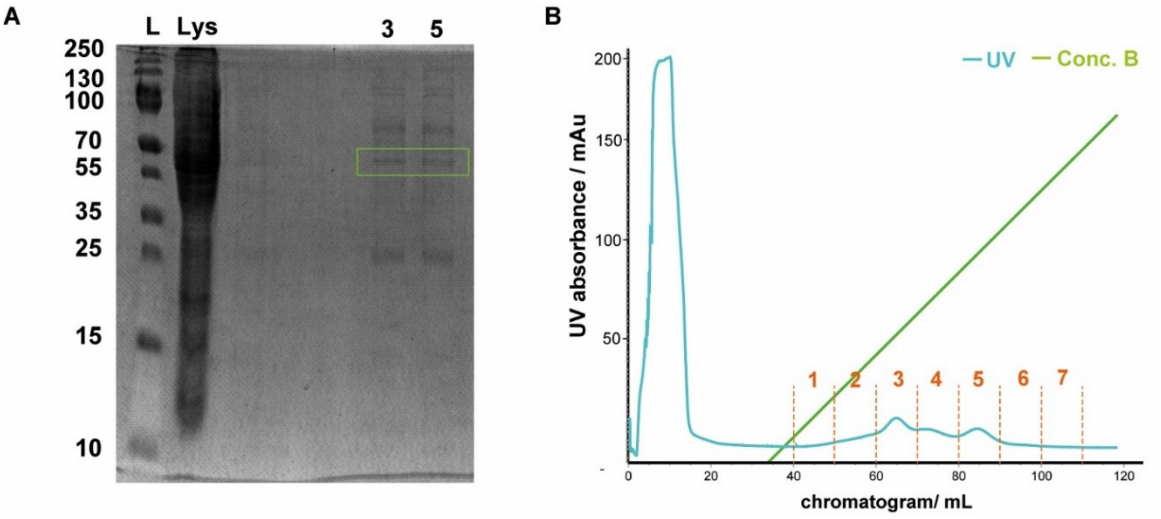


Figure 2.5. Purification of N-His$_6$-KDM6A BR242 by Ni^{2+} IMAC chromatography A. *SDS-PAGE gel. Low intensity band corresponding to N-His$_6$-KDM6A BR242 expected mass (59 kDa) present in addition to several other contaminating bands of similar low intensity. Green box indicates combined fractions* ***L:*** *ladder,* ***Lys****: Lysate,* ***No.****: numbered elution fractions.* ***B.*** *FPLC chromatogram showing IMAC program (green) and ultraviolet (UV) absorbance at 280 nm (blue) and fractions (orange).*

Low UV absorbance of elution fractions indicated that BR242 did not bind strongly to the HiTrap Heparin HP column, significantly reducing yield. Elution fractions were analysed by SDS-PAGE (5 µL of 1:1 fraction and 2x loading buffer per lane). A faint band corresponding to the expected molecular weight (59 kDa) was visible, but several contaminating bands were also present. Additionally, precipitate was observed on concentration of the combined elution fractions. The impure BR242 (5 µM) was incubated with H3K27Me3 21mer peptide (20 µM), Fe^{2+} (50 µM) and 2-oxoglutarate (300 µM) in 50mM HEPES 50mM NaCl pH7.5 at 37°C for 60 minutes before quenching with methanol. Upon analysing the results by MALDI-MS no reduction in percentage H3K27Me3 was seen indicating that the BR242 was either at insufficient concentration to effect detectable demethylation (due to low purity), or was inactive.

2.3 Batch-to-batch variability of KDM6A activity assessed by MALDI-MS

Expression and purification of KDM6A BR71 had been previously undertaken by Jan Kristensen (JK) and Alex Brooks (AB). To evaluate the activity of the different constructs and purifications the purified KDM6A proteins BR71 JK, AB and BR281 KD (purified by Kate Dunne, section 2.2.1) were evaluated using the MALDI-MS assay. BR71 JK, AB and BR281 KD (2.5 μM) were incubated with H3K27Me3 21mer peptide (20 μM), Fe^{2+} (50 μM) and 2-oxoglutarate (300 μM) in 50mM HEPES 50mM NaCl pH7.5 at 37°C and quenched with methanol after 60 minutes incubation.

Construct/Batch	Purification method	Specific activity/ μmoles min^{-1} mg^{-1}
BR281 KD	Histrap™ HP	4.39e-4
BR71 JK	Protino® Ni-TED/Size exclusion	2.91e-4
BR71 AB	Histrap™ HP /Size exclusion	4.75e-4

Table 2.2. *Purification method and specific activity of KDM6A purified by Kate Dunne (BR281 KD), Jan Kristensen (BR71 JK) and Alex Brooks (BR71 AB). Specific activity indicates μmoles of H3K27Me3 peptide substrate demethylated per mg of KDM6A enzyme per minute.*

Overall activity was relatively low for all constructs/batches (maximum demethylation after 60 minutes = 21%, BR71 AB). BR71 AB and BR281 KD had comparable activity against H3K27Me3, with specific activity values of (4.75 and 4.39 μM min^{-1} mg^{-1} respectively). BR71 JK had a lower specific activity of 2.91 μM min^{-1} mg^{-1} and precipitate was observed in the sample after incubation, which may explain the lower activity. The KDM6A with the highest specific activity, BR71 AB, was further evaluated using the MALDI-MS activity assay at 2.5, 5 and 10 μM. However, significant precipitation was present in the 5 and 10 μM reaction mixtures. This may impact the ability of the enzyme to catalyse demethylation.

2.4 Dynamic light scattering assessment of BR71 JK reveals aggregation

Dynamic light scattering (DLS) is a technique used for the determination of the size distribution of particles. Particles in solution scatter light, and the temporal fluctuation of this scattering is related to the Brownian motion of the particles. Since Brownian motion is related to particle size, or hydrodynamic radius, the temporal fluctuation of light scattering can be used to determine particle size. This technique is used to screen protein samples for aggregation. To this end, BR71 JK was diluted to 20 µM in 50mM HEPES 50mM NaCl pH7.5, and assessed using a Viscotek 802 dynamic light scattering instrument (Figure 2.6).

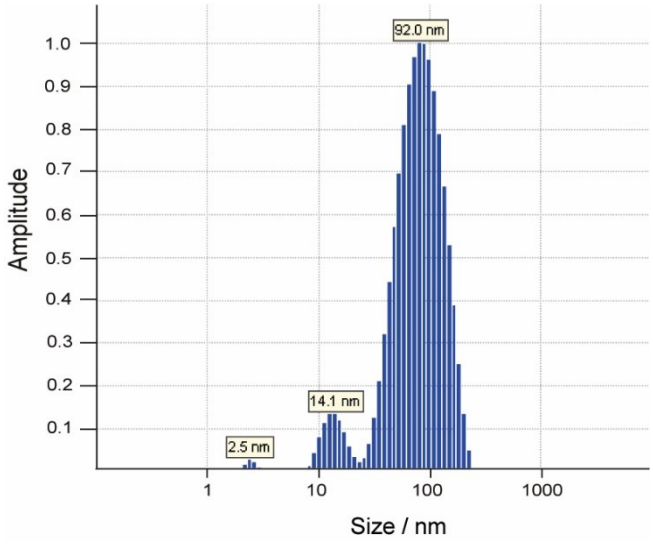


Figure 2.6 DLS Intensity distribution of BR71 JK. *BR71 JK was diluted to 20 µM in 50mM HEPES 50mM NaCl pH7.5, and assessed using a Viscotek 802 dynamic light scattering instrument Sample incubated at 4°C.*

The resulting intensity distribution was polydisperse with a large population of particles with maximum amplitude at 92 nm. The expected hydrodynamic radius for a protein of 50-100 kDa is 2-5 nm, indicating the presence of aggregates in the sample. A small population of particles at ~2.5 nm may correspond to BR71 monomeric particles.

Due to the sample requirements of the technique, further experiments could not be undertaken. Large quantities of protein sample are required for each measurement due to the volume of the quartz cuvette used for the available Viscotek 802 instrument (minimum 200 µLl/ sample). Based on the above results, aggregation is a likely cause of the observed KDM6A catalytic inactivity. Future experiments would include a solubility screen to identify optimal buffer conditions for purification and activity of KDM6A constructs using DLS or thermal shift assay, but this was outside the scope of this thesis.

2.5 Expression and purification of KDM6B

Plasmid encoding *N*-His_6-TRX-tagged $KDM6B_{1141-1641}$ on a pNH-TrxT vector backbone, JMJD3A-C031, was acquired from the SGC. This plasmid encodes both the JmjC and zinc-binding domains, both of which are required for catalytic activity. As with KDM6A, due to the abundance of rare codons in the sequence, expression was undertaken in Rossetta2(DE3) *E. Coli*, which carry a pRARE2 plasmid encoding tRNAs for seven rare codons.

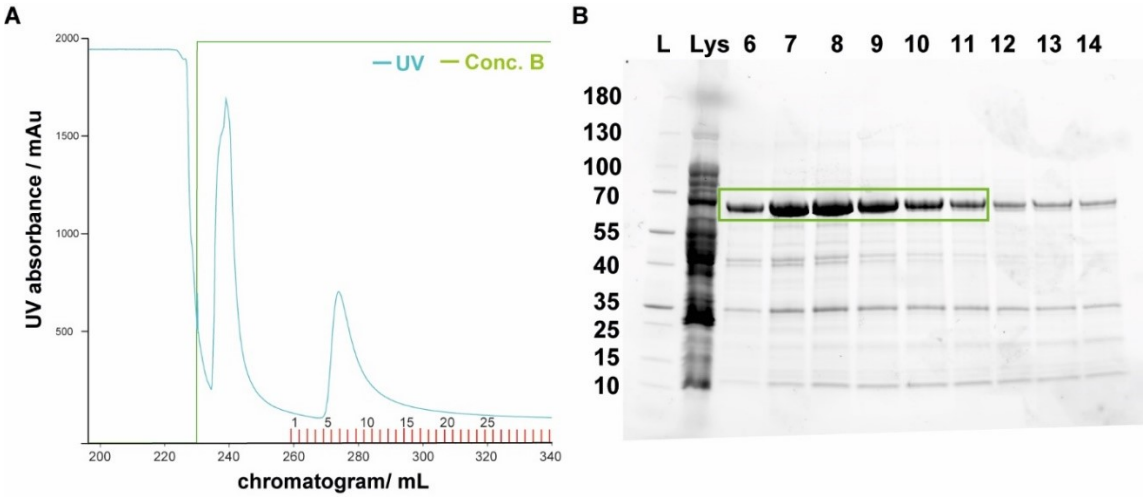


Figure 2.7. Purification of KDM6B by Ni^{2+} IMAC. A. *FPLC chromatogram showing IMAC program (green) and UV absorbance at 280 nm (blue).* ***B.*** *Corresponding SDS-PAGE gel. Band corresponds to expected mass of N-His_6-TRX-tagged KDM6B. Liquid Chromatography Mass Spectrometry (LC-MS) analysis of N-His_6-TRX-tagged KDM6B revealed an observed mass of 71135 Da, corresponding to the expected mass of 71135 Da (Appendix 4, Figure A4).* ***L:*** *ladder,* ***Lys:*** *cell lysate,* ***No.****: numbered elution fractions. Green box indicates combined fractions.*

KDM6B was purified from lysate via FPLC. Lysate was loaded on to a Protino® Ni-TED column (Figure 2.7, A), and bound KDM6B was eluted with binding buffer containing 250 mM imidazole. Eluted fractions were analysed by (SDS-PAGE) (5 µL of 1:1 fraction and 2x loading buffer per lane) (Figure 2.7). The major band corresponded to the molecular weight (MW) of KDM6B (71 kDa), judged to be of approximately 90% purity. Liquid Chromatography Mass Spectrometry (LC-MS) analysis of N-His6-TRX-tagged KDM6B revealed an observed mass of 71135 Da, corresponding to the expected mass of 71135 Da (Appendix 4, Figure A4). Selected fractions were buffer exchanged to remove imidazole using a PD-10 desalting column and concentrated using a centrifugal protein concentrator (30kDa, Amicon®), Aliquots were snap-frozen using liquid nitrogen and stored at -80°C.

2.6 Assessment of KDM6B activity by MALDI-MS activity assay

The MALDI-MS activity assay described above was utilised to assess the activity of *N*-His_6-TRX-tagged $KDM6B_{1141-1641,}$ purified in Section 2.5, against H3K27Me3 peptide substrate (21mer). KDM6B (4 µM), was incubated with H3K27Me3 21mer peptide (25 µM), Fe^{2+} (50 µM), ascorbate (4 mM) and 2-oxoglutarate (300 µM) in 50mM HEPES 150mM NaCl pH7.5 at 37°C and quenched with methanol at each time point. Increased intensity was seen at peaks corresponding to H3K27Me2-0, (Figure 2.8, B) indicating that KDM6B is active and catalyses the demethylation of Me3, Me2 and Me1 methylation states. As above, percentage demethylation was calculated (equation, figure 2.3, C), yielding the time course below. No significant increase in percentage demethylation was seen between 10 and 30 minutes. Additionally, the maximum percentage demethylation achieved was only 84.4%. Together these results may indicate time-dependent inactivation of KDM6B.

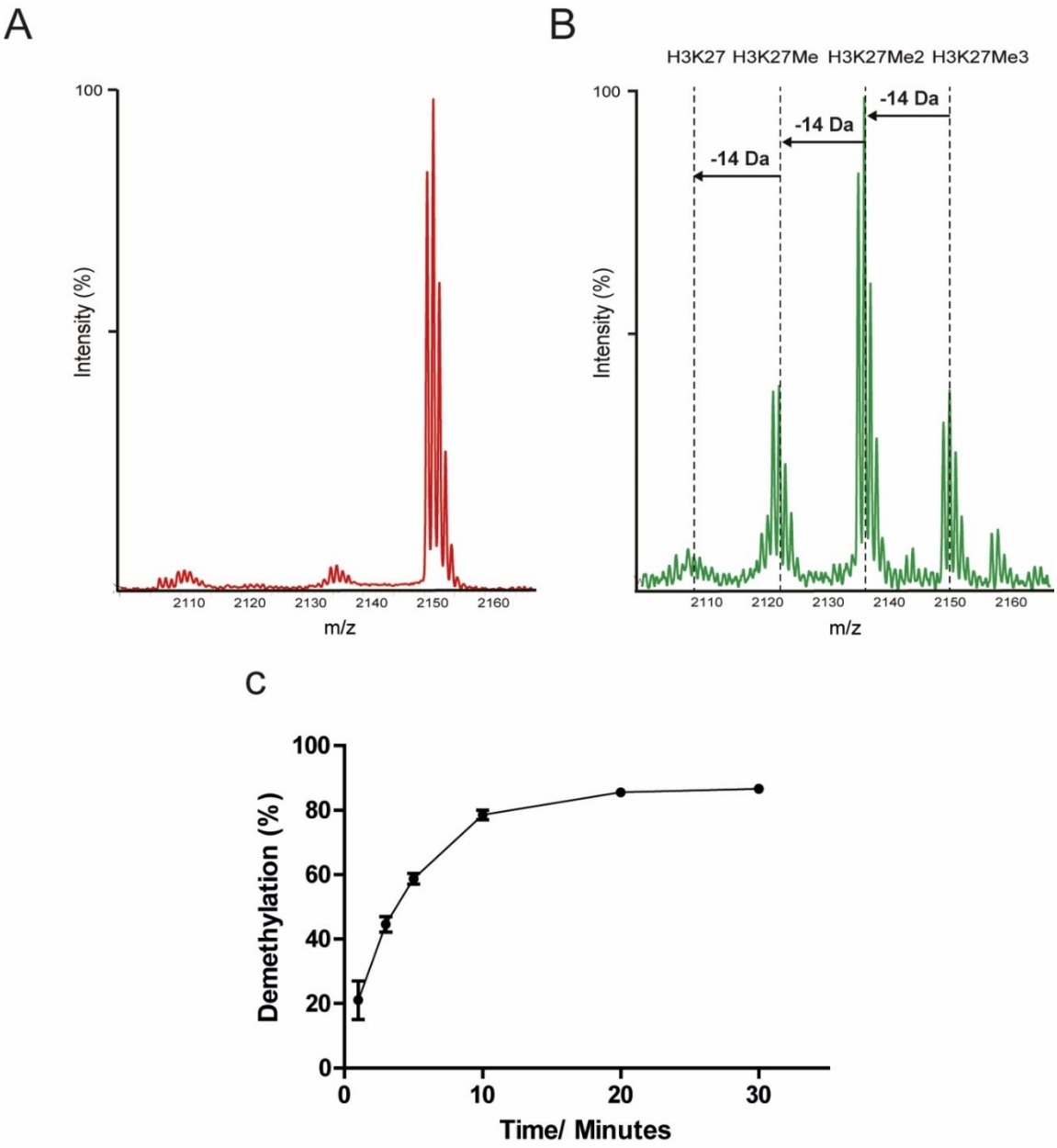


Figure 2.8. Assessment of KDM6B activity by MALDI-MS. *KDM6B (4 µM), was incubated with H3K27Me3 21mer peptide (25 µM), Fe^{2+} (50 µM), ascorbate (4 mM) and 2-oxoglutarate (300 µM) in 50mM HEPES 150mM NaCl pH7.5 at 37°C and quenched with methanol at each time point.* ***A, B MALDI-MS spectra of A, No enzyme control.*** *H3K27Me3 peptide incubated with Fe^{2+}, ascorbate and 2OG for 30 minutes.* ***B. KDM6B*** *incubated with H3K27Me3 peptide incubated with Fe^{2+}, ascorbate and 2OG for 30 minutes. Increased intensity of peaks corresponding to mass of demethylation products indicates demethylase activity* ***C. Percentage demethylation (%) of H3K27Me3 21mer peptide plotted versus time.*** *Error bars represent standard deviation, N=3 technical repeats.*

2.7 Kinetic characterisation of KDM6B by MALDI-MS

Evaluation of the steady-state parameters of KDM6B is required to inform the design of activity and inhibition assays. Thus, experiments were undertaken to determine the

Michaelis constant, K_m, for H3K27Me3 substrate peptide. KDM6B (4 µM), was incubated with Fe^{2+} (50 µM), ascorbate (4 mM) and 2-oxoglutarate (300 µM) and H3K27Me3 21mer peptide (10-200 µM) in 50mM HEPES 150mM NaCl pH7.5 at 37°C and quenched with methanol at each time point. The resulting time courses were used to determine the linear range of reaction and initial rate was calculated at each concentration to allow determination of K_m(H3K27Me3) (Figure 2.9). However, the analysis of initial rates at high peptide concentration was difficult due to the limitations of the MALDI-MS equipment. As stated above, the relative intensity of peaks is used to calculate percentage demethylation. At high substrate concentration, the absolute amount of H3K27Me2/1/0 product may increase, but this may be difficult to detect as a change in relative peak intensity due to the high proportion of substrate present. As an additional confounding factor, loss of peak resolution due to MALDI-MS equipment failure (Chapter 4) further reduced the sensitivity of the MALDI assay to small changes in substrate: product ratios. As a result, alternate assays were sought to allow kinetic characterisation of KDM6B.

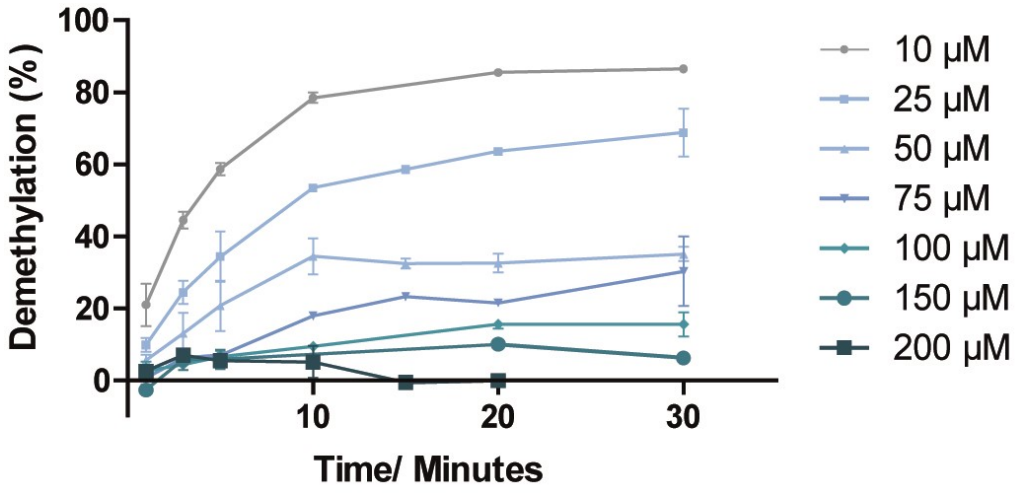


Figure 2.9. Time course analysis of KDM6B catalysed demethylation of H3K27Me3 21mer peptide (10-200 µM). *KDM6B (4 µM), was incubated with H3K27Me3 21mer peptide (10-200 µM), Fe^{2+} (50 µM), ascorbate (4 mM) and 2-oxoglutarate (300 µM) in 50mM HEPES 150mM NaCl pH7.5 at 37°C and quenched with methanol at each time point. Percentage demethylation (%) of H3K27Me3 21mer peptide plotted versus time. Error bars represent standard deviation, N=3 technical repeats.*

2.8 Alternate assays for the evaluation of KDM6 demethylase activity

Due to ongoing equipment failure preventing use of the MALDI-MS assay, work was undertaken to establish an alternate assay suitable for kinetic characterisation of KDM6B.

Of the available assays, the formaldehyde dehydrogenase assay was selected. JmjC-histone demethylases generate formaldehyde as a by-product of demethylation catalysis. In the formaldehyde dehydrogenase (FDH) coupled assay, this formaldehyde is oxidised to formic acid by FDH, with a concomitant reduction of nicotinamide adenine dinucleotide (NAD+) to NADH. The NADH produced is detected by fluorescence spectroscopy, allowing indirect measurement of histone demethylase activity (Figure 2.10). The FDH assay facilitates continuous monitoring of the rate of enzymatic reaction over time, making calculation of the rate of reaction facile and enabling precise identification of the linear range of the reaction.

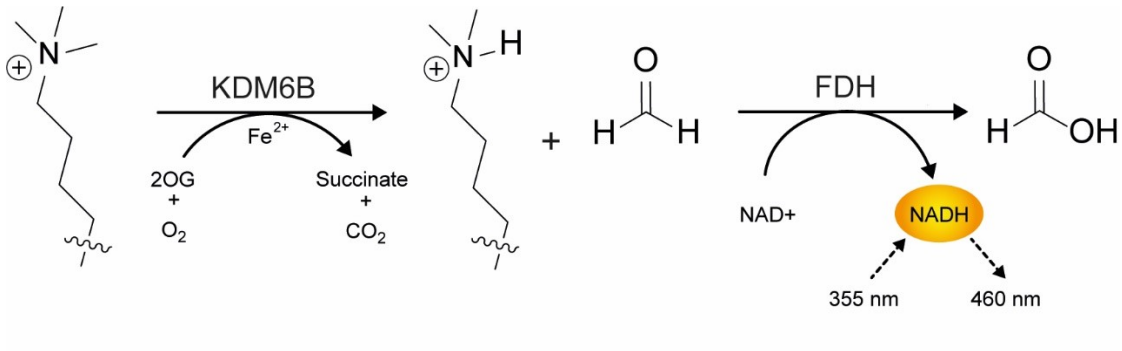


Figure 2.10. Principle of formaldehyde dehydrogenase (FDH)-coupled KDM assay. *Formaldehyde generated by KDM6B demethylase activity is oxidised to formic acid by FDH with concomitant reduction of NAD+ to NADH. NADH production is detected by fluorescence spectroscopy (excitation at 355 nm and emission at 460 nm).*

2.9 Purification of cleaved KDM6B for use in FDH assays

The MALDI-MS assays described above were undertaken using *N*-His_6-TRX-tagged $KDM6B_{1141-1641}$. The His_6 affinity tag and thioredoxin (TRX) fusion protein are left in place as the TRX fusion protein has a solubilising effect. However, TRX oxidises NADH to NAD+, interfering with the FDH assay and thus it was necessary to remove the tag. The 'JMJD3A-C031' KDM6B expression plasmid encodes a tobacco etch virus (TEV) protease cleavage site after the *N*-His_6-TRX-tag.

2.9.1 KDM6B Purification 1 – Small-scale TRX cleavage

A small-scale cleavage was undertaken in the first instance using aliquots of *N*-His_6-TRX-tagged $KDM6B_{1141-1641}$ from a previous purification. *N*-His_6-tagged TEV was incubated with *N*-His_6-TRX-tagged $KDM6B_{1141-1641}$ at a 50:1 ratio for 14 hours at 4°C. Cleavage mixture was then directly eluted through a Protino® Ni-TED column to remove uncleaved KDM6B and *N*-His_6-tagged TEV. SDS-PAGE analysis showed bands corresponding to the expected mass for cleaved KDM6B (57 kDa) (5 µL of 1:1 fraction and 2x loading buffer per lane). LC-MS analysis of cleaved KDM6B revealed an observed mass of 57198 Da, corresponding to the expected mass 57208 (Appendix 5, Figure A5). Selected fractions (Figure 2.11, B) were concentrated using a centrifugal protein concentrator (30 kDa, Amicon®). Aliquots were snap-frozen using liquid nitrogen and stored at -80°C.

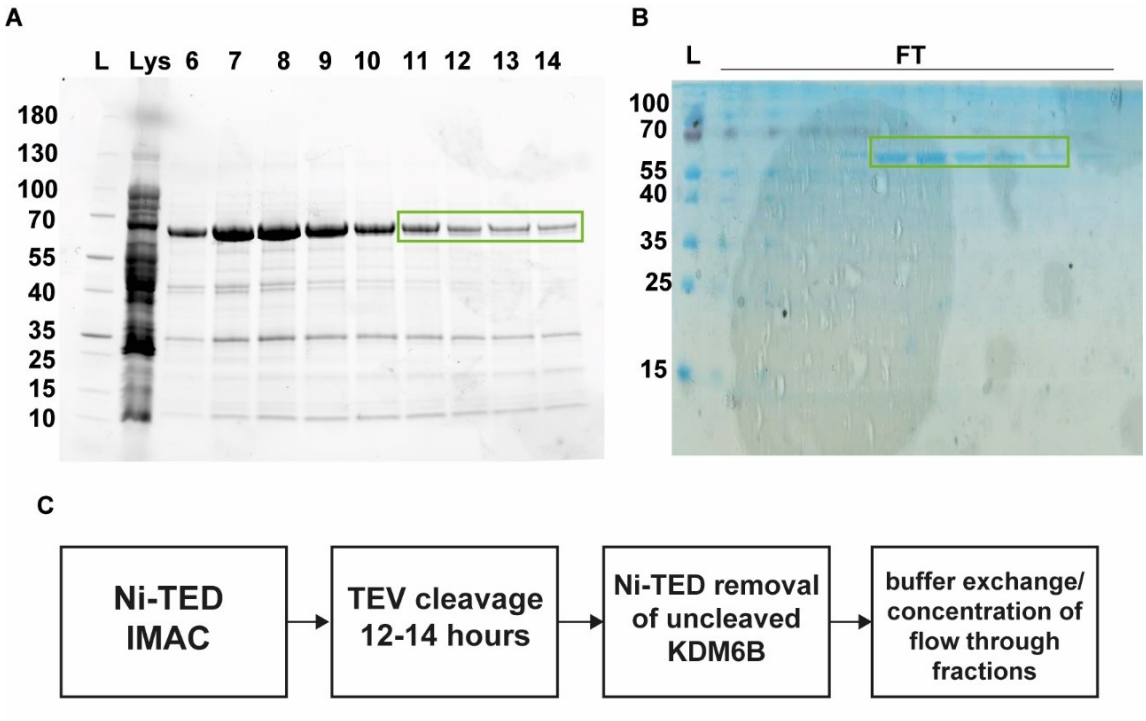


Figure 2.11. Purification of KDM6B by Ni^{2+} IMAC chromatography A. *SDS-PAGE gel of Ni-TED IMAC purification.* ***L:*** *ladder ,**Lys**: Lysate* ***No.**: numbered elution fractions. Green box indicates selected fractions.* ***B.*** *SDS-PAGE gel of Ni-TED IMAC flow through fractions following TEV cleavage* ***L:*** *ladder ,**Lys**: Lysate* ***No.**: numbered elution fractions. Green box indicates selected fractions. Expected MW of N-His_6-TRX-tagged $KDM6B_{1141-1641}$ and cleaved KDM6B is 71 kDa and 57 kDa respectively.* ***C. Purification steps.***

Activity of KDM6B was assessed by FDH assay. Briefly, KDM6B (2.5 µM, 5 µM) was incubated with H3K27Me3 21mer peptide (50 µM), Fe^{2+} (50 µM), ascorbate (4 mM) and 2-oxoglutarate (300 µM), NAD+ (500 µM), and FDH (1 Unit/ml) in 50mM HEPES pH7.5 0.01% tween20 at 37°C. Enzyme and substrate mixes were prepared separately. Substrate mix was preincubated at 37°C for 5 minutes prior to initiation of the reaction with enzyme mix. Production of NADH was fluorescently monitored using a PHERAstar FS plate reader (BMG Labtech). Readings were taken over 120 cycles with a cycle time of 30 seconds. The cleaved KDM6B was active at both concentrations tested, as demonstrated by the increased fluorescence during the reaction (Figure 2.12).

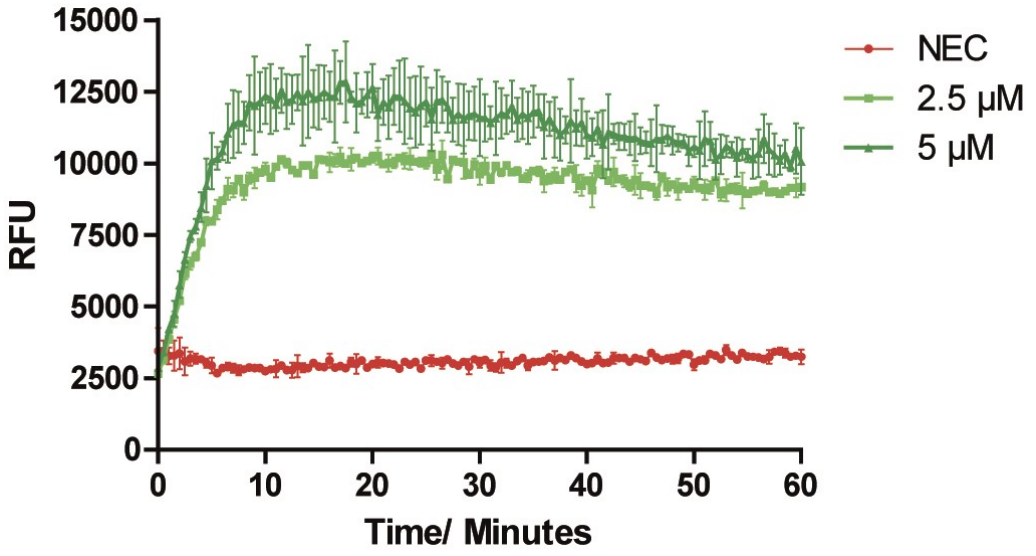


Figure 2.12. Assessment of cleaved KDM6B activity by FDH assay. *KDM6B (endonuclease reaction mixture, 10 µl) was incubated with H3K27Me3 21mer peptide (50 µM), Fe^{2+} (50 µM), ascorbate (4 mM), 2-oxoglutarate (300 µM), NAD+ (500 µM), and FDH (1 Unit/ml) in 50mM HEPES pH7.5 0.01% tween20 at 37°C for 60 minutes Increased fluorescence intensity indicates activity of cleaved KDM6B against H3K27Me3 21mer peptide. Red – No enzyme control (NEC), light green 2.5 µM cleaved KDM6B, dark green 5 µM cleaved KDM6B. Error bars represent standard deviation, N=3 technical repeats. RFU – relative fluorescence units.*

2.9.2 KDM6B Purification 2 - Expression and scaled-up cleavage and purification of KDM6B results in inactive enzyme

Following the successful production of a small amount of catalytically active cleaved KDM6B above, a large-scale expression and purification was undertaken. KDM6B was expressed in Rossetta2(DE3) as before, and purified from lysate by Ni^{2+} IMAC using a Protino® Ni-TED column (GE Healthcare) (Figure 2.13, A), eluted with binding buffer containing 250 mM imidazole. Eluted fractions were analysed by (SDS-PAGE) (Figure 2.13, B) and selected fractions were combined before incubation with N-His6-tagged TEV 50:1 ratio for 15 hours at 4°C. After cleavage, buffer exchanged to remove imidazole using a using a centrifugal protein concentrator (30kDa, Amicon®). Cleavage mixture was then eluted through a Protino® Ni-TED column to remove uncleaved KDM6B and N-His6-tagged TEV. SDS-PAGE analysis showed a major band corresponding to the expected mass for cleaved KDM6B (57 kDa) (5 µL of 1:1 fraction and 2x loading buffer per lane), judged to be of greater than 90% purity (Figure 2.13, C)

(5 µL of 1:1 fraction and 2x loading buffer per lane). Selected fractions were concentrated using a centrifugal protein concentrator (30kDa, Amicon®). Aliquots were snap-frozen using liquid nitrogen and stored at -80°C prior to activity assays.

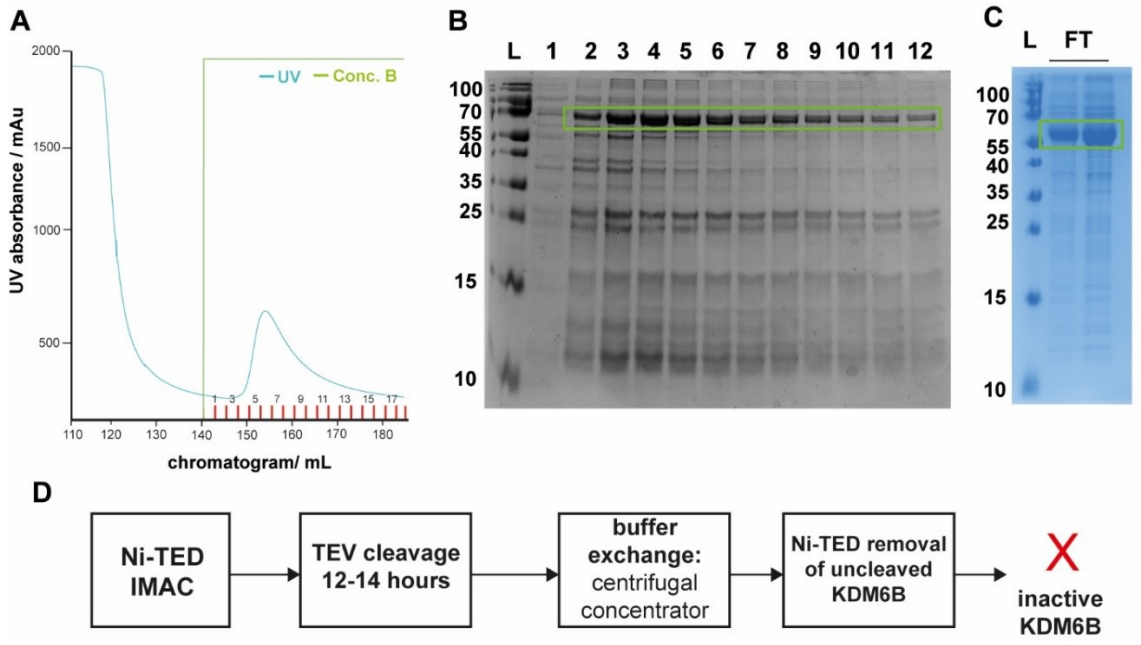


Figure 2.13. Purification of cleaved KDM6B by Ni^{2+} IMAC chromatography A. *FPLC chromatogram showing IMAC program (green) and UV absorbance at 280 nm (blue).* ***B.*** *SDS-PAGE gel of Ni-TED IMAC purification showing band at expected mass of N-His_6-TRX-tagged $KDM6B_{1141-1641}$ 71 kDa* ***C.*** *SDS-PAGE gel of Ni-TED IMAC flow through fractions showing band at expected mass of cleaved $KDM6B_{1141-1641}$ 57 kDa* ***L:*** *ladder,* ***Lys****: Lysate* ***FT:*** *flow through* ***No.****: numbered elution fractions. Green box indicates selected fractions.* ***D. Purification steps.***

As above, the activity of cleaved KDM6B P2 was evaluated using the FDH assay. Active cleaved KDM6B from the small-scale purification (KDM6B P1) was also included as a positive control. KDM6B P1/P2 (5 µM) was incubated with H3K27Me3 21mer peptide (50 µM), Fe^{2+} (50 µM), ascorbate (4 mM), 2-oxoglutarate (300 µM), NAD+ (500 µM), and FDH (1 Unit/ml) in 50mM HEPES pH7.5 0.01% tween20 at 37°C. An increase in fluorescence was seen for KDM6B P1, but no increase in fluorescence was seen after 55 minutes in wells containing KDM6B P2 (Figure 2.14).

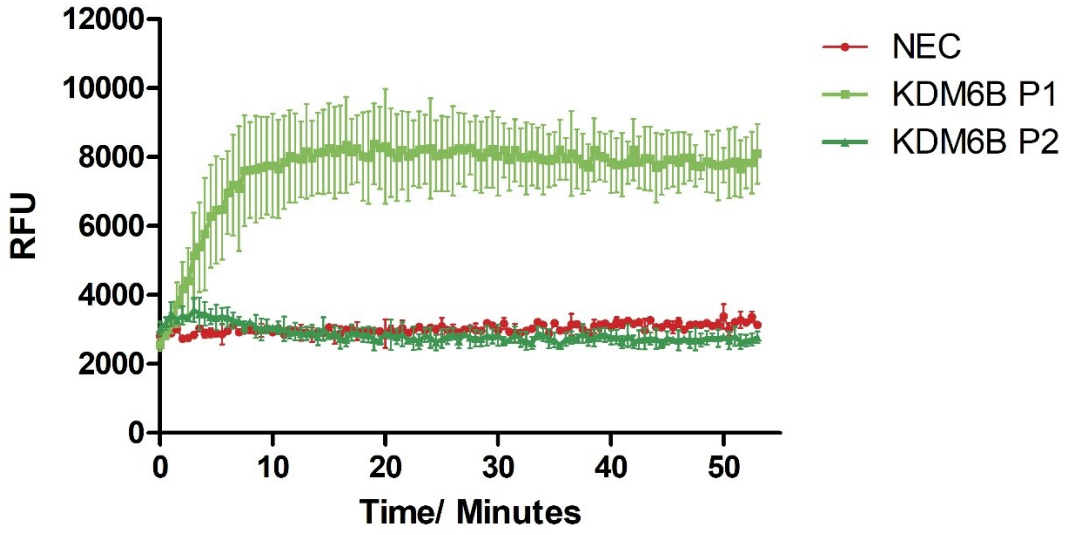


Figure 2.14. Assessment of cleaved KDM6B activity from purification 1 and purification 2 (KDM6B P2) by FDH assay. *KDM6B P1/P2, 5 µM was incubated with H3K27Me3 21mer peptide (50 µM), Fe^{2+} (50 µM), ascorbate (4 mM), 2-oxoglutarate (300 µM), NAD+ (500 µM), and FDH (1 Unit/ml) in 50mM HEPES pH7.5 0.01% tween20 at 37°C for 55 minutes. Increased fluorescence intensity indicates activity of cleaved KDM6B P1 against H3K27Me3 21mer peptide. However, no increase was seen in wells containing KDM6B P2, indicating inactivity of KDM6B P2. Error bars represent standard deviation, N=3 technical repeats. RFU – relative fluorescence units.*

Samples of reaction mixture from the FDH assay were evaluated using MALDI-MS (Figure 2.15). Consistent with the FDH results, increased intensity was seen at peaks corresponding to H3K27Me2-0, in the KDM6B P1 sample, whereas this increase was not observed in the KDM6B P2 sample, indicating the KDM6B P2 batch of enzyme is inactive.

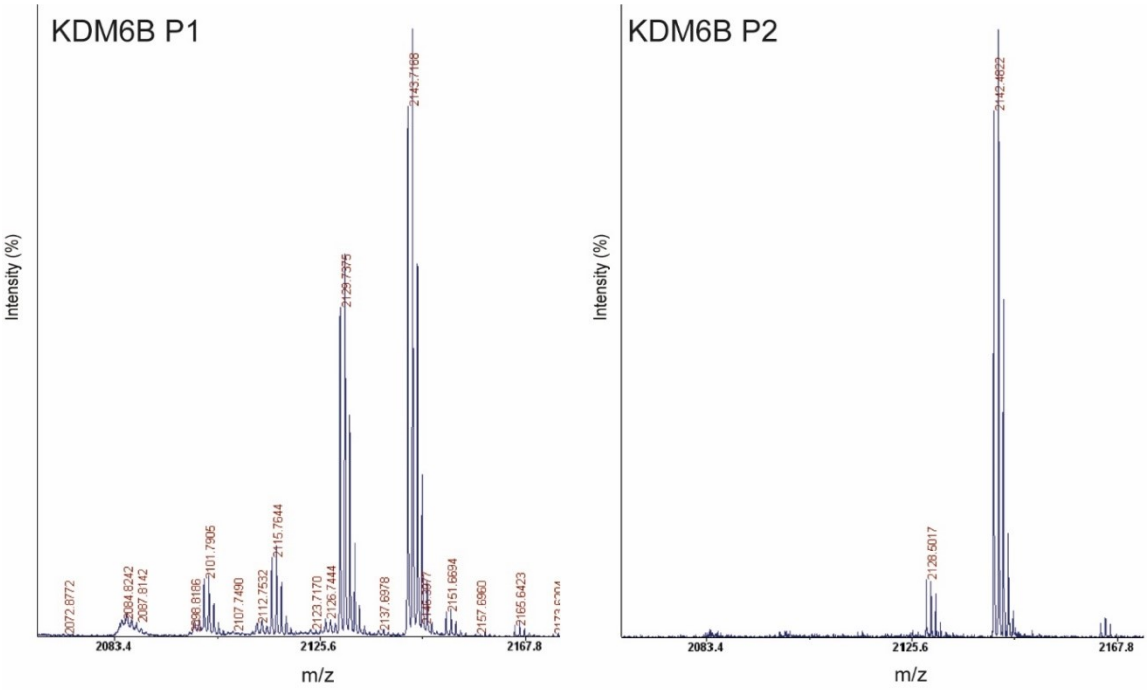


Figure 2.15. Assessment of KDM6B activity by MALDI-MS. Aliquots (1 µl) of FDH assay mixture containing KDM6B P1 and KDM6B P2 were analysed by MALDI-MS. KDM6B P1 *Increase in intensity of H3K27Me2/1/0 peptide mass peaks indicates activity of KDM6B P1.* ***KDM6B P2 A****bsence of increased intensity* ***of*** *H3K27Me2/1/0 peptide mass peaks indicates inactivity of KDM6B P2.*

2.9.3 KDM6B Purification 3 – Alteration of cleavage and purification method used to purify KDM6B again results in inactive enzyme

Differential activity of the cleaved KDM6B purification batches may arise from changes in the purification protocol used. Different buffer exchange methods were used in each purification to remove imidazole. In the test purification this was achieved using a PD-10 desalting column (GE Healthcare) whereas in the second purification this was achieved via the 'washing out' technique using a protein concentrator (30 kDa, Amicon®). Protein concentration can cause precipitation or aggregation leading to inactivation; however, buffer exchange using a PD-10 desalting column also requires a protein concentration step using a centrifugal protein concentrator, and so it was unexpected that this change in buffer exchange method would affect KDM6B activity. An additional concern was the time cost of both buffer exchange methods, either of which add several hours to the overall purification duration, potentially causing a loss in activity.

To address these concerns, the purification of KDM6B was repeated, adapting the protocol to eliminate the buffer exchange step by utilising concurrent TEV cleavage and dialysis. KDM6B was purified from lysate by Ni^{2+} IMAC using a Protino® Ni-TED column (GE Healthcare) (Figure 2.16, A), eluted with binding buffer containing 250 mM imidazole. Eluted fractions were analysed by SDS-PAGE (Figure 2.16, B) and selected fractions were combined before incubation with *N*-His_6-tagged TEV at a 50:1 ratio. The KDM6B/TEV cleavage mixture (~10mL) was sealed in dialysis tubing and incubated, stirring, in 200 volumes of dialysis buffer (50mM HEPES, 500mM NaCl, 5% glycerol) for 16 hours at 4°C. Cleavage mixture was then eluted through a Protino® Ni-TED column to remove uncleaved KDM6B and *N*-His_6-tagged TEV. SDS-PAGE analysis showed bands corresponding to the expected mass for cleaved KDM6B (57 kDa), judged to be of greater than 90% purity (Figure 2.16, C) (5 µL of 1:1 fraction and 2x loading buffer per lane).

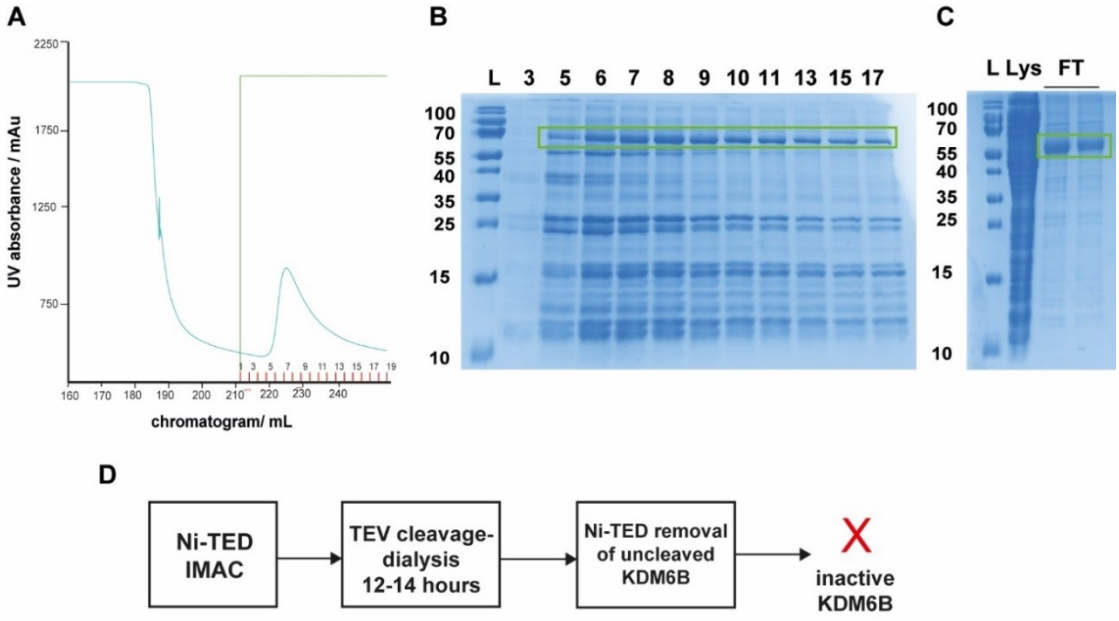


Figure 2.16. Purification of cleaved KDM6B (KDM6B P3) by Ni^{2+} IMAC chromatography A. *FPLC chromatogram showing IMAC program (green) and UV absorbance at 280 nm (blue).* ***B.*** *SDS-PAGE gel of Ni-TED IMAC purification showing band at expected mass of N-His_6-TRX-tagged $KDM6B_{1141-1641}$ 71 kDa* ***C.*** *SDS-PAGE gel of Ni-TED IMAC flow through fractions showing band at expected mass of cleaved $KDM6B_{1141-1641}$ 57 kDa.* ***L:*** *ladder ,**Lys**: Lysate* ***FT:*** *flow through* ***No.****: numbered elution fractions. Green box indicates selected fractions.* ***D. Purification steps.***

Selected fractions (Figure 2.16) were concentrated using a centrifugal protein concentrator (30kDa, Amicon®). Finally, aliquots were snap-frozen using liquid nitrogen and stored at -80°C prior to activity assays.

As above, the activity of cleaved KDM6B P1 and KDM6B P3 was evaluated using the FDH assay. KDM6B (5, 10 µM) was incubated with H3K27Me3 21mer peptide (50 µM), Fe^{2+} (50 µM), ascorbate (4 mM, 2-oxoglutarate (300 µM), NAD+ (500 µM), and FDH (1 Unit/ml) in 50mM HEPES pH7.5 0.01% Tween20 at 37°C. No increase in fluorescence was seen after 60 minutes even at 10 µM KDM6B P3, indicating the enzyme was again inactive (Figure 2.17).

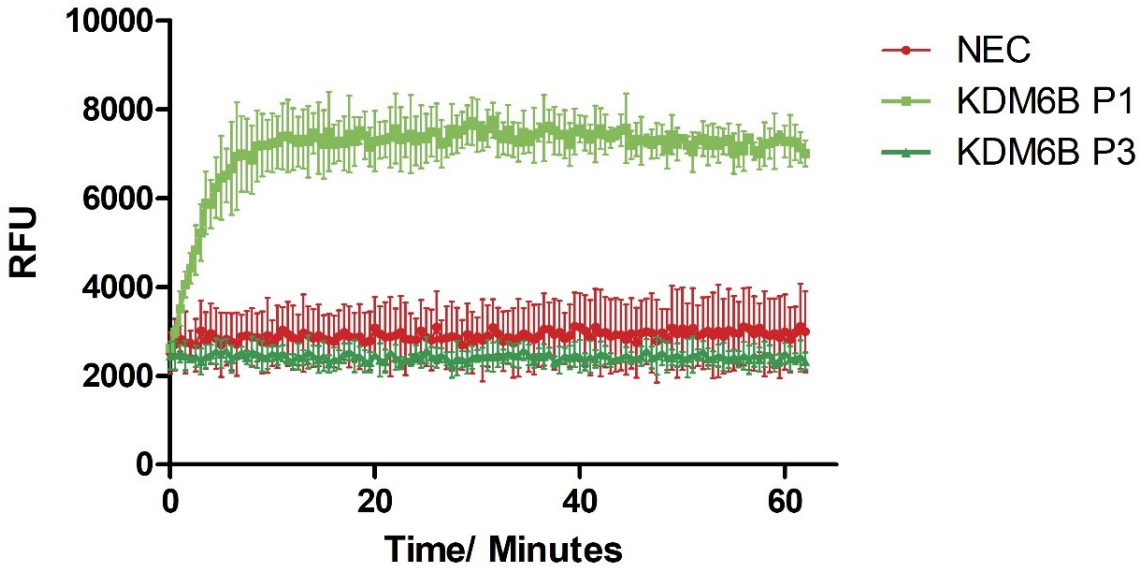


Figure 2.17. Assessment of cleaved KDM6B P3 activity by FDH assay. *KDM6B P1/P3 (5 µM) was incubated with H3K27Me3 21mer peptide (50 µM), Fe2+ (50 µM), ascorbate (4 mM), 2-oxoglutarate (300 µM), NAD+ (500 µM), and FDH (1 Unit/ml) in 50mM HEPES pH 7.5 0.01% tween20 at 37°C for 64 minutes. Increased fluorescence intensity indicates activity of KDM6B P1 against H3K27Me3 21mer peptide. No increase in fluorescence intensity after 60 minutes indicates inactivity of KDM6B P2 against H3K27Me3 21mer peptide. Error bars represent standard deviation, N=3 technical repeats. RFU – reference fluorescence units.*

2.9.10 UV-Vis spectrometry identifies contamination of inactive KDM6B batches

Following unsuccessfully attempts to purify cleaved KDM6B, (Table 2.3) protein samples underwent analysis by UV-vis spectroscopy.

Batch	IMAC method	Buffer exchange method	Post-cleavage IMAC method	Activity
KDM6B P1	Protino® Ni-TED	N/A	Protino® Ni-TED	Active
KDM6B P2	Protino® Ni-TED	Centrifugal protein concentration	Protino® Ni-TED	Inactive
KDM6B P3	Protino® Ni-TED	Dialysis	Protino® Ni-TED	Inactive

Table 2.3. *Purification methods used in production of active and inactive cleaved KDM6B batches.*

UV-vis spectroscopy is a commonly used technique to quantify the concentration of protein solutions and assess purity. Aromatic amino acid side chains, such as tryptophan, phenylalanine, tyrosine and histidine, within proteins are responsible for characteristic absorbances at 280 nm and 230 nm. The concentration of a protein solution may be calculated based on absorbance at 280 nm using the Beer-Lambert law. Absorbances at other wavelengths can indicate the presence of contaminants in a protein solution. On inspection of the UV-vis spectra of the purified KDM6B batches, it was found that a contaminant absorbing at 260 nm was present in both inactive batches of KDM6B (Table 2.3, Figure 2.18).

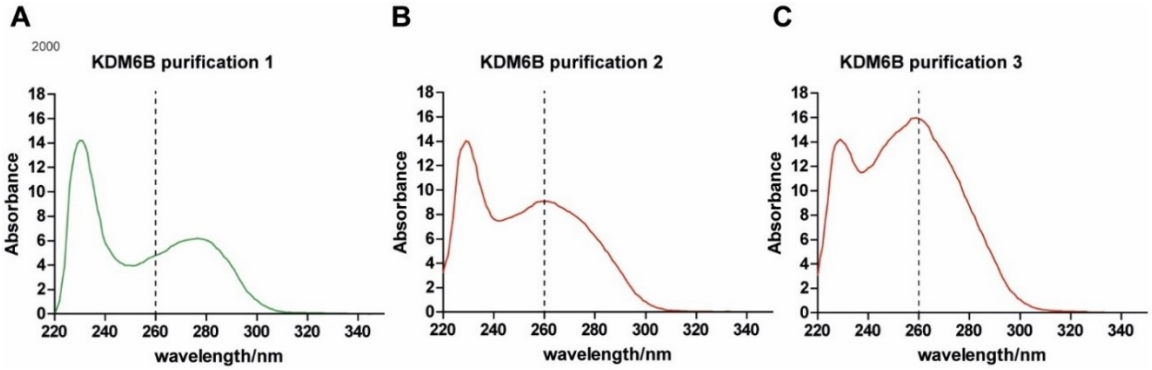


Figure 2.18. UV-vis spectroscopy reveals contamination of KDM6B samples. A. *KDM6B purification 1 shows expected UV-vis spectrum with characteristic protein absorbances at 230 nm and 280 nm.* ***B, C*** *KDM6B P2 and KDM6B P3 show strong absorbance at 260 nm, corresponding to absorbance by DNA.*

Nucleic acids absorb UV light at 260 nm due to the aromatic base moieties within their structure. Calculation of the A_{280}/A_{260} ratio is a common method to assess protein purity, and was originally developed by Warburg and Christian to assess the presence of DNA in protein samples.[17] An A_{260}/A_{280} ratio of 0.6 is considered to be 'pure' protein, whilst the relative percentage of protein and DNA present in a sample can be approximately calculated using equation 2.1. Absorbance at 260 nm was seen in both samples from KDM6B purification 3 (KDM6B P3) and KDM6B purification 2 (KDM6B P2). The A_{260}/A_{280} ratios of protein samples from KDM6B P 1, 2 and 3 were 0.8, 1.46 and 1.82 respectively, indicating a percentage protein of 98%, 86% and 59% respectively, according to equation 2.1.

$$Protein\ (\%) = \frac{100 - (11.6\mathrm{R} - 6.32)}{2.16 - R}$$

Equation 2.1. Calculation of approximate percentage protein in a protein solution containing DNA derived by Warburg et al.[17] ***R =*** A_{260}/A_{280} ratio.

Further characterisation was undertaken to confirm that the contaminant causing absorbance at 260 nm was indeed DNA. SybrSafe DNA gel stain binds to DNA. The resulting DNA-dye-complex absorbs blue light (509 nm) and emits green light (524 nm), allowing visualisation of DNA by fluorescence spectroscopy. The lower limit of detection of SYBRSafe gel staining is 500pg/ band allowing sensitive detection of DNA in

samples.[18] DNA gel loading dye (6X,1 µl, ThermoScientific) was added to samples of protein from each purification (5 µl) and loaded to an agarose gel (2.5%), stained with SybrSafe DNA gel stain. The gel was run at 85V for 50 minutes and visualised using a ChemiDock MP gel imager (BioRad) (Figure 2.19)

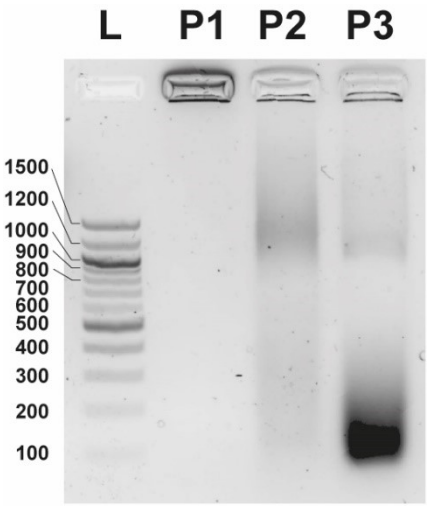


Figure 2.19. Agarose gel electrophoresis indicates DNA contamination of KDM6B P2 and KDM6B P3. *Samples of protein from each purification (P1, P2, P3) (5 µl) was mixed with 6x DNA loading dye (1 µl) and loaded to a 2.5% agarose gel stained with SybrSafe DNA gel stain (5 µl). The broad band present in the KDM6B P3 sample between 100-200 bp indicates DNA contamination, whilst dark smear in P2 sample indicates lesser DNA contamination.*

As expected, no band was detected in the KDM6B P1 sample. A large broad band was seen between 100-200 base pairs (bp) in the KDM6B P3 sample, strongly indicating the sample is contaminated with DNA. Whilst no band was present in the KDM6B P2 sample, a dark smear was present indicating lesser contamination relative to KDM6B P3, consistent with their A_{260}/A_{280} values.

2.10 Endonuclease treatment of contaminated KDM6B restores catalytic activity

DNA may be removed from protein solutions by treatment with endonucleases, such as DNase I and Benzonase®, which degrade DNA to oligonucleotide of less than 5 bp in length.[19] Relatively high salt concentration is present in the KDM6B samples (50mM HEPES 500mM NaCl 5% glycerol pH 7.5). Benzonase® activity may be inhibited by monovalent cation concentrations exceeding 300mM,[19] and therefore the activity of

Benzonase® and DNase I was evaluated at these buffer conditions. Plasmid DNA (pNH-TrxT, 7575 bp, 500ng) was incubated with DNase I (0.01 mg/mL) and Benzonase® (0.09 U/ng) in 50mM HEPES 500mM NaCl 1mM $MgCl_2$ 5% glycerol pH7.5 and incubated for 30 minutes at 4°C. A sample of the reaction mixture was analysed by agarose gel electrophoresis as above. No band corresponding to plasmid DNA could be detected in the reaction mixture (Figure 2.20), indicating that endonuclease activity is maintained under the reaction conditions.

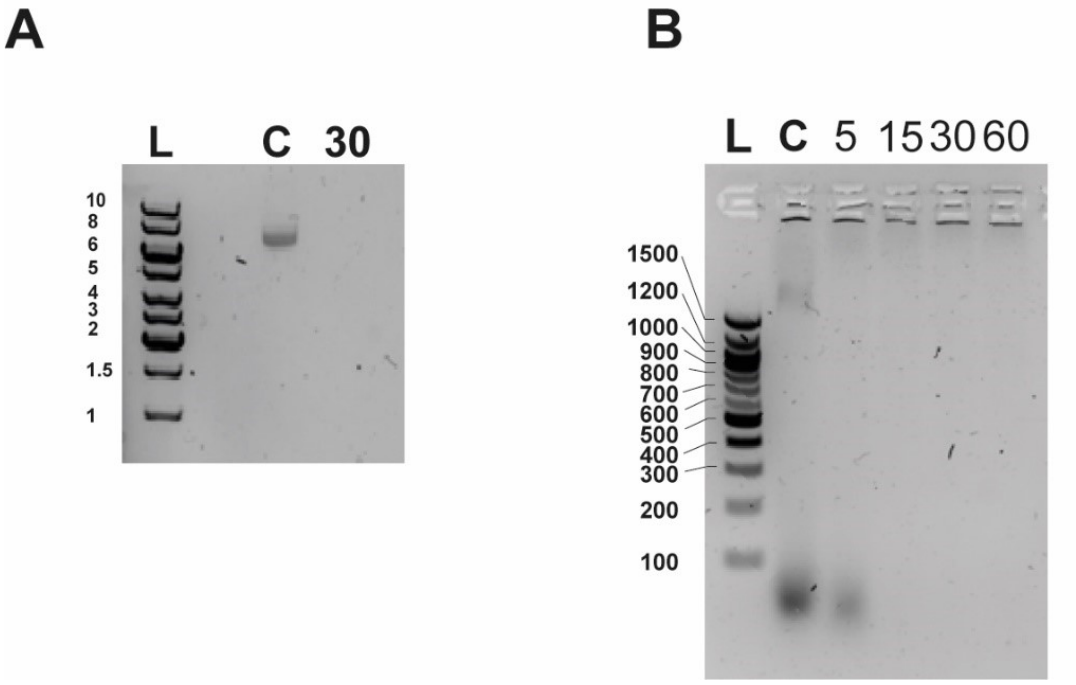


Figure 2.20. Endonuclease treatment results in reduced DNA observable by agarose gel electrophoresis. ***A****. Incubation of plasmid DNA (pNH-TrxT, 7575 bp, 500ng) with DNase I and Benzonase® for 30 minutes at 4°C results in complete degradation, as observed by loss of band in 30 minute incubation sample versus no enzyme control* ***B.*** *Treatment of KDM6B P3 with DNase I and Benzonase® results in reduction of DNA contamination observable by reduction in intensity of broad band at <100 bp. (5 µL of 5:1 reaction mixture and 6x loading buffer loaded per lane in each gel).*

To test if endonuclease treatment would remove contamination, a sample of KDM6B P3 incubated with DNase I (0.01 mg/mL) and Benzonase® (0.09 U/ng) at 4°C. An aliquot of reaction mixture was snap frozen using liquid nitrogen at each time point 5, 15, 30 and 60 minutes and samples were then analysed by agarose gel electrophoresis as above. No

DNA band was detectable in the sample after 15 minutes incubation (Figure 2.20, B), further confirming that the contamination is highly likely to be DNA.

To assess the effect of treatment with Benzonase® and DNase I on the activity of contaminated KDM6B, KDM6B P3 was treated with DNase I (0.01 mg/mL) and Benzonase® (0.09 U/ng) in 50mM HEPES 500mM NaCl 1mM $MgCl_2$ 5% glycerol pH7.5 and incubated for 30 minutes at 4°C. The activity of endonuclease treated KDM6B P3 was then immediately assessed by FDH and MALDI-MS activity assays.

KDM6B (10 ul endonuclease reaction mixture) was incubated with H3K27Me3 21mer peptide (50 µM), Fe^{2+} (50 µM), ascorbate (4 mM), 2-oxoglutarate (300 µM), NAD+ (500 µM), and FDH (1 Unit/ml) in 50mM HEPES pH7.5 0.01% tween20 at 37°C for 60 minutes. No increase in fluorescence was seen after 60 minutes, although fluorescence intensity increased in active control wells containing KDM6B P1, indicating endonuclease treated KDM6B P3 was again inactive (Figure 2.21).

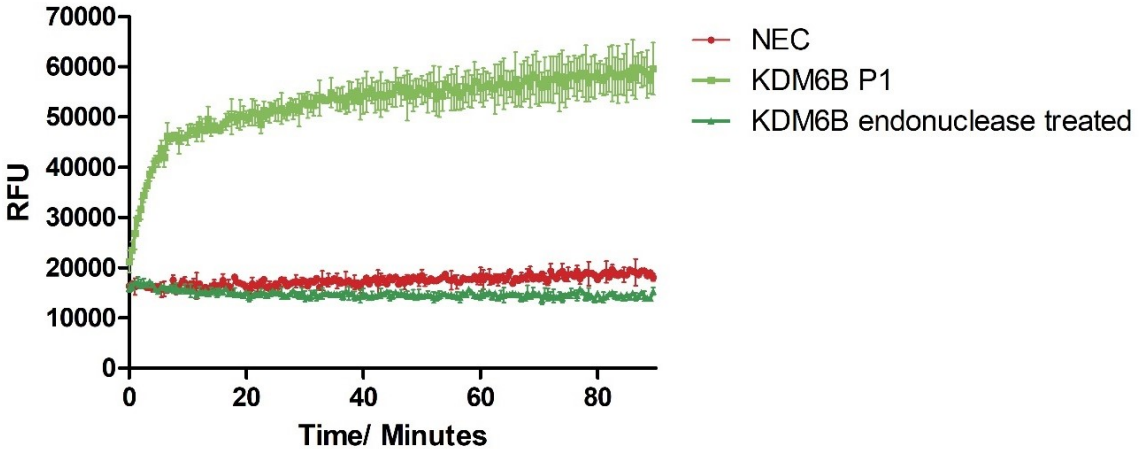


Figure 2.21 Assessment of endonuclease treated KDM6B P3 activity by FDH assay. *KDM6B P1/endonuclease treated P3 (5 µl endonuclease reaction mixture) was incubated with H3K27Me3 21mer peptide (50 µM), Fe2+ (50 µM), ascorbate (4 mM), 2-oxoglutarate (300 µM), NAD+ (500 µM), and FDH (1 Unit/ml) in 50mM HEPES pH7.5 0.01% tween20 at 37°C for 85 minutes. Increased fluorescence intensity indicates activity of KDM6B P1 against H3K27Me3 21mer peptide. No increase in fluorescence intensity after 60 minutes indicates inactivity of endonuclease treated KDM6B P3 against H3K27Me3 21mer peptide. Error bars represent standard deviation, N=3 technical repeats. RFU – reference fluorescence units.*

However, samples of FDH reaction mixture were analysed by MALDI-MS. Increased intensity was seen at peaks corresponding to H3K27Me2, (Figure 2.22, B) indicating that treatment of contaminated KDM6B with Benzonase® and DNase I restored KDM6B activity. This apparent disparity between the MALDI-MS and FDH results may indicate that the oligonucleotides/ digested DNA fragments could interfere with the FDH assay.

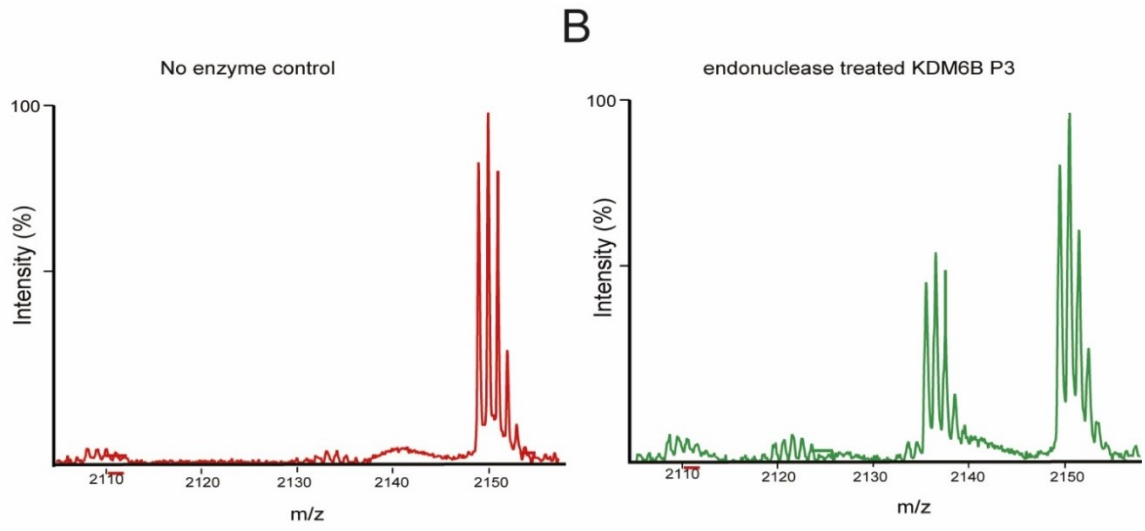


Figure 2.22. Assessment of endonuclease treated KDM6B P3 activity by MALDI-MS. *KDM6B (endonuclease reaction mixture, 10 µl) was incubated with H3K27Me3 21mer peptide (50 µM), Fe2+ (50 µM), ascorbate (4 mM), 2-oxoglutarate (300 µM), NAD+ (500 µM), and FDH (1 Unit/ml) in 50mM HEPES pH7.5 0.01% tween20 at 37°C for 60 minutes.* ***A.*** *No enzyme control.* ***B.*** *Endonuclease treated KDM6B P3.*

2.11 Purification of KDM6B P2 via heparin affinity chromatography removes contamination and restores activity

HiTrap Heparin HP columns are commonly used for high-resolution purification of DNA-binding proteins which co-purify with DNA. These columns effect separation of protein from DNA by biomimetic ligand affinity and ion exchange chromatography. The resin consists of Heparin which is covalently coupled to sepharose beads. Heparin mimics the backbone of DNA, and at low salt concentration is negatively charged causing protein binding, at which time contaminating DNA elutes from the column. At high salt concentration the ionic interaction is disrupted, and the protein elutes. Whilst endonuclease treatment was successful both in digesting DNA contamination and

restoring catalytic activity, it did not provide separation of the KDM6B from the digested DNA. Additionally, for activity/ inhibition studies of KDM6B, further purification would need to be undertaken to remove the endonucleases. As heparin affinity chromatography provides separation of DNA and enzyme in a single step, test purification of KDM6B P2 by heparin affinity chromatography was undertaken.

KDM6B P2 was diluted 1:10 in 50mM HEPES pH 7.5 to yield KDM6B P2 in 50mM HEPES, 50mM NaCl pH7.5 which was loaded on to a pre-equilibrated 1 mL HiTrap Heparin HP column. After washing with 5 volumes of 50 mM NaCl 50 mM HEPES pH 7.5, KDM6B P2 was eluted with a gradient of 0-100% 50mM HEPES 1M NaCl pH7.5. Eluted fractions were analysed by SDS-PAGE (5 μL of 1:1 fraction and 2x loading buffer per lane). The major band corresponded to the MW of KDM6B (71 kDa), judged to be of approximately 90% purity. Fraction 10 was concentrated using a centrifugal protein concentrator (30kDa, Amicon®), and analysed by UV-vis spectroscopy (Figure 2.23). Aliquots were snap-frozen using liquid nitrogen and stored at -80°C.

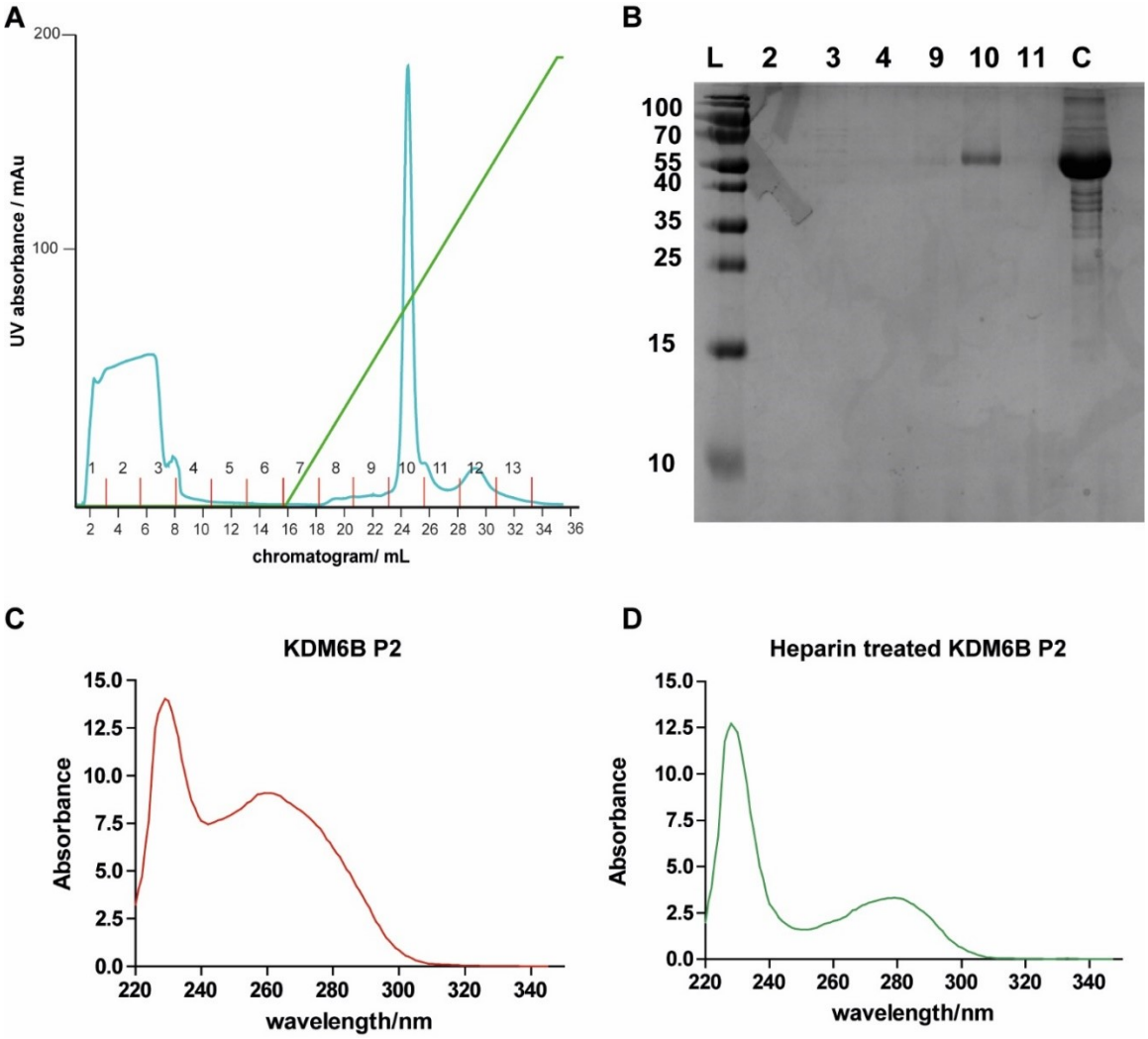


Figure 2.23. Purification of KDM6 P2 by heparin affinity chromatography removes DNA contamination . SDS-PAGE gels from A. *FPLC chromatogram showing IMAC program (green) and UV absorbance (blue).* ***B.*** *SDS-PAGE gel showing fractions and concentrated fraction 10 band corresponds to expected mass of cleaved KDM6B$_{1141-1641}$ 57 kDa* ***L:*** *ladder,* ***C:*** *concentrated heparin purified KDM6B P2* ***No.****: numbered elution fractions.* ***C.****UV-vis spectrum of KDM6 P2 prior to heparin affinity purification, showing strong absorbance at 260 nm.* ***D****. UV-vis spectrum of KDM6 P2 after heparin affinity purification, showing reduced absorbance at 260 nm, indicating removal of contaminating DNA.*

Comparison of the UV-Vis spectra of KDM6B P2, and heparin treated KDM6B P2 (Figure 2.23, C, D) revealed that heparin affinity chromatography had reduced the absorbance at 260 nm, indicating successful removal of the DNA contamination.

The activity of heparin treated KDM6B P2 was evaluated using the MALDI-MS activity assay. KDM6B (4 μM), was incubated with H3K27Me3 21mer peptide (25 μM), Fe^{2+} (50 μM), ascorbate (4 mM) and 2-oxoglutarate (300 μM) in 50mM HEPES 150mM NaCl

pH7.5 at 37°C and quenched with methanol at each time point. Increased intensity was seen at peaks corresponding to H3K27Me2-0, (Figure 2.24, B) indicating that as expected, KDM6B catalyses the demethylation of Me3, Me2 and Me1 methylation states, demonstrating successful purification of active protein.

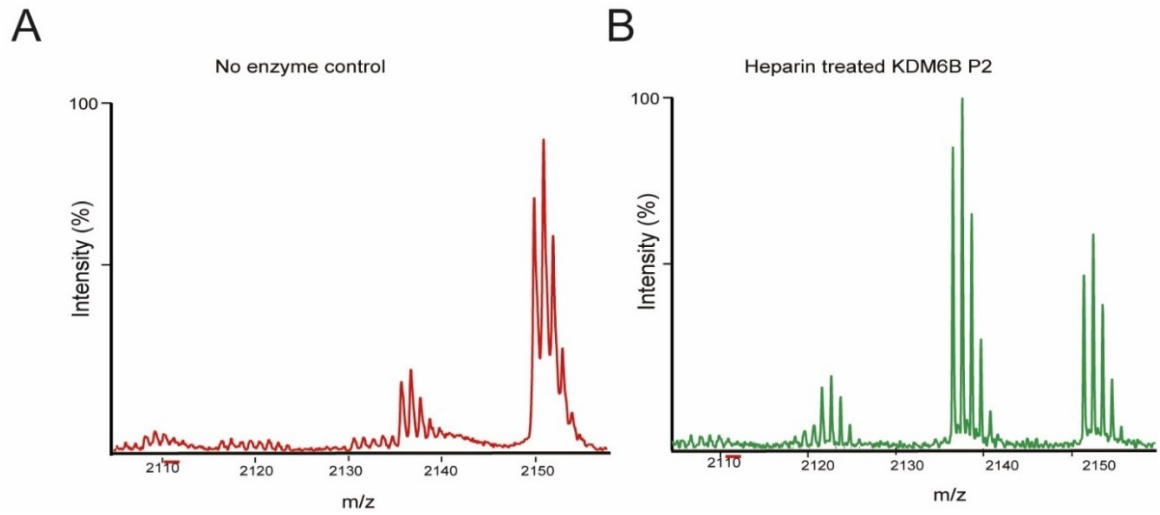


Figure 2.24. Assessment of endonuclease treated KDM6B P3 activity by MALDI-MS. *KDM6B (4 µM), was incubated with H3K27Me3 21mer peptide (25 µM), Fe^{2+} (50 µM), ascorbate (4 mM) and 2-oxoglutarate (300 µM) in 50mM HEPES 150mM NaCl pH7.5 at 37°C and quenched with methanol at each time point.* ***A, B MALDI-MS spectra of A, No enzyme control.*** *H3K27Me3 peptide incubated with Fe2+, ascorbate and 2OG for 60 minutes.* ***B. Heparin treated KDM6B P2*** *incubated with H3K27Me3 peptide incubated with Fe2+, ascorbate and 2OG for 60 minutes. Increased intensity at masses corresponding to demethylated products indicates demethylase activity of heparin treated KDM6B P2.*

2.12 Efforts towards establishment of an KDM6B binding assays

In order to investigate potential interaction between KDM6B and DNA which may be indicated above, it was desirable to establish a KDM6B binding assay.

The Amplified Luminescent Proximity Homogeneous Assay (Alpha) Screen is a bead-based fluorescent assay which can be used to study both inhibition and binding interactions. In AlphaScreen binding assays, the donor bead is conjugated to an anti-His antibody, which binds to a 6×His-tag on the protein of interest, the acceptor bead is conjugated to streptavidin which binds to biotinylated peptide. Binding between protein and peptide brings the donor and acceptor beads in close proximity. Donor beads contain

a photosensitiser which convert dissolved O_2 to $^1O_2$ when excited at 680 nm. The $^1O_2$ then transfers energy to acceptor beads producing emission at 520-630 nm. The magnitude of the signal is proportional to the strength of the binding interaction (Figure 2.25).

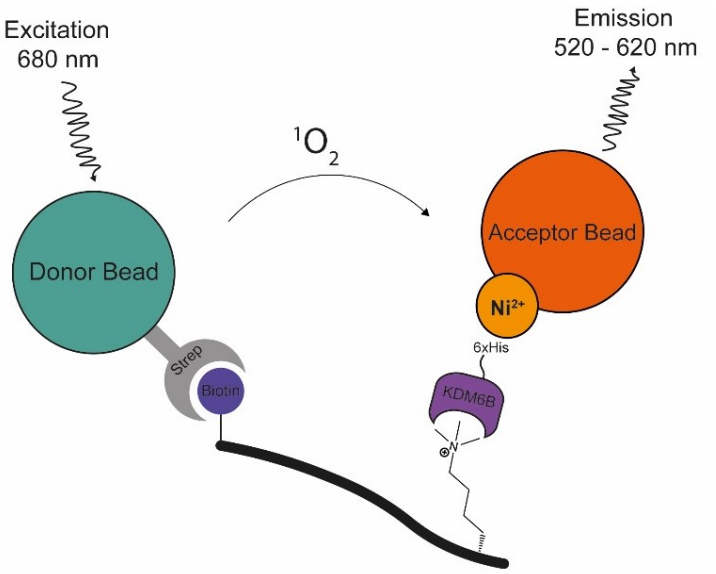


Figure 2.25. AlphaScreen Binding assay principle. *Donor and acceptor beads are ligated to biotinylated H3K27Me3 peptide via streptavidin, and His_6-taggedKDM6B via Ni^{2+} respectively. When KDM6B binds biotinylated H3K27Me3 peptide, the beads are brought in close proximity. This allows singlet oxygen, produced by excitation of a photosensitiser at 680 nm within the donor beads to transfer energy to the acceptor beads, where it is emitted via chemiluminescence at 520-620 nm. Signal is proportional to binding, allowing study of binding interactions.*

Evaluation of peptide substrates and small molecule binding modulators has previously been evaluated via competition AlphaScreen binding assay. In this assay dosing of a binding partner inhibits binding between biotinylated peptide and enzyme, reducing luminescence signal. This assay format has the advantage that it detects binding interactions which impact substrate binding within the active site, and are therefore likely to effect catalysis. Conversely, the assay may be less sensitive to binding outside the catalytic site.

Experiments were undertaken to establish a KDM6B AlphaScreen binding assay. Initial experiments were undertaken to identify the optimal peptide and enzyme concentrations to maximise signal intensity. A peak in signal is expected, beyond which signal decreases,

due to the hook effect. The hook effect arises because excess binding molecules beyond the binding capacity of each bead type cause saturation. Biotinylated-H3K27Me3 16mer peptide and *N*-His_6-TRX-tagged $KDM6B_{1141-1641}$ were co-incubated in 50mM HEPES, 0.01% Tween20, 0.1% BSA 150mM NaCl at variable concentration for 15 minutes, followed by incubation with beads for 60 minutes (Figure 2.26).

Whilst the titration result produced curves with a local maxima as would be expected from the Hooke effect, these were at concentrations 30 fold higher than that seen for other histone demethylases.[20] This indicates that the signal observed is likely due to precipitation of the KDM6B bringing detection beads in close proximity.

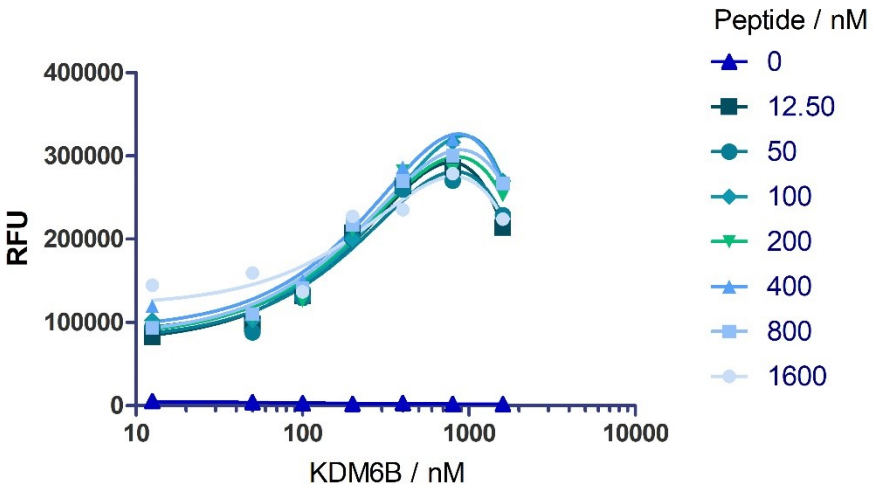


Figure 2.26 AlphaScreen binding enzyme peptide titration. *N-His_6-TRX-tagged $KDM6B_{1141-1641}$ and Biotinylated-H3K27Me3 16mer peptide were co-incubated in 50mM HEPES, 0.01% Tween20, 0.1% BSA 150mM NaCl at variable concentration for 15 minutes, followed by incubation with beads for 60 minutes. Signal maxima independent of peptide concentration, and occur at high enzyme concentration, together indicating precipitation.* ***RFU*** *– reference fluorescence units.*

To address this issue, the peptide enzyme titration experiment was repeated at different buffer conditions (Figure 2.27). In buffer A, a local maximum was present, but signal intensity was independent of peptide concentration, indicating that signal was again likely due to precipitation rather than KDM6B-peptide binding. Buffer C resulted in a reduction

in signal intensity relative to the other buffers. NaCl concentrations exceeding 300 mM are known to interfere with the AlphaScreen assay.

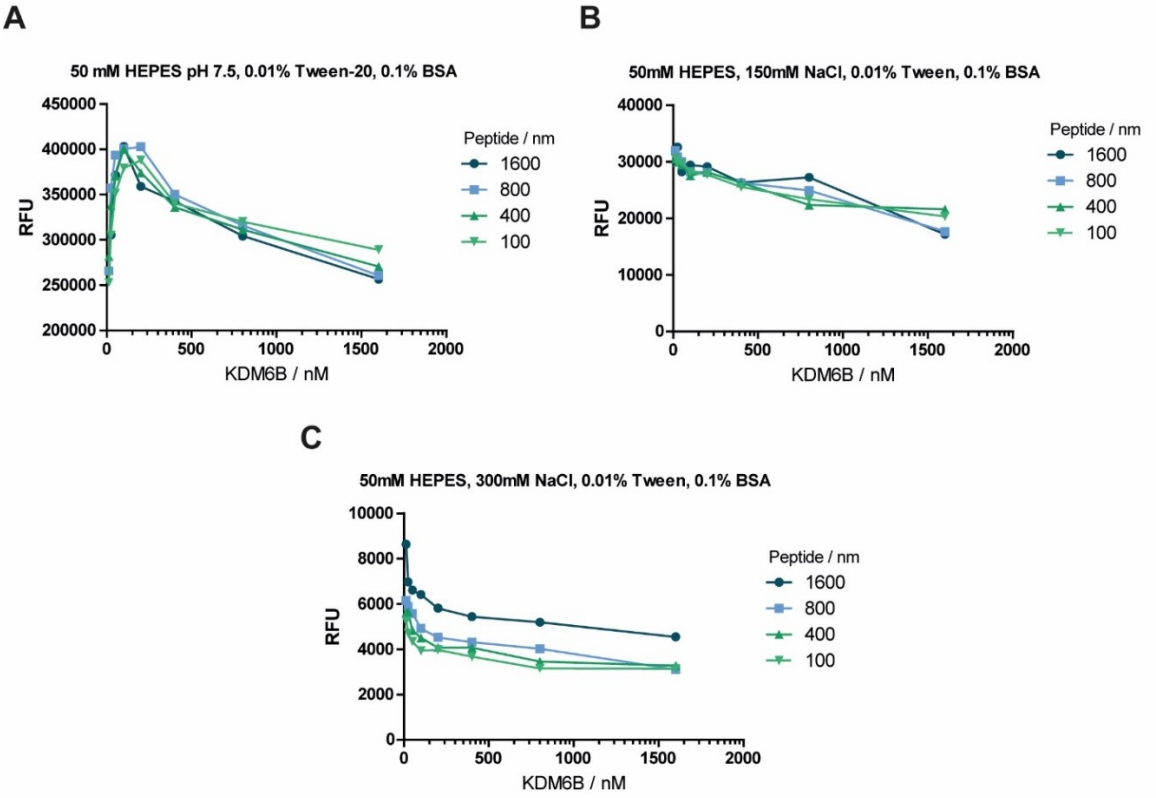


Figure 2.27 AlphaScreen binding enzyme peptide titration. *N-His_6-TRX-tagged $KDM6B_{1141-1641}$ and Biotinylated-H3K27Me3 16mer peptide were co-incubated at variable concentration for 15 minutes, followed by incubation with beads for 60 minutes.* ***A****. 50mM HEPES, 0.01% Tween20, 0.1% BSA* ***B****. 50mM HEPES, 0.01% Tween20, 0.1% BSA 150mM NaCl* ***C****. 50mM HEPES, 300mM NaCl, 0.01% Tween, 0.1% BSA.* ***RFU*** *– reference fluorescence units.*

The experiment was repeated with the addition of stabilising components NOG and $NiCl_2$, which stabilise the catalytic site by occupying the 2OG binding site and Fe^{2+} centre. Finally, incubation was attempted at 4°C and 21°C. In each case, no improvement was seen.

Biolayer interferometry is an optical analytical technique for the characterisation of biomolecular interactions and was thus considered as an alternative KDM6B-DNA binding assay. Protein is immobilised at the terminus of an optical sensor forming a surface against which light is reflected. Binding of a ligand to the immobilised protein effectively increased the thickness of the surface and alters the wavelength at which light

is reflected back in to the sensor, allowing detection and characterisation of binding. Initial experiments were undertaken to optimise a biolayer interferometry binding assay for KDM6B. However, no change in signal was seen on addition of substrate peptide under a range of buffer conditions, likely due to instability of KDM6B.

Alternate binding assays, such as fluorescence polarisation or isothermal calorimetry, would also require longer incubation times and so experiments to optimise stability and solubility of KDM6B would be the logical next step. Buffer screening using circular dichroism, thermal shift or DLS could be used to improve KDM6B stability.

DNA oligomers (30mer) were evaluated using the AlphaScreen inhibition assay (section Chapter 4, Section 4.2). DNA sequences were selected to include GATA transcription factor binding sites from the promotor region of KDM6B target gene *Mef2c*.[21] No concentration-dependent effect on KDM6B activity was observed. This may be due to interference of the DNA oligomers with the assay, as both inhibition and enhancement of activity was observed. The effect of DNA oligomers on KDM6B activity will be further evaluated once an inhibition assay becomes available.

2.13 Discussion

The aim of the work reported in this chapter was the expression, purification and characterisation of KDM6A and KDM6B to support further biochemical study of their activity and inhibition.

Expression and purification of three KDM6A constructs, BR71, BR242 and BR281 was undertaken and activity of the resulting recombinant enzyme was assessed using a MALDI-MS activity assay. BR281 showed activity towards the H3K27Me3 peptide, and was evaluated against samples of active KDM6A BR71 previously produced in the group. Overall activity was prohibitively low in all cases (maximum demethylation after 60

minutes = 21%, BR71 AB 2.5 μM), and this was further compounded by precipitation observed at higher enzyme concentrations. A solubility screen to identify optimal buffer conditions for purification and activity of KDM6A constructs using DLS or thermal shift assay would be useful moving forward. Cloning of alternate constructs could also improve solubility. The addition of fusion proteins such as protein G B1 domain, TRX or maltose binding protein can significantly enhance solubility, provided that the tags do not interfere with downstream applications.[22]

Expression and purification of *N*-His_6-TRX-tagged $KDM6B_{1141-1641}$ was undertaken and activity of the resulting enzyme was assessed using a MALDI-MS activity assay. Increased intensity was seen at mass spectra peaks corresponding to H3K27Me2/1/0, (Figure 2.8, B) indicating that KDM6B catalyses the demethylation of Me3, Me2 and Me1 methylation states. *N*-His_6-TRX-tagged KDM6B was taken forward for kinetic analysis and K_m determination of H3K27Me3 21mer peptide was attempted. However, ongoing problems with MALDI-MS equipment reduced the resolution of spectra attained, which prevented accurate quantification of demethylation at high substrate: product ratios (Chapter 4, Section 4.4).

The FDH enzyme-coupled assay was investigated as an alternate assay suitable for kinetic characterisation of KDM6B. This required the removal of the *N*-His_6-TRX-tag as TRX oxidises NADH to NAD+, interfering with the FDH assay. A small-scale cleavage was undertaken on previously purified *N*-His_6-TRX-tagged KDM6B, which yielded active cleaved KDM6B. Subsequent large-scale purifications failed to produce active KDM6B. On inspection of the UV-Vis spectra of the active and inactive KDM6B samples, a contamination absorbing at 260 nm was identified in the inactive samples only. Nucleic acids absorb UV light at 260 nm due to the aromatic base moieties within their structure. Contamination by DNA was further confirmed by agarose gel electrophoresis using

SYBR Safe, a DNA-binding fluorescent dye. Further to this, treatment of contaminated KDM6B sample with endonucleases removed contamination as assessed by agarose gel electrophoresis. Treatment of DNA contaminated KDM6B with endonucleases restored catalytic activity, as did purification by heparin affinity chromatography.

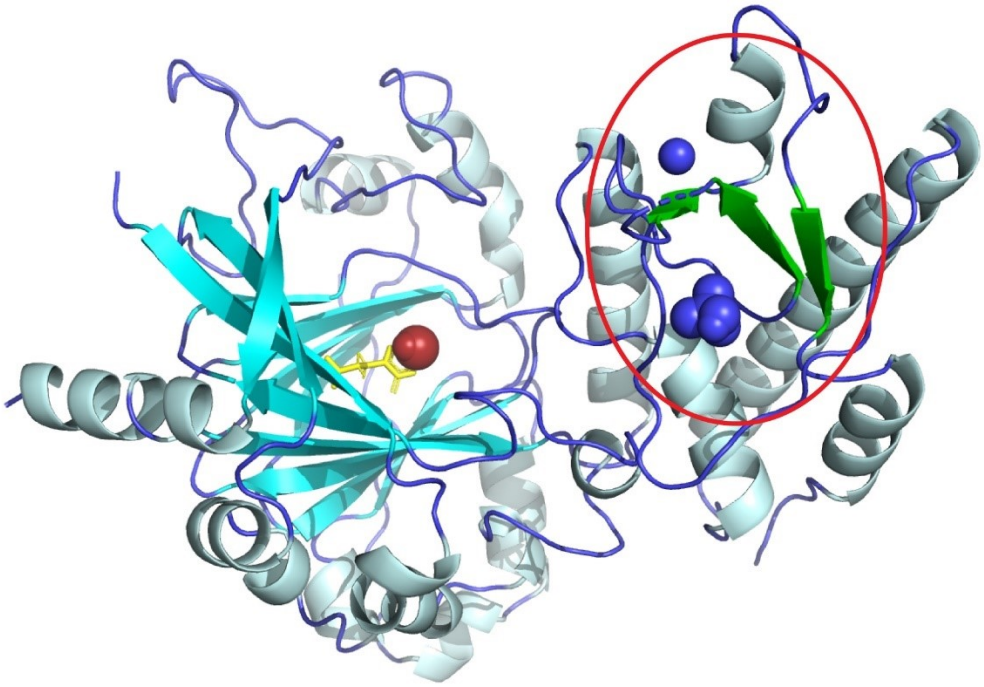


Figure 2.28 Structural features of the KDM6B catalytic region. *View from crystal structure (adapted from PDB ID:2XUE using pyMOL), showing conserved double stranded beta helix, catalytic Fe^{2+} with NOG bound (yellow). GATA-like zinc binding domain encircled in red. KDM6B crystallography construct used in determination of crystal structure 2XUE encodes residues 1157-1641, KDM6B construct used for in vitro activity studies encodes residues 1141-1641. Both constructs encode the JmjC domain and GATA-like zinc binding domain.*

The mechanism by which histone demethylases are targeted to and bind at DNA histone complexes is not well understood. Other members of the 2OG oxygenase family, TET proteins and fat mass and obesity associated protein (FTO), catalyse oxidation of oligonucleotide substrates.[23,24] Both KDM6A and KDM6B have GATA-like zinc binding domains (Figure 2.28), so-called because of their sequence homology to DNA binding zinc finger domains within GATA transcription factors.[13] Other JmjC-KDMs, such as KDM2A and the KDM5 sub-family, contain DNA-binding domains ARID and

CXXC.[25,26] No DNA binding domain has been identified within KDM6B, but it is possible that one exists within the boundaries of the constructs tested above. Unfortunately, attempts to establish Alpha Binding and biolayer interferometry assays to investigate potential binding of DNA to KDM6A and KDM6B were not successful, likely due to instability of KDM6B in solution. Nevertheless, the restoration of KDM6B activity on removal of contaminating DNA is an interesting preliminary result. Future work will focus on optimisation of buffer conditions to stabilise KDM6B. Once MALDI-MS equipment becomes available, the effect of oligonucleotides of different lengths and sequence on KDM6B activity will be evaluated.

Kinetic studies of the JmjC histone demethylases, which require oxygen for catalysis, indicate that their activity is reduced in an oxygen concentration dependent manner.[27] Characterisation of the oxygen sensitivity of recombinant KDM6A and KDM6B (truncated, catalytic domains) has been previously studied *in vitro* using the MALDI-MS activity assay (conducted by Grasilda Zenkeviciute, unpublished data, Chapter 3, Figure 3.3). This demonstrated that the activity of both KDM6A and KDM6B was decreased with decreasing oxygen concentration. In a cellular context, this oxygen sensitivity could potentially result in aberrant epigenetic regulation in hypoxic conditions. Chapter 3 details work undertaken to determine whether this observed *in vitro* oxygen sensitivity translates to a reduction of KDM6 activity in a cellular context.

2.14 References

1. Hong, S. *et al.* Identification of JmjC domain-containing UTX and JMJD3 as histone H3 lysine 27 demethylases. *Proc. Natl. Acad. Sci. U. S. A.* **104,** 18439–44 (2007).
2. De Santa, F. *et al.* The histone H3 lysine-27 demethylase Jmjd3 links inflammation to inhibition of polycomb-mediated gene silencing. *Cell* **130,** 1083–94 (2007).
3. Lan, F. *et al.* A histone H3 lysine 27 demethylase regulates animal posterior development. *Nature* **449,** 689–94 (2007).
4. Lee, M. G. *et al.* Demethylation of H3K27 regulates polycomb recruitment and H2A ubiquitination. *Science* **318,** 447–50 (2007).
5. Walport, L. J. *et al.* Human UTY(KDM6C) is a male-specific Nϵ-methyl lysyl demethylase. *J. Biol. Chem.* **289,** 18302–13 (2014).
6. Welstead, G. G. *et al.* X-linked H3K27me3 demethylase Utx is required for embryonic development in a sex-specific manner. *Proc. Natl. Acad. Sci. U. S. A.* **109,** 13004–9 (2012).
7. Ohtani, K. *et al.* Jmjd3 controls mesodermal and cardiovascular differentiation of embryonic stem cells. *Circ. Res.* **113,** 856–62 (2013).
8. Agger, K. *et al.* UTX and JMJD3 are histone H3K27 demethylases involved in HOX gene regulation and development. *Nature* **449,** 731–734 (2007).
9. Burchfield, J. S., Li, Q., Wang, H. Y. & Wang, R.-F. JMJD3 as an epigenetic regulator in development and disease. *Int. J. Biochem. Cell Biol.* **67,** 148–157 (2015).
10. Van der Meulen, J. *et al.* The H3K27me3 demethylase UTX is a gender-specific tumor suppressor in T-cell acute lymphoblastic leukemia. *Blood* **125,** 13–21 (2015).
11. Hausinger, R. P. Fe(II)/α-Ketoglutarate-Dependent Hydroxylases and Related Enzymes. *Crit. Rev. Biochem. Mol. Biol.* **39,** 21–68 (2004).
12. Sengoku, T. & Yokoyama, S. Structural basis for histone H3 Lys 27 demethylation by UTX/KDM6A. *Genes Dev* **25,** 2266–2277 (2011).
13. Kruidenier, L. *et al.* A selective jumonji H3K27 demethylase inhibitor modulates the proinflammatory macrophage response. *Nature* **488,** 404–8 (2012).
14. Kristensen, J. B. L. *et al.* Enzyme kinetic studies of histone demethylases KDM4C and KDM6A: towards understanding selectivity of inhibitors targeting oncogenic

histone demethylases. *FEBS Lett.* **585,** 1951–6 (2011).

15. Williams, S. T. *et al.* Studies on the catalytic domains of multiple JmjC oxygenases using peptide substrates. *Epigenetics* **9,** 1596–603 (2014).
16. Chen, H. *et al.* Nickel ions inhibit histone demethylase JMJD1A and DNA repair enzyme ABH2 by replacing the ferrous iron in the catalytic centers. *J. Biol. Chem.* **285,** 7374–83 (2010).
17. Joint ProteomicS Laboratory (JPSL) of the Ludwig Institute for Cancer Research & Walter and Eliza Hall Institute of Medical Research, Melbourne, Australia. Measuring Protein Concentration in the Presence of Nucleic Acids by A_{280}/A_{260}: The Method of Warburg and Christian. *Cold Spring Harb. Protoc.* **2006,** pdb.prot4252 (2006).
18. ThermoFisher. SYBR® Safe Frequently Asked Questions. Available at: https://www.thermofisher.com/us/en/home/life-science/dna-rna-purification-analysis/nucleic-acid-gel-electrophoresis/dna-stains/sybr-safe/sybr-safe-faq.html. (Accessed: 9th December 2017)
19. EMD Millipore. *Application note, Benzonase® endonuclease*.
20. Kawamura, A. *et al.* Development of homogeneous luminescence assays for histone demethylase catalysis and binding. *Anal. Biochem.* **404,** 86–93 (2010).
21. Dodou, E., Verzi, M. P., Anderson, J. P., Xu, S.-M. & Black, B. L. Mef2c is a direct transcriptional target of ISL1 and GATA factors in the anterior heart field during mouse embryonic development. *Development* **131,** 3931–3942 (2004).
22. Esposito, D. & Chatterjee, D. K. Enhancement of soluble protein expression through the use of fusion tags. *Curr. Opin. Biotechnol.* **17,** 353–358 (2006).
23. Gerken, T. *et al.* The obesity-associated FTO gene encodes a 2-oxoglutarate-dependent nucleic acid demethylase. *Science* **318,** 1469–72 (2007).
24. Hu, L. *et al.* Structural insight into substrate preference for TET-mediated oxidation. *Nature* **527,** 118–22 (2015).
25. Tu, S. *et al.* The ARID domain of the H3K4 demethylase RBP2 binds to a DNA CCGCCC motif. *Nat. Struct. Mol. Biol.* **15,** 419–421 (2008).
26. Dimitrova, E., Turberfield, A. H. & Klose, R. J. Histone demethylases in chromatin biology and beyond. *EMBO Rep.* **16,** 1620–39 (2015).
27 Hancock, R. L., Dunne, K., Walport, L. J., Flashman, E. & Kawamura, A. Epigenetic regulation by histone demethylases in hypoxia. *Epigenomics* 1–21 (2015). doi:10.2217/epi.15.24

Chapter 3: Studies of the cellular oxygen dependence of KDM6B activity

3.1 Introduction

Oxygen is required for aerobic respiration, and is essential to cell survival in eukaryotes. As the diffusion limit of oxygen is only 100-200 μm in tissue, oxygen is delivered via perfusion.[1] Oxygen in the air we breathe is at 21%, whilst oxygen concentrations in the lungs, kidney and brain are 9.5, 5.6 and 4.4% respectively.[2] Oxygen concentrations ≤2% are considered hypoxic. Whilst hypoxic conditions are essential to some processes, such as development, they are associated with pathologies including cancer and cardiovascular disease. [3]

Adaptive cellular and physiological responses to hypoxia are termed the 'hypoxic response'. Physiological compensatory responses include the hypoxic ventilatory response, erythropoiesis and angiogenesis. Cellular responses to hypoxia include altered metabolism, cell-cycle arrest, and secretion of survival and proangiogenic factors.[4] These responses are predominantly regulated by the hypoxia induced transcription factor (HIF) family which bind to hypoxic response elements in the promotor regions of HIF target genes (Chapter 1, Figure 1.9).[5–7] The transcriptionally active HIF complex is a heterodimer consisting of HIF-α and HIF-β. Three isoforms of HIF-α, HIF-1α, HIF-2α and HIF-3α, are present in mammals. HIF-1α and HIF-β are ubiquitously expressed in cells, whereas HIF-2α and HIF-3α are expressed only in certain cells types, allowing cell- and tissue-specific tailoring of the hypoxic response. Under normoxic conditions the level and activity of the HIF-α subunit is regulated by post-translational hydroxylation, catalysed by enzymes known as the HIF hydroxylases. Prolyl hydroxylase domain (PHD) enzymes catalyse hydroxylation of proline residues within the HIF-α oxygen-dependent

degradation domains, enabling binding of pVHL and ubiquitination by ubiquitin ligase targeting HIF-α for ubiquitination and degradation by the proteasome. FIH catalyses hydroxylation of asparaginyl residues within the HIF-α transactivation domain, reducing its binding affinity for transcriptional coactivator proteins thus reducing its activity. The activity of the HIF hydroxylases is highly sensitive to oxygen availability. Under hypoxic conditions, the activity of the HIF hydroxylases is reduced, leading to stabilisation of HIF levels and activity. Kinetic studies of recombinant PHD2 and FIH were undertaken and their Michaelis-Menten constants with respect to oxygen, $K_M^{app}(O_2)$, were determined.[8–11] The $K_M^{app}(O_2)$ is the concentration of oxygen at which the rate of catalysis is half its maximum value. $K_M^{app}(O_2)$ values for PHD2 have been reported between 230 μM and 1.7 mM,[8–11] reflecting the high sensitivity of its activity to oxygen concentration. The $K_M^{app}(O_2)$ value of FIH is lower at 90-150 μM indicating it's activity is less sensitive to oxygen availability than PHD2.[12,13] Reduction of activity in hypoxia has also been demonstrated for both PHD2 and FIH in cells.[14,15] As reflected by the lower $K_M^{app}(O_2)$ value of FIH relative to PHD2, cellular FIH activity was less sensitive to oxygen concentration, and FIH-catalysed hydroxylation is maintained in RCC4 cells exposed to an environment of 0.25% oxygen.[15]

It is increasingly recognised that the hypoxic response is not mediated solely by HIF, and that epigenetic regulation plays an important role in both immediate and longer-term hypoxic responses by alteration of the epigenetic landscape before and during the hypoxic response.[16]

The interaction between histone methylation and the hypoxic response is proposed to occur via several mechanisms (Figure 3.2). In the first mechanism histone demethylases and transferases maintain 'priming' epigenetic modifications on HIF target genes allowing for immediate expression upon HIF stabilisation and binding. A study by Xia *et*

al. demonstrated that HIF preferentially bound to genes with activating H3K4Me3 marks in their promotor.[17] In the second mechanism, epigenetic modifiers alter chromatin in response to hypoxia resulting in both gene activation and silencing. Numerous studies have demonstrated altered histone methylation status in cells after exposure to hypoxia.[18–24] In the third mechanism upregulation of histone demethylases is mediated by HIF. A number of the JmjC-histone demethylases, including KDM6B, are known to be encoded by HIF target genes and are upregulated in a HIF-dependent manner in hypoxia.[18,25–30] In the final mechanism, reduced oxygen availability reduces the activity of histone demethylases, potentially resulting in gene regulation in an oxygen dependent manner.

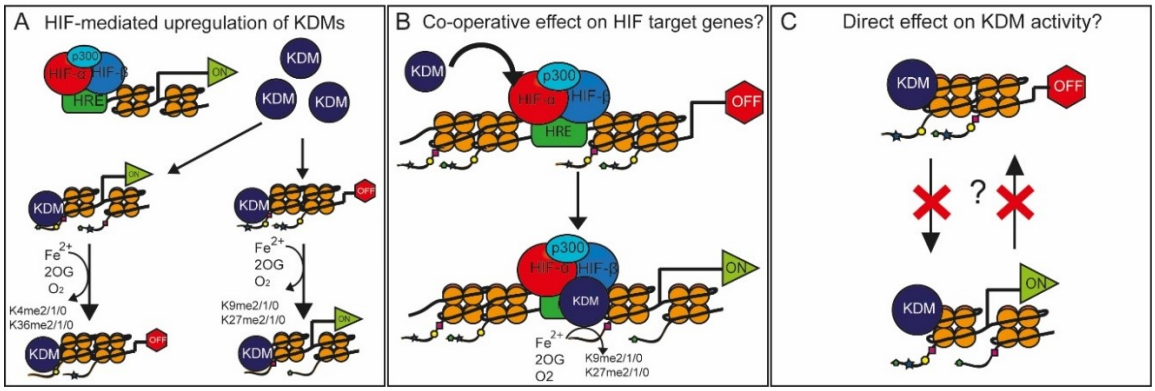


Figure 3.2 – Potential mechanisms of KDM-mediated gene regulation in hypoxia A. *HIF mediated upregulation of the JmJC-KDMs in hypoxia is proposed to increase demethylation of methylated lysine residues, altering gene expression.* ***B.*** *Co-operative effect between HIF and JmjC-KDMs. HIF recruits JmjC-KDMs to the gene locus, enabling removal of repressive marks and activation of gene expression.* ***C.*** *Direct oxygen-dependent changes in KDM activity results in gene expression changes. Figure adapted from Hancock et al with permission from Future Medicine.*[3]

The HIF hydroxylases are members of the Fe^{2+}/2OG-dependent oxygenase family, which has over 60 members, the structure and mechanism of which is conserved across the family. The JmjC-histone demethylases enzymes are themselves Fe^{2+}/2OG-dependent oxygenases with an absolute requirement for oxygen for catalysis. As such, reduced oxygen availability would also have an impact on their catalytic activity. $K_m^{app}(O_2)$ values for various 2OG oxygenases including PHD2, FIH and KDM4A/C/E have been

determined (Table 3.1). As with the HIF hydroxylases, different histone demethylases have different oxygen sensitivities. Within the KDM4 family, KDM4A, KDM4C and KDM4E all have $K_m^{app}(O_2)$ values which lie between those of FIH and PHD2 indicating they have the potential to act as biochemical oxygen sensors.

Enzyme	$K_m(O_2)$/ µM	Substrate	References
$PHD2_{181-426}$	230-1746	$HIF\text{-}1\alpha_{556-574}$ CODD	8–11
FIH	90 -150	$HIF\text{-}1\alpha_{788-822}$ CAD	12,13
$KDM4A_{1-359}$	57 - 173	$H3_{7-14}K9me3$	31,32
$KDM4C_{1-366}$	158 ± 13	$H3_{7-14}K9me3$	31
$KDM4E_{1-337}$	197 ± 16	$H3_{7-14}K9me3$	31
$KDM4E_{1-337}$	>93	$H3_{7-14}K9me3$	33

Table 3.1 Differential sensitivity of 2OG oxygenases in vitro. *Table adapted and updated from Hancock et al.*[3]

KDM6A and KDM6B have key roles in development. Cardiac defects and embryonic lethality is seen in KDM6A deficient mice, whilst KDM6B deficient embryos die at the blastocyst stage.[34,35] A number of studies have shown that demethylation of H3K27Me3 by KDM6A and KDM6B is essential to normal development, and in particular with regard to embryonic cardiac, neural and lung development.[34–38] The gestation environment is hypoxic, with low oxygen concentrations maintained until after foetal circulation has been established.[39,40] These studies suggest KDM6A and KDM6B may still retain activity in hypoxic conditions. Conversely, studies by Dehne *et al* and Chang *et al*, have demonstrated hypoxic inhibition of KDM6B catalysed H3K27Me3 and subsequent loss of gene expression.[24,41] Characterisation of the biochemical and cellular oxygen dependence of KDM6 family would shed light on these seemingly disparate results.

$K_m^{app}(O_2)$ values for KDM6A and KDM6B have previously been determined by Grasilda Zenkeviciute (unpublished data, Figure 3.3). Recombinant KDM6A and KDM6B were expressed and purified by Grasilda Zenvenciute. The purified enzymes were utilised for *in vitro* studies using the MALDI-MS activity assay. In this assay enzyme (KDM6A or KDM6B) was incubated with H3K27Me3, 2-oxoglutarate, Fe^{2+} (ferrous ammonium sulphate) and ascorbate (table 3.2), prior to quenching and subsequent analysis of product formation by MALDI-MS analysis, using the conditions listed in table 3.2. Initial experiments were undertaken to determine the linear range of reaction for each enzyme; 7-minute incubation time was selected for KDM6A, 2-minute incubation for KDM6B.

	KDM6B	KDM6A
Enzyme/μM	0.5	4.5
2OG/μM	200	100
H2K27Me3 21mer /μM	20	300
Fe^{2+}/μM	10	50
Ascorbate/μM	100	500
K_m(2OG) /μM	5.4 ± 1.0[42]	14.7 ± 2.2[42]
K_m (H3K27Me3 21mer) /μM	ND	97 ± 7

Table 3.2. Assay conditions utilised in $K_m^{app}(O_2)$ determination and K_m(2OG) and K_m (H3K27Me3 21mer) values for KDM6A and KDM6B by Grasilda Zenceviciute. *Recombinant KDM6A and KDM6B were expressed and purified by Grasilda Zenvenciute. K_m (H3K27Me3 21mer) value for KDM6A determined by Jan Kristensen by FDH assay. ND – not determined.*

The following protocol was then used for $K_m^{app}(O_2)$ determination, at the assay conditions listed in table 3.2. Buffer and peptide mix (94 μL) was equilibrated in a sealed vial at the desired oxygen concentration for 10 minutes at 37°C. Next, 50x 2OG/ascorbate mix (2 μL) and 50x Fe^{2+} (2 μL) were added. The reaction was then immediately initiated by addition of 50x enzyme stock (2 μL) and mixed via syringe. After the desired incubation time, the reaction was quenched using MeOH (100 μL) and placed in to liquid nitrogen.

Samples (1 µL) of each reaction were then analysed by MALDI-MS. This procedure was repeated at a range of oxygen concentrations using a mass flow controller. The initial rates of reaction calculated in each oxygen concentration and the Michaelis-Menten model was then used to determine $K_m^{app}(O_2)$ from the resulting initial rate curve (Figure 3.3).

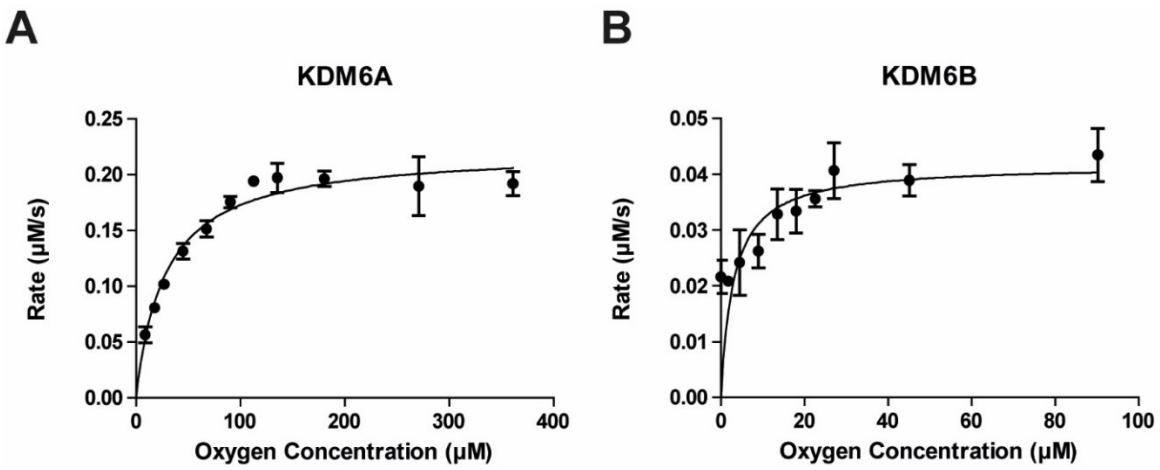


Figure 3.3. Kinetic analysis of recombinant KDM6A and KDM6B using a MALDI-MS activity assay. The activity of both KDM6A and KDM6B is reduced in an oxygen concentration dependant manner. A. KDM6A initial rate curve. *N-His_6-KDM6A (4.5 µM), was incubated with H3K27Me3 21mer peptide (300 µM), Fe^{2+} (50 µM), ascorbate (500 µM) and 2-oxoglutarate (100 µM) in 50mM HEPES 150mM NaCl pH7.5 at 37°C at indicated oxygen concentrations and quenched with methanol after 7 minutes.* ***B KDM6B initial rate curve.*** *N-His_6-KDM6B (0.5 µM), was incubated with H3K27Me3 21mer peptide (20 µM), Fe^{2+} (10 µM), ascorbate (100 µM) and 2-oxoglutarate (200 µM) in 50mM HEPES 150mM NaCl pH7.5 at 37°C at indicated oxygen concentrations and quenched with methanol after 2 minutes. Analysis of initial rate curves was used to determine $K_m^{app}(O_2)$. Curves fitted by linear regression using the Michaelis-Menten model on GraphPad Prism. N=3 biological repeats. Error bars represent standard deviation.*

The activity of both enzymes displayed sensitivity to oxygen availability. $K_m^{app}(O_2)$ value of KDM6A was 28.4 µM (95% confidence interval 22.4 – 34.4 µM), whilst the $K_m^{app}(O_2)$ value of KDM6B was 3.1 µM (95% confidence interval 0.5 – 5.6 µM). It is noteworthy that these values were significantly lower than those determined for KDM4A, FIH and PHD2, potentially suggesting that KDM6A and KDM6B are less sensitive to decreasing oxygen availability under these assay conditions.

Due to the difficulty in producing pure, active KDM6A, a relatively high enzyme concentration of 4.5 µM was used in these kinetic studies, which could affect the validity

of the quasi-steady-state assumption in the Michaelis-Menten model. Similarly, the peptide concentration used in $K_m^{app}(O_2)$ determination for KDM6B was only 20 μM. As K_m (H3K27Me3 21mer) has not been determined, it is possible that the peptide concentration was not saturating and thus not at steady state conditions. While efforts were made to undertake a more comprehensive kinetic characterisation of KDM6A and KDM6B in the current study (Chapter 2), these were unable to be completed due to break-down of MALDI-MS equipment (Chapter 4, Figure 4.6). These issues especially impacted kinetic studies because of the requirement to quantify changes in small amounts of substrate turnover, and thus low substrate signal. Alternative assays, such as oxygen consumption, radioactive 2OG turnover or FDH activity assays have been used for $K_m^{app}(O_2)$ determination.[8,9,31,43] However uncoupled turnover, i.e. oxidative decarboxylation of 2OG in the absence of substrate, can lead to over-estimation of $K_m^{app}(O_2)$ values acquired using oxygen consumption and 2OG turnover assays. Likewise, the effect of oxygen availability on enzyme coupled assays, such as FDH assays, needs to be thoroughly evaluated. Whilst these factors may affect the accuracy of the $K_m^{app}(O_2)$ values, the results clearly demonstrate KDM6A and KDM6B activity is oxygen dependent *in vitro*. As such loss of KDM6 activity could have important implications in hypoxic gene regulation, and the effect of hypoxia on KDM6 activity in a cellular context is therefore of interest.

3.1.1 Chapter aims

The aim of the experiments detailed in this this chapter was to establish cellular activity assays for the KDM6 sub-family of histone demethylases, and use these assays to evaluate the cellular oxygen dependence of KDM6 activity.

3.2 Establishment of a cellular immunofluorescence activity assay

To assess the effect of oxygen availability on cellular activity of the KDM6 sub-family of histone demethylases, a previously described immunofluorescence assay was adapted.[38,44] In this assay mammalian cells are transiently transfected with plasmids encoding full length wild-type enzyme with an N-terminal polypeptide protein tag, such as FLAG or Myc (WT). As a control, cells are also transfected with plasmids encoding the catalytically inactive mutant enzyme (MUT), wherein alanine takes the place of key active site residues involved in iron coordination. The use of mutant controls is essential to allow the detection of any nonspecific effect of inhibitors or treatments on histone demethylation, which may be independent of catalytic inhibition.

The HeLa cell line, derived from human cervical adenocarcinoma, was selected for these experiments. HeLa are strongly adherent making them suited to immunofluorescent staining protocols, and high levels of transfection efficiency, up to 100%, can be achieved.[45] This cell line has been used successfully for a number of histone demethylase immunofluorescence assays, including KDM6B.[46]

A typical protocol consisted of the following steps. Cells were treated with plasmid and transfection reagent. After incubation for a given time (transfection window, Figure 3.4, A), the transfection reagent was removed and replaced with cell culture media. Many transfection reagents are cytotoxic and so the transfection window is optimised to maximise transfection efficiency whilst eliminating or minimising cytotoxic effects. Cells were incubated ± treatment for 24 hours (treatment window, Figure 3.4, A). After this, cells were fixed, permeabilised and were used for primary antibody staining against transfection markers (FLAG, Myc) and H3K27Me3, before final treatment with fluorescent-dye conjugated secondary antibodies and 4',6-diamidino-2-phenylindole (DAPI) nuclear stain (Figure 3.4, A).

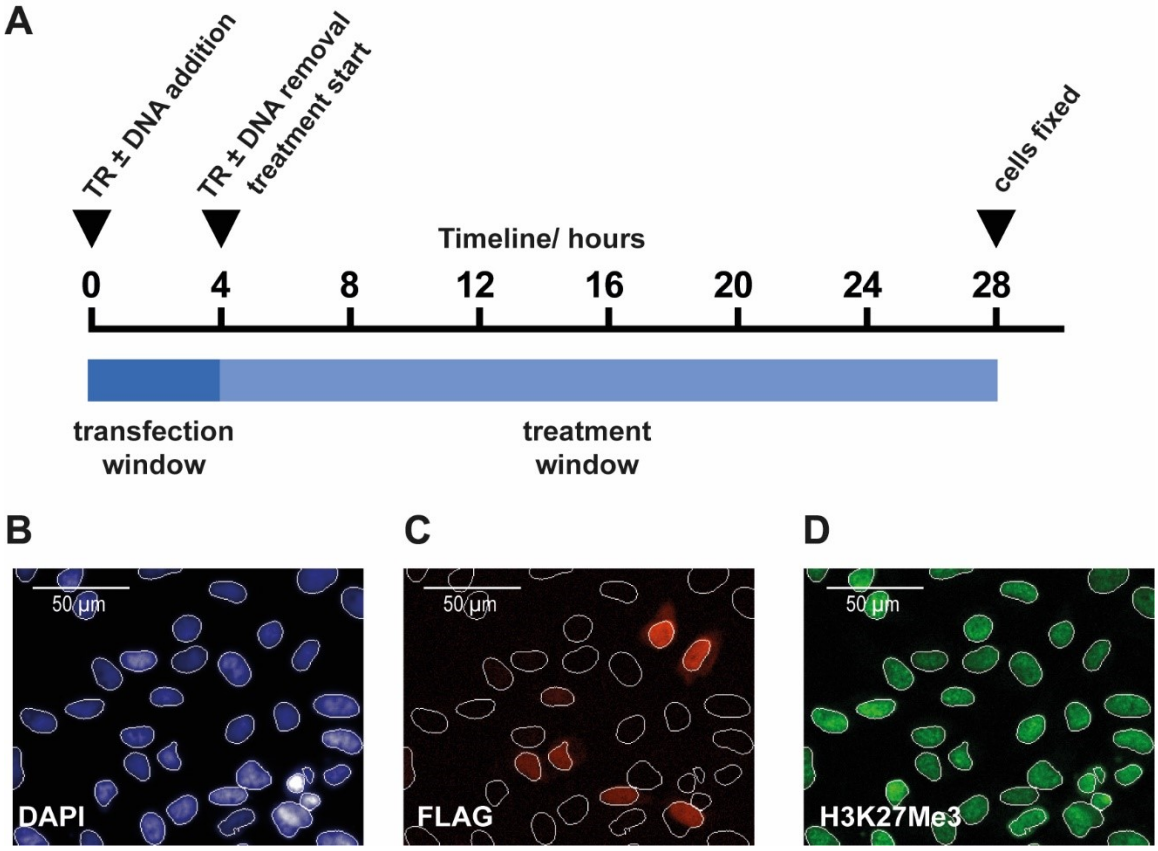


Figure 3.4. Overview of immunofluorescence assay protocol and image analysis. A. Immunofluorescence assay protocol timeline. *After addition of transfection reagent (TR) ± DNA, cells are incubated for the duration of the transfection window, 4 hours. TR is then removed and replaced with fresh media ± treatment and cells are incubated for the duration of the treatment window before fixation, 24 hours.* ***B, C, D Image analysis using Harmony™ software. B.*** *DAPI fluorescence intensity used to define area of each nucleus, bounded in white.* ***C, D****. Resulting nucleus area, bounded in white, used to calculate nuclear FLAG fluorescence intensity* ***C****, and H3K27Me3 intensity,* ***D****. 20x magnification.*

Fluorescent microscopy images were acquired using an Operetta® high content imaging system, and analysed using Harmony™ analysis software. Since both H3K27Me3 and ectopic expression of KDM6A/B/C is localised to the nucleus, nuclear intensity of FLAG/Myc and H3K27Me3 are used in analysis. HeLa nuclei have an oval, bean-like nuclear morphology. DAPI fluorescence is used to define the area of each nucleus (Figure 3.4, B, C, D).

3.3 Selection of transfected cells based on nuclear FLAG fluorescence intensity

Transfected cells are detected by identification of their flag fluorescence. Overexpression of a transfected construct is not homogeneous. The amount of construct expressed is proportional to the detected FLAG fluorescence, and so transfection of N-terminal flag-tagged KDM6B (WT) and the catalytically inactive mutant (H1390A, MUT) was undertaken to assess the assay window and determine appropriate selection criteria for transfected cells. HeLa cells were transiently transfected with KDM6B WT and KDM6B and staining. MUT using Fugene® HD transfection reagent and incubated for 24 hours before fixing

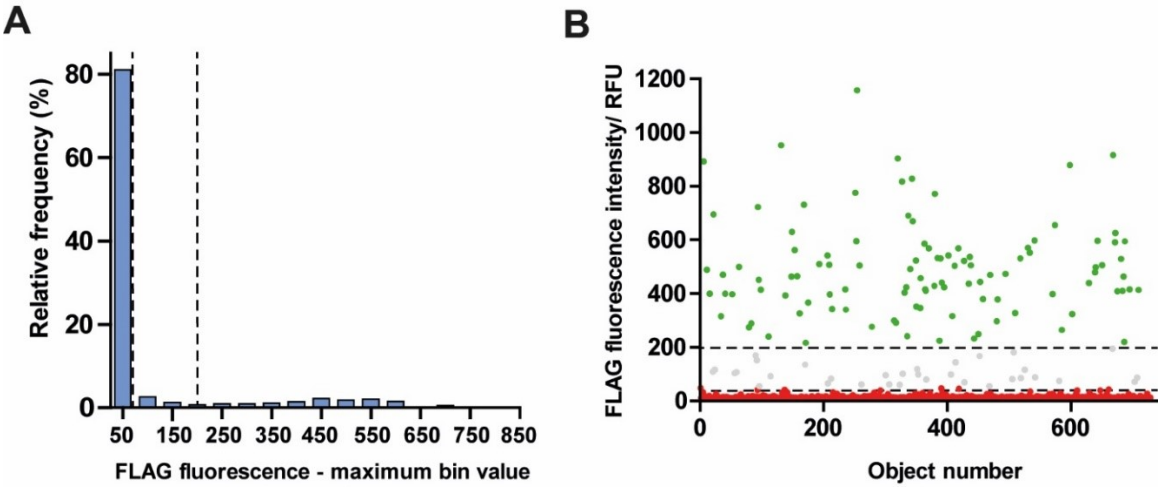


Figure 3.5. Selection of transfected KDM6B WT population based on FLAG fluorescence. A. *Frequency distribution of FLAG fluorescence of cell population after KDM6B WT transfection treatment. 81% of cells have FLAG intensity <50 RFU.* ***B.*** *FLAG fluorescence of cell population after KDM6B WT transfection treatment. Red – 81% of cells have flag fluorescence lower than 50 RFU eliminated from transfected population, Grey – Cells eliminated from transfected population due to low FLAG fluorescence intensity. Green – Selected transfected cell population. Dashed lines indicate 50 RFU and 200 RFU, cells above 200 RFU selected as transfected. (N=1 technical replicate, representative data).*

Analysis of FLAG intensity showed that most cells did not over-express KDM6B WT or KDM6B MUT; 81% of the cells had a global FLAG intensity of less than 50 relative fluorescence units (RFU) (Figure 3.5, A). The remaining cells had a broad frequency distribution of FLAG intensity, indicating high cell-to-cell variability in the amount of

KDM6B expressed (Figure 3.5 B). This variability could obscure the effect of treatment, for example by inhibitors, and thus it was necessary to select a more homogenous, highly overexpressing, population of transfected cells according to their FLAG fluorescence. Therefore, cells with FLAG fluorescence intensity above 200 RFU were selected for analysis (Figure 3.5), resulting in a transfection efficiency of only 14.4%. As the magnitude and frequency distribution of flag intensity changes across experiments, a unique cut-off value used for selection of transfected cells was determined in each experiment.

With the application of these selection criteria, it was observed that H3K27Me3 fluorescence was lower in cells overexpressing KDM6B WT compared to non-transfected control cells and cells overexpressing KDM6B MUT, indicating demethylation by KDM6B (Figure 3.6). Percentage demethylation of H3K27Me3 can be calculated by normalising the average fluorescence intensity of global H3K27Me3 in transfected WT cells per well versus MUT control or non-transfected control cells (NTC) (Figure 3.6, C).

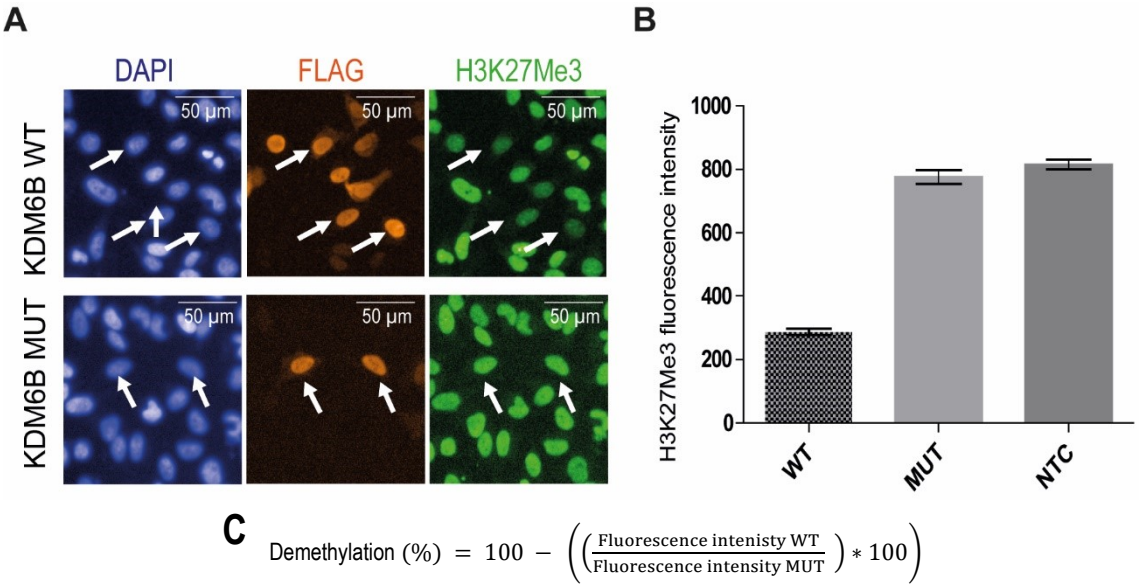


Figure 3.6. Reduction of H3K27Me3 indicates demethylase activity of over-expressed KDM6B. A*. HeLa cells transfected with Flag-tagged KDM6B WT or MUT, stained with anti-Flag and anti-H3K27Me3.* ***B****. H3K27Me3 fluorescence of WT KDM6B overexpressing is reduced relative to MUT, indicating demethylation by KDM6B. NTC – non-transfected control C. Formula used to calculate percentage demethylation. (Data mean +/- standard error of the mean (SEM), >500 cells analysed per data (N=3, technical). N=1 biological replicate). 20x magnification.*

3.4 Establishment of an optimal transfection protocol for KDM6A/B/C in HeLa

Though initial results were promising, the transfection efficiency of HeLa cells transfected with KDM6B dropped dramatically in subsequent experiments; the average transfection efficiency of these experiments was <2%. As such, there were insufficient cells for analysis.

Percentage demethylation of H3K27Me3 is calculated using per-well mean values. It is therefore important to ensure that the population in each well is sufficient to determine the true mean with high confidence. The standard error of the mean (Formula 3.1, A) indicates the variability of the mean across the population, and takes into account the effect increasing sample size has on the precision of the mean value. A formula for determining sample size can be derived by approximating sample mean with a normal distribution, according to the central limit theorem (Formula 3.1).[47]

A. $$Standard\ error\ of\ the\ mean = \frac{\sigma}{\sqrt{n}}$$

B. $$n = \frac{16\sigma^2}{W^2}$$

***Formula 3.1. Formulas used in calculation of required sample size**. **A**. Standard error of the mean. **B.** Sample size formula derived from **A**, applying the central limit theorem.*

Applying this formula to data from the initial experiment, and selecting a 95% confidence interval window of 100 RFU results in a required sample size of 132 cells. Therefore, insufficient transfected cells were obtained in the experiments with average transfection efficiency <2% (average cell number 17 per well).

Whilst it is possible to increase seeding density of HeLa cells to obtain a higher number of transfected cells, this strategy can be problematic as over-confluence can result from the increased cell number. This places increased stress on the cells which could result in changes to histone methylation and cell morphology. Therefore, experiments were mounted to identify the optimal transfection reagent and protocol for transfection.

Transfection of all three KDM6-sub family enzymes, KDM6A/B/C was undertaken. KDM6C catalyses demethylation of H3K27 peptides *in vitro* analogously to KDM6B and KDM6A, although cellular activity has yet to be demonstrated.[48]

As negatively charged plasmid DNA is unable to cross cells membranes, transfection reagents form complexes, such as liposomes or micelles, which can fuse to or cross the cell membrane, releasing plasmid DNA in to the cell. The optimal choice of transfection reagent and conditions for each cell type must be systematically determined as cell-type dependent characteristics such as membrane permeability or cytotoxic tolerance affect transfection efficiency.

HeLa were transiently transfected with the KDM6A/B/C WT and KDM6A/B/C MUT constructs using a panel of commercially available transfection reagents selected based on previous successful use in the group; Fugene® HD (Promega), GeneJuice® (Merck), Lipofectamine® 2000 and Lipofectamine® 3000. Two transfection reagent: DNA (TR:DNA) ratios were tested per reagent, as per the manufacturer's protocols. Cells were incubated for 24 hours before fixing and staining. As before, fluorescent microscopy images were acquired using an Operetta® high content imaging system, and analysed using Harmony™ analysis software.

A large reduction in the number of HeLa cells per well, indicating cytotoxicity, was seen on treatment with Lipofectamine® 2000 and Lipofectamine® 3000 across all constructs tested (Average number cells per well Fugene® HD treatment 1374, Lipofectamine® 2000 treatment 209, Lipofectamine® 3000 treatment 394, N=6) (Figure 3.7). Lipofectamine® 2000 and Lipofectamine® 3000 are cationic lipids which form liposomes in complex with DNA, whereas Fugene® HD and GeneJuice® form non-liposomal complexes which are reported to have lower cell toxicity, potentially accounting for the difference in cytotoxicity observed.

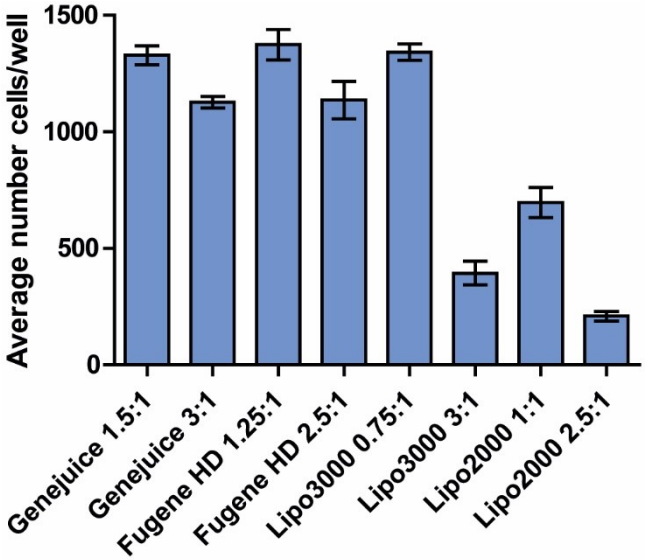


Figure 3.7. *Treatment of HeLa with Lipofectamine® 2000 and Lipofectamine® 3000 reduces average cell number/well indicating cytotoxicity. Data = mean N=3 technical replicates, N=1 biological replicate*

Transfection efficiency was calculated for each treatment for KDM6B and KDM6C (Table 3.3). It was not possible to conduct this analysis for KDM6A due to a failure in the antibody staining of the KDM6A Myc tag which prevented the identification of transfected cells. Comparable transfection efficiencies were obtained for KDM6B WT and KDM6B MUT using GeneJuice® at both TR:DNA ratios, and Fugene® HD at 2.5:1 TR:DNA ratio. However, transfection efficiency dropped to <2% on treatment using Fugene® HD at 2.5:1 TR:DNA ratio. Higher transfection efficiencies were obtained for KDM6C WT and KDM6B MUT on treatment with Fugene® HD than on treatment with GeneJuice® (max transfection GeneJuice® = 6.9%, max transfection efficiency Fugene® HD = 12.6%). Transfection of KDM6A WT and MUT was repeated using Fugene® HD at 2.5:1 TR:DNA ratio and resulted in transfection efficiencies of 27.6% and 3.2% respectively. The lack of consensus in transfection efficiency versus transfection reagent/ TR:DNA ratio across the different constructs tested reinforces the requirement to establish the best TR and protocol for each plasmid.

	GeneJuice® 1.5:1	GeneJuice® 3:1	Fugene® HD 1.25:1	Fugene® HD 2.5:1
KDM6B WT	17.9	14.0	1.8	14.7
KDM6B MUT	15.6	12.7	1.8	15.1
KDM6C WT	6.9	1.7	9.2	7.7
KDM6C MUT	0.9	2.7	12.6	8.3

Table 3.3. Transfection efficiency of HeLa transfected with KDM6B WT and MUT and KDM6C WT and MUT (%). *HeLa were treated with GeneJuice® or Fugene® HD and plasmid DNA. Two TR:DNA ratios were tested per reagent, as per the manufacturer's protocols. Cells were incubated for 24 hours before fixing and staining.*

3.5 Evaluation of cellular demethylase activity of KDM6A/C in HeLa cells

Having successfully transfected KDM6A WT, and KDM6C WT and MUT in to HeLa cells, their cellular activity was evaluated (Figure 3.8). As above, transfected cells were selected according to their FLAG or Myc fluorescence. Average H3K27Me3 fluorescence per well of transfected KDM6A WT, KDMC WT, KDM6C MUT and corresponding NTC was then calculated.

No reduction of H3K27Me3 fluorescence was seen in cells overexpressing KDM6A WT compared to non-transfected control, indicating a lack of cellular KDM6A activity in HeLa cells (Figure 3.8, A). Similarly, no reduction of H3K27Me3 fluorescence was seen in cells overexpressing KDM6C WT compared to KDM6C MUT or non-transfected control, indicating a lack of cellular KDM6C activity in HeLa cells (Figure 3.8, B). In both cases however, average H3K27Me3 fluorescence of WT transfected cells was higher than that of corresponding MUT and NTC. This hypermethylation could result from unproductive enzyme binding to H3K27Me3, effectively 'protecting' the mark from endogenous demethylation, resulting in the global increase seen.

Although cellular activity has not yet been reported for KDM6C, cellular demethylase activity has been demonstrated for KDM6A in COS-7 cells.[49] Both recombinant KDM6A and KDM6C enzymes catalyse demethylation of H3K27Me3 peptides *in vitro*.[44,50] It is possible that the cellular demethylase activity of KDM6A and KDM6C is limited to specific targets and/or cellular contexts, and is dependent on the epigenetic landscape of specific cell lines or types. Alternatively, as endogenous KDM6 enzymes operate as part of a multi-component complex, it is possible that KDM6A and KDM6C have a higher requirement for these components than KDM6B.

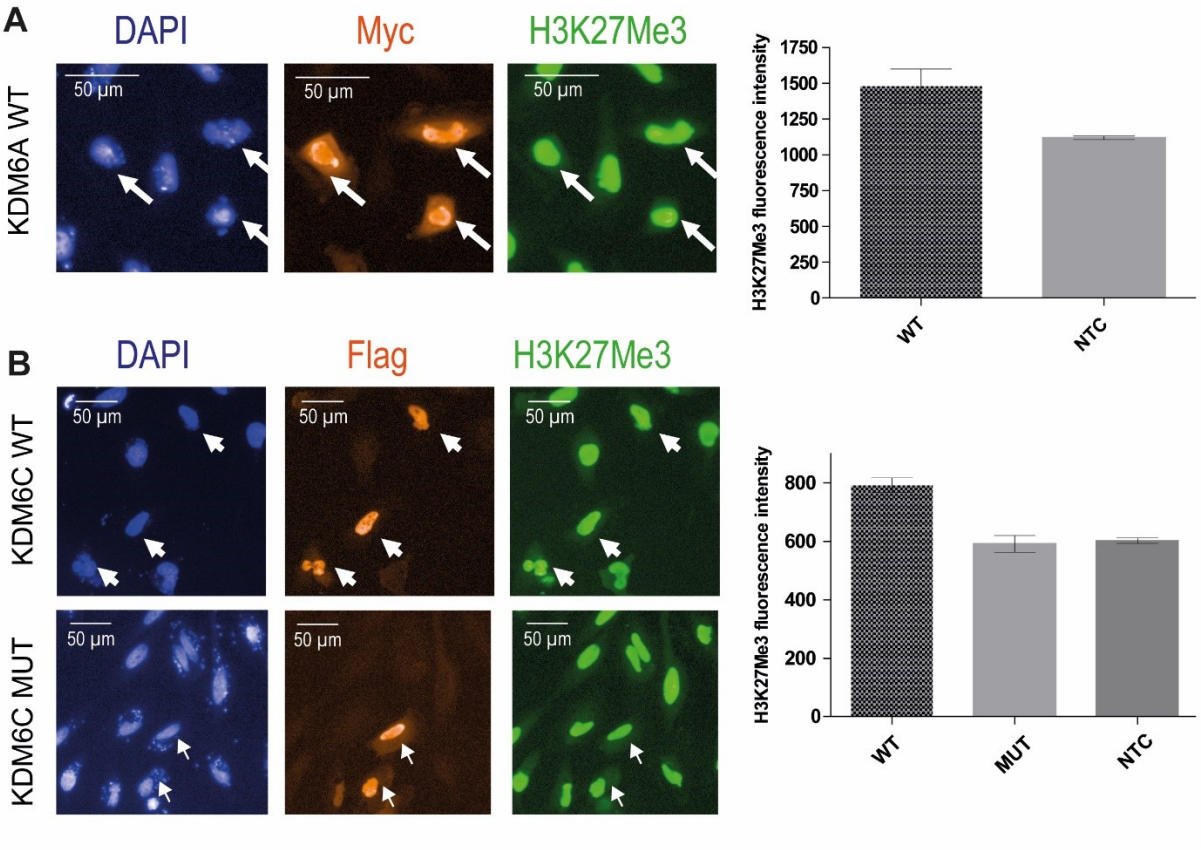


Figure 3.8. Over-expression KDM6A and KDM6C in HeLa does not reduce global H3K27Me3 fluorescence. A. *Fluorescence images of HeLa cells transfected with Myc-tagged KDM6A WT and NTC stained with DAPI, anti-Myc and anti-H3K27Me3.* ***B.*** *Average H3K27Me3 fluorescence of KDM6A WT transfected cells is increased relative to NTC.* ***C.*** *Fluorescence images of HeLa cells transfected with FLAG-tagged KDM6C WT FLAG-tagged, KDM6C MUT and NTC stained with DAPI, anti-FLAG and anti-H3K27Me3.* ***D.*** *Average H3K27Me3 fluorescence of KDM6C WT transfected cells is increased relative to KDM6C MUT and NTC. (Data mean ± SEM, N=3, technical. N=1 biological replicate.) 20x magnification.*

3.6 Effect of transfection window duration on transfection efficiency

As neither KDM6A nor KDM6C displayed cellular demethylase activity, KDM6B alone was selected for further optimisation of the transfection protocol. Whilst good transfection efficiencies had been achieved using GeneJuice® and Fugene® HD above (maximum 15.6% and 15.1% respectively), it was desirable to evaluate the transfection time on transfection efficiencies. After 24 hours H3K27Me3 fluorescence intensity is reduced in KDM6B WT versus KDM6B MUT and NTC. This might reduce the signal window available during the treatment window, potentially obscuring treatment effects. Additionally, a protocol consisting of a 24 hour transfection window followed by a 24

hour treatment window could be problematic because of the requirement to keep cells within a 'goldilocks' range of cell density. Seeding of cells at very low cell densities results in slow and patchy cell growth, whereas allowing cells to reach high confluence can result in stress and apoptosis. Therefore, a shorter transfection window would be desirable and so experiments were undertaken to evaluate the effect of transfection treatment duration on resulting transfection efficiencies.

HeLa cells were transfected with KDM6B WT and MUT constructs using Fugene® HD or GeneJuice®, and incubated with transfection reagent for 4, 6 and 8 hours. Media was then replaced with fresh media prior to fixing and staining after 24 hours. Cells were also fixed after 24 hours incubation with transfection reagent, as above (Figure 3.9).

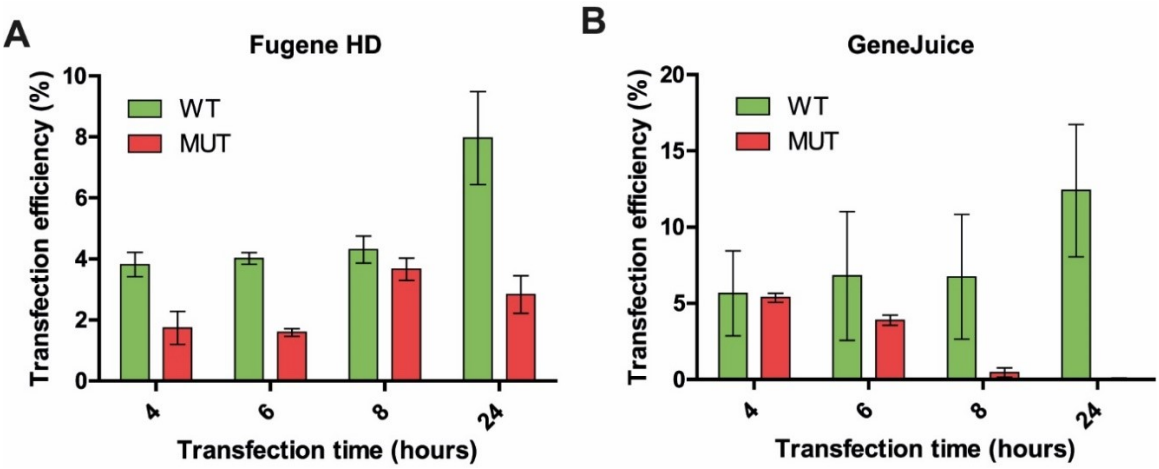


Figure 3.9 Transfection efficiency moderately increases with increasing transfection window duration. A, B. *HeLa were treated with Fugene® HD (A) or GeneJuice® (B) and KDM6B plasmid DNA, as per the manufacturer's protocols, for a transfection window of 4, 6 or 8 hours. Culture media was then replaced, and cells were fixed after 24 hours. Cells were also incubated with TR for 24 hours before fixing and staining, as above. Data mean ± SEM, N=3, technical. N=1 biological replicate.*

In cells transfected with KDM6B WT using Fugene® HD, there was little change in transfection efficiency between four and eight hours treatment duration, although an increase was seen at 24 hours incubation. A slight increase was seen at 8 and 24 hours incubation versus 4 and 6 hours cells transfected using Fugene HD. A similar trend was seen in cells transfected with KDM6B WT and MUT using GeneJuice®, but there was a

large well-to-well variability in transfection efficiency. Transfection efficiency of the 24 hour treatment cells was lower compared with the initial transfection experiments utilising the same experimental conditions (Figure 3.7, Table 3.3). For both reagents the number of transfected cells achieved was still more than sufficient for analysis (average cells per well, 558 KDM6B WT, 217 KDM6B MUT, Fugene® HD, 24 hours, N=3) according to sample size calculation above, section 3.4.

On the basis of the results of the transfection optimisation experiments, the transfection protocol selected was transfection using Fugene® HD, with a transfection window of 6 hours.

3.7 Evaluation of oxygen-dependence of cellular KDM6B activity in HeLa

The immunofluorescence activity assay optimised above was employed to investigate the effect of oxygen availability on cellular KDM6B activity. HeLa cells were transiently transfected with N-terminal FLAG-tagged KDM6B WT and the corresponding catalytically inactive mutant (H1390A, MUT) using Fugene® HD, as above. After 6 hours media was replaced, and plates were transferred to hypoxic workstations (InvivoX, Ruskin) at 1.0% and 5.0% oxygen normoxia to 21%. Cells were incubated for a further 24 hours before fixing and staining. As before, fluorescent microscopy images were acquired using an Operetta® high content imaging system, and analysed using Harmony™ analysis software.

Percentage demethylation of H3K27Me3 was calculated by normalising the average fluorescence intensity of global H3K27Me3 in transfected WT cells per well versus transfected MUT within the same treatment group, and plotted versus percentage oxygen (Figure 3.10). Relative activity of KDM6B in hypoxia was calculated by normalising

percentage demethylation of H3K27Me3 at 0.1% and 5% to percentage demethylation at 21% (normoxia).

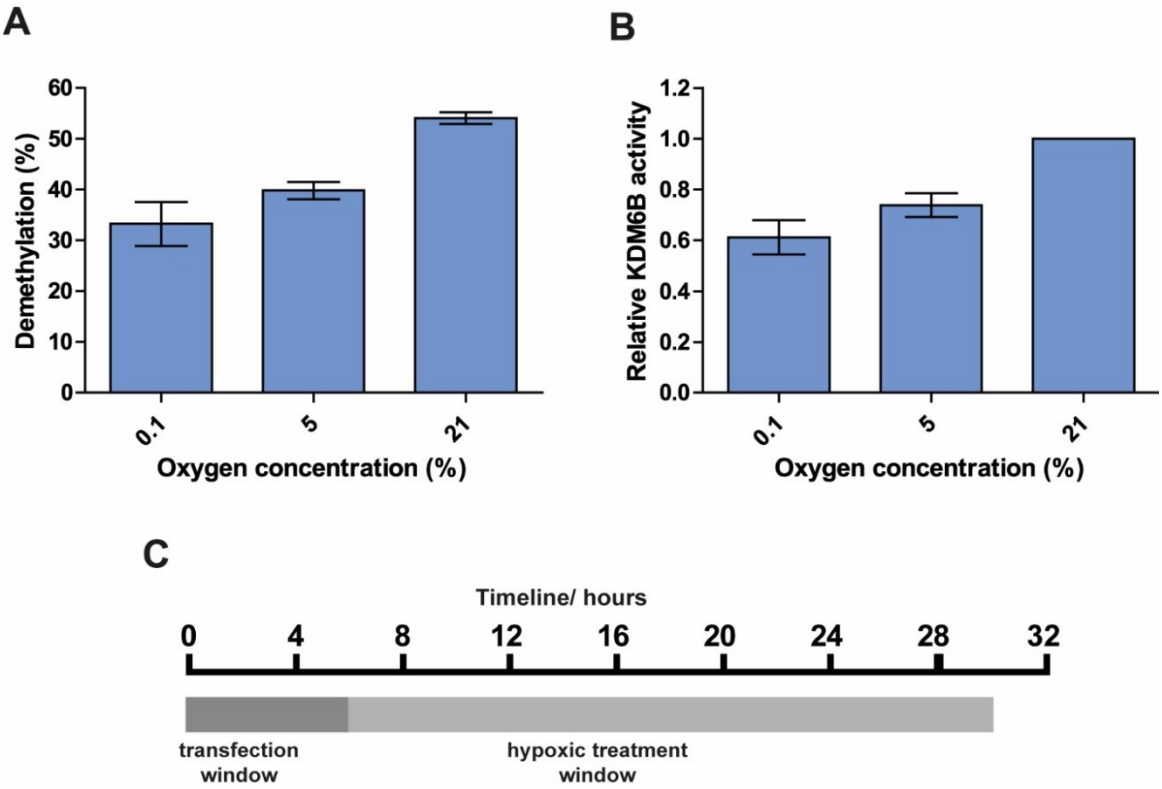


Figure 3.10. KDM6B activity demonstrates a graded response to oxygen concentration in HeLa cells. *HeLa were treated with Fugene® HD and plasmid DNA, as per the manufacturer's protocols, for a transfection window of 6 hours. Culture media was then replaced and cells were transferred to a hypoxic chamber or incubator at 0.1, 5, and 21% O_2 and fixed and stained after 24 hours incubation.* ***A. Percentage demethylation of H3K27Me3 decreases with decreasing oxygen concentration.*** *Percentage demethylation of H3K27Me3, calculated using mean H3K27Me3 fluorescence of cells transfected with KDM6B WT and KDM6B MUT incubated in equivalent O_2 conditions, as per equation described in Figure 3.6, C.* ***B. Relative activity of KDM6B decreases with decreasing oxygen concentration.*** *Relative activity of KDM6B calculated by normalising percentage demethylation of H3K27Me3 at 0.1% and 5% to percentage demethylation at 21% (normoxia).* ***C.*** *Timeline of treatment protocol.*

As oxygen concentration decreases, so does the percentage demethylation catalysed by KDM6B, indicating that the activity of KDM6B against H3K27Me3 in HeLa cells is reduced in an oxygen concentration dependent manner (Figure 3.10, B). However, although there is a 39% reduction in relative activity at the lowest oxygen concentration tested, 0.1% KDM6B is still active under these conditions.

3.8 Evaluation of the effect of normoxic transfection window on oxygen-dependence of cellular KDM6B activity

In the above protocol, cells undergo treatment with transfection reagent for six hours at normoxia, prior to replacement of the culture media and transfer to the hypoxic chambers. It is possible that demethylation by KDM6B occurring within this normoxic window could prevent the observation of total loss of KDM6B activity in hypoxia. To investigate this further, the above oxygen titration protocol was altered to eliminate the normoxic transfection window (Figure 3.11, A). HeLa cells were transiently transfected with N-terminal FLAG-tagged KDM6B WT and inactive KDM6B MUT (H1390A) using Fugene® HD, as above. Hypoxic treatment plates were then directly transferred to hypoxic workstations (Invivo400 Ruskin) at 1.0% and 5.0% oxygen, with normoxia treatment plate incubated at 21% oxygen and incubated for 24 hours before fixing and staining.

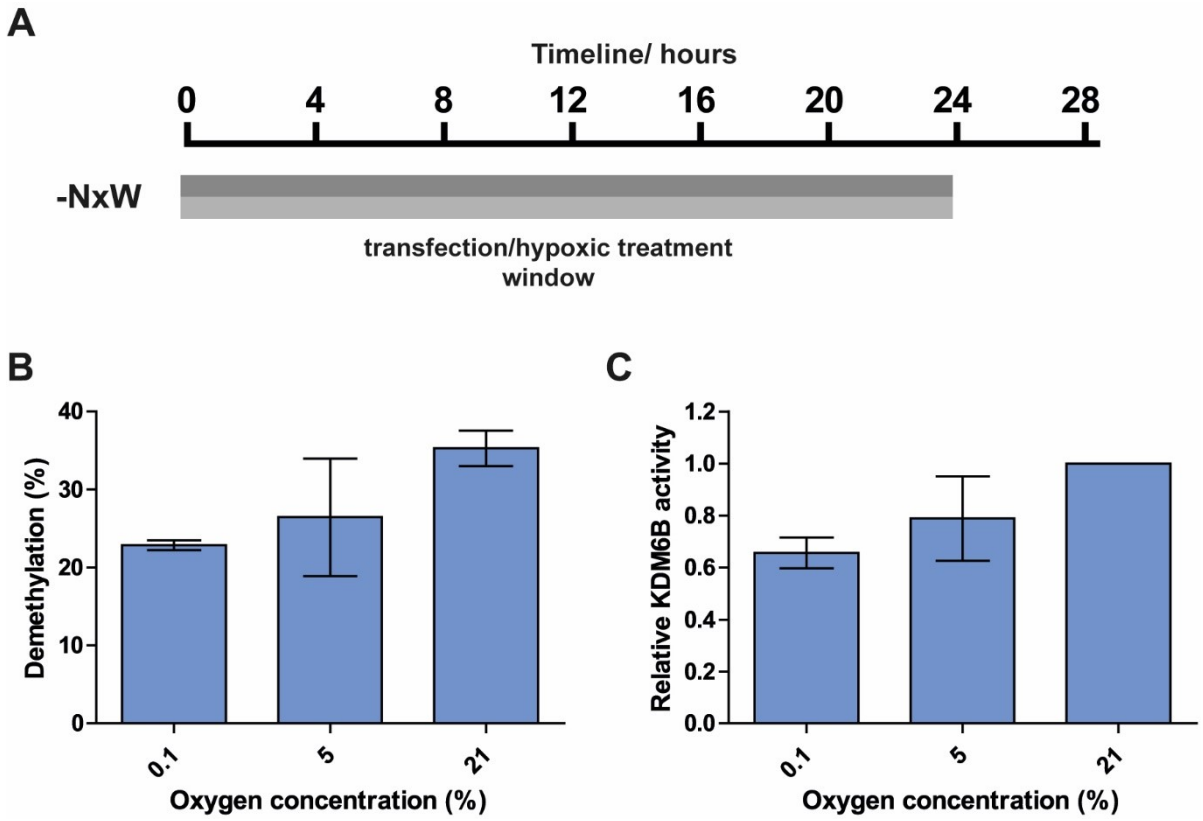


Figure 3.11. HeLa cells incubated for 24 hours in hypoxia show graded KDM6B activity. *HeLa were treated with Fugene® HD and plasmid DNA, as per the manufacturer's protocols. Cells were transferred directly to a hypoxic chamber or incubator at 0.1, 5, and 21% O_2 and fixed and stained after 24 hours incubation.* ***A.*** *Timeline of treatment protocol.* ***B. Percentage demethylation of H3K27Me3 decreases with decreasing oxygen concentration.*** *Percentage demethylation of H3K27Me3, calculated using mean H3K27Me3 fluorescence of cells transfected with KDM6B WT and KDM6B MUT incubated in same O2 conditions, as per equation above, Figure 3.6, C.* ***C. Relative activity of KDM6B decreases with decreasing oxygen concentration.*** ***C****. Relative activity of KDM6B calculated by normalising percentage demethylation of H3K27Me3 at 0.1% and 5% to percentage demethylation at 21% (normoxia).*

As before, percentage demethylation by KDM6B decreases with decreasing oxygen concentration, indicating that the activity of KDM6B against H3K27Me3 in HeLa cells is reduced in an oxygen concentration dependent manner (Figure 3.11).

Two different transfection protocols were utilised to evaluate the effect of normoxic transfection window on the observed oxygen dependence of KDM6B activity. In the first protocol, +NxW, cells undergo treatment with transfection reagent for six hours at normoxia, prior to replacement of the culture media and transfer to the hypoxic chambers. In the second protocol, -NxW, cells were incubated with transfection reagent for 24 hours

at 0.1, 5 and 21% oxygen, eliminating the normoxic transfection window (Figure 3.12, A).

Comparing results from the +NxW protocol with the results from the -NxW protocol, there is a difference in the percentage demethylation observed (54% demethylation +NxW versus 35% demethylation -NxW, 21% Oxygen). This increased percentage demethylation observed in +NxW treated cells versus -NxW treated cells could result from the increased incubation time (+NxW, 30 hours, -NxW 24 hours). Despite this difference in absolute activity, relative KDM6B activity values at 0.1% and 5% oxygen for +NxW and -NxW are within error of each other (Figure 3.12, B).

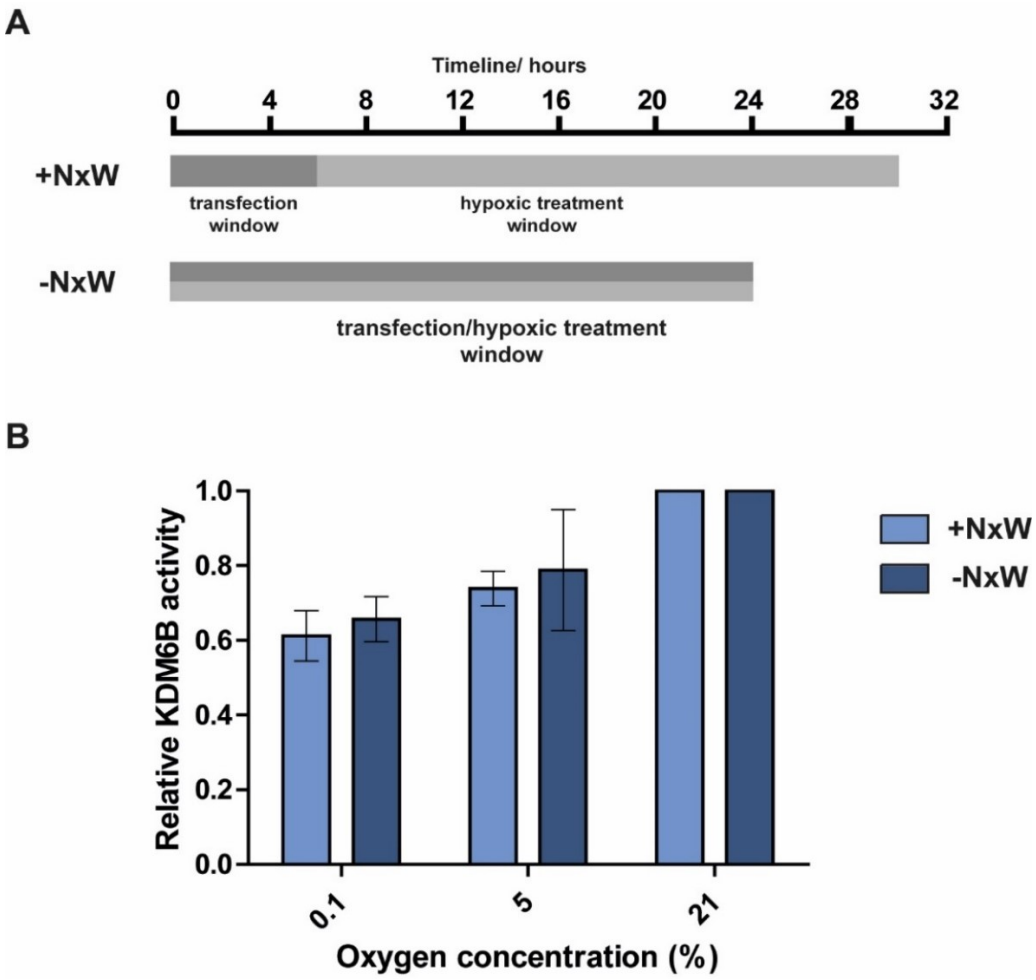


Figure 3.12. Oxygen dependence of relative KDM6B activity is unaltered by normoxic transfection window *HeLa were treated with Fugene® HD and plasmid DNA, as per the manufacturer's protocols. Cells were incubated in a hypoxic chamber or incubator at 0.1, 5, and 21% O_2 according to +NxW protocol or -NxW protocol. Relative activity of KDM6B calculated by normalising percentage demethylation of H3K27Me3 at 0.1% and 5% to percentage demethylation at 21% (normoxia) for each treatment.* ***A.*** *Timeline of treatment protocol.* ***C.*** *Relative activity of KDM6B decreases with decreasing oxygen concentration, for both hypoxic treatment protocols.*

Oxygen dependence of relative KDM6B activity is unaltered by a normoxic transfection window. In the -NxW protocol, all all KDM6B is expressed under hypoxic conditions, it still retains some activity even at 0.1% oxygen. Together these results demonstrate that although KDM6B activity is markedly reduced in hypoxia, it still retains some activity, and thus KDM6B activity may be less sensitive to oxygen availability compared to other JmjC-KDMs for which oxygen dependence of cellular activity has been determined.

3.9 Identification of unusual HeLa morphology

The results of the immunofluorescence oxygen titrations were confounded by identification of an unusual nuclear phenotype within HeLa cell stocks; nuclei displayed a horse-shoe shape accompanied by nuclear blebbing. This nuclear morphology was present across all cell groups, including WT, MUT and non-transfected controls (Figure 3.13). Additionally, 'speckles' of DAPI staining were present outside the nucleus, although these were not present in NTC wells. Once the unusual morphology was identified, fluorescent microscopy images from previous experiments were re-examined. The presence of cells with the unusual morphology was variable and inconsistent, increasing gradually in experiments undertaken within the previous 2 months.

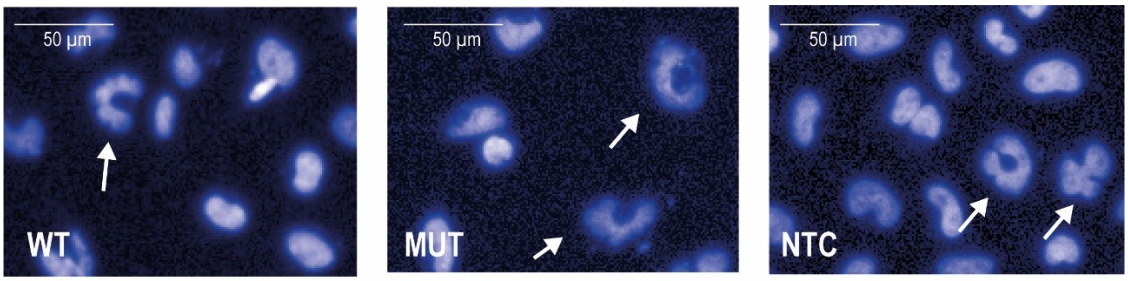


Figure 3.13. Observation of unusual nuclear morphology. *Fluorescence images of HeLa cells transfected with KDM6B WT, KDM6B MUT and NTC stained with DAPI.* ***White arrows*** *– horseshoe nuclei phenotype. 20x magnification.*

The boundary and area of the nucleus, from which nuclear fluorescence is determined, is detected based on DAPI fluorescence. Due to the unusual nuclear morphology, the boundary and area of the nucleus was unable to be determined accurately using automated image analysis, which often overestimated nuclear size. This is likely to interfere with determination of the nuclear fluorescence intensity of FLAG/Myc and H3K27Me3, both of which are used in analysis.

Since DAPI speckles can be an indication of mycoplasma infection, cells were tested for mycoplasma using a commercial MycoAlert^{TM} kit. This is a biochemical test which

detects the presence of enzymes found in mycoplasma but not eukaryotic cells within cell lysates and/ or conditioned media. If these mycoplasma enzymes are present, they will react with a proprietary MycoAlert™ substrate and catalyse the conversion of ADP to ATP which is converted to light via luciferase. The ratio of luminescence before and after addition of MycoAlert™ substrate indicates whether there is mycoplasma present. HeLa cell lysates and conditioned media tested negative for mycoplasma. DAPI speckling can also result from particles of plasmid DNA-transfection reagent complex which adhere to cell culture plates. This may be the cause of the speckling, considering that these speckles are not present in the NTC wells.

Bacterial or fungal infection were not detected by inspection of cell cultures using a light microscope. Having ruled out biological contamination, cells were sub-cultured systematically to try and identify cell culture reagents which may be causing the phenotype. Culture in multiple batch numbers of fetal bovine serum (FBS), Dulbecco's Modified Eagle's medium (DMEM) and GlutaMAX™ failed to resolve the nuclear morphology.

Authenticated HeLa cell stocks were acquired from the American Type Culture Collection (ATCC) and thawed and cultured in Eagle's Minimum Essential Medium according to ATCC recommendations, but they also showed the same morphology after fixing and staining. After conferring with colleagues in the Müller-Knapp group, it became clear that they had also experienced the same unusual HeLa morphology accompanied by an unexplained drop in transfection efficiency (Figure 3.14). As these cells were cultured in different research centres, using different cell culture protocols and reagents, no further attempts to resolve the morphology were made.

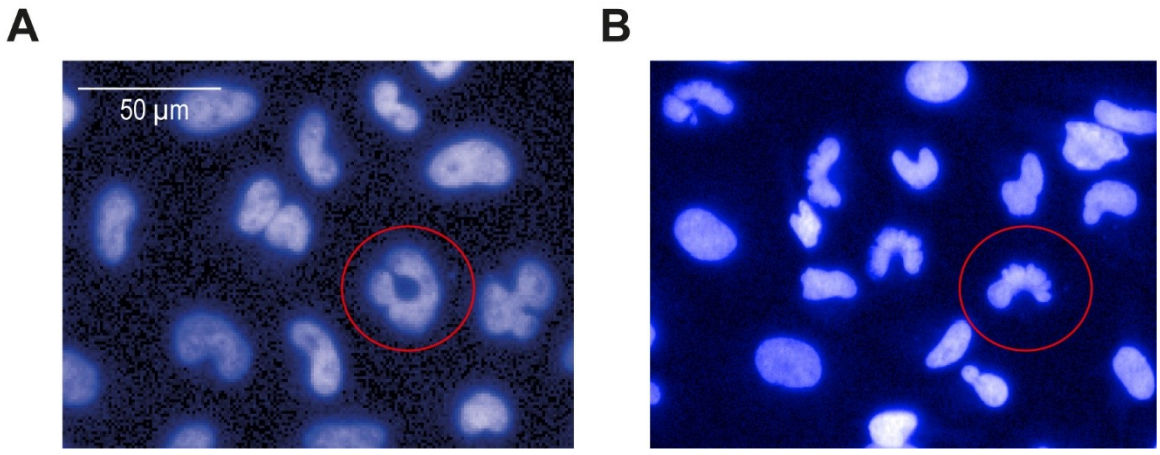


Figure 3.14. Identification of nuclear morphology in unrelated HeLa stocks. **A**. *Nuclear blebbing and horse-shoe morphology cells from Kawamura group.* ***B***. *Nuclear blebbing and horse-shoe morphology of HeLa cells from Muller-Knapp group. (Micrograph A collected at 20x magnification, Micrograph B provided without calibration bar, collected at 20x magnification.)*

Since no evidence of infection, such as by mycoplasma, or chemical contamination, such as through reagents, was found, and change of reagents or cell source did not resolve the unusual morphology experimentation using the HeLa cell line was halted in favour of COS-7 cells.

3.10 Evaluation of cellular KDM6A/B/C activity in COS-7 cells

As an alternate to HeLa, the COS-7 cell line, derived from monkey kidney fibroblasts, was selected for these experiments. Like HeLa, COS-7 are strongly adherent making them suited to immunofluorescent staining protocols, and high levels of transfection efficiency, up to 80%, can be achieved.[45] This cell line has been used to demonstrate cellular activity of KDM6A and KDM6B.[49]

COS-7 cells were transiently transfected with FLAG or Myc tagged KDM6A/B/C WT MUT using Fugene® HD transfection reagent and incubated for 24 hours before fixing and staining. Fluorescent microscopy images were acquired using an Operetta® high content imaging system, and analysed using Harmony™ analysis software.

Average H3K27Me3 fluorescence per well of transfected KDM6A/B/C WT and MUT, and corresponding NTC was then calculated (Figure 3.15).

COS-7 cells displayed a regular, round nuclear morphology consistent with images of their morphology from the literature.[49] There was however, increased extranuclear FLAG staining compared with HeLa. Studies have identified nucleocytoplasmic shuttling of KDM6B and dynamic regulation of its sub-cellular localisation.[51] There may be differential sub-cellular localisation or KDM6B expression level between COS-7 and HeLa, resulting in the observed difference of staining.

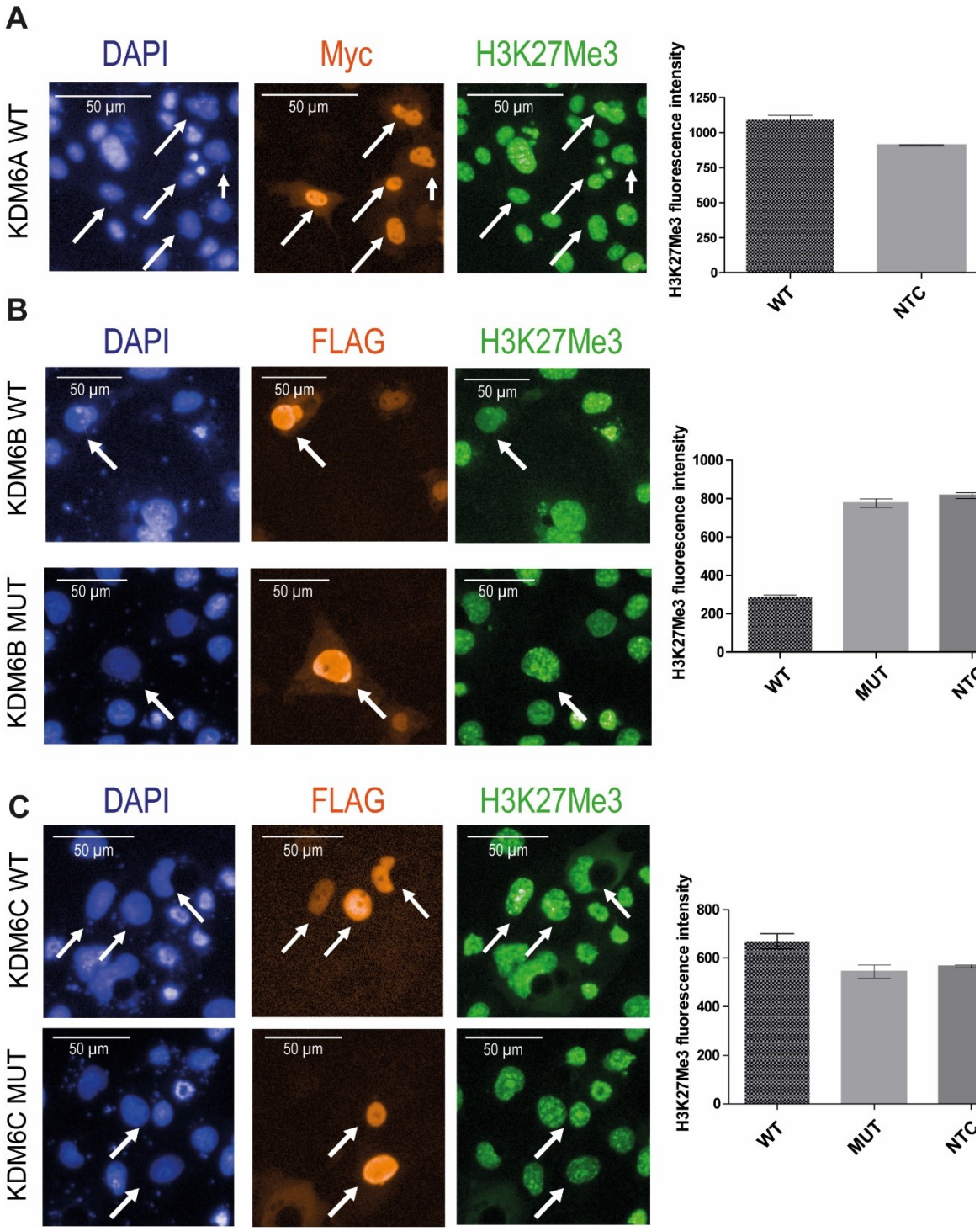


Figure 3.15. Over-expression KDM6A/BC WT and MUT in COS-7. A. *Fluorescence images of COS-7 cells transfected with Myc-tagged KDM6A WT and NTC stained with DAPI, anti-Myc and anti-H3K27Me3. Average H3K27Me3 fluorescence of KDM6A WT transfected cells is increased relative to NTC.* ***B.*** *Fluorescence images of COS-7 cells transfected with FLAG-tagged KDM6B WT, KDM6B MUT and NTC stained with DAPI, anti-FLAG and anti-H3K27Me3. Average H3K27Me3 fluorescence of KDM6B WT transfected cells is reduced relative to KDM6B MUT and NTC.* ***C.*** *Fluorescence images of COS-7 cells transfected with FLAG-tagged KDM6C WT, FLAG-tagged, KDM6C MUT and NTC stained with DAPI, anti-FLAG and anti-H3K27Me3. Average H3K27Me3 fluorescence of KDM6C WT transfected cells is increased relative to KDM6C MUT and NTC. (Data mean ± SEM, N=3, technical. N=1 biological replicate.) 20x magnification.*

No reduction of H3K27Me3 fluorescence was seen in cells overexpressing KDM6A WT compared to non-transfected control, indicating a lack of cellular KDM6A activity in COS-7 cells (Figure 3.15, A).

H3K27Me3 fluorescence was lower in cells overexpressing KDM6B WT compared to non-transfected control cells and cells overexpressing KDM6B MUT, indicating demethylation by KDM6B (Figure 3.15, B), consistent with literature reports of cellular KDM6B activity in COS-7.[49]

No reduction of H3K27Me3 fluorescence was seen in cells overexpressing KDM6C WT compared to KDM6C MUT or non-transfected control, indicating a lack of cellular KDM6C activity in HeLa cells (Figure 3.15, C). As seen in HeLa, average H3K27Me3 fluorescence of WT transfected cells was higher than that of corresponding MUT and NTC. This hypermethylation could result from unproductive binding to H3K27Me3 which may shield the mark from endogenous demethylation.

3.11 Establishment of an optimal transfection protocol for KDM6AB in COS-7

The transfection optimisation protocol established above was utilised to identify the best transfection reagent and TR:DNA ratio for transfection of KDM6B WT and MUT.

COS-7 were transiently transfected with the KDM6B WT and KDM6B MUT constructs using a panel of commercially available transfection reagents as above; Fugene® HD (Promega), GeneJuice®® (Merck), Lipofectamine® 2000 and Lipofectamine® 3000 fectamine3000. Two TR:DNA ratios were tested per reagent, as per the manufacturer's protocols. Cells were incubated for 24 hours before fixing and staining. As before, fluorescent microscopy images were acquired using an Operetta® high content imaging system, and analysed using Harmony™ analysis software.

	GeneJuice® 1.5:1	GeneJuice® 3:1	Fugene® HD 1.25:1	Fugene® HD 2.5:1	L2000 1:1	L2000 2.5:1	L3000 0.75:1	L3000 1.5:1
KDM6B WT	11.2	11.0	1.4	22.6	10.4	15.3	24.6	25.4
KDM6B MUT	10.1	8.1	1.1	12.2	5.1	11.7	12.5	23.2

Table 3.4. Transfection efficiency of COS-7 transfected with KDM6B WT and MUT. *HeLa were treated with GeneJuice®, Lipofectamine® 2000, Lipofectamine®3000 or Fugene® HD and plasmid DNA. Two TR:DNA ratios were tested per reagent, as per the manufacturer's protocols. Cells were incubated for 24 hours before fixing and staining.*

Unlike HeLa, no reduction in cell number on treatment of COS-7 with Lipofectamine® 2000 or Lipofectamine® 3000 was seen. Transfection of HeLa and COS-7 resulted in comparable transfection efficiency for each treatment. The highest transfection efficiencies of KDM6B WT and MUT in COS-7 were achieved by treatment with Lipofectamine® 3000 at a 1.5:1 TR:DNA ratio. This treatment was selected for use in further experiments.

3.12 Evaluation of oxygen-dependence of cellular KDM6B activity in COS-7

The immunofluorescence activity assay optimised above was employed to investigate the effect of oxygen availability on cellular KDM6B activity. COS-7 cells were transiently transfected with N-terminal FLAG-tagged KDM6B WT and the corresponding MUT (H1390A) using Lipofectamine® 3000, as above, and transferred directly to hypoxic workstations (InvivoX, Ruskin) at 0.1, 1.0 and 5.0% oxygen and a normoxic incubator at 21% oxygen. Cells were incubated for 24 hours before fixing and staining. Fluorescent microscopy images were acquired using an Operetta® high content imaging system, and analysed using Harmony™ analysis software. Percentage demethylation of H3K27Me3 was calculated by normalising the average fluorescence intensity of global H3K27Me3 in transfected WT cells per well versus transfected MUT within the same treatment group,

and plotted versus percentage oxygen (Figure 3.16). Relative activity was calculated for each concentration versus Nx control.

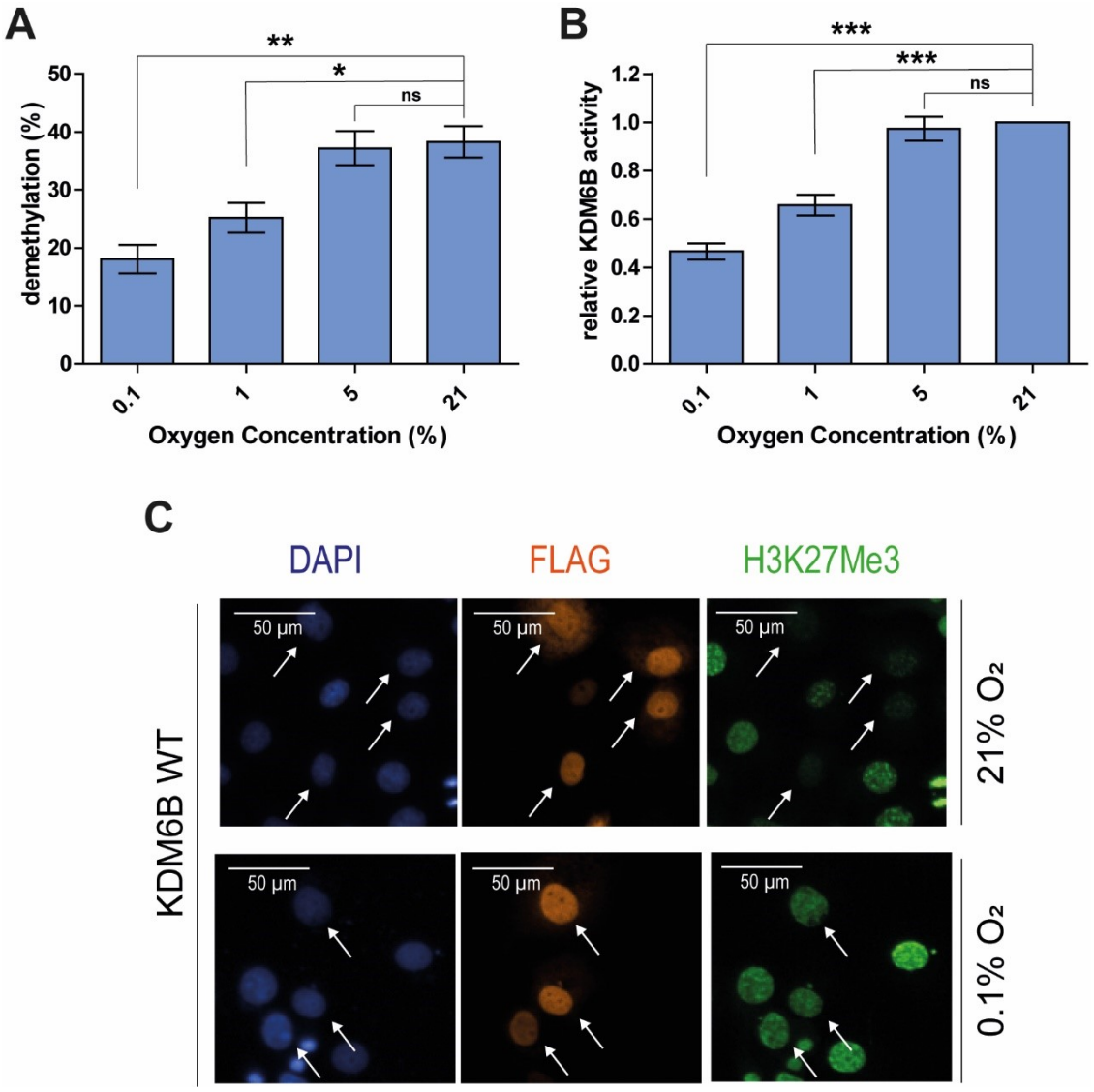


Figure 3.16. KDM6B activity demonstrates a graded response to oxygen concentration in COS-7 cells. *COS-7 were treated with Lipofectamine® 3000 and plasmid DNA, as per the manufacturer's protocols. Cells were transferred to a hypoxic chamber or incubator at 0.1, 5, and 21% oxygen. Cells were fixed and stained after 24 hours incubation.* ***A. Percentage demethylation of H3K27Me3 decreases with decreasing oxygen concentration.*** *Percentage demethylation of H3K27Me3, calculated using mean H3K27Me3 fluorescence of cells transfected with KDM6B WT and KDM6B MUT incubated in same oxygen conditions, as per equation above, Figure 3.6, C.* ***B. Relative activity of KDM6B decreases with decreasing oxygen concentration. C****. Relative activity of KDM6B calculated by normalising percentage demethylation of H3K27Me3 at 0.1% and 5% to percentage demethylation at 21% (normoxia). N=3 biological repeats, error bars = std.err. One-way ANOVA and Dunnetts multiple comparison test against 21% oxygen result was performed using GraphPad Prism. 20x magnification.*

As in HeLa cells, both the percentage demethylation by KDM6B and relative KDM6B activity decreases with decreasing oxygen concentration, indicating that the activity of KDM6B against H3K27Me3 in COS-7 cells is reduced in an oxygen concentration dependent manner.

Relative KDM6B WT activity in COS-7 is lower than in HeLa at 0.1% (COS-7 0.46, HeLa 0.66). Oxygen concentration of cell media in both experiments was measured using an OxyLite^{TM} oxygen sensor; values were in the range of 0.0-0.2 mmHg, indicating severe hypoxia. Whilst this confirms that oxygen concentration in the media of these cells was within a narrow range, the subcellular variation of oxygen concentration is not well understood, and may be subject to cell type, resulting in the difference in relative activity seen between HeLa and COS-7 cells.

3.13 Discussion

Previous kinetic studies of KDM6A and KDM6B, conducted by Grasilda Zenkeviciute revealed that their activity is oxygen dependent. $K_m^{app}(O_2)$ values for KDM6A and KDM6B (28.4 μM and 3.1 μM respectively) were lower than those of PHD2, FIH and KDM4A (230 μM, 150 μM and 173 μM, respectively) potentially indicating that KDM6A and KDM6B activity may be less sensitive to oxygen availability. As these studies may not have been conducted at steady-state conditions, efforts were undertaken to undertake a more comprehensive kinetic characterisation of KDM6A and KDM6B (Chapter 1), but these were not completed due to break-down of MALDI-MS equipment (Chapter 4, Figure 4.6).

Overall, *in vitro* studies of KDM6A and KDM6B to date show that their activity is oxygen dependent, which could have important implications for gene regulation in hypoxia. To determine whether these *in vitro* results translate to reduced KDM6 activity

in a cellular context, a cellular immunofluorescence assay in HeLa was established. Reduction of H3K27Me3 indicated demethylase activity of over-expressed KDM6B WT in HeLa cells, but this reduction was not seen in cells transfected with KDM6A WT or KDM6C WT, and so KDM6B alone was taken forward for immunofluorescence oxygen titration experiments. Cellular activity of KDM6B displayed a graded response to oxygen concentration, but was not abolished entirely, even in severe hypoxia (0.1% oxygen). The protocol used in these first experiments included a normoxic transfection window which could prevent complete elimination of KDM6B activity, and so a second data set was acquired. The experimental protocol was adapted so that cells were immediately transferred to hypoxia upon transfection, and therefore all KDM6B overexpression would occur under hypoxic conditions. Although there was a difference in absolute KDM6B activity between these data sets, relative KDM6B activity was within error, confirming the observation that KDM6B maintains some activity, even in severe hypoxia.

Unfortunately, an unusual nuclear morphology was identified in the HeLa, and extensive attempts to identify the cause or eliminate the morphology were unsuccessful. To validate the above results, the immunofluorescence assay was established in an alternate cell line, COS-7. Although KDM6A and KDM6B activity against global H3K27Me3 in COS-7 has been reported,[49] reduction of H3K27Me3 fluorescence versus NTC was only present in cells transfected with KDM6B WT, and not in cells transfected with KDM6A WT nor KDM6C WT. Instead, H3K27Me3 fluorescence was increased in cells transfected with KDM6A WT and KDM6C WT versus NTC. Non-catalytic binding of KDM6A and KDM6C may effectively shield the marks from endogenous demethylases, although interestingly H3K27Me3 fluorescence was not similarly increased in KDM6C MUT transfected cells.

As in HeLa, cellular activity of KDM6B showed a graded response to oxygen availability in COS-7, with a 54% reduction in relative activity at 0.1% oxygen relative to 21% oxygen. The cellular oxygen dependence of KDM4A activity has been characterised in a study by Hancock et al (Figure 3.17). The $K_m^{app}(O_2)$ of KDM6B is lower than that of KDM4A ($K_m^{app}(O_2)$ values 28.4 μM and 173 μM, respectively), indicating activity of KDM6B is less sensitive to oxygen concentration than KDM4A. However, values for relative cellular activity of KDM4A and KDM6B determined at 0.1, 1.0 and 5.0% oxygen are within error of one another (Figure 3.17). As stated above, the $K_m^{app}(O_2)$ value for KDM6B was not determined at steady state conditions, and thus further study of the *in vitro* oxygen dependence of KDM6B activity is needed to draw further conclusions.

The effect of oxygen concentration of TET1 activity using an analogous immunofluorescence activity assay was assessed in preliminary data collected by Dr Rebecca Hancock and Dr Akane Kawamura (N=1 biological replicate) (Figure 3.17). The relative cellular activity of TET1 is reduced compared with KDM4A and KDM6B at each concentration tested. This indicates that TET1 is highly sensitive to oxygen concentration, consistent with recent publications demonstrating reduction of TET1 activity and corresponding gene regulation in hypoxia.[52,53] This data also demonstrates the potential of cellular immunofluorescence assays to detect differential oxygen sensitivity.

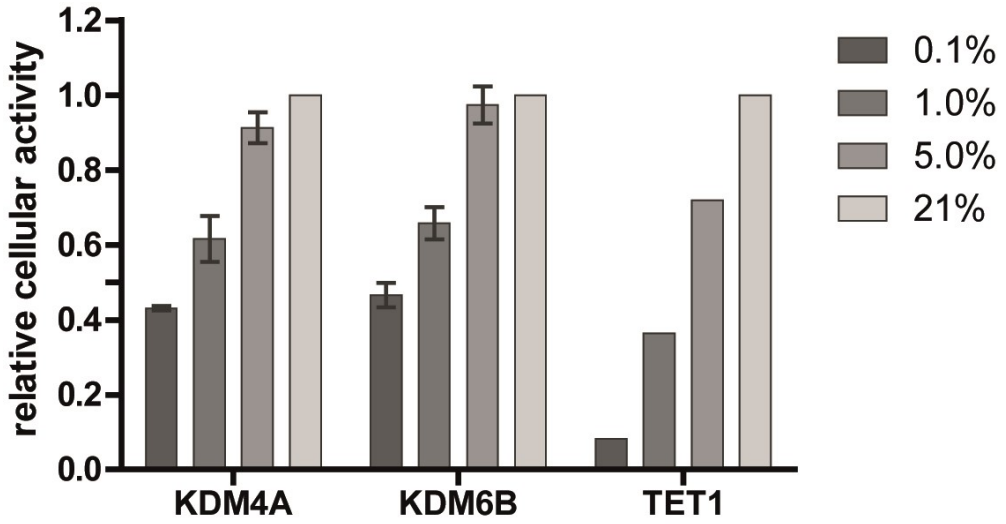


Figure 3.17. The activity of KDM4A, KDM6A and TET1 is reduced in an oxygen concentration dependent manner. *Immunofluorescence experiments: U2OS stably overexpressing FLAG-tagged full length KDM4A, U2OS stably overexpressing FLAG-tagged catalytic domain of TET1, COS-7 transiently overexpressing KDM6B were transferred to a hypoxic chamber or incubator at 0.1, 5, and 21% oxygen. Cells were fixed and stained after 24 hours incubation and relative activity at each oxygen concentration was determined against activity at 21% oxygen. KDM4A, KDM6B: N=3 biological repeats, error bars = std.err. TET1: N=1 biological replicate.*

Other factors may influence the activity of 2OG oxygenase enzymes in hypoxic conditions, and account for differences in *in vitro* and cellular oxygen sensitivities. The concentration of tricarboxylic acid cycle intermediates is known to be perturbed in hypoxia, with some intermediates reaching mM cellular concentrations.[54] KDM6B activity is inhibited by many of these metabolites (Chapter 4) which could result in loss of activity that may not be seen *in vitro*.

The interaction between hypoxia, HIF regulation, and the activity and expression of KDM6B is complex, and more work is required to assess the impact of hypoxia on KDM6B mediated gene regulation in a physiological context. Regardless, the data in this chapter demonstrates that KDM6B activity is significantly reduced in hypoxia in a cellular context, and this is likely to have important consequences for KDM6B mediated gene regulation in both disease and development.

3.13 References

1. Jain, R. K., Au, P., Tam, J., Duda, D. G. & Fukumura, D. Engineering vascularized tissue. *Nat. Biotechnol.* **23,** 821–823 (2005).

2. Carreau, A., Hafny-Rahbi, B. El, Matejuk, A., Grillon, C. & Kieda, C. Why is the partial oxygen pressure of human tissues a crucial parameter? Small molecules and hypoxia. *J. Cell. Mol. Med.* **15,** 1239–1253 (2011).

3. Hancock, R. L., Dunne, K., Walport, L. J., Flashman, E. & Kawamura, A. Epigenetic regulation by histone demethylases in hypoxia. *Epigenomics* 1–21 (2015). doi:10.2217/epi.15.24

4. Majmundar, A. J., Wong, W. J. & Simon, M. C. Hypoxia-inducible factors and the response to hypoxic stress. *Mol. Cell* **40,** 294–309 (2010).

5. Semenza, G. L. Oxygen Sensing, Hypoxia-Inducible Factors, and Disease Pathophysiology. *Annu. Rev. Pathol. Mech. Dis.* **9,** 47–71 (2014).

6. Myllyharju, J. Prolyl 4-hydroxylases, master regulators of the hypoxia response. *Acta Physiol.* **208,** 148–165 (2013).

7. Kaelin, W. G. & Ratcliffe, P. J. Oxygen Sensing by Metazoans: The Central Role of the HIF Hydroxylase Pathway. *Mol. Cell* **30,** 393–402 (2008).

8. Ehrismann, D. *et al.* Studies on the activity of the hypoxia-inducible-factor hydroxylases using an oxygen consumption assay. *Biochem J* **401,** 227–234 (2007).

9. Hirsilä, M., Koivunen, P., Günzler, V., Kivirikko, K. I. & Myllyharju, J. Characterization of the human prolyl 4-hydroxylases that modify the hypoxia-inducible factor. *J. Biol. Chem.* **278,** 30772–80 (2003).

10. Tarhonskaya, H. *et al.* Investigating the contribution of the active site environment to the slow reaction of hypoxia-inducible factor prolyl hydroxylase domain 2 with oxygen. *Biochem. J.* **463,** 363–372 (2014).

11. Dao, J. H. *et al.* Kinetic characterization and identification of a novel inhibitor of hypoxia-inducible factor prolyl hydroxylase 2 using a time-resolved fluorescence resonance energy transfer-based assay technology. *Anal. Biochem.* **384,** 213–23 (2009).

12. Ehrismann, D. *et al.* Studies on the activity of the hypoxia-inducible-factor hydroxylases using an oxygen consumption assay. *Biochem. J.* **401,** 227–34 (2007).

13. Tarhonskaya, H. *et al.* Kinetic Investigations of the Role of Factor Inhibiting Hypoxia-

inducible Factor (FIH) as an Oxygen Sensor. *J. Biol. Chem.* **290,** 19726–42 (2015).

14. Chan, D. A., Sutphin, P. D., Yen, S.-E. & Giaccia, A. J. Coordinate Regulation of the Oxygen-Dependent Degradation Domains of Hypoxia-Inducible Factor 1. *Mol. Cell. Biol.* **25,** 6415–6426 (2005).

15. Tian, Y.-M. *et al.* Differential Sensitivity of Hypoxia Inducible Factor Hydroxylation Sites to Hypoxia and Hydroxylase Inhibitors. *J. Biol. Chem.* **286,** 13041–13051 (2011).

16. Watson, J. A., Watson, C. J., McCann, A. & Baugh, J. Epigenetics, the epicenter of the hypoxic response. *Epigenetics* **5,** 293–6 (2010).

17. Xia, X. & Kung, A. L. Preferential binding of HIF-1 to transcriptionally active loci determines cell-type specific response to hypoxia. *Genome Biol.* **10,** R113 (2009).

18. Xia, X. *et al.* Integrative analysis of HIF binding and transactivation reveals its role in maintaining histone methylation homeostasis. *Proc. Natl. Acad. Sci.* **106,** 4260–4265 (2009).

19. Costa, M. *et al.* Nickel carcinogenesis: epigenetics and hypoxia signaling. *Mutat Res* **592,** 79–88 (2005).

20. Islam, K. N. & Mendelson, C. R. Permissive effects of oxygen on cyclic AMP and interleukin-1 stimulation of surfactant protein A gene expression are mediated by epigenetic mechanisms. *Mol Cell Biol* **26,** 2901–2912 (2006).

21. Chen, H., Yan, Y., Davidson, T. L., Shinkai, Y. & Costa, M. Hypoxic stress induces dimethylated histone H3 lysine 9 through histone methyltransferase G9a in mammalian cells. *Cancer Res* **66,** 9009–9016 (2006).

22. Johnson, A. B., Denko, N. & Barton, M. C. Hypoxia induces a novel signature of chromatin modifications and global repression of transcription. *Mutat Res* **640,** 174–179 (2008).

23. Osumek, J. E., Revesz, A., Morton, J. S., Davidge, S. T. & Hardy, D. B. Enhanced Trimethylation of Histone H3 Mediates Impaired Expression of Hepatic Glucose 6-Phosphatase Expression in Offspring From Rat Dams Exposed to Hypoxia During Pregnancy. *Reprod. Sci.* **21,** 112–121 (2014).

24. Tausendschön, M., Dehne, N. & Brüne, B. Hypoxia causes epigenetic gene regulation in macrophages by attenuating Jumonji histone demethylase activity. *Cytokine* **53,** 256–262 (2011).

25. Beyer, S., Kristensen, M. M., Jensen, K. S., Johansen, J. V & Staller, P. The histone

demethylases JMJD1A and JMJD2B are transcriptional targets of hypoxia-inducible factor HIF. *J Biol Chem* **283,** 36542–36552 (2008).

26. Pollard, P. J. *et al.* Regulation of Jumonji-domain-containing histone demethylases by hypoxia-inducible factor (HIF)-1alpha. *Biochem J* **416,** 387–394 (2008).

27. Wellmann, S. *et al.* Hypoxia upregulates the histone demethylase JMJD1A via HIF-1. *Biochem. Biophys. Res. Commun.* **372,** 892–897 (2008).

28. Niu, X. *et al.* The von Hippel–Lindau tumor suppressor protein regulates gene expression and tumor growth through histone demethylase JARID1C. *Oncogene* **31,** 776–786 (2012).

29. Yang, J. *et al.* Role of hypoxia-inducible factors in epigenetic regulation via histone demethylases. *Ann. N. Y. Acad. Sci.* **1177,** 185–97 (2009).

30. Lee, H.-Y., Choi, K., Oh, H., Park, Y.-K. & Park, H. HIF-1-dependent induction of Jumonji domain-containing protein (JMJD) 3 under hypoxic conditions. *Mol. Cells* **37,** 43–50 (2014).

31. Cascella, B. & Mirica, L. M. Kinetic analysis of iron-dependent histone demethylases: α-ketoglutarate substrate inhibition and potential relevance to the regulation of histone demethylation in cancer cells. *Biochemistry* **51,** 8699–701 (2012).

32. Hancock, R. L., Masson, N., Dunne, K., Flashman, E. & Kawamura, A. The Activity of JmjC Histone Lysine Demethylase KDM4A is Highly Sensitive to Oxygen Concentrations. *ACS Chem. Biol.* **12,** 1011–1019 (2017).

33. Sanchez-Fernandez, E. M. *et al.* Investigations on the oxygen dependence of a 2-oxoglutarate histone demethylase. *Biochem J* **449,** 491–496 (2013).

34. Ohtani, K. *et al.* Jmjd3 controls mesodermal and cardiovascular differentiation of embryonic stem cells. *Circ. Res.* **113,** 856–62 (2013).

35. Lee, S., Lee, J. W. & Lee, S.-K. UTX, a histone H3-lysine 27 demethylase, acts as a critical switch to activate the cardiac developmental program. *Dev. Cell* **22,** 25–37 (2012).

36. Estarás, C. *et al.* Genome-wide analysis reveals that Smad3 and JMJD3 HDM co-activate the neural developmental program. *Development* **139,** 2681–91 (2012).

37. Li, Q. *et al.* Stage-dependent and locus-specific role of histone demethylase Jumonji D3 (JMJD3) in the embryonic stages of lung development. *PLoS Genet.* **10,** e1004524 (2014).

38. Agger, K. *et al.* UTX and JMJD3 are histone H3K27 demethylases involved in HOX gene regulation and development. *Nature* **449,** 731–734 (2007).

39. Simon, M. C. & Keith, B. The role of oxygen availability in embryonic development and stem cell function. *Nat. Rev. Mol. Cell Biol.* **9,** 285–96 (2008).

40. Ufer, C. & Wang, C. C. The Roles of Glutathione Peroxidases during Embryo Development. *Front. Mol. Neurosci.* **4,** 12 (2011).

41. Chang, S. *et al.* Hypoxic reprograming of H3K27me3 and H3K4me3 at the *INK4A* locus. *FEBS Lett.* (2016). doi:10.1002/1873-3468.12375

42. Hopkinson, R. J. *et al.* 5-Carboxy-8-hydroxyquinoline is a broad spectrum 2-oxoglutarate oxygenase inhibitor which causes iron translocation. *Chem. Sci.* **4,** 3110 (2013).

43. Koivunen, P., Hirsilä, M., Günzler, V., Kivirikko, K. I. & Myllyharju, J. Catalytic properties of the asparaginyl hydroxylase (FIH) in the oxygen sensing pathway are distinct from those of its prolyl 4-hydroxylases. *J. Biol. Chem.* **279,** 9899–904 (2004).

44. Walport, L. J. *et al.* Human UTY(KDM6C) is a male-specific Nϵ-methyl lysyl demethylase. *J. Biol. Chem.* **289,** 18302–13 (2014).

45. Calvin, S., Calvin, J. E., Wang, J., Jacobsen, L. & Pitz, S. FuGENE®HD Transfection Reagent: Choice of a Transfection Reagent with Minimal Off-Target Effect as Analyzed by Microarray Transcriptional Profiling. *Nat. Methods | Appl. Notes, Publ. online 17 Oct. 2006; | doi10.1038/an2079* (2006). doi:10.1038/an2079

46. Hatch, S. B. *et al.* Assessing histone demethylase inhibitors in cells: lessons learned. *Epigenetics Chromatin* **10,** 9 (2017).

47. Pathak, R. R. Small size sampling. *http://www.ijbcp.com/?mno=27649* (2012).

48. Walport, L. J. *et al.* Human UTY(KDM6C) is a male-specific Nϵ-methyl lysyl demethylase. *J. Biol. Chem.* **289,** 18302–13 (2014).

49. Hong, S. *et al.* Identification of JmjC domain-containing UTX and JMJD3 as histone H3 lysine 27 demethylases. *Proc. Natl. Acad. Sci. U. S. A.* **104,** 18439–44 (2007).

50. Kristensen, J. B. L. *et al.* Enzyme kinetic studies of histone demethylases KDM4C and KDM6A: towards understanding selectivity of inhibitors targeting oncogenic histone demethylases. *FEBS Lett.* **585,** 1951–6 (2011).

51. Kamikawa, Y. & Donohoe, M. The localization of histone H3K27me3 demethylase Jmjd3 is dynamically regulated. *Epigenetics* **9,** (2014).

52. Thienpont, B., Galle, E. & Lambrechts, D. TET enzymes as oxygen-dependent tumor suppressors: exciting new avenues for cancer management. *Epigenomics* **8,** 1445–1448

(2016).

53. Thienpont, B. *et al.* Tumour hypoxia causes DNA hypermethylation by reducing TET activity. *Nature* **537,** 63–68 (2016).

54. Czibik, G., Steeples, V., Yavari, A. & Ashrafian, H. Citric acid cycle intermediates in cardioprotection. *Circ. Cardiovasc. Genet.* **7,** 711–9 (2014).

Chapter 4. Inhibition of KDM6B activity by tricarboxylic acid intermediates

4.1 Introduction

The tricarboxylic acid (TCA) cycle, also known as the citric acid cycle or Krebs cycle, is the principle biochemical hub in cellular energy metabolism. Pyruvate derived from glycolysis enters the cycle and undergoes eight sequential redox reactions producing $FADH_2$, NADH and ATP in addition to various metabolites used in biosynthesis.

It is well established that hypoxia causes changes to the concentration of TCA cycle intermediates.[1,2] This arises due to changes in metabolite and cofactor concentrations resulting from anaerobic metabolism, causing antegrade flow through several TCA cycle steps and accumulation of TCA cycle intermediates, in particular succinate and fumarate.[3] Hypoxic intramitochondrial succinate levels as high as 6mM have been recorded, and increased succinate levels have been demonstrated in various contexts including cerebral ischemia, hypoxic cardiomyocytes and in the tissues of diving animals.[4–6] L-2-hydroxyglutarate (L-2HG) is , in part, produced by the enzymatic reduction of 2OG by lactate dehydrogenase A (LDHA) driven by increased expression of LDHA under hypoxia, and increased availability of 2OG and NADH cofactor.[7]

Both loss and gain of function mutations of TCA cycle enzymes result in the accumulation of the so-called oncometabolites fumarate, succinate and D-2-hydroxyglutarate (D-2HG).[8–10] Loss of function mutations of fumarate hydratase (FH) and succinate dehydrogenase (SDH) increase the concentration of fumarate and succinate respectively to high intracellular concentrations.[11] Similarly gain of function mutations to isocitrate dehydrogenase 1 and 2 (IDH1/2) lead to the catalytic conversion of 2OG to D-2HG.[8,9]

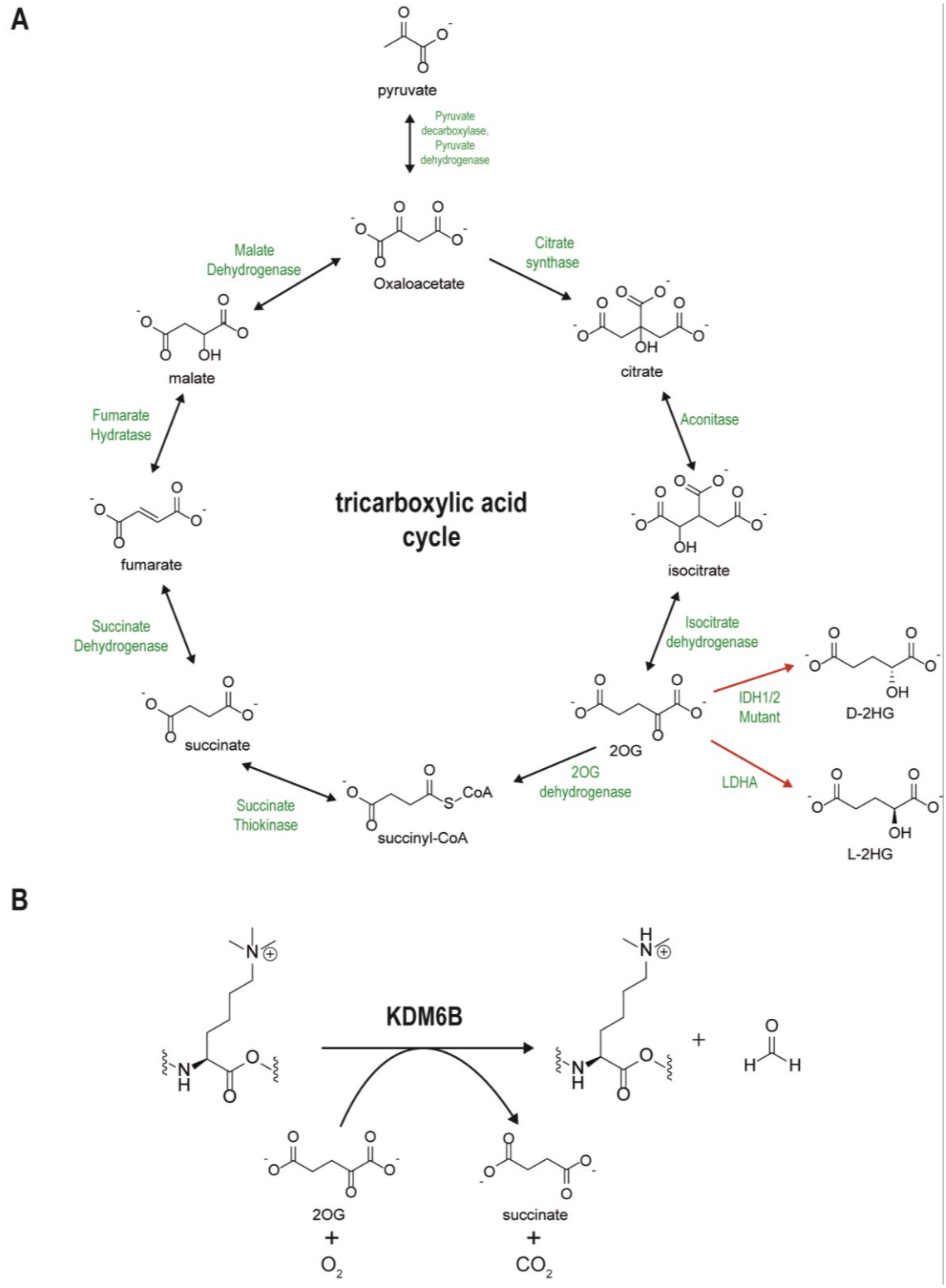


Figure 4.1 *Schematic representation of the TCA cycle. Enzymes labelled in green.* ***B****. KDM6B catalysed demethylation of H3K27Me3.*

Of the TCA cycle intermediates, 2OG and succinate are the co-substrate and co-product in 2OG oxygenase catalysis (TCA metabolite structures and 2OG oxygenase mechanism

shown above, Figure 4.1). Because of their structural similarity to 2OG, the TCA cycle intermediates and related metabolites have the potential to inhibit 2OG oxygenases. A number of studies have characterised the inhibition of different 2OG oxygenase families by TCA intermediates including the HIF prolyl hydroxylases, histone demethylases and Ten-eleven translocation enzymes (TETs) (Table 4.4).[12,13] Inhibition of the HIF prolyl hydroxylases and the consequent stabilisation of HIF results in a pro-oncogenic pseudo-hypoxic response mediated by HIF.[14–16] TET inhibition by succinate and fumarate has been shown to modulate the expression of HIF target genes, demonstrating the potential for a link between cellular metabolism and epigenetic regulation.[2]

Preliminary *in vitro* data established in Chapter 3 indicated that oxygen availability is rate limiting with respect to KDM6B activity both *in vitro* and in cells. Various TCA cycle intermediates (TCAI) are known to reach high intracellular concentration under hypoxia, and enzyme inhibition by these compounds has been demonstrated for other 2OG oxygenases. It is possible that inhibition by TCAI could contribute to the loss of KDM6B activity seen in hypoxia.

4.1.1 Chapter aims

The aim of this chapter is to characterise the inhibition of KDM6B by TCAI utilising both biochemical *in vitro* assays and cellular immunofluorescence assays. A panel of seventeen TCAI and related metabolites were first screened using the AlphaScreen inhibition assay. The IC_{50} values of selected TCAI where then further evaluated using AlphaScreen and an MALDI-MS inhibition assay. Finally, a selection of these compounds was tested in the cellular immunofluorescence activity assay, as described in the previous chapter.

KDM6B used in the AlphaScreen inhibition assay was provided by the Structural Genomics Consortium. The AlphaScreen inhibition assay was adapted from the established protocol optimised for this protein batch by Dr Anthony Tumber.

4.2 AlphaScreen™ inhibition assay

The Amplified Luminescent Proximity Homogeneous Assay (AlphaScreen™) is a high throughput luminescence assay technology which has been adapted to allow the study of KDM6B activity and inhibition. KDM6B is incubated with Fe^{2+} (ferrous ammonium sulphate), ascorbate, 2OG and biotinylated H3K27Me3 peptide before being quenched. The production of H3K27Me2 is then quantified using the AlphaScreen™ luminescence bead system.

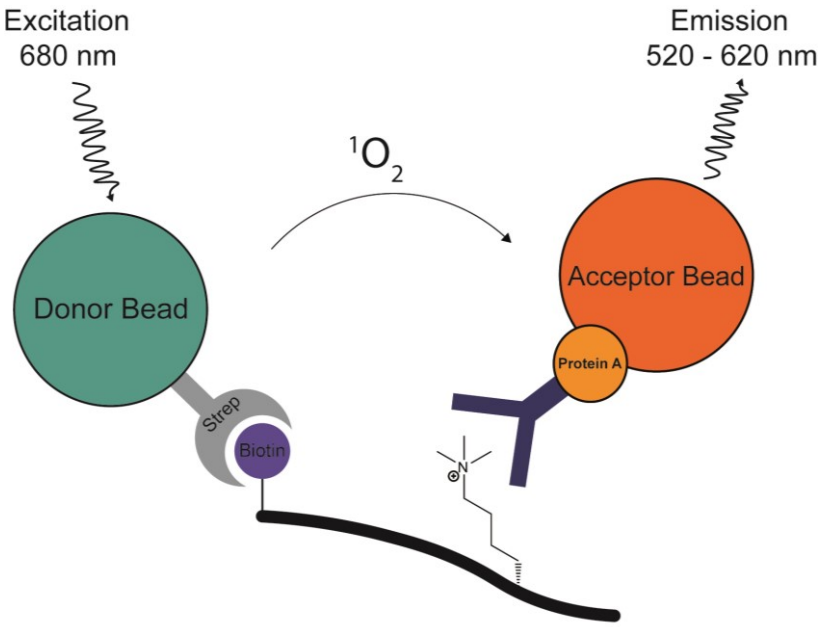


Figure 4.2 AlphaScreen peptide turnover assay principle. *The assay uses a methyl-state-specific antibody to detect H3K27Me2 peptide produced by catalytic demethylation of H3K27Me3 peptide by KDM6B. Using an AlphaScreen IgG detection kit (streptavidin-coated donor beads and protein-A-coated acceptor beads), interaction of antibody with biotinylated peptide can be detected. On excitation, donor beads emit singlet oxygen, which is quenched by the acceptor bead, leading to emission of light.*

Donor beads, coated in streptavidin, bind the biotinylated peptide. Acceptor beads bind specifically to H3K27Me2 peptide via a methyl-state-specific antibody, bringing acceptor and donor beads in to close proximity in the presence of H3K27Me2 peptide. Donor

beads contain a photosensitiser which convert dissolved O_2 to $^1O_2$ when excited at 680 nm. The $^1O_2$ then transfers energy to acceptor beads catalysing emission at 520-630 nm. In this way luminescence can be used to quantify the production of H3K27Me2 (Figure 4.2).

4.2.2 Screening of TCAI by KDM6B AlphaScreen™ inhibition assay

An AlphaScreen™ assay protocol was previously established for KDM6B by Dr Anthony Tumber (Structural Genomic Consortium, University of Oxford). KDM6B from the same protein batch used to establish the assay was kindly gifted and utilised in the studies below, allowing use of the established assay conditions.

A panel of seventeen TCAI and related metabolites were selected according to inhibition data available for other histone demethylases and screened against KDM6B using an adapted form of the KDM6B AlphaScreen™ assay. KDM6B was pre-incubated with compound (15 minutes, 22°C), prior to initiation of the reaction with Fe^{2+} (ferrous ammonium sulphate), 2OG, ascorbate and biotinylated H3K27Me3 peptide at the concentrations indicated (Table 4.1). After incubation (10 minutes, 22°C), the reaction was quenched using a solution of ethylenediaminetetracetic acid (EDTA) and NaCl (30 mM EDTA, 1600 mM NaCl). The amount of H3K27Me2 produced was detected using the AlphaScreen antibody-bead system, as described in the previous chapter. As previous studies demonstrated that TCA cycle inhibitors are competitive for 2OG,[12,17] the concentration of 2OG in the assay was kept at a concentration corresponding to the K_M(2OG) for KDM6B, as determined MALDI-MS (8.2 +/- 1 μM by MALDI-MS, Walport *et al*,[18]).

Component	Concentration
KDM6B	0.1 nM
2OG	10 μM
Fe^{2+}	10 μM
Ascorbate	100 μM
H3K27Me3 peptide	60 nM

Table 4.1. *Reaction conditions used in MALDI-MS inhibition assays.*

Initially, dimethyl sulfoxide (DMSO) compound stocks were prepared so that results if the AlphaScreen could be directly compared with previous AlphaScreen results for small molecule inhibitors. However, many of the TCA cycle intermediates tested are poorly soluble or insoluble in DMSO, and so buffered, pH-adjusted aqueous stock solutions (pH 7.5) were used instead for compound dosing. These stocks were used to prepare 3-fold serial dilutions in assay buffer yielding a final concentration range of 20 mM -19 μM. IOX1, a known KDM6B inhibitor with an (IC_{50} 0.2 μM, Chapter 1) was dosed at 100 μM and used as the 100% inhibition control wells, whilst buffer only was dosed in to the active control wells. The 100% inhibition control wells were used to measure background fluorescence in the assay which is subtracted from the signal of all other wells. Activity was then normalised against the active control wells. Every assay included each inhibitor concentration in duplicate, and each assay was carried out in triplicate. The resulting six replicates were then used in calculation of IC_{50} values and 95% confidence intervals using nonlinear regression with normalized dose–response fit on GraphPad® Prism, listed below (Figure 4.3, Table 4.2). (Additional IC_{50} curves of the remaining TCAI tested are included in Appendix 6).

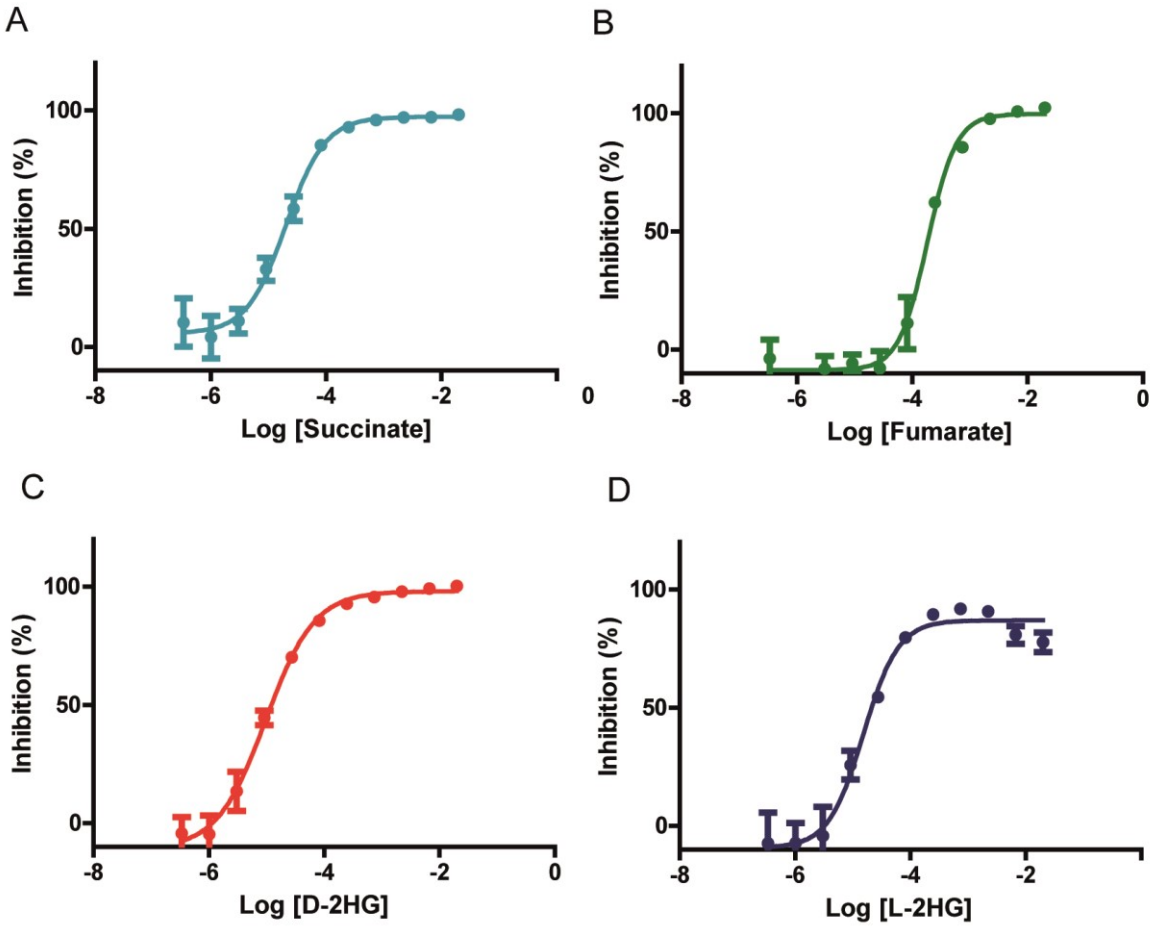
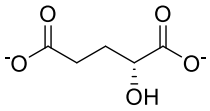
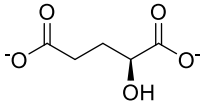
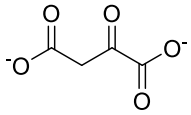
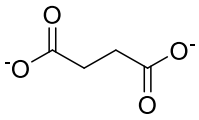
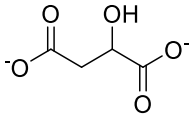
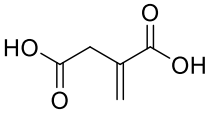
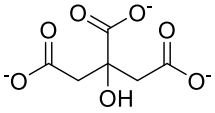
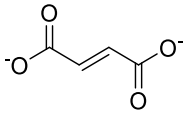
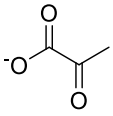
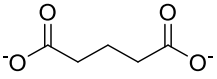
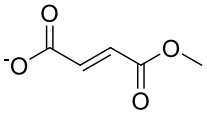
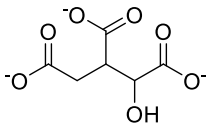
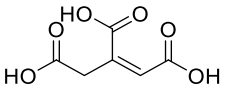


Figure 4.3. *Representative Inhibition of KDM6B by TCAI, determined by AlphaScreen assay. Assay conditions: 0.1 nM KDM6B, 60nM biotinylated H3K27Me3 peptide, 10µM Fe^{2+}, 13 µM 2OG, 100 µM Ascorbate. KDM6B was pre-incubated with inhibitor (10 minutes, 22°C) prior to reaction (15 minutes, 22°C) IC_{50} value for oxaloacetate determined using pre-quenched assay wells in place of IOX1 inhibitor control for background fluorescence determination. IC_{50} values and 95% confidence intervals calculated using nonlinear regression with normalized dose–response fit on Prism GraphPad®. IC_{50} values calculated using N=6 data set. Data = mean Error bars represent STDERR. N=2 technical repeats, N=3 biological repeats.*

Compound	Structure	IC_{50} /μM	95% CI /μM
D-2HG		9.7	7.1 to 13
L-2HG		15	11 to 22
Oxaloacetate		20	16 to 24
Succinate		20	15 to 28
L-Malate		55	37 to 83
Itaconic acid		80	61 to 105
Citrate		86	41.3 to 177
Fumarate		180	150 to 230
Pyruvate		210	160 to 270
Glutarate		270	200 to 360
Monomethylf umarate		300	220 to 410
Isocitrate		330	210 to 500
cis-aconitic acid		550	350 to 860

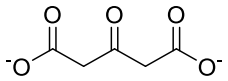
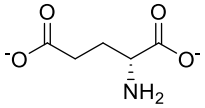
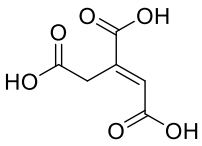
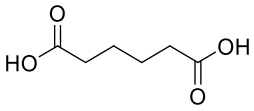
Compound	Structure	IC_{50} /μM	95% CI /μM
3-OG		820	530 to 1300
D-Glutamate		900	480 to 1700
Trans-acontitic acid		930	770 to 1120
Adipic acid		4000	1100 to 14300

Table 4.2. Table of IC_{50} values of TCA cycle intermediates against KDM6B, determined by AlphaScreen assay. *Assay conditions: 0.1 nM KDM6B, 60nM biotinylated H3K27Me3 peptide, 10μM Fe^{2+}, 13 μM 2OG, 100 μM Ascorbate. KDM6B was pre-incubated with inhibitor (10 minutes, 22°C) prior to reaction (15 minutes, 22°C). IC_{50} value for oxaloacetate determined using pre-quenched assay wells in place of IOX1 inhibitor control for background fluorescence determination. IC_{50} values and 95% confidence intervals calculated using nonlinear regression with normalized dose–response fit on Prism GraphPad®. IC_{50} values calculated using N=6 data set. N=2 technical repeats, N=3 biological repeats.*

KDM6B activity was inhibited, to varying degrees, by many of the compounds tested. D-2HG, L-2HG, oxaloacetate and succinate were found to be the most potent inhibitors with IC_{50} values of 9.7, 15, 20 and 20 μM respectively. These results indicate that reduction of KDM6B activity seen in hypoxia could potentially be in part caused by inhibition by TCA cycle intermediates, such as succinate, whose cellular concentration has been found to be increased in hypoxia.[4–6] Succinate is the by-product of KDM6B catalysed histone lysine demethylation, and so it is possible that product inhibition of KDM6B may occur. D-2HG and L-2HG have been found to inhibit a number of 2OG oxygenases with varying degrees of potency. There is some evidence that D-2HG and L-2HG may have differential potencies due to their altered binding/stereochemistry,[13] but the AlphaScreen results for KDM6B do not indicate such differential inhibition for KDM6B.

4.3 Evaluation of TCAI inhibitors using a MALDI-MS inhibition assay

An orthogonal mass spectrometry based assay was used to further validate the most potent TCAI identified by the AlphaScreen. To this end, the MALDI-MS activity assay described in Chapter 1 was adapted for the study of enzyme inhibition. Recombinant *N*-His_6-TRX-tagged $KDM6B_{1141-1641}$ (purification detailed in Chapter 2, Section 2.5) was utilised. A pre-incubation step, where compound and enzyme are incubated together prior to initiation of reaction was included. The purpose of this step is to allow compounds to reach a binding equilibrium with the enzyme; slow-binding compounds might otherwise appear not to inhibit. A time course was conducted to determine the linear range of the reaction (Figure 4.4) after a 10-minute preincubation of the enzyme at 22°C. KDM6B (1µM) was pre-incubated with buffer (10 minutes, 22°C) prior to initiating the reaction with the addition of Fe^{2+} (ferrous ammonium sulphate), 2OG, ascorbate and H3K27Me3 21mer peptide at the indicated concentrations (Table 4.3). At each time point, the reaction was quenched by addition of 1:1 volume of methanol. Choosing an incubation time within the linear range of the reaction ensures that substrate concentration does not become limiting, product inhibition does not affect reaction rate and the enzyme has not become inactivated. An incubation time of 4 minutes was selected as being within the linear range (Figure 4.4).

Component	Concentration /µM
KDM6B	1
2OG	10
Fe^{2+}	10
Ascorbate	100
H3K27Me3 peptide	20

Table 4.3. *Reaction conditions used in MALDI-MS inhibition*

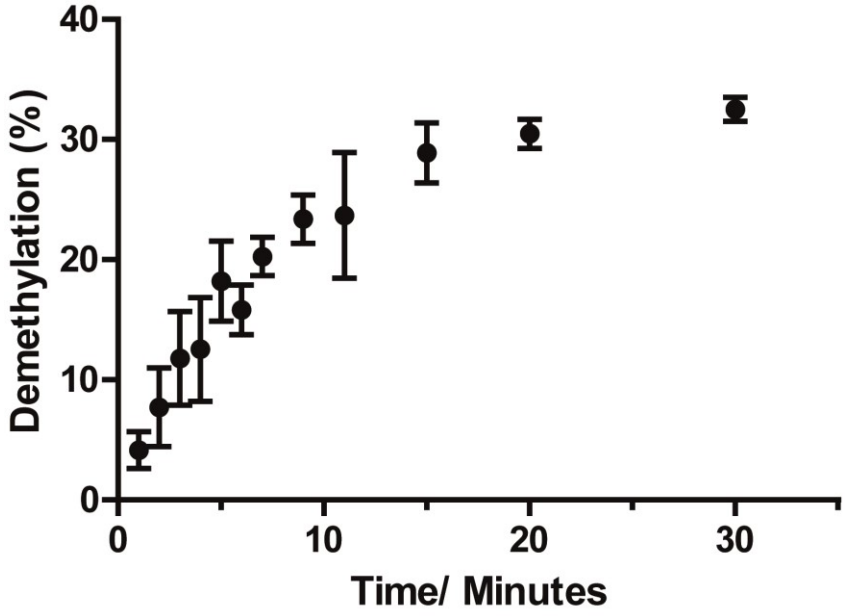
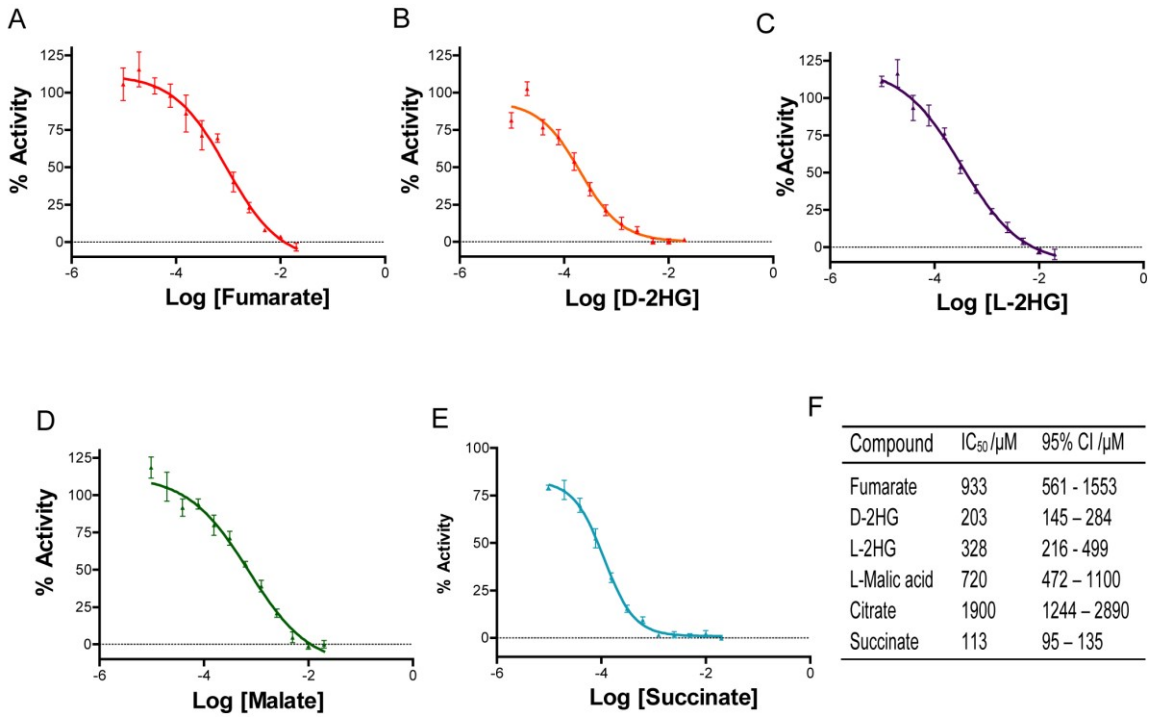


Figure 4.4. *Time course analysis of KDM6B demethylation of H3K27me3 by MALDI-TOF MS. Percentage demethylation (%) of H3K27Me3 21mer peptide plotted versus time. Assay conditions: 1 µM KDM6B Fe^{2+}(10 µM), 2OG (10 µM), ascorbate (100 µM) and H3K27Me3 21mer peptide (20 µM) in 50 mM HEPES 50 mM NaCl pH 7.5. KDM6B was pre-incubated with inhibitor (10 minutes, 22°C) prior to reaction (22°C) and quenched with methanol at each time point. Error bars represent standard deviation, N=3 technical repeat.*

As discussed above, 2OG-competitive inhibition and binding of TCA cycle intermediates at the 2OG binding site has been observed in KDM5B. Therefore, a 2OG concentration of 10 µM, near KDM6B K_m for 2OG, was used in activity assays. The following protocol was then used in inhibition studies; KDM6B was pre-incubated with compound (10 minutes, 22°C) prior to initiating the reaction with the addition of Fe^{2+} (ferrous ammonium sulphate), 2OG, ascorbate and H3K27Me3 21mer peptide at the concentrations indicated above (Table 4.3). After 4 minutes, the reaction was quenched with 1:1 volume of methanol. Quenched samples were spotted 1:1 with CHCA matrix on a MALDI plate and dried prior to analysis by MALDI-TOF mass spectrometry.

Every assay included each inhibitor concentration in triplicate, and each assay was carried out in duplicate. The resulting six replicates were then used in calculation of IC_{50} values and 95% confidence intervals using nonlinear regression with normalized dose–response fit on GraphPad® Prism, listed below (Figure 4.5).



Compound	IC_{50}/μM	95% CI /μM
Fumarate	933	561 - 1553
D-2HG	203	145 – 284
L-2HG	328	216 - 499
L-Malic acid	720	472 – 1100
Citrate	1900	1244 – 2890
Succinate	113	95 – 135

Figure 4.5. Inhibition of KDM6B by TCAI. A. *fumarate,* ***B.*** *D-2HG,* ***C.*** *L-2HG,* ***D.*** *malate,* ***E.*** *succinate,* ***F.*** *Table of IC_{50} values. Assay conditions: 1 μM KDM6B Fe^{2+}(10 μM), 2OG (10 μM), ascorbate (100 μM) and H3K27Me3 21mer peptide (20 μM) in 50 mM HEPES 50 mM NaCl pH 7.5. KDM6B was pre-incubated with inhibitor (10 minutes, 22°C) prior to reaction (22°C) and quenched with methanol (1 volume) after 4 minutes reaction incubation. IC_{50} values and 95% confidence intervals calculated using nonlinear regression with normalized dose–response fit on Prism GraphPad®. IC_{50} values calculated using Data = mean. Error = STDERR. N=6 data set. N=3 technical repeats, N=2 biological repeats.*

A much higher peptide concentration (>300 fold) is required in the MALDI-MS assay as the technique has a much lower detection limit. However, MALDI-MS allows direct measurement of H3K27Me3 demethylation, which confirms that the inhibition observed in the AlphaScreen assay is not only due to intereference with the detection beads, antiobody/peptide binding etc. As a result of this increased peptide concentration, a higher KDM6B concentration is required to achieve sufficicent demethylation detection by MALDI-MS. Overall this results in higher IC_{50} values obtained using the MALDI-MS versus the AlphaScreen assay, however, although the values obtained differ by order of magnitude, the trend in inhibition is consistent between the two assays. Succinate, D-2HG and L-2HG, were found to be the most potent inhibitors with IC_{50} values of 113, 203 and 328 μM respectively, a consistent trend with the KDM6B AlphaScreen results. Further

characterisation of other potent TCAI inhibitors, such as oxaloacetate, could not be undertaken due to failure of MALDI-MS equipment.

4.4 Efforts towards establishment of alternate KDM6B activity assays

Full characterisation of TCAI inhibition of KDM6B was frustrated by repeated break down of MALDI-MS equipment. In addition to the significant delays caused by extended instrument down time, the quality of spectra acquired using the instrument during periods of operation significantly declined over time (Figure 4.6). This led to an increased time required to obtain spectra of sufficient quality for accurate quantification of relative peak intensities.

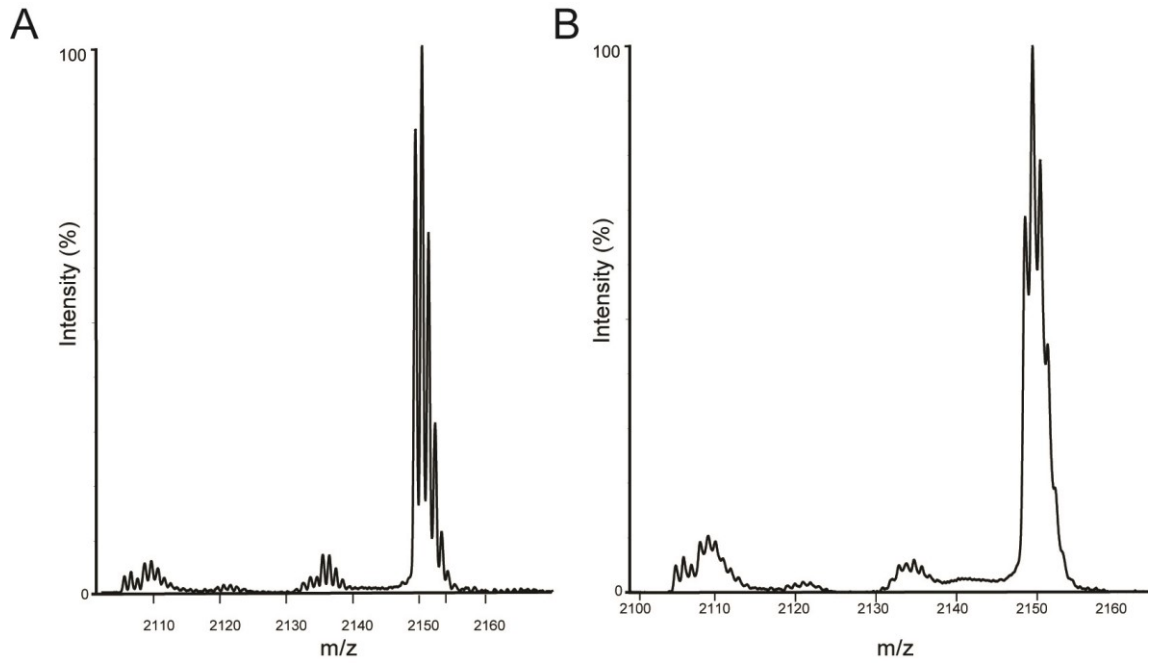


***Figure 4.6. Representative MALDI-MS spectra**. Assay conditions: 1 µM KDM6B Fe^{2+}(10 µM), 2OG (10 µM), ascorbate (100 µM) and H3K27Me3 21mer peptide (20 µM) in 50 mM HEPES 50 mM NaCl pH 7.5. KDM6B was pre-incubated with inhibitor (10 minutes, 22°C) prior to reaction (4 minutes, 22°C) and quenched with methanol (1 volume). **A.** MALDI-MS spectrum with isotopic resolution of H3K27Me3/2 peptide masses. **B.** Representative oversaturated MALDI-MS spectra showing loss of isotopic resolution of peaks and baseline distortion.*

After a time, the quality of spectra was reduced considerably further, such that accurate quantification was no longer possible. As no alternative MALDI-MS equipment was available, alternative mass spectrometry methods for quantification of histone peptide

activity assays were explored. Preliminary experiments were undertaken to adapt a RapidFire™ mass spectrometry assay for KDM6B from the literature. As in the MALDI-MS assay, after chromatography step, relative amounts of K27Me3 peptide and its demethylation products are quantified using mass spectrometry. Samples are loaded to a C18 solid phase extraction cartridge using an auto sampler, before being eluted and applied directly to the ion source. Time course assays were run using 21mer H3K27Me3 peptide and a shorter 16mer peptide, as used in the literature RapidFire™ protocol. Reaction was initiated by mixing equal volumes of a 2x substrate mix containing Fe^{2+} (ferrous ammonium sulphate) (20 μM), 2OG (20 μM), ascorbate (200 μM) and peptide (various) and a 2x KDM6B (various) solution. Samples were quenched at each time point by addition of 0.5 volumes of trifluoracetic acid (0.5%). Less than 10% demethylation of the 16mer peptide was seen at 200nM KDM6B after 45 minutes (Figure 4.7). As with MALDI-MS, it is important to have sufficient product turn over such that the proportion of product versus starting material can be determined. However, when an increased KDM6B concentration of 1 μM was used, significant ion suppression was seen, reducing the ion count below quantifiable levels (data not shown).

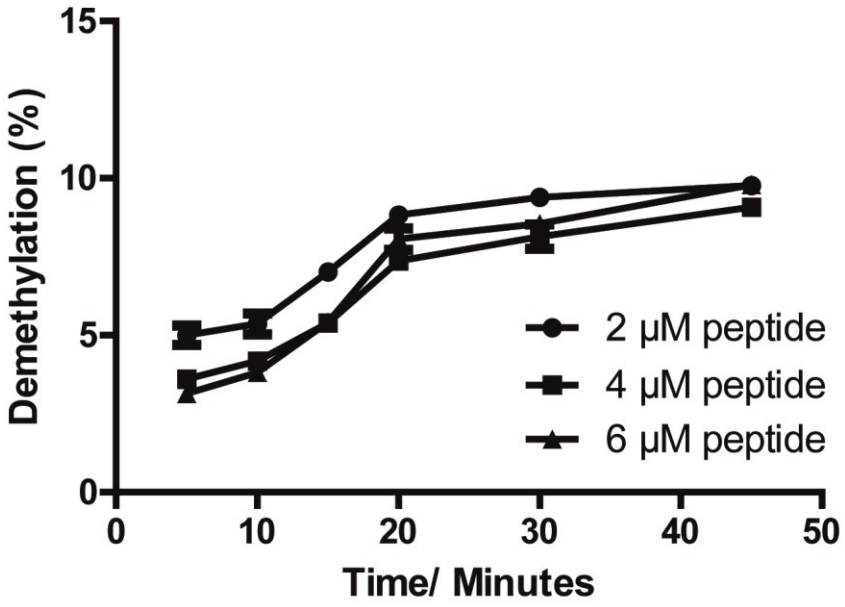


Figure 4.7. *Time course analysis of KDM6B demethylation of H3K27me3 by RapidFire MS. Assay conditions: KDM6B (200 nM), Fe^{2+}(10 µM), 2OG (10 µM), ascorbate (100 µM) and H3K27Me3 21mer peptide (20 µM) in 50 mM HEPES 50 mM NaCl pH 7.5. Reaction (22°C) was quenched with addition of 0.5 volumes of trifluoracetic acid (0.5%) at each time point. Percentage demethylation (%) of H3K27Me3 16mer peptide plotted versus time. Error bars represent standard deviation, N=3 technical repeats.*

Finally, attempts were made to utilise a FDH coupled assay. Formaldehyde released from the demethylase reaction is converted to formic acid by FDH. This oxidation is coupled to the reduction of NAD^+ to NADH, the concentration of which can be monitored by fluorescence spectroscopy. Attempts to utilise this assay were delayed by difficulty in producing sufficient active, TRX tag cleaved KDM6B (further discussed in Chapter 2).

Break down of MALDI-MS equipment prevented completion of the MALDI-MS studies of TCAI inhibition of KDM6B activity. The preliminary data set is encouraging, and the trend in inhibition seen in AlphaScreen assays correlates to inhibition in the MALDI-MS assay.

4.5 Cellular inhibition studies

The effect of TCAI inhibitors and 2OG on cellular KDM6B activity was then assessed using the immunofluorescence protocol discussed in Chapter 3.

COS-7 cells, transiently transfected with full length, N-terminally FLAG tagged KDM6B, and the catalytically inactive mutant (H1390A, MUT), were dosed with TCAI in order to assess their effect on KDM6B activity in cells. After 4 hours of transfection with the KDM6B plasmid the media was replaced, and 3-fold serial dilutions of the compounds were added. Cells were then incubated for a further 24 hours prior to fixing with 4% paraformaldehyde. Fixed cells were permeabilised and blocked prior to primary antibody staining overnight against H3K27Me3 and FLAG, and finally underwent secondary antibody staining and DAPI nuclear staining. Cell were imaged using a Perkin Elmer Operetta instrument, and the Harmony software was used to quantify nuclear Flag and H3K27Me3 fluorescence intensity.

Oxaloacetate, D-2HG and L-2HG were selected for testing as they were the most potent inhibitors *in vitro* (Section 4.2.2), and 2OG was tested to evaluate the effect of cellular KDM6B activity with increased 2OG. IOX1 was used as a positive control inhibitor on each plate. Since 2OG, D-2HG and L-2HG are poorly cell permeable owing to their polarity, cell permeable ester derivates di-methyl 2OG (dm-2OG) and n-octyl D/L-2HG (no-2HG) were utilised;[12,19] these esters undergo hydrolysis within the cell to release the desired acid. As in the *in vitro* experiments oxaloacetate was prepared as a pH-adjusted aqueous solution in 50mM HEPES pH 7.5, whereas dm-2OG and IOX1 stocks were prepared in DMSO and thus all wells contained a final concentration of 0.5 mM HEPES and 1% DMSO. Similarly, D-2HG and L-2HG were prepared in ethanol due to their increased solubility versus DMSO, and so all wells in this plate contained a final concentration of 1% ethanol and 1% DMSO.

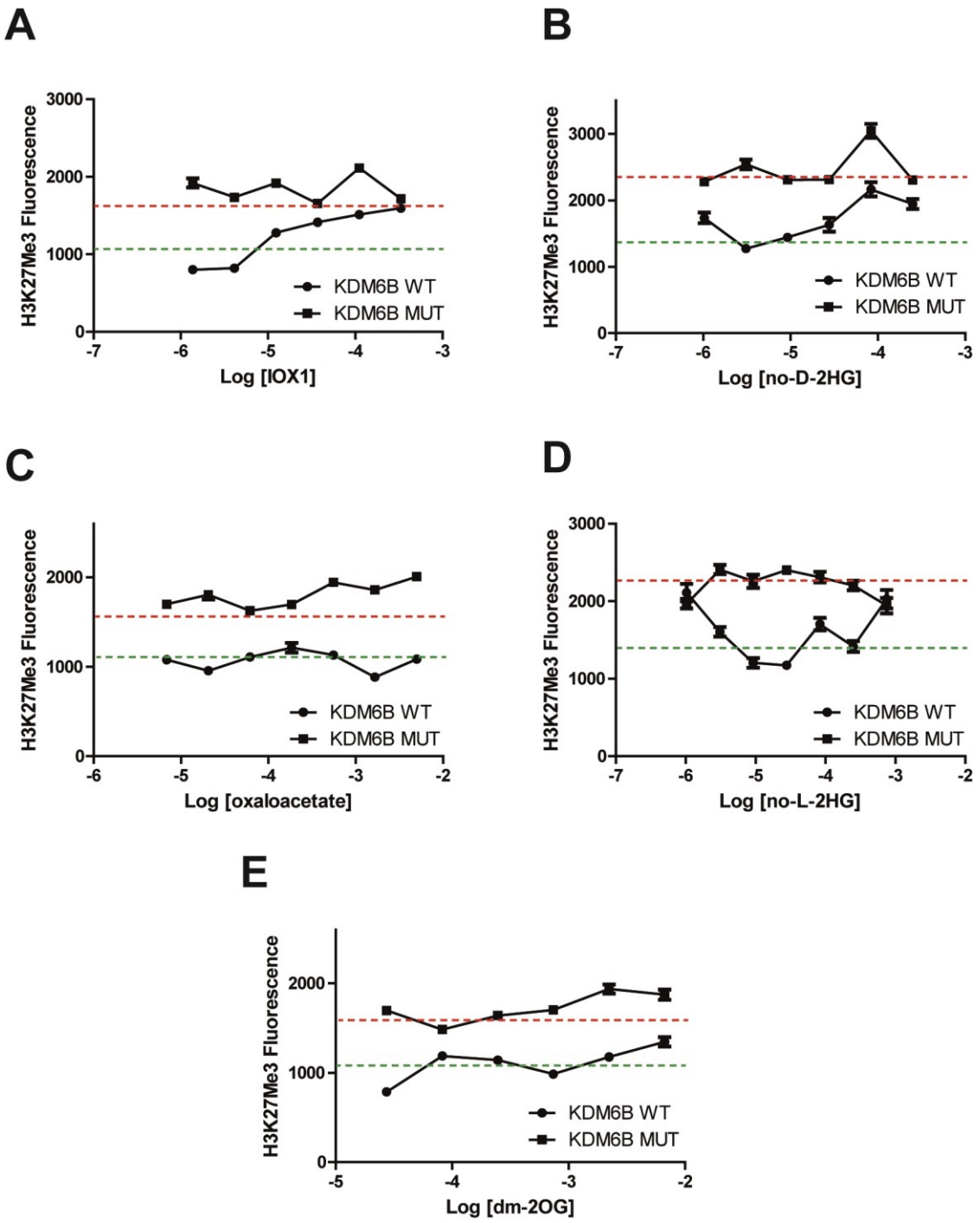


Figure 4.8. TCA cycle intermediate dosing fails to reduce cellular KDM6B activity. *H3K27Me3 fluorescence intensity of COS-7 cells overexpressing FLAG-tagged KDM6B WT and H1390A catalytically inactive variant (KDM6B MUT) versus Log[inhibitor]/M. Cells were treated with transfection reagent and plasmid (4 hours). The media was then replaced, and 3-fold serial dilutions of the compounds were added. Cells were then incubated for a further 24 hours prior to fixing with 4% paraformaldehyde.* ***A.*** *IOX1* ***B.*** *octyl-D-2HG* ***C.*** *oxaloacetate* ***D.*** *octyl-L-2HG* ***E.*** *dm-2OG. Dashed lines represent average H3K27Me3 fluorescence of vehicle treated WT (lower limit) and MUT (higher limit) controls. Data = mean, error bars represent standard error. N=1 biological replicate >141 cells per well.*

Cells transfected with WT KDM6B showed the expected decrease in H3K27Me3 fluorescence versus MUT KDM6B transfected cells and non-transfected control cells. Increased H3K27Me3 fluorescence was seen in the highest concentrations of octyl-D-2HG and octyl-L-2HG, indicating that these compounds could be inhibitory in a cellular context. However, further experiments are required to confirm these observations and to expand the concentration range tested with the aim of determining a cellular IC_{50} value. No decrease in H3K27Me3 was seen on dm-2OG dosing, indicating 2OG levels might be saturating in these conditions.

4.6 Discussion

Preliminary *in vitro* data established in Chapter 3 indicates that oxygen availability is rate limiting with respect to KDM6B activity both *in vitro* (Chapter 3, Figure 3.3) and in cells (Chapter 3, Figure 3.16). Various TCAI are known to reach high intracellular concentrations under hypoxia, and enzyme inhibition by these compounds has been demonstrated for other 2OG oxygenases. It is possible that inhibition by TCAI might contribute to loss of KDM6B activity in hypoxia. The aim of the work described in this chapter was to assess the inhibition of KDM6B by TCAI.

The effect of seventeen TCAI and related metabolites on KDM6B activity was evaluated using an AlphaScreen activity assay. Of these compounds, D-2HG, L-2HG, oxaloacetate and succinate were the most potent inhibitors with IC_{50} values of 9.7, 15, 20 and 20 μM respectively (KDM6B assay concentration 0.1 nM).

Further characterisation of six compounds, D-2HG, L-2HG, succinate, fumarate, malate and citrate, was undertaken using a MALDI-MS activity assay. This yielded IC_{50} values of 203, 328, 113, 933, 720 and 1900 μM, respectively (KDM6B assay concentrations 1μM). The MALDI-MS results confirmed that true inhibition of KDM6B had been

observed in the AlphaScreen assay, rather than interference of the assay setup. Unfortunately, further characterisation of the TCAI was frustrated by breakdown of the MALDI-MS equipment.

KDM6B activity was potently inhibited by succinate and L-2HG, and was inhibited to a much lesser degree by fumarate (IC_{50} values of 15, 20 and 180 μM respectively). Cellular succinate, fumarate and L-2HG concentrations are known to be increased in hypoxia.[3] This suggests that reduction of KDM6B in hypoxia could, at least in part, be due to increased concentration of inhibitory TCAI and metabolites. In order to explore this further, it would be interesting to determine whether dosing of dimethyl-2OG rescues hypoxic inhibition of cellular KDM6B activity.

The inhibitory effect of TCAI on 2OG oxygenase enzymes has been investigated in a number of studies (Table 4.4).

Enzyme	Enzyme conc./ μM	IC_{50} / μM				K_m^{app}(2OG)/ μM	IC_{50} method
		Succinate	Fumarate	D-2HG	L-2HG		
KDM4A	2[13]	NR	NR	24±2[13]	26±3[13]	6[13]	FDH
KDM4C	1[13]	NR	NR	79±7[13]	97±24[13]	4[13]	FDH
KDM4E	2[20]	320[20]	2.3[20]	NR	NR	13.2[21]	FDH
KDM2A	2[13]	NR	NR	106±22[13]	48±15[13]	12.5[13]	FDH
FIH	1[13]	NI	NI	1500±400[13]	189±34[13]	110±20[22]	FDH
ABH2	2[13]	NR	NR	424±77[13]	150±20[13]	10[13]	FDH
TET1	NR	540±100[2]	390±160[2]	4000[23]	1000[23]	55±20[2]	Radiometric assay
TET2	NR	570±190[2]	400±70[2]	5000[23]	1600[23]	60±15[2]	Radiometric assay
KDM5B	0.6[12]	62±19[12]	210±80[12]	203±90[12]	150±40[12]	2.6±0.6[12]	MALDI- MS
KDM3A	250nM[24]	NR	NR	169 (95% C.I 77-373)[24]	300 (188-478) [24]	30±10[24]	MALDI- MS
PHD2	0.5[13]	19	3	7300±3300[13]	419±150[13]	13±2[22]	MALDI- MS
BBOX	0.025[13]	NR	NR	13200±1100[13]	142±30[13]	470[22]	NMR
KDM6B	1	113 (95 – 135)	933 (561 – 1553)	203 (145 – 284)	328 (216 – 499)	8.2 +/- 1 μM[18]	MALDI- MS

Table 4.4. *IC_{50} values of selected TCA cycle intermediates versus a number of 2OG oxygenases. Not inhibitory (NI), Not reported (NR). IC_{50} values quoted with 95% confidence intervals.*

Loss-of-function and gain-of-function mutations in the IDH1/2, SDH and fumarate hydratase enzymes occur with a high prevalence in various cancers including glioma, renal cell carcinomas and acute myeloid leukaemia. The consequent increase in the concentration of the oncometabolites L-2HG, D-2HG, succinate and fumarate stimulate tumorigenesis by inhibition of the HIF hydroxylases causing a pro-oncogenic pseudo-

hypoxic response. Inhibition of the histone demethylases by these oncometabolites may also contribute to pathogenesis by alteration of epigenetic regulation of gene expression. Inhibition of KDM6B by 2HG (both D-2HG and L-2HG with IC_{50} values of 203 μM and 328 μM respectively) was lower than that previously observed for KDM4A (IC_{50} values of 24 μM, 26 μM respectively), but was on par with KDM5B (IC_{50} values of 203 μM, 150 μM respectively) (Table 4.4). This differential inhibition of histone demethylases by D-2HG and L-2HG could have important implications for epigenetic gene regulation in these cancers.

Monomethyl fumarate (ALKS 8700, Alkermes) is a monomethyl fumarate prodrug which is currently undergoing phase III clinical trials as a novel oral treatment for relapsing multiple sclerosis, whilst dimethyl fumarate (Tecfidera, marketed by Biogen) is an approved first line treatment for multiple sclerosis. Dimethyl fumarate treatment has been shown to reduce NF-κB-mediated expression of proinflammatory cytokines in glial cells. Although monomethyl fumarate inhibits KDM6B activity only modestly, with an IC_{50} value of 296 μM, the potential for inhibition of other 2OG oxygenases, such as the HIF prolyl hydroxylases, could have important implications, especially considering dimethyl fumarate treatment has been shown to alter HIF levels and activity.[25]

Crystal structures and K_i determination for the most potent TCAI inhibitors of KDM5B demonstrated inhibitor binding within the 2OG binding site, consistent with the structural similarity between TCAI and 2OG (Figure 4.9). In KDM5B 2OG is coordinated to the active site metal in a bidentate manner. 2OG is stabilised within the active site by a number of interactions; hydrogen bonding between the C-1 2OG carboxylate group to Ser507 and C-5 carboxylate oxygen to Tyr425, electrostatic interactions between the C-5 carboxylate groups with Lys517, Asn509 and Tyr425 and hydrophobic interactions between C-3 and C-4 methylenes and the side chains of Trp514 and Phe496. Most of

these residues are conserved in the active site of KDM6B, with the exception of Phe 496, which is replaced with Thr1387, and Tyr425 which is replaced with Phe1328 and Lysine 517, where a significant shift of position is seen in the corresponding KDM6B Lysine1381 residue. The largest difference in observed IC_{50} values for KDM5B and KDM6B is in the IC_{50} of fumarate (IC_{50} values 210 μM versus 933 μM respectively). In KDM5B fumarate forms interactions with the hydroxyl group of Tyr425 which is not present in the Phe1328 of the KDM6B active site.

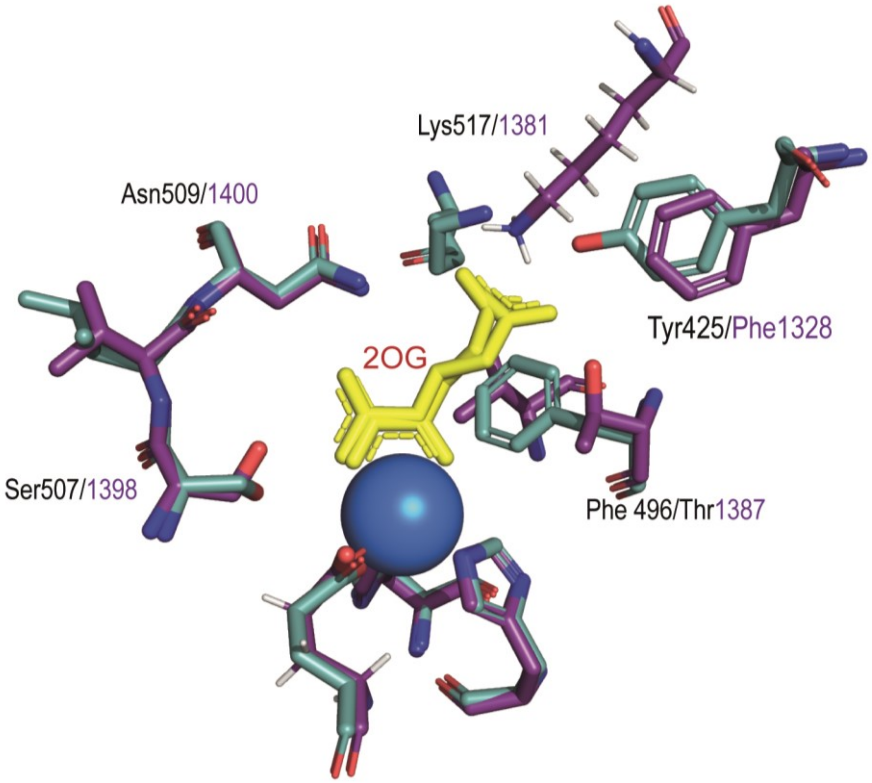


Figure 4.9. *Overlay of crystal structure of active sites of KDM5B and KDM6B (PDB ID: 5FUP, 2XUE) in complex with 2OG. Key 2OG binding residues in active site of KDM5B are shown as teal sticks, corresponding residues in active site of KDM6B are shown as purple sticks. 2OG shown as yellow sticks.* Fe^{2+} *centre shown as blue sphere.*

Overall none of the TCAI tested showed strong cellular inhibition of KDM6B. As the TCAI are likely to be 2OG-competative inhibitors, this lack of cellular inhibition could be due to saturating cellular 2OG concentrations. Consistent with this, no increase in KDM6B activity was seen when cells were treated with exogenous dm-2OG.

Cellular KDM6B inhibition was observed at the highest concentrations of octyl-D-2HG and octyl-L-2HG tested (750 μM); since intracellular D-2HG concentrations can reach up to mM levels it is possible that KDM6B inhibition occurs in IDH1/2 mutant tumour environments. Interestingly, no cellular inhibition of KDM6B was observed for oxaloacetate at any concentration despite the relatively high structural similarity between oxaloacetate, D-2HG and L-2HG. TCAI intermediate levels are at homeostasis within cells, raising the possibility that lack of cellular inhibition could be due to immediate sequestering of the dosed TCAI in to cellular TCA cycle pool. However, quantification of intracellular succinate concentration by ultra-performance liquid chromatography - tandem mass spectrometry (UPLC-MS/MS) undertaken by Laukka *et al*, showed 3-fold increase in cytosolic succinate concentration on dosing with dimethyl succinate, and 2-fold increase in cytosolic fumarate concentration on dosing with di-ethyl fumarate, indicating that this is not the case.[2]

In addition to variable inhibition by the TCAI across the KDMs, there is also variation in K_M^{app}(2OG) values which could impact 2OG-competative inhibition. KDM6B has a relatively low K_M^{app}(2OG) of 8.2 +/- 1 μM,[26] meaning KDM6B may be saturated with respect to 2OG under normal cellular conditions. As studies in KDM5B showed that TCAI inhibitors of JmjC-KDMs are likely to compete for the 2OG binding site,[12] fluctuation of cellular 2OG concentration is important when considering inhibition by the TCAI.

The results of this chapter demonstrate that multiple TCAI can inhibit KDM6B. It is possible that the cumulative concentration of multiple 2OG-competitive TCAI could overcome 2OG concentration depending on the flux of cellular metabolism. Further knowledge of the temporal concentration shifts of the TCAI and their localisation within the cell, for example through metabolomics, is needed to properly evaluate the

physiological relevance of the results of this chapter. As 2OG concentration may be reduced in hypoxia,[27] it would be of interest to compare cellular IC_{50} values determined in normoxia and hypoxia. Additionally, investigating the effect of combined dosing of TCAI at physiological concentrations would be of merit.

In vitro data described in this chapter demonstrated potent inhibition of KDM6B activity by several TCAI. It is possible that inhibition by TCAI contributes to hypoxic inhibition of KDM6B activity, though further work is needed to address this in a physiological context. Currently available data supports the potential of TCA cycle intermediates to regulate the activity of the 2OG oxygenases, which could have important implications for epigenetic gene regulation.

4.7 References

1. Chinopoulos, C. Which way does the citric acid cycle turn during hypoxia? The critical role of α-ketoglutarate dehydrogenase complex. *J. Neurosci. Res.* **91,** 1030–1043 (2013).
2. Laukka, T. *et al.* Fumarate and Succinate Regulate Expression of Hypoxia-inducible Genes via TET Enzymes. *J. Biol. Chem.* **291,** 4256–65 (2016).
3. Czibik, G., Steeples, V., Yavari, A. & Ashrafian, H. Citric acid cycle intermediates in cardioprotection. *Circ. Cardiovasc. Genet.* **7,** 711–9 (2014).
4. Cerebral metabolism in hypoxic hypoxia. II. Citric acid cycle intermediates and associated amino acids. *Brain Res.* **86,** 45–54 (1975).
5. Hochachka, P. W., Owen, T. G., Allen, J. F. & Whittow, G. C. Multiple end products of anaerobiosis in diving vertebrates. *Comp. Biochem. Physiol. B.* **50,** 17–22 (1975).
6. J.Folbergrova, B.Ljunggren, K.Norberg, B. K. S. Influence of complete ischemia on glycolytic metabolites, citric acid cycle intermediates, and associated amino acids in the rat cerebral cortex. *Brain Res.* **80,** 265–279 (1974).
7. Intlekofer, A. M. *et al.* Hypoxia Induces Production of L-2-Hydroxyglutarate. *Cell Metab.* **22,** 304–11 (2015).
8. Borger, D. R. *et al.* Frequent Mutation of Isocitrate Dehydrogenase (IDH)1 and IDH2 in Cholangiocarcinoma Identified Through Broad-Based Tumor Genotyping. *Oncologist* **17,** 72–79 (2012).
9. Paschka, P. *et al.* IDH1 and IDH2 Mutations Are Frequent Genetic Alterations in Acute Myeloid Leukemia and Confer Adverse Prognosis in Cytogenetically Normal Acute Myeloid Leukemia With *NPM1* Mutation Without FLT3 Internal Tandem Duplication. *J. Clin. Oncol.* **28,** 3636–3643 (2010).
10. Nowicki, S. & Gottlieb, E. Oncometabolites: tailoring our genes. *FEBS J.* **282,** 2796–2805 (2015).
11. Castro-Vega, L. J. *et al.* Germline mutations in FH confer predisposition to malignant pheochromocytomas and paragangliomas. *Hum. Mol. Genet.* **23,** 2440–2446 (2014).
12. Tarhonskaya, H. *et al.* Studies on the Interaction of the Histone Demethylase KDM5B with Tricarboxylic Acid Cycle Intermediates. *J. Mol. Biol.* **429,** 2895–2906 (2017).
13. Chowdhury, R. *et al.* The oncometabolite 2-hydroxyglutarate inhibits histone lysine demethylases. *EMBO Rep.* **12,** 463–9 (2011).
14. Yang, M., Soga, T., Pollard, P. J. & Adam, J. The emerging role of fumarate as an

oncometabolite. *Front. Oncol.* **2,** 85 (2012).

15. MacKenzie, E. D. *et al.* Cell-Permeating -Ketoglutarate Derivatives Alleviate Pseudohypoxia in Succinate Dehydrogenase-Deficient Cells. *Mol. Cell. Biol.* **27,** 3282–3289 (2007).

16. Hewitson, K. S. *et al.* Structural and Mechanistic Studies on the Inhibition of the Hypoxia-inducible Transcription Factor Hydroxylases by Tricarboxylic Acid Cycle Intermediates. *J. Biol. Chem.* **282,** 3293–3301 (2007).

17. Chowdhury, R. *et al.* The oncometabolite 2-hydroxyglutarate inhibits histone lysine demethylases. *EMBO Rep* **12,** 463–469 (2011).

18. Walport, L. J. *et al.* Human UTY(KDM6C) is a male-specific Nϵ-methyl lysyl demethylase. *J. Biol. Chem.* **289,** 18302–13 (2014).

19. Lu, C. *et al.* IDH mutation impairs histone demethylation and results in a block to cell differentiation. *Nature* **483,** 474–478 (2012).

20. Rose, N. R. *et al.* Inhibitor Scaffolds for 2-Oxoglutarate-Dependent Histone Lysine Demethylases. *J. Med. Chem.* **51,** 7053–7056 (2008).

21. Sakurai, M. *et al.* A miniaturized screen for inhibitors of Jumonji histone demethylases. *Mol. Biosyst.* **6,** 357–64 (2010).

22. Tarhonskaya, H. *et al.* Kinetic Investigations of the Role of Factor Inhibiting Hypoxia-inducible Factor (FIH) as an Oxygen Sensor. *J. Biol. Chem.* **290,** 19726–42 (2015).

23. Koivunen, P. *et al.* Transformation by the (R)-enantiomer of 2-hydroxyglutarate linked to EGLN activation. *Nature* **483,** 484–8 (2012).

24. Shamo Schiller, R. Unpublished data, D.Phil thesis. (2016).

25. Dimethyl fumarate inhibits the expression and function of hypoxia-inducible factor-1α (HIF-1α). *Biochem. Biophys. Res. Commun.* **448,** 303–307 (2014).

26. Walport, L. J. *et al.* Arginine demethylation is catalysed by a subset of JmjC histone lysine demethylases. *Nat. Commun.* **7,** 11974 (2016).

27. Chinopoulos, C. Which way does the citric acid cycle turn during hypoxia? The critical role of α-ketoglutarate dehydrogenase complex. *J. Neurosci. Res.* **91,** 1030–1043 (2013).

Chapter 5: Efforts towards a phenotypic cellular assay of foam cell formation

5.1 Introduction

Atherosclerosis is a chronic inflammatory disorder characterised by the formation of fatty plaques, or lesions, on blood vessel walls. These plaques can grow large enough to occlude blood flow, or break apart causing a blockage downstream. Either case can result in myocardial infarction or stroke, and atherosclerosis is fast becoming the leading cause of death and disability in the developed world.[1]

Atherosclerotic plaque development involves a number of steps (Figure 5.1).[2] Low density lipoprotein migrates from the blood in to vessel walls where it undergoes enzymatic and oxidative modification to form oxidised LDL (oxLDL). Activation of the vessel wall endothelium by oxLDL causes expression of adhesion molecules and recruitment of monocytes, which migrate in to the vessel wall and differentiate in to macrophages. These macrophages then take up oxLDL via scavenger receptors such as type A scavenger receptor and cluster of differentiation 36 (CD36),[3,4] becoming engorged lipid droplet-filled 'foam cells', which make up the core of an expanding atherosclerotic plaque. Macrophages produce proinflammatory cytokines and chemokines after stimulation with oxLDL particles or other proinflammatory stimuli in the plaque. Both lipid uptake and inflammatory signalling molecules are cytotoxic and cause the release of inflammatory mediators on apoptosis of the foam cells. These inflammatory mediators cause recruitment of even more monocytes, creating an inescapable trap.[5] Foam cell formation is thus a key step in the initiation and propagation of plaque development. Late stage atherosclerotic plaques become fibrotic, containing a necrotic core of dead foam

cells lined by a fibrous cap composed of smooth muscle cells. Eventually this cap fails, causing plaque rupture and thrombus formation.[6]

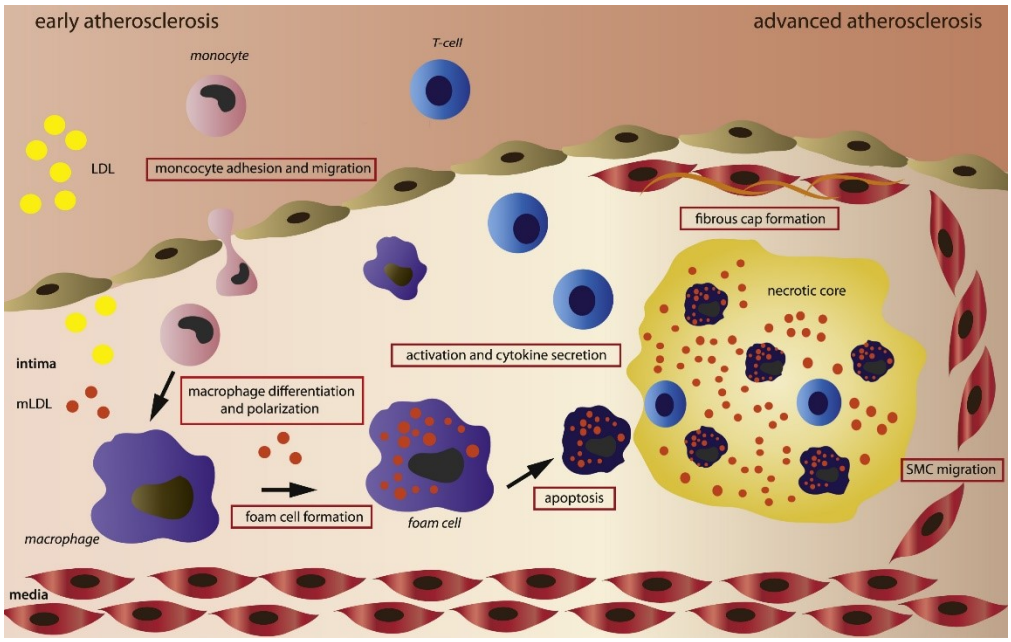


Figure 5.1 – Schematic representation of foam cell formation. *LDL undergoes enzymatic and oxidative modification in the intima of arteries leading to the formation of modified LDL (mLDL), also known as oxidised LDL (oxLDL). This results in endothelial activation and expression of adhesion molecules. Monocytes adhere to the activated endothelium and migrate into the intima where they differentiate into macrophages. These macrophages take up mLDL, forming foam cells. Ultimately in advanced atherosclerosis mLDL uptake results in cytotoxicity, apoptosis and necrotic core formation. Figure reproduced with permission from Neele et al Elsevier.* [2]

Immune cells such as monocytes and macrophages are constantly undergoing phenotypic change in response to binding of ligands such as cytokines, pathogen-associated molecular patterns (PAMPs) and lipids to membrane bound and nuclear receptors. This plasticity results from finely tuned control of gene activation and repression. It is well established that alterations in gene expression which regulate macrophage phenotypes are orchestrated largely by epigenetic regulation.[7–10]

Global DNA hypomethylation is characteristic of advanced atherosclerotic lesions and in human, rabbit and atherosclerosis-prone hyperlipidaemic apolipoprotein E (ApoE)-deficient mice.[11–13] Both hypo- and hypermethylation has been observed at inflammatory and atherogenic genes, whilst oxLDL induced hypermethylation of gene promotors by

DNMT1 and DNMT3b enhanced atherosclerosis in ApoE deficient mice.[14–16]Activation of inflammatory and atherogenic gene expression by HDACs is supported by a large body of data.[7] Broad spectrum HDAC inhibition has been shown to blunt inflammatory gene responses, but its effect on foam cell formation is controversial with both increased and unaltered foam cell formation observed.[17,18]

Though less well studied than DNA methylation and histone acetylation, alteration of histone methylation status in atherosclerosis is being increasingly reported. H3K4Me3, an activating mark, is increased at the promotor region of inflammatory genes on treatment of macrophages with oxLDL, and this increase was abrogated by pre-treatment with a broad spectrum histone methyl transferase inhibitor.[19] Several groups have identified reduction of global H3K27Me3 levels in atherosclerotic plaques.[20–22] Studies by Greißel et al showed that reduction of global H3K27Me3 correlated with disease severity, and was present in inflammatory cells within the plaque.[20,22] Monocytes isolated from patients with symptomatic atherosclerotic lesions displayed increased H3K4Me3 and decreased H3K27Me3 levels at the promotor of tumour necrosis factor α (TNF-α), a master regulator of inflammation.[23] KDM6B, which specifically demethylates H3K27Me3, has been extensively linked to inflammatory gene regulation,[24–26] and more tentatively, to atherosclerosis.[26–28] Inhibition of KDM6B by cell permeable inhibitor GSK-J4 was shown to reduce the proinflammatory response in macrophages.[29] KDM6B is induced in macrophages treated with the inflammatory mediator SAA resulting in a reduction of H3K27Me3 levels at the promotor regions of IL-23p19, G-CSF and TREM-1 and increased expression of these inflammation associated genes. Silencing of KDM6B using shRNA abrogates SAA induced inflammatory gene expression, and was also shown to prevent SAA enhancement of oxLDL stimulated foam cell formation.[26] Recently, KDM6B was identified as a novel regulator of the pro-fibrotic signature of peritoneal

foam cells.[28] In another study, macrophages depleted of KDM6B using specific shRNAs displayed compromised ability to generate foam cells in an infection model of foam cell formation, and KDM6B was found to regulate expression of scavenger receptor CD36 in this same model.[27] The role of other histone demethylases is currently not well established, although a recent publication reported upregulation of KDM4A in macrophages treated with oxLDL, resulting in KDM4A dependent induction of inflammatory cytokine expression.[30]

Atherosclerotic plaques have an expanding core made up of lipid droplet filled foam cells. Since oxygen has a diffusion limit of 100-200 μm in tissues, cells at the centre of the expanding plaque become hypoxic, and oxygen concentration can drop to below 1%. Hypoxia accelerates the progression of atherosclerosis by increasing inflammatory cytokine production, scavenger acceptor expression and the rate of foam cell formation. Inflammatory genes whose expression is upregulated in hypoxia include the KDM6B target genes CD36, IL-6 and TNF-α.[31–34] Hypoxia induced HIF-1α stimulates the expression of KDM3A, KDM4B, KDM4C, and KDM6B.[35] However, hypoxic inhibition of histone demethylase activity has been demonstrated for the KDM4 family in addition to other enzymes of this class.[36,35] Hypoxic inhibition of KDM6B has been shown to attenuate inflammatory responses by reducing catalytic activity and preventing removal of repressive H3K27Me3 by KDM6B.[37,38]

Epigenetic regulation is emerging as a key factor in the regulation and pathogenesis of inflammatory conditions such as atherosclerosis. Modification of the epigenetic status of macrophages has the potential to offer novel therapies for diseases including atherosclerosis, but a better understanding of the epigenetic mechanisms involved is required. This may help to rationalise the relationship between environmental factors, such as oxygen availability and nutrition, and atherogenesis.

4.1.1 Chapter Aims

The aim of the work described in this chapter was to establish a phenotypic cellular assay to allow the evaluation of the effect of cellular stimuli (e.g. hypoxia) and small molecular inhibitors, especially those of epigenetic regulators, on foam cell formation.

5.2 Techniques for the evaluation of foam cell formation

Though the modulation of foam cell formation is reported frequently, usually in complement to gene expression studies, there is a broad variation in the cell line, staining protocol and quantification method used.[39–41] Generally, the protocol is as follows: macrophages are treated with stimulant and incubated for a given time prior to fixing, lipid staining and quantification of foam cell formation via microscopy. Foam cells are identified by the accumulation of lipid droplets. The initial foam cell assay protocol selected was adapted from Xu *et al* (optimised Oil Red oxLDL foam cell protocol),[40] and Yan *et al* (KDM6B attenuates SAA enhancement of foam cell formation) (Figure 5.2).[26]

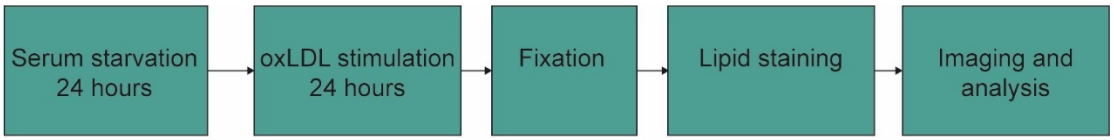


Figure 5.2 *– Foam cell formation assay protocol.*

5.3 Evaluation of THP-1 and RAW 264.7 cell lines for use in the foam cell formation assay

Though the use of primary cells for screening assays is increasing, these cells can be extremely difficult to handle and maintain. Various immortalised cell lines are used in the study of macrophage inflammation and foam cell formation, of which the most commonly used are THP-1 and RAW 264.7. THP-1 is a non-adherent human monocytic suspension cell line which can be differentiated to adherent macrophages by treatment

with phorbol 12-myristate 13-acetate (PMA), whilst RAW 264.7 is an adherent murine macrophage cell line.

Each cell line was evaluated to determine which would be most tractable for use in a phenotypic cellular screen. THP-1 cells (1×10^6 cells/mL) were treated with PMA (25 nM final concentration in complete RPMI media) and 0.1mL/well was transferred to a 96 well microplate (CellCarrier^{TM} Ultra, PerkinElmer). Cells were incubated for 48 hours at 37°C in 5% CO_2. Undifferentiated cells were removed, and adherent cells were washed with PBS prior to fixation with 4% paraformaldehyde and nuclear staining using DAPI. Cells were imaged using an Operetta® high content imaging system (PerkinElmer) (Figure 5.3).

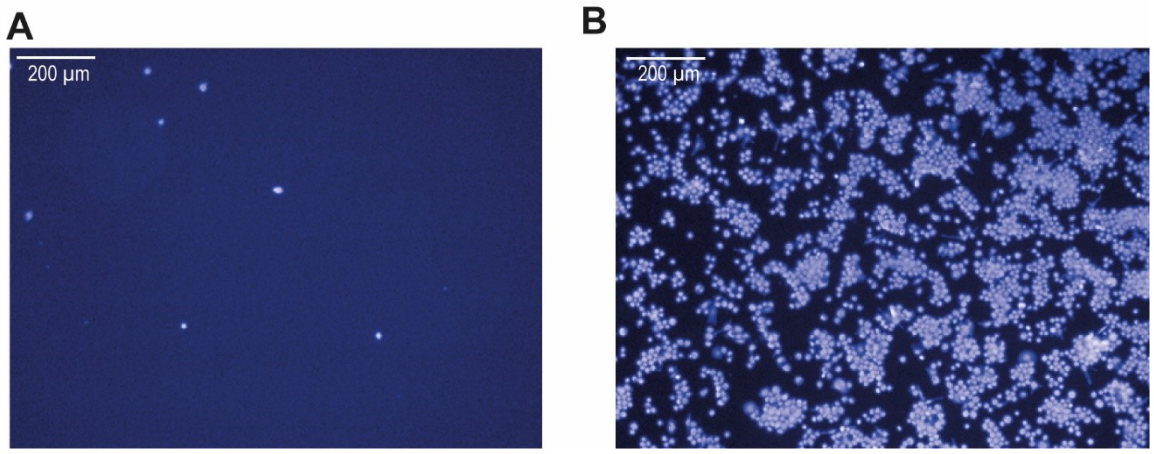


Figure 5.3 – THP-1 differentiation assay. *Cells were washed to remove non-adherent cells (phosphate buffered saline), fixed (4% paraformaldehyde) and stained using DAPI nuclear stain to identify adherent cells.* ***A****. THP-1 cells (48 hour incubation)* ***B****. THP-1 cells treated with PMA (25 nM, 48 hour incubation). Treatment with PMA induces transformation to an adherent phenotype. 10x magnification.*

Treatment of THP-1 cells with PMA successfully induced differentiation to an adherent cell type, as shown by increased number of adherent cells in treated versus untreated wells (Figure 5.3). However, cell adhesion was heterogeneous, resulting in 'clumps' of cells. This clumping of cells would be problematic for imaging analysis as it increases the difficulty of assigning features, such as lipid droplets, to individual cells, reducing the accuracy of analysis. It is possible to detach the differentiated THP-1 cells and re-seed

them to obtain a more homogeneous distribution of cells across the well, but this step would add an additional 12-16 hours for cells to adhere before initiation of the assay.

RAW 264.7 were seeded in a 96 well microplate (CellCarrier™ Ultra, PerkinElmer) at a concentration of 5000 cells/well and allowed to adhere for 14 hours. Cell media was replaced on the wells and they were further incubated for 24 hours at 37°C in 5% CO_2. Cells were washed with PBS prior to fixation with 4% paraformaldehyde and nuclear staining using DAPI. Fluorescent microscopy images were captured using an Operetta® high content imaging system (PerkinElmer) (Figure 5.4). The resultant images showed an even distribution of nuclei across the well.

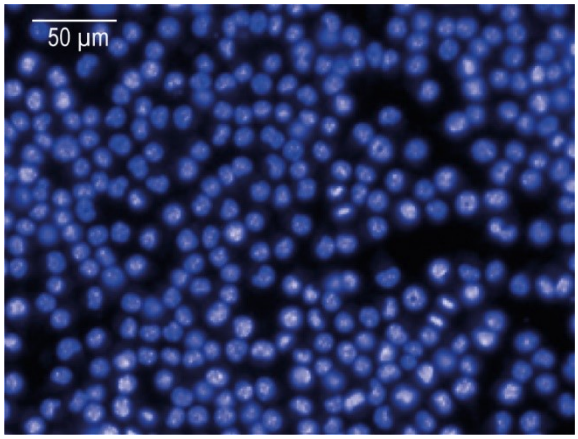


Figure 5.4 DAPI staining of RAW 264.7 reveals even distribution of cells. *RAW 264.7 (5000/well, 24 hours incubation) were washed (phosphate buffered saline), fixed (4% paraformaldehyde) and stained using DAPI nuclear stain. DAPI staining reveals an even distribution of cells. 20x magnification.*

Culture and fluorescent imaging of each cell line was undertaken to assess which cell line would be most suitable for use in the phenotypic screening assay. The use of THP-1 monocytes first requires their differentiation to adherent macrophages by treatment with PMA over 48 hours, and this time cost is extended by the need to re-seed cells to achieve a homogenous distribution across the well. An additional concern was that PMA treatment has been shown to attenuate inflammatory gene expression responses of THP-1 cells, potentially overwhelming 'weak' inflammatory responses, which could interfere

with the assay.[42] Overall, culture of the THP-1 cell line was less tractable than RAW 264.7, which was selected for use in the phenotypic assay.

5.4 Treatment of RAW 264.7 with oxLDL and acLDL produces a lipid droplet filled macrophage phenotype

Induction of foam cell formation by oxidised LDL (oxLDL) is a classic pathogenic feature of both early and late atherogenesis.[40] oxLDL is formed by the oxidation of LDL via radical and transition-metal ion-dependent reactions, in addition to enzyme catalysis within smooth muscle cells, vascular endothelial cells and macrophages.[43,44] Similar to oxLDL, acetylated LDL (acLDL) stimulates foam cell formation and related changes in gene expression via binding to macrophage receptors including CD36, although it is not present *in vivo*.[43,45] Foam cell formation can be modelled *in vitro* by the treatment of macrophages with oxLDL or acLDL, resulting in the formation of lipid-droplet filled foam cells, which may be identified by staining of the lipid droplets. Lipid droplet accumulation is characteristic of foam cell formation.

Oil Red O is a lipid-soluble di-azo dye which stains lipid droplets and has been used widely to evaluate foam cell formation.[40] However, the use of organic solvents in Oil Red O staining, required due to its poor solubility, has been shown to alter lipid droplet morphology.[46,47] Lipid droplets can also be visualised using osmium tetroxide, or fluorescent dyes including LipidTOX™ Red (Invitrogen) , BODIPY and Nile Red. LipidTOX™ Red was selected as it is easily handled in aqueous solutions, and has enhanced signal and reduced background fluorescence versus Nile Red.[48]

A pilot experiment was undertaken to evaluate the effect of oxLDL and acLDL treatment on lipid droplet accumulation on RAW 264.7, using a protocol adapted from Xu *et al*.[40] RAW 264.7 were incubated in low serum media (DMEM supplemented with 2mM L-

glutamine and 0.5% fetal bovine serum (FBS)) for 24 hours. RAW 264.7 were then seeded in a 96 well microplate (CellCarrier™ Ultra, PerkinElmer, 5000 cells/well) in regular culture media (DMEM supplemented with 2mM L-Glutamine and 10% FBS) and incubated overnight for 16 hours at 37°C in 5% CO_2. Cell media was then replaced with regular culture media containing 0, 50 and 100 µg/mL oxLDL. Cells were then incubated for 24 hours at 37°C in 5% CO_2. Cells were washed with PBS prior to fixation with 4% paraformaldehyde, nuclear staining using DAPI and lipid staining using LipidTOX™ Red lipid stain. Widefield fluorescent microscopy images were captured using an Operetta® high content imaging system (PerkinElmer) (Figure 5.5).

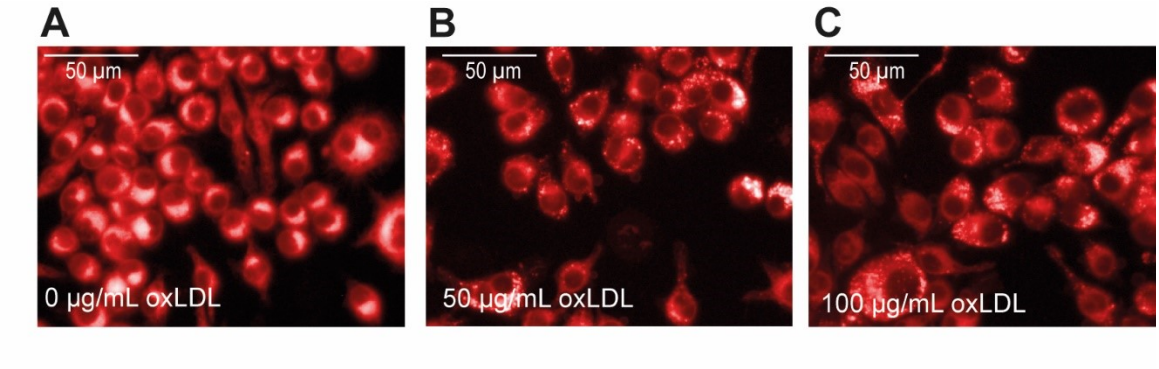


Figure 5.5 – Treatment of RAW 264.7 macrophages with oxLDL stimulates transformation to a lipid droplet filled phenotype. *RAW 264.7 were incubated in low serum media for 24 hours, seeded overnight in regular culture media and then treated with regular media containing* ***A****. 0 µg/mL oxLDL* ***B****. 50 µg/mL oxLDL and* ***C****. 100 µg/mL oxLDL for 24 hours. Fixed cells were stained using LipidTOX™ lipid stain and imaged using an Operetta® HCS system. 40x magnification.*

Foam cells are lipid laden macrophages which are formed as a result of binding and uptake of modified LDL, such as oxLDL. This stimulates upregulation of scavenger receptor expression, whereas efflux-associated proteins are down regulated. As a result of this dysregulation of lipid homeostasis, excess intracellular lipid is stored in cytoplasmic lipid droplet, giving the cells a 'foamy' appearance.[49]

As expected, a lipid-droplet filled phenotype was observed in RAW 264.7 cells treated with oxLDL at both 50 and 100 µg/mL oxLDL, consistent with foam cell formation.

An analogous pilot experiment was undertaken to evaluate the effect of acLDL treatment on lipid droplet accumulation in RAW 264.7. RAW 264.7 were incubated in low serum media (as above) for 24 hours, seeded in a 96 well microplate (CellCarrier^{TM} Ultra, PerkinElmer, 5000 cells/well) in regular culture media (as above) and incubated overnight for 15 hours at 37°C in 5% CO_2. Cell media was then replaced with treatment media containing 0 and 50 µg/mL acLDL. Cells were then incubated for 24 hours at 37°C in 5% CO_2. Cells were washed with PBS prior to fixation with 4% paraformaldehyde, nuclear staining using DAPI and lipid staining using LipidTOX™ Red lipid stain. Fluorescent microscopy images were captured using an Operetta® high content imaging system (PerkinElmer) (Figure 5.6).

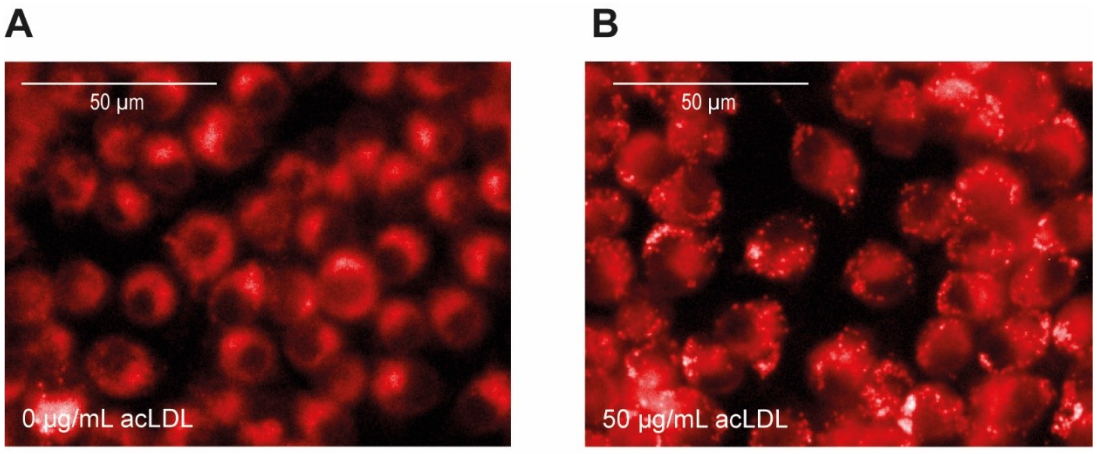


Figure 5.6 – Treatment of RAW 264.7 macrophages with acLDL stimulates transformation to a lipid droplet filled phenotype. *RAW 264.7 were incubated in low serum media for 24 hours, seeded overnight in regular culture media and then treated with regular media containing* ***A****. 0 µg/mL acLDL* ***B****. 50 µg/mL acLDL for 24 hours. Fixed cells were stained using LipidTOX™ lipid stain and imaged using an Operetta® HCS system. 40x magnification.*

RAW 264.7 cells treated with acLDL at 50 µg/mL presented with a lipid-droplet filled phenotype indicating the formation of foam cells.

Both oxLDL and acLDL are available commercially and are produced by chemical modification of LDL derived from blood samples. oxLDL is produced by copper-oxidation of LDL, whilst acLDL is produced by acetylation of LDL using acetic

anhydride. Initiation of the pilot oxLDL experiments was delayed due to the difficulty in acquiring oxLDL. oxLDL has a short shelf life of only 4-6 weeks from synthesis as it is unstable and degrades in solution. This gives a restricted window within which to conduct experiments. Due to its increased stability versus oxLDL, acLDL has a longer shelf life of 3-4 months. Treatment of RAW 264.7 with both oxLDL and acLDL stimulated lipid droplet accumulation. Degradation of oxLDL between experiments could alter inflammatory and morphological responses. Because of its enhanced stability, acLDL was selected for use in further experiments.

5.5 Optimisation of fluorescence microscopy image acquisition method

Accumulation of lipid droplets in oxLDL and acLDL treated RAW 264.7 was evident from the fluorescent microscopy images captured of the pilot experiments. However, there was evident 'blurring' of the images, which could reduce the accuracy of image analysis (Figure 5.6). These fluorescent microscopy images were acquired using widefield microscopy in which all light transmitted through the sample reaches the detector. As a result, unfocused light from outside the focal plane is also captured, resulting in blurring of the final image. Widefield microscopy is ideal for applications with lower resolution requirements and is relatively high throughput. Confocal microscopy solves the issue of image blurring by elimination of light not within the focal plane. This has the effect of producing image 'slices' through the sample, also known as optical sectioning.

In order to optimise the imaging protocol, foam cell formation of RAW 264.7 was stimulated using 50 µg/mL acLDL, following the above protocol. Cells were washed with PBS prior to fixation with 4% paraformaldehyde, nuclear staining using DAPI and lipid staining using LipidTOX™ Red lipid stain. Spinning disk laser confocal fluorescent

microscopy images were captured using an Operetta® high content imaging system (PerkinElmer) (Figure 5.7).

The resulting z-stack of images can be processed in a number of ways. Each image could be analysed individually. However, as the dimension of the lipid droplets is larger than the space between images in the stack (1 μm) lipid droplets appear across multiple images, which could result in overestimation of lipid droplet parameters (number, intensity etc). Three-dimensional rendering can be used to calculate the shape and volume of lipid droplets. However, the accuracy of this method depends on the number of images per stack acquired, increasing the number of images required and thus the time required for image acquisition. Additionally, 3D rendering of z stack images is prohibitively time consuming. Maximum intensity projection (MIP) creates a 2D image by identifying the highest intensity for each pixel and in the Z-stack resulting in a single sharply focused image. As long as each lipid droplet is captured in one image, it will be included in the MIP. Since the MIP comprises extracted information from all planes, image analysis can be achieved much more quickly compared to analysis of each plane individually.

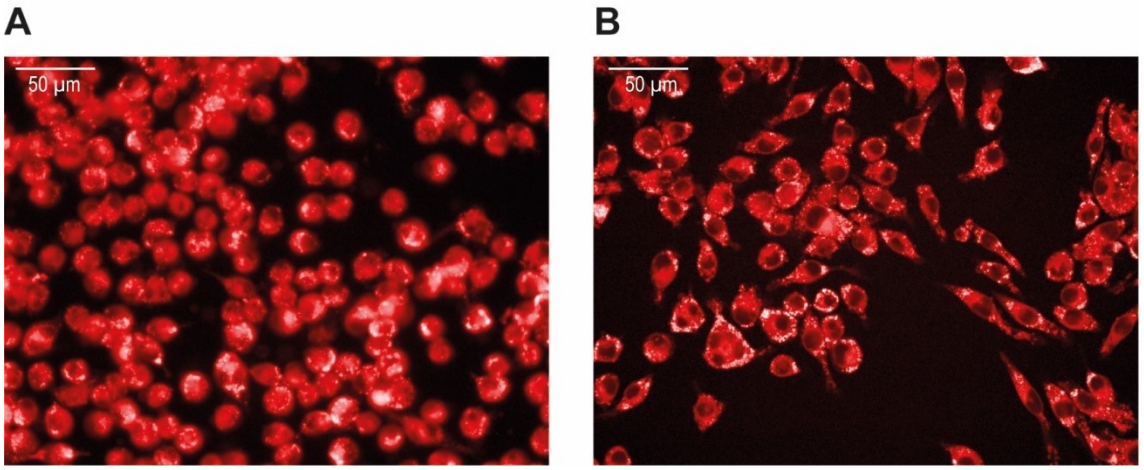


Figure 5.7 – Confocal microscopy enhances resolution of lipid droplets in acLDL treated RAW 264.7. *RAW 264.7 were incubated in low serum media for 24 hours, seeded in regular culture media (16 hours) and then treated with regular media containing 50 μg/mL acLDL for 24 hours.* ***A.*** *Widefield microscopy of acLDL treated RAW 264.7 stained with LipidTOX™ Red.* ***B.*** *Maximum intensity projection of spinning disk laser confocal microscopy images of acLDL treated RAW 264.7 stained with LipidTOX™ Red. 40x magnification.*

The MIP derived from spinning disk confocal microscopy images resulted in an image with improved resolution relative to widefield microscopy (Figure 5.7), and this imaging method was selected for use in further experiments.

5.6 Establishment of an imaging analysis pipeline

An imaging pipeline was established in the image analysis software Harmony®. As discussed above, the MIP of each z-stack of images was used for image analysis. DAPI nuclear staining was used to identify and count nuclei, and nuclei overlapping the edge of images were eliminated from analysis. Lipid droplets were detected from the LipidTOX™ Red fluorescence channel using a relative intensity method, which identifies the boundary of spots based on the intensity of each pixel relative to the surrounding pixels. The parameters, relative intensity coefficient, nuclei splitting function etc, for each analysis block were optimised using the parameter tune function within the Harmony analysis software. Finally, the number, area and intensity of lipid droplets were calculated, and the software assigned lipid droplets to a given cell according to their proximity to nuclei and background LipidTOX^{TM} Red cytoplasm staining (Figure 5.8).

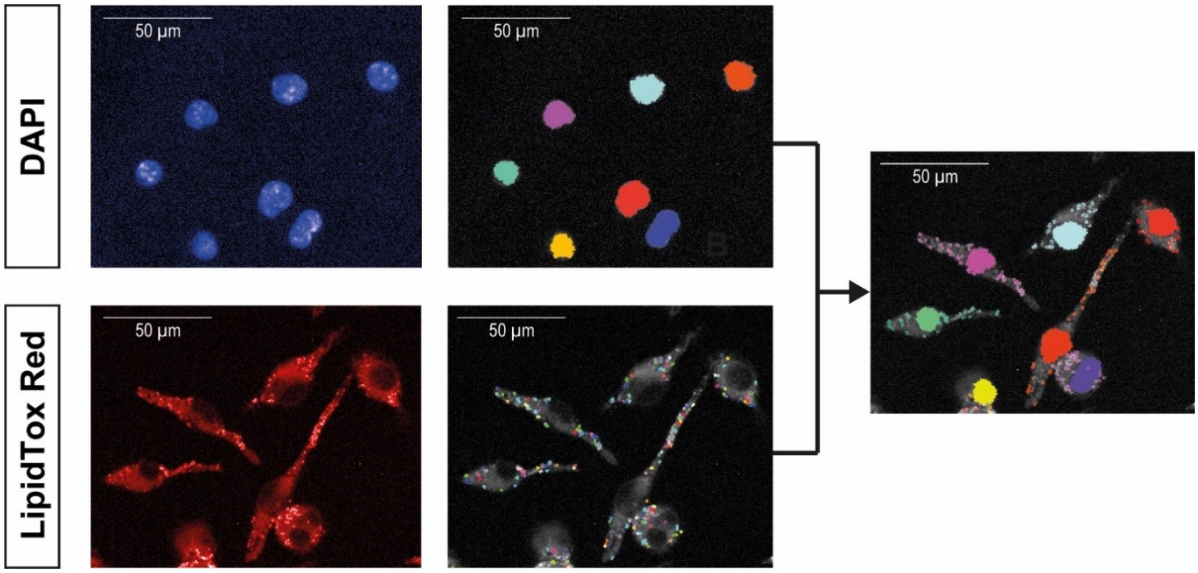


Figure 5.8 – Automated quantification of lipid droplet accumulation in RAW 264.7. *RAW 264.7 were incubated in low serum media for 24 hours, seeded in regular culture media (16 hours) and then treated with regular media containing 50 µg/mL acLDL for 24 hours. An image analysis pipeline was developed in Harmony® image analysis software. DAPI channel was used to identify nuclei and eliminate edge cells. LipidTOX™ Red intensity used to identify lipid droplet outlines and calculate morphology properties. Intensities of LipidTOX™ background fluorescence and DAPI background fluorescence were used to assign lipid droplets to each cell. Per cell lipid droplet metrics were then calculated. Left column: Blue – DAPI, Red – LipiTox Red. Centre column top: Each colour indicates individual droplet. Centre column bottom: Each colour indicates individual nuclei. Right column: Each colour indicates nuclei and associated lipid droplets. 40x magnification.*

5.7 acLDL treatment induces lipid droplet accumulation in RAW 264.7 in a concentration-dependent manner

Following the establishment of an imaging pipeline, RAW 264.7 cells were treated with a titration of acLDL (0-300 µg/mL acLDL) to evaluate the effect of acLDL dosing concentration on the magnitude of lipid droplet accumulation, and identify a suitable concentration of acLDL for use in screening.

RAW 264.7 were incubated in low serum media (as above) for 24 hours, seeded in a 96 well microplate (CellCarrier™ Ultra, PerkinElmer, 5000 cells/well) in regular culture media and incubated overnight for 15 hours at 37°C in 5% CO_2. Cell media was then replaced with treatment media containing 0-300 µg/mL acLDL. Cells were then incubated for 24 hours at 37°C in 5% CO_2. Cells were washed with PBS prior to fixation with 4% paraformaldehyde, nuclear staining using DAPI and lipid staining using

LipidTOX™ Red lipid stain. Spinning disk fluorescent laser confocal microscopy images were captured using an Operetta® high content imaging system (PerkinElmer), and analysed using Harmony image analysis software using the above imaging pipeline (section 5.6). The number of lipid droplets per cell mean per well was then determined (Figure 5.9).

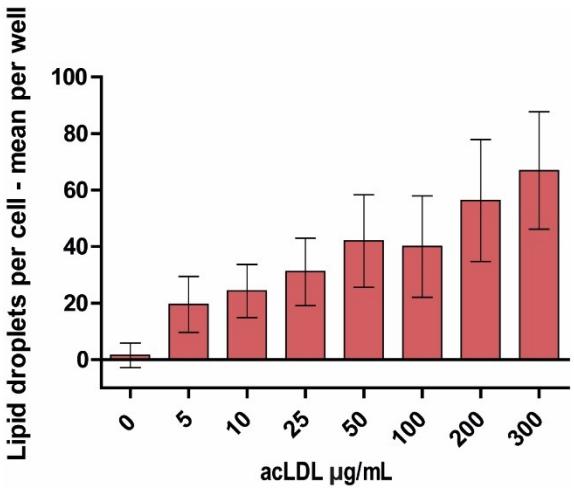


Figure 5.9 – Treatment of RAW 264.7 macrophages with acLDL stimulates transformation to a lipid droplet filled phenotype in a concentration dependent manner. *Number of lipid droplets per cell mean per well increases with increasing acLDL concentration. RAW 264.7 were incubated in low serum media for 24 hours, seeded overnight in regular culture media and then treated with regular media 0-300 µg/mL acLDL for 24 hours. Fixed cells were stained using LipidTOX™ neutral lipid stain, imaged using an Operetta® HCS system and images were analysed using Harmony image analsysis software. Error bars = standard deviation. N=1 technical replicate, >50 cells per well.*

The number of lipid droplets per cell mean per well increased with increasing acLDL concentration. Treatment at concentrations above 50 µg/mL acLDL caused a reduction in cell number, possibly due to cytotoxicity and so a concentration of 50 µg/mL acLDL was selected for further experiments.

5.8 Hypoxia enhances foam cell formation in RAW 264.7 cells

Like a growing tumour, the centre of an expanding atherosclerotic plaque is hypoxic. The role of hypoxia in the pathogenesis of atherosclerosis is being increasingly recognised. Work by Boström *et al* demonstrated enhancement of oxLDL stimulated foam cell formation and accumulation of lipids within human macrophages incubated in hypoxia.[50]

To assess the effect of hypoxic incubation on acLDL-stimulated lipid droplet accumulation in RAW 264.7, the foam cell assay protocol above was carried out at 0.1, 1 and 21% oxygen. Because of limited access to hypoxic workstations, incubations at 0.1 and 1% oxygen were carried out in separate experiments, each with their own normoxic (21% oxygen) control. Briefly, RAW 264.7 were incubated in low serum media (as above) for 24 hours, seeded in a 96 well microplate (CellCarrier^{TM} Ultra, PerkinElmer, 5000 cells/well) in regular culture media and incubated overnight for 15 hours at 37°C in 5% CO_2. Cell media was then replaced with regular culture media containing 0 and 50 µg/mL acLDL. For plates incubated in hypoxia, hypoxic treatment media was first incubated for 1 hour in hypoxia, and was applied to cells inside the hypoxic workstation. Cells were then incubated for 24 hours at 0.1, 1 and 21% oxygen within a hypoxic workstation (InvivO2 400, Baker Ruskinn) or normoxic incubator. Cells were washed with PBS prior to fixation with 4% paraformaldehyde, nuclear staining using DAPI and lipid staining using LipidTOX™ Red lipid stain.

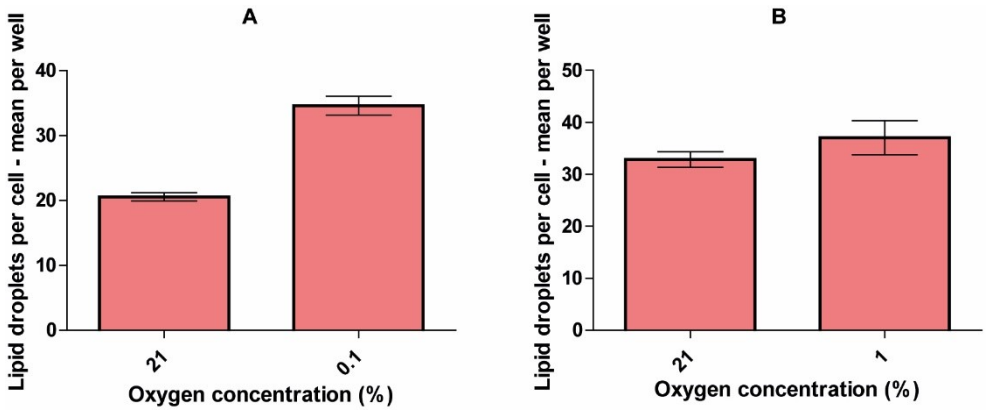


Figure 5.10 – Hypoxic incubation of RAW 264.7 macrophages enhances acLDL induced foam cell formation at 0.1% oxygen, but not 1% oxygen. *Number of lipid droplets per cell mean per well is increased in acLDL treated cells incubated in hypoxia versus normoxic cells at 0.1%, but not at 1% oxygen. RAW 264.7 were incubated in low serum media for 24 hours, seeded overnight in regular culture media and incubated at 0.1, 1 and 21% oxygen for 24 hours. Incubations at 0.1% (**A**) and 1% (**B**) oxygen were carried out in separate experiments, each with their own normoxic control. Fixed cells were stained using LipidTOX™ neutral lipid stain, imaged using an Operetta® HCS system and images were analysed using Harmony image analysis software. Error bars = SEM. >29 cells per well.*

Confocal fluorescent microscopy images were captured using an Operetta® high content imaging system (PerkinElmer), and analysed using Harmony image analysis software using the above imaging pipeline. The number of lipid droplets per cell mean per well was then determined (Figure 5.10). Hypoxic incubation of RAW 264.7 enhanced acLDL stimulated foam cell formation at 0.1% oxygen, as demonstrated by increased number of lipid droplets per cell mean per well in the acLDL treated sample incubated at 0.1% oxygen versus that incubated in normoxia (Figure 5.10). However, the same effect was not observed in acLDL treated RAW 264.7 cells incubated at 1% oxygen. This was unexpected, as previous work by Boström *et al* demonstrated hypoxic enhancement of oxLDL stimulated foam cell formation at 1% oxygen.[50] However, this work utilised alternative staining and quantification methods and was carried out in primary human macrophages, so the results may not be directly comparable.

4.8.1 Hypoxia induces foam cell formation even in the absence of acLDL

On inspection of the untreated control wells (i.e. not dosed with acLDL) it was observed that foam cell formation had occurred in RAW 264.7 incubated in hypoxia, even in the absence of acLDL (Figure 5.11). Incubation of RAW 264.7 in hypoxia at 0.1% and 1% oxygen lead to an increase in the number of lipid droplets per cell mean per well compared with those incubated at normoxia (21% oxygen).

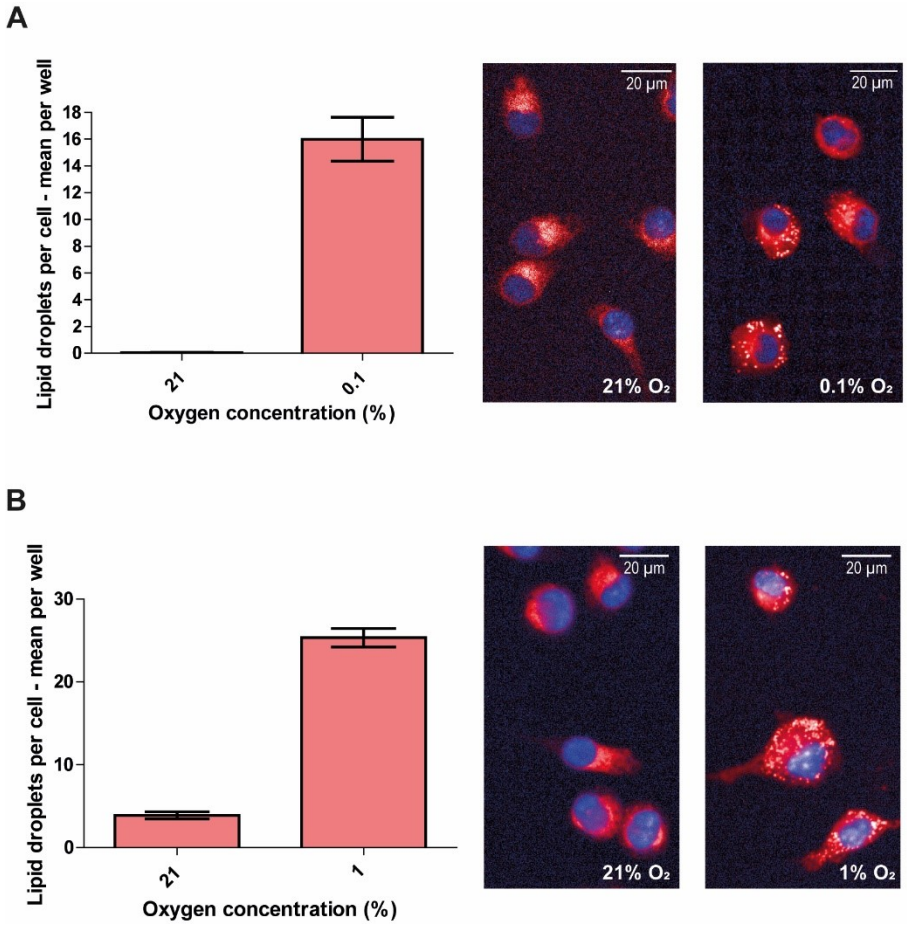


Figure 5.11 – Hypoxic incubation of RAW 264.7 macrophages stimulates spontaneous lipid droplet accumulation in the absence of acLDL. *Number of lipid droplets per cell mean per well is increased in cells incubated in hypoxia versus normoxic cells. RAW 264.7 were incubated in low serum media for 24 hours, seeded overnight in regular culture media and incubated at 0.1, 1 and 21% oxygen for 24 hours. Incubations at 0.1 and 1% oxygen were carried out in separate experiments, each with their own normoxic control. Fixed cells were stained using LipidTOX™ neutral lipid stain,imaged using an Operetta® HCS system and images were analysed using Harmony image analysis software. Error bars = SEM. >83 cells per well. 40x magnification.*

Spontaneous foam cell formation under hypoxic conditions may arise due to dysregulation of scavenger receptor expression, or because of changes to cellular metabolism and lipid homeostasis.[51,52] A number of the JmjC histone demethylases are upregulated in hypoxia including KDM6B,[53,54] which has recently been reported to regulate expression of the macrophage scavenger receptor CD36.[55]

The effect of KDM6B inhibition on hypoxic foam cell formation was assessed using the cell permeable small molecule inhibitor GSK-J4. The effect of SP600125, a small molecule c-Jun N-terminal kinase 2 inhibitor was also evaluated. JNK2-dependent

phosphorylation of scavenger receptor A (SR-A) promotes uptake of lipids in macrophages. Inhibition of JNK2 by SP600125 has been shown to reduce foam cell formation by up to 80% in cellular models.[41,56–59]

RAW 264.7 were incubated in low serum media (as above) for 24 hours, seeded in a 96 well microplate (CellCarrier™ Ultra, PerkinElmer, 5000 cells/well) in regular culture media and incubated overnight for 15 hours at 37°C in 5% CO_2. Cells were pre-incubated with media containing 1% DMSO ± GSK-J4 (0.1-100 μM final concentration) or SP600125 (0.03-50 μM final concentration) for 1 hour before initiation of hypoxic treatment. Hypoxic treatment media ± DMSO(1%) ± GSK-J4 (0.1-100 μM final concentration) or SP600125 (0.03-50 μM final concentration), was first incubated for 1 hour in hypoxia, and then applied to cells within the hypoxic workstation. Cells were then incubated for 24 hours at 0.1 and 21% oxygen within a hypoxic workstation (Invivo400 Hypoxic workstation, Ruskinn) or normoxic incubator respectively. Cells were washed with PBS prior to fixation with 4% paraformaldehyde, nuclear staining using DAPI and lipid staining using LipidTOX™ Red lipid stain. Confocal fluorescent microscopy images were captured using an Operetta® high content imaging system (PerkinElmer), and analysed using Harmony image analysis software using the established imaging pipeline (section 4.6). The number of lipid droplets per cell mean per well was then determined (Figure 5.12).

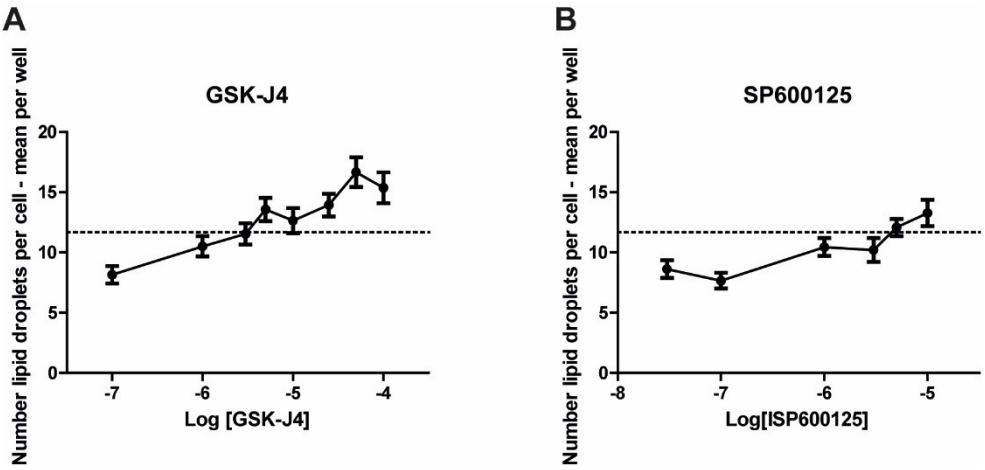


Figure 5.12 – Small molecule inhibitors GSK-J4 and SP600125 do not inhibit hypoxic induction of foam cell formation. *RAW 264.7 were incubated in low serum media for 24 hours, seeded overnight in regular culture media and incubated at 0.1, and 21% oxygen +/- **A**. GSK-J4 and **B**. SP600125 compound dilutions (final DMSO concentration 1%) for 24 hours. Fixed cells were stained using LipidTOX™ neutral lipid stain, imaged using an Operetta® HCS system and images were analysed using Harmony image analysis software. Error bars = SEM. >83 cells per well. Dotted line indicates number of lipid droplets per cell mean per well for DMSO (1% final concentration) well incubated at 1% oxygen. Number of lipid droplets per cell mean per well in media only normoxic control = 0.0356.*

Incubation with GSK-J4 or SP600125 did not eliminate lipid droplet accumulation in RAW 264.7 cells incubated in hypoxia. A small increase in the number of lipid droplets per cell mean per well was seen on increasing GSK-J4 concentration, though there was no reduction of cell number at any concentration which might indicate cytotoxicity. A small reduction in the number of lipid droplets per cell mean per well was seen at the lowest concentration of SP600125 tested, but not at higher concentrations. At concentrations of SP600125 greater than 10 μM, a significant reduction in cell number was seen indicating cytotoxicity. It is not clear how hypoxia affects SR-A expression, whose activity is reduced on SP600125 dosing, reducing lipid uptake, with differing reports of both up-and downregulation in the literature.[52] Gene expression studies would be helpful in confirming the hypoxic upregulation of KDM6B in this cellular context (section 4.11), to shed light on these results.

5.9 Evaluation of treatment with small molecule inhibitors on acLDL induced foam cell formation in normoxia

To probe more widely for a role of KDM histone demethylases in foam cell formation, the effect of small molecule inhibitors on acLDL stimulated foam cell formation was evaluated. The panel tested included IOX1 and Octyl IOX1, cell permeable broad spectrum 2OG oxygenase inhibitors, GSK-J4 and MC3119, KDM6B inhibitors, KDOAM25, an inhibitor of the KDM5 sub family of histone demethylases, and SP600125.

RAW 264.7 were incubated in low serum media for 24 hours, seeded in a 96 well microplate (CellCarrier^{TM} Ultra, PerkinElmer, 5000 cells/well) in regular culture media and incubated overnight for 16 hours at 37°C in 5% CO_2. Cells were pre-incubated with media containing 1% DMSO ± test compound for 1 hour before initiation of acLDL treatment. Cells were then treated with 0 and 50 μg/mL acLDL ± DMSO (1%) ± test compound (concentrations indicated Figure 5.13) incubated for 24 hours. Cells were washed with PBS prior to fixation with 4% paraformaldehyde, nuclear staining using DAPI and lipid staining using LipidTOX™ Red lipid stain. Confocal fluorescent microscopy images were captured using an Operetta® high content imaging system (PerkinElmer), and analysed using Harmony image analysis software using the established imaging pipeline (Section 5.6). The number of lipid droplets per cell mean per well (LDPCMW) was then determined (Figure 5.13). The compounds were tested in two groups in different experiments (Group 1: GSK-J4, KDOAM25, SP600125 Group 2:MC3119, IOX1 and Octyl IOX1).

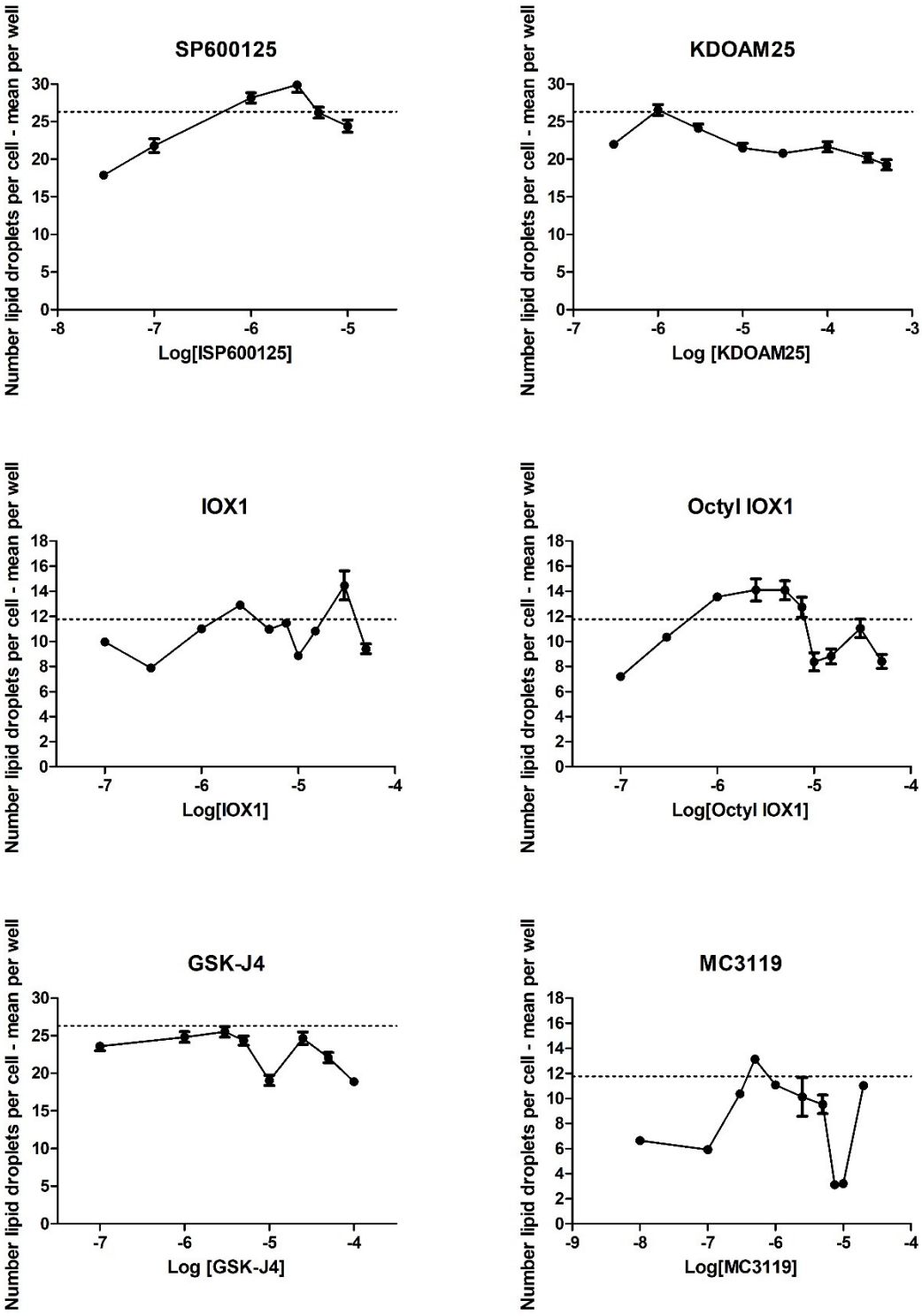


Figure 5.13 – Treatment of acLDL stimulated RAW 264.7 with small molecule inhibitors fails to ablate foam cell formation. *RAW 264.7 were incubated in low serum media for 24 hours and seeded overnight in regular culture media for 16 hours. Cells were treated ± acLDL 50 µg/mL ± DMSO (1%) ± compound (final concentration indicated above) for 24 hours at 37°C in 5% CO_2. Fixed cells were stained using LipidTOX™ lipid stain, imaged using an Operetta® HCS system and images were analysed utilising the established image analysis pipeline (section 4.6) within Harmony®. Error bars = SEM. >181 cells analysed per well. Dotted line indicates number of lipid droplets per cell mean per well for acLDL 50 µg/mL and DMSO (1%) treated cells. Separate experiments were undertaken to evaluate each of the two inhibitor groups (GSK-J4, SP600125, KDOAM25 and IOX1, Octyl-IOX1 and MC32119 respectively). Number of lipid droplets per cell mean per well in media only control = 0.0356.*

Overall no compound entirely ablated foam cell formation at any concentration tested. A small, dose dependent reduction in LDPCPW was seen on treatment with KDOAM25. Treatment with MC3119 lead to a 50% reduction in the mean LDPCMW, however this effect displayed no dose dependence. A marginal reduction in the mean LDPCPW was seen on treatment with GSK-J4 at the two highest concentrations tested (100, 50 μM respectively). The role of epigenetic regulation by the histone demethylases (JmjC-KDMs) in foam cell formation is not well understood, and so the lack of effect on inhibition of cell formation may indicate that epigenetic regulation involved with this process through JmjC-KDMs is marginal, and acts only to fine tune gene expression.

However, no reduction of LDPCPW was seen on treatment with SP600125 at any concentration. This was surprising as SP600125 inhibition of foam cell formation has been widely reported, including in independent studies in which the same cell line (RAW 264.7) and stimulant (acLDL, 50 μg/mL) and incubation time (24 hours) as those used above. This result prompted statistical analysis to evaluate the power of the assay to detect inhibition.

5.10 Statistical analysis reveals small dynamic range of foam cell assay

Calculation of Z' (Z-prime) is used as a measure of screening assay quality, and indicates the separation of the distributions of positive and negative controls, i.e. the dynamic range of the assay. Z′ therefore indicates the likelihood of detecting change within the dynamic range. Values between 0.5 and 1 are excellent, values between 0 and 0.5 may be acceptable but may require additional replicates, whereas values less than 0 indicate the assay is unlikely to be tractable in a high-throughput context. The Z' is calculated from the mean value (μ) and standard deviation (σ) of the positive (p) and negative (n) control populations, assuming a normal distribution of each population. It compares the data variation within each control with the dynamic range: the difference between the average

response of the positive and negative controls (Figure 5.14). In the foam cell formation assay, a strong Z' value would correspond to distinct acLDL-treated and untreated populations, each with low standard deviation.

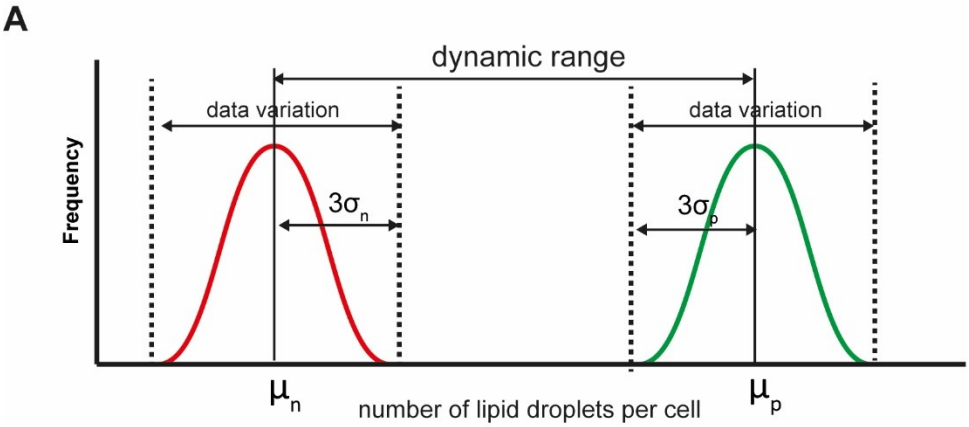


Figure 5.14. Z' calculation and graphical representation. A. Graphical representation of the Z'*, which compares the data variation within each control, with the dynamic range of the data set. Adapted from Zhang et al., 1999.*[60] ***B. Calculation of Z'****. Sample mean (μ), standard deviation (σ) of positive (p) and negative (n) controls.*

Z' was calculated using the mean number of lipid droplets per cell and standard deviation values for RAW 264.7 treated with 0 and 50 μg/mL acLDL according to the foam cell assay protocol described above.

This returned a Z' value of -0.65. This low Z' value indicates that there is overlap between the distributions of the positive and negative control populations. The data was graphically represented by plotting the frequency distribution data of the mean number of lipid droplets per cell for the two control groups (Figure 5.14). A robust assay will have a large dynamic range and a small distribution of each populations such that calculation of Z' returns a value as close to 1 as possible. As seen in Figure 5.15, acLDL treatment population has a wide distribution, causing the distributions to overlap and resulting in a

small dynamic range. This reduces sensitivity of the assay, possibly accounting for the apparent failure of SP600125 to reduce acLDL induced foam cell formation.

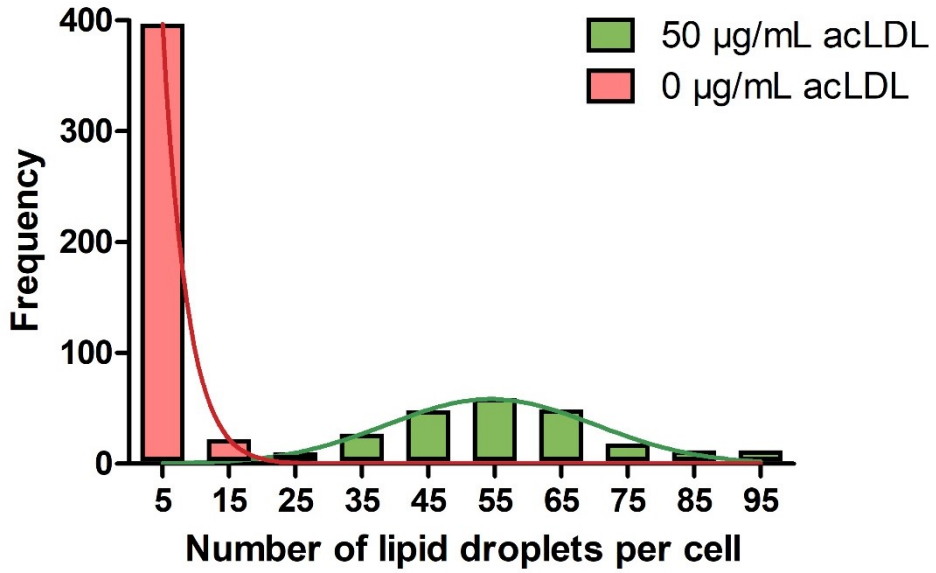


Figure 5.15. Frequency distribution histograms and gaussian distributions of number of lipid droplets per cell. *RAW 264.7 were incubated in low serum media for 24 hours, seeded in regular culture media (16 hours) and then treated with regular media containing 0 and 50 µg/mL acLDL for 24 hours. Poor dynamic range between 0 µg/mL acLDL (red, negative control) and 50 µg/mL acLDL (green, positive control) populations, due to wide frequency distribution of 50 µg/mL acLDL population. Frequency distribution and gaussian nonlinear regression curves generated using GraphPad Prism.*

Given the low Z' value acquired by quantification of the number of lipid droplet per cell, it was desirable to find an alternative measure to quantify phenotypic differences in positive and negative controls which would result in a larger dynamic range. To this end, Z' was calculated for a number of lipid droplet and cellular properties (Table 5.1). DAPI staining, nuclei location and LipidTOX™ staining enabled detection of the boundary of individual cells; the area of the nuclei was then subtracted from the whole cell leaving a measurement of the cytoplasm area.

Measurement	Z' Value
Spots per cell	-0.65
Spot area per cell	-0.56
Spots per cytoplasm area	-0.07
Spot area per cytoplasm area	0.02
Relative spot intensity	-2.55

Table 5.1 – Z' values calculated for different quantification measures of foam cell formation. *Value calculated using 0 µg/mL acLDL (negative control) and 50 µg/mL acLDL (positive control) sample populations as above.*

Spot area per cytoplasm area yielded the highest Z' calculated at a value of 0.02. However, this value still lies at the bottom of the acceptable Z' range.

Fluorescent microscopy images for the experiment testing the effect of SP600125 inhibition of acLDL stimulated lipid droplet accumulation described above, (Section 5.9, Figure 5.13) were re-analysed and the spot area per cytoplasm area – mean per well value was calculated (Table 5.1). However, this analysis also showed a lack of SP600125 inhibition on acLDL stimulated lipid droplet accumulation (Figure 5.16). Multiple studies have shown that SP600125 treatment reduces foam cell formation in various cell models, including SAA stimulated RAW 264.7 and acLDL stimulated peritoneal mouse macrophages.[41,56–59] Variation of cell line, foam cell assay culture method, staining and quantification methods may account for the apparent lack of foam cell formation inhibition on SP600125 treatment observed in this study, in addition to the limited sensitivity of the foam cell assay.

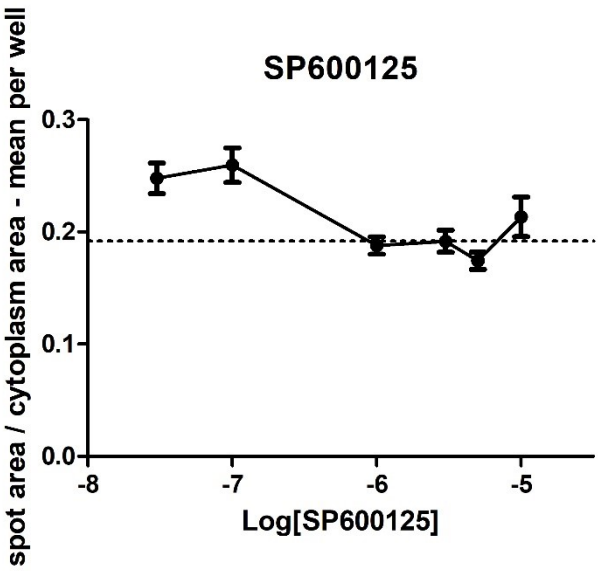


Figure 5.16 – Treatment of acLDL stimulated RAW 264.7 with SP600125 fails to reduce foam cell formation as evaluated by spot area/cytoplasm area mean per well. *RAW 264.7 were incubated in low serum media for 24 hours and seeded overnight in regular culture media for 16 hours. Cells were treated ± acLDL 50 µg/mL ± DMSO (1%) ± SP600125 (final concentration indicated above) for 24 hours at 37°C in 5% CO2. Fixed cells were stained using LipidTOX™ lipid stain, imaged using an Operetta® HCS system and images were analysed utilising the established image analysis pipeline (section 4.6) within Harmony®. Error bars = SEM. >213 cells analysed per well. Dotted line indicates number of spot area/ cytoplasm area mean per well for acLDL 50 µg/mL treated cells.*

To improve the current foam cell formation assay protocol, it will be essential to find an effective control inhibitor which reduces acLDL induced foam cell formation. This would allow further development of the imaging and analysis pipelines to identify changes in lipid droplet phenotypes. Though efficacy of SP600125 in similar conditions has been reported, it is possible that some factor in the experimental setup obscures potential inhibition, and thus systematic variation of the experimental set up may be fruitful. For example, the presence of inflammatory mediators in commercial FBS is known to vary between batches, which could alter baseline inflammatory state of RAW 264.7. (However, it is worth noting that the same FBS batch was utilised in culture media in all experiments but the pilot oxLDL and acLDL experiments). Additionally, it would be of interest to identify the temporal dependence of acLDL and hypoxia induced gene expression changes to identify the optimal dosing window for epigenetic tool compounds.

Preliminary efforts towards gene expression analysis are briefly described in the following section (5.11).

5.11 Discussion

Epigenetic regulation by the histone demethylases has been shown to modulate gene expression changes associated with atherosclerosis and inflammation. The activity and expression of these enzymes is modulated in hypoxic conditions, and reduced oxygen availability also been shown to contribute to the pathogenesis of atherosclerosis. In order to test the effect of inhibitors of epigenetic modulators including the JmjC histone demethylases on atherogenesis, efforts were undertaken to establish a cellular phenotypic assay of foam cell formation.

The murine macrophage cell line RAW 264.7 was selected for pilot experiments. Treatment of RAW 264.7 with both acLDL and oxLDL stimulated foam cell formation as demonstrated by the formation of lipid droplets visualised using LipidTOX™ Red lipid stain. acLDL was selected as a stimulant of foam cell formation for further experiments due to its enhanced stability versus oxLDL. Whilst lipid droplet accumulation was evident from widefield fluorescent microscopy captured of acLDL and oxLDL treated RAW 264.7 cells, the images were of insufficient resolution to allow quantification of lipid droplet morphology due to apparent blurring of the images.

MIPs of spinning disk laser confocal microscopy images had improved resolution compared with widefield microscopy and were utilised for quantification analysis. An imaging pipeline was established to identify and characterise lipid droplet morphology, resulting in an output of mean number of lipid droplets per cell per well. Utilising this imaging analysis pipeline, a dose dependent increase in the number of lipid droplets per cell mean per well was observed in RAW 264.7 treated with 0-300 g/mL.

The effect of hypoxic incubation at 0.1 and 1% oxygen on acLDL-stimulated lipid droplet accumulation was assessed. Incubation at 0.1, but not 1% oxygen enhanced acLDL stimulated foam cell formation. Additionally, foam cell formation was observed in cells incubated at 0.1 and 1% oxygen in the absence of stimulant. These results confirm literature reports of hypoxic induction of foam cell formation and enhancement of modified LDL stimulated foam cell formation. Hypoxic enhancement or stimulation of foam cell formation is likely to have important clinical implications for atherosclerosis, as chronic or intermittent hypoxia is often associated with diseases co-morbid with atherosclerosis.[61,62]

The effect of a panel of compounds including broad spectrum 2OG oxygenase inhibitors IOX1 and Octyl IOX1, KDM6B inhibitor GSK-J4 and MC3119, KDM5 inhibitor KDOAM25 and JNK2 inhibitor SP600125 on acLDL and hypoxia induced foam cell formation was evaluated. No reduction in number of lipid droplets per cell mean per well was observed, even on treatment with SP600125, which is widely reported to inhibit oxLDL and acLDL stimulated foam cell formation.[41,56–59]

Z' analysis, which accounts for the distribution and separation of positive and negative control populations, revealed a poor dynamic range which could account for the apparent lack of inhibition. Z' value of various phenotypic measures of lipid droplet accumulation was calculated to find an improved measure of foam cell lipid droplet morphology. However, the highest Z' value obtained, lipid area/cytoplasm area – mean per well, was only 0.02 which was still prohibitively low. Further work would prioritize identification of an effect control inhibitor, in addition to systematic optimisation of the experimental conditions to better capture change in lipid droplet morphology. Live cell imaging using fluorescently labelled acLDL may be useful in order to observe both acLDL uptake, and lipid droplet formation using LipidTOX™ lipid stain. It would be interesting to evaluate

histone methyltransferase inhibitors in addition to other inhibitors of epigenetic enzyme classes such as HDACs.

The temporal regulation of epigenetic modulator expression and atherosclerosis associated genes in macrophages in response to acLDL and hypoxia is not well characterised. An understanding of the magnitude and duration of gene expression changes could be useful in targeting compound dosing to achieve maximal effect. Consequently, real-time quantitative PCR (RT-qPCR) gene expression studies were mounted to evaluate the effect of hypoxia and acLDL treatment on the expression of genes including HIF, KDM6B and atherogenesis related genes. Evaluation of housekeeping genes, used for relative quantification of gene expression changes, was undertaken. cDNA libraries were generated from RAW 264.7 cells incubated at 1% and 21% oxygen ± acLDL (50 μg/mL). A concentration of 1% was selected to be in line with RT-qPCR studies of KDM6B upregulation at reported by Guo *et al*.[54] Analysis of Cq values using BestKeeper software revealed GAPDH was the most appropriate housekeeping gene, maintaining consistent expression levels across the different treatments.[63] cDNA libraries were generated for KDM6B expression over 48 hours in both hypoxia and normoxia. However, both KDM6B and HIF mRNA levels were prohibitively low in all samples, reflected by Ct values >35 cycles. These levels are below the limits of the technique, and presented a major barrier to further gene expression studies.

Epigenetic pathways in atherosclerosis may yield opportunities for novel therapeutic interventions. Although the studies above failed to demonstrate attenuation of foam cell formation, in part, due to the assay window, and also due to the lack of good chemical probes for all KDMs, the role of histone methylation status in inflammation and atherogenesis is increasingly recognised.[2,7] The interplay between hypoxia, epigenetic

regulation and inflammation and atherosclerosis is interesting, particularly considering recent publications investigating the effect of intermittent hypoxia on atherosclerosis and epigenetic marks,[64] which might rationalise the apparent disparity between observed histone methylation changes and reduced histone demethylase activity in hypoxic atherosclerotic lesions.

References

1. Barquera, S. *et al.* Global Overview of the Epidemiology of Atherosclerotic Cardiovascular Disease. *Arch. Med. Res.* **46,** 328–338 (2015).
2. Neele, A. E., Van den Bossche, J., Hoeksema, M. A. & de Winther, M. P. J. Epigenetic pathways in macrophages emerge as novel targets in atherosclerosis. *Eur. J. Pharmacol.* **763,** 79–89 (2015).
3. Park, Y. M. CD36, a scavenger receptor implicated in atherosclerosis. *Exp. Mol. Med.* **46,** e99–e99 (2014).
4. Kzhyshkowska, J., Neyen, C. & Gordon, S. Role of macrophage scavenger receptors in atherosclerosis. *Immunobiology* **217,** 492–502 (2012).
5. Ramji, D. P. & Davies, T. S. Cytokines in atherosclerosis: Key players in all stages of disease and promising therapeutic targets. *Cytokine Growth Factor Rev.* **26,** 673–85 (2015).
6. Tabas, I., García-Cardeña, G. & Owens, G. K. Recent insights into the cellular biology of atherosclerosis. *J. Cell Biol.* **209,** 13–22 (2015).
7. Bekkering, S., Joosten, L. A. B., van der Meer, J. W. M., Netea, M. G. & Riksen, N. P. The Epigenetic Memory of Monocytes and Macrophages as a Novel Drug Target in Atherosclerosis. *Clin. Ther.* **37,** 914–923 (2015).
8. Wierda, R. J., Geutskens, S. B., Jukema, J. W., Quax, P. H. A. & van den Elsen, P. J. Epigenetics in atherosclerosis and inflammation. *J. Cell. Mol. Med.* **14,** 1225–1240 (2010).
9. Turunen, M. P., Aavik, E. & Ylä-Herttuala, S. Epigenetics and atherosclerosis. *Biochim. Biophys. Acta - Gen. Subj.* **1790,** 886–891 (2009).
10. Khyzha, N., Alizada, A., Wilson, M. D. & Fish, J. E. Epigenetics of Atherosclerosis: Emerging Mechanisms and Methods. *Trends Mol. Med.* **23,** 332–347 (2017).
11. Laukkanen, M. O. *et al.* Local hypomethylation in atherosclerosis found in rabbit ec-sod gene. *Arterioscler. Thromb. Vasc. Biol.* **19,** 2171–8 (1999).
12. Lund, G. *et al.* DNA Methylation Polymorphisms Precede Any Histological Sign of Atherosclerosis in Mice Lacking Apolipoprotein E. *J. Biol. Chem.* **279,** 29147–

29154 (2004).

13. Hiltunen, M. O. *et al.* DNA hypomethylation and methyltransferase expression in atherosclerotic lesions. *Vasc. Med.* **7,** 5–11 (2002).

14. Hiltunen, M. O. & Ylä-Herttuala, S. DNA methylation, smooth muscle cells, and atherogenesis. *Arterioscler. Thromb. Vasc. Biol.* **23,** 1750–3 (2003).

15. Dong, C., Yoon, W. & Goldschmidt-Clermont, P. J. DNA methylation and atherosclerosis. *J. Nutr.* **132,** 2406S–2409S (2002).

16. Du, H.-P. *et al.* DNA methylation in cystathionine-γ-lyase (CSE) gene promoter induced by ox-LDL in macrophages and in apoE knockout mice. *Biochem. Biophys. Res. Commun.* **469,** 776–782 (2016).

17. Choi, J.-H. *et al.* Trichostatin A Exacerbates Atherosclerosis in Low Density Lipoprotein Receptor-Deficient Mice. *Arterioscler. Thromb. Vasc. Biol.* **25,** 2404–2409 (2005).

18. Van den Bossche, J. *et al.* Inhibiting epigenetic enzymes to improve atherogenic macrophage functions. *Biochem. Biophys. Res. Commun.* **455,** 396–402 (2014).

19. Bekkering, S. *et al.* Oxidized Low-Density Lipoprotein Induces Long-Term Proinflammatory Cytokine Production and Foam Cell Formation via Epigenetic Reprogramming of Monocytes. *Arterioscler. Thromb. Vasc. Biol.* **34,** 1731–1738 (2014).

20. Greißel, A. *et al.* Alternation of histone and DNA methylation in human atherosclerotic carotid plaques. *Thromb. Haemost.* **114,** 390–402 (2015).

21. Wierda, R. J. *et al.* Global histone H3 lysine 27 triple methylation levels are reduced in vessels with advanced atherosclerotic plaques. *Life Sci.* **129,** 3–9 (2015).

22. Greißel, A. *et al.* Histone acetylation and methylation significantly change with severity of atherosclerosis in human carotid plaques. *Cardiovasc. Pathol.* **25,** 79–86 (2016).

23. Bekkering, S. *et al.* Innate immune cell activation and epigenetic remodeling in symptomatic and asymptomatic atherosclerosis in humans in vivo. *Atherosclerosis* **254,** 228–236 (2016).

24. Salminen, A., Kaarniranta, K., Hiltunen, M. & Kauppinen, A. Histone demethylase Jumonji D3 (JMJD3/KDM6B) at the nexus of epigenetic regulation of inflammation and the aging process. *J. Mol. Med.* **92,** 1035–1043 (2014).

25. De Santa, F. *et al.* The histone H3 lysine-27 demethylase Jmjd3 links inflammation to inhibition of polycomb-mediated gene silencing. *Cell* **130,** 1083–94 (2007).

26. Yan, Q. *et al.* Jmjd3-mediated epigenetic regulation of inflammatory cytokine gene expression in serum amyloid A-stimulated macrophages. *Cell. Signal.* **26,** 1783–91 (2014).

27. Holla, S. *et al.* MUSASHI-Mediated Expression of JMJD3, a H3K27me3 Demethylase, Is Involved in Foamy Macrophage Generation during Mycobacterial Infection. *PLOS Pathog.* **12,** e1005814 (2016).

28. Neele, A. E. *et al.* Macrophage Kdm6b controls the pro-fibrotic transcriptome signature of foam cells. *Epigenomics* **9,** 383–391 (2017).

29. Kruidenier, L. *et al.* A selective jumonji H3K27 demethylase inhibitor modulates the proinflammatory macrophage response. *Nature* **488,** 404–8 (2012).

30. Wang, X. *et al.* Identification of the histone lysine demethylase KDM4A/JMJD2A as a novel epigenetic target in M1 macrophage polarization induced by oxidized LDL. *Oncotarget* **8,** (2017).

31. Matsui, H. *et al.* Induction of interleukin (IL)-6 by hypoxia is mediated by nuclear factor (NF)-κB and NF-IL6 in cardiac myocytes. *Cardiovasc. Res.* **42,** (1999).

32. White, J. R. *et al.* Genetic amplification of the transcriptional response to hypoxia as a novel means of identifying regulators of angiogenesis. *Genomics* **83,** 1–8 (2004).

33. Cramer, T. *et al.* HIF-1alpha is essential for myeloid cell-mediated inflammation. *Cell* **112,** 645–57 (2003).

34. Mwaikambo, B. R., Yang, C., Chemtob, S. & Hardy, P. Hypoxia up-regulates CD36 expression and function via hypoxia-inducible factor-1- and phosphatidylinositol 3-kinase-dependent mechanisms. *J. Biol. Chem.* **284,** 26695–707 (2009).

35. Hancock, R. L., Dunne, K., Walport, L. J., Flashman, E. & Kawamura, A.

Epigenetic regulation by histone demethylases in hypoxia. *Epigenomics* 1–21 (2015). doi:10.2217/epi.15.24

36. Hancock, R. L., Masson, N., Dunne, K., Flashman, E. & Kawamura, A. The Activity of JmjC Histone Lysine Demethylase KDM4A is Highly Sensitive to Oxygen Concentrations. *ACS Chem. Biol.* **12,** 1011–1019 (2017).

37. Dehne, N. & Brüne, B. Hypoxic inhibition of JMJD3 reduces H3K27me3 demethylation and induction of the STAT6 target gene CCL18. *Biochim. Biophys. Acta - Gene Regul. Mech.* **1859,** 1490–1501 (2016).

38. Chang, S. *et al.* Hypoxic reprograming of H3K27me3 and H3K4me3 at the *INK4A* locus. *FEBS Lett.* (2016). doi:10.1002/1873-3468.12375

39. Deutsch, M. J., Schriever, S. C., Roscher, A. A. & Ensenauer, R. Digital image analysis approach for lipid droplet size quantitation of Oil Red O-stained cultured cells. *Anal. Biochem.* **445,** 87–89 (2014).

40. Xu, S. *et al.* Evaluation of foam cell formation in cultured macrophages: an improved method with Oil Red O staining and DiI-oxLDL uptake. *Cytotechnology* **62,** 473–481 (2010).

41. Etzion, Y. *et al.* An unbiased chemical biology screen identifies agents that modulate uptake of oxidized LDL by macrophages. *Circ. Res.* **105,** 148–57 (2009).

42. Park, E. K. *et al.* Optimized THP-1 differentiation is required for the detection of responses to weak stimuli. *Inflamm. Res.* **56,** 45–50 (2007).

43. Chen, C. & Khismatullin, D. B. Oxidized low-density lipoprotein contributes to atherogenesis via co-activation of macrophages and mast cells. *PLoS One* **10,** e0123088 (2015).

44. Yoshida, H. & Kisugi, R. Mechanisms of LDL oxidation. *Clin. Chim. Acta* **411,** 1875–1882 (2010).

45. Klinkner, A. M., Waites, C. R., Kerns, W. D. & Bugelski, P. J. Evidence of foam cell and cholesterol crystal formation in macrophages incubated with oxidized LDL by fluorescence and electron microscopy. *J. Histochem. Cytochem.* **43,** 1071–8 (1995).

46. Kinkel, A. D. *et al.* Oil red-O stains non-adipogenic cells: a precautionary note.

Cytotechnology **46,** 49–56 (2004).

47. Fukumoto, S. & Fujimoto, T. Deformation of lipid droplets in fixed samples. *Histochem. Cell Biol.* **118,** 423–428 (2002).

48. Ford, M. J. *et al. LipidTOX™ Dyes for Adipocyte Staining in Routine Imaging Applications*.

49. Yu, X.-H., Fu, Y.-C., Zhang, D.-W., Yin, K. & Tang, C.-K. Foam cells in atherosclerosis. *Clin. Chim. Acta* **424,** 245–252 (2013).

50. Bostrom, P. *et al.* Hypoxia Converts Human Macrophages Into Triglyceride-Loaded Foam Cells. *Arterioscler. Thromb. Vasc. Biol.* **26,** 1871–1876 (2006).

51. Lattimore, J.-D. L. *et al.* Repetitive hypoxia increases lipid loading in human macrophages—a potentially atherogenic effect. *Atherosclerosis* **179,** 255–259 (2005).

52. Crucet, M. *et al.* Hypoxia enhances lipid uptake in macrophages: Role of the scavenger receptors Lox1, SRA, and CD36. *Atherosclerosis* **229,** 110–117 (2013).

53. Lee, H.-Y., Choi, K., Oh, H., Park, Y.-K. & Park, H. HIF-1-dependent induction of Jumonji domain-containing protein (JMJD) 3 under hypoxic conditions. *Mol. Cells* **37,** 43–50 (2014).

54. Guo, X. *et al.* Regulation of histone demethylase KDM6B by hypoxia-inducible factor-2. *Acta Biochim. Biophys. Sin. (Shanghai).* **47,** 106–113 (2015).

55. Holla, S. *et al.* MUSASHI-Mediated Expression of JMJD3, a H3K27me3 Demethylase, Is Involved in Foamy Macrophage Generation during Mycobacterial Infection. *PLoS Pathog.* **12,** e1005814 (2016).

56. Ricci, R. *et al.* Requirement of JNK2 for Scavenger Receptor A-Mediated Foam Cell Formation in Atherogenesis. *Science (80-.).* **306,** 1558–1561 (2004).

57. Oh, J. *et al.* 1,25(OH)2 vitamin d inhibits foam cell formation and suppresses macrophage cholesterol uptake in patients with type 2 diabetes mellitus. *Circulation* **120,** 687–98 (2009).

58. Rahaman, S. O. *et al.* A CD36-dependent signaling cascade is necessary for macrophage foam cell formation. *Cell Metab.* **4,** 211–21 (2006).

59. Lee, H. Y. *et al.* Serum amyloid A stimulates macrophage foam cell formation via

lectin-like oxidized low-density lipoprotein receptor 1 upregulation. *Biochem. Biophys. Res. Commun.* **433,** 18–23 (2013).

60. Zhang, J.-H., Chung & Oldenburg. A Simple Statistical Parameter for Use in Evaluation and Validation of High Throughput Screening Assays. *J. Biomol. Screen.* **4,** 67–73 (1999).

61. Lévy, P. *et al.* Obstructive Sleep Apnea and Atherosclerosis. *Prog. Cardiovasc. Dis.* **51,** 400–410 (2009).

62. Bäck, M. Atherosclerosis, COPD and chronic inflammation. *Respir. Med. COPD Updat.* **4,** 60–65 (2008).

63. Pfaffl, M. W., Tichopad, A., Prgomet, C. & Neuvians, T. P. Determination of stable housekeeping genes, differentially regulated target genes and sample integrity: BestKeeper – Excel-based tool using pair-wise correlations. *Biotechnol. Lett.* **26,** 509–515 (2004).

64. Cortese, R. *et al.* Aorta macrophage inflammatory and epigenetic changes in a murine model of obstructive sleep apnea: Potential role of CD36. *Sci. Rep.* **7,** 43648 (2017).

Chapter 6: Summary and Conclusions

The JmjC-KDMs are epigenetic enzymes which regulate gene expression by catalysing the removal of methyl groups, from lysine residues within histone tails resulting in both transcriptional activation and repression. Of the KDM6-sub family of JmjC-KDMs, KDM6A and KDM6B catalyse demethylation of H3K27Me3, activating gene expression.[1,2] The third family member, KDM6C, also demethylates H3K27Me3 but this has only been demonstrated *in vitro*, and at very low activity relative to KDM6A and KDM6B.[3] Both KDM6A and KDM6B have key roles in development, and in various disease states including cancer and inflammation.[4,5] The JmjC-KDMs are part of a wider superfamily of 2OG oxygenase enzymes which also includes the oxygen sensing HIF hydroxylases. Like the HIF hydroxylases, the JmjC-KDMs have an absolute requirement for oxygen and the oxygen sensitivity of several JmjC-KDMs has been demonstrated.[6,7] In a cellular context, hypoxia also causes alterations to metabolic pathways including the tricarboxylic acid (TCA) cycle, of which the 2OG oxygenase co-substrate 2OG is a key metabolite. Many TCA cycle intermediates (TCAI) are structurally similar to 2OG, and inhibition of other 2OG oxygenases by TCAI has been demonstrated.[8,9] The activity of KDM6A/B may be reduced in the context of cellular hypoxia due to reduced oxygen availability, or due to the presence of inhibitory TCAI. KDM6A and KDM6B have been associated with several hypoxic disease states including cancer and atherosclerosis.[10,11] Understanding the activity of KDM6A and KDM6B within these cellular environments may shed light on the mechanism by which these enzymes drive disease-related gene expression changes.

The aim of this project was to evaluate KDM6 activity in the context of cellular hypoxia, both in terms of reduced oxygen availability and alterations to the metabolic milieu.

Further to this, efforts were made to establish a phenotypic cellular assay for atherosclerosis, a hypoxic disease state in which epigenetic regulation of macrophage functions, including by KDM6B, plays a central role.

Experiments described in Chapter 2 detailed efforts towards the expression, purification and kinetic characterisation of recombinant KDM6A and KDM6B, including towards oxygen. Expression and purification of three KDM6A constructs, each consisting of the catalytic region, was undertaken resulting in production of KDM6A BR281 of approximately 80% purity. A MALDI-MS assay, which detects the various methylation states of the H3K27Me3 21mer peptide according to their mass, was used to evaluate BR281 activity. BR281 had very low activity. Significant enzyme precipitation was observed in experiments utilising active BR71, previously purified by Jan Kristensen. Dynamic light scattering analysis of BR71 in solution revealed high particle polydispersity and the presence of large (100 nm) particles likely to be aggregates. Future work would aim to identify optimal buffer conditions for enhancement of recombinant KDM6A stability, and clone new expression constructs with the addition of fusion proteins to enhance solubility.

Expression and purification of His-tagged KDM6B yielded enzyme active as assessed by the MALDI-MS activity. However, preliminary kinetic studies unfortunately came to a halt due to the failure of MALDI-MS equipment. The use of an alternative assay, the FDH assay, has been well established for various JmjC-KDMs including KDM6B.[12] However, the KDM6B construct used for recombinant expression, JMJD3A-C031, includes an N-terminal TRX fusion tag in addition to the N-terminal his-tag. TRX interferes with the FDH assay and thus the production of cleaved KDM6B was necessary. A small-scale purification of cleaved KDM6B yielded active enzyme, but two large-scale purifications resulted in enzyme for which no activity could be detected by either FDH or

MALDI-MS. UV-vis spectroscopy of the cleaved KDM6B samples revealed a contamination, absorbing at 260 nm, in the inactive KDM6B enzyme batches, but this was not present in the active KDM6B enzyme batch. DNA absorbs at 260 nm, and the contamination was confirmed to be DNA by agarose gel electrophoresis using the DNA chelating dye SYBR Safe. Interestingly, removal of this DNA by endonuclease treatment and by heparin affinity column purification restored KDM6B activity. These results demonstrate that these recombinant KDM6B batches are likely to be inactivated by the presence of the DNA contamination, rather than being both inactive, and also contaminated with DNA. Further work in the chapter aimed to establish KDM6B binding assays in order to further characterise this potential interaction between KDM6B and DNA, but this was unsuccessful due to the limited stability of KDM6B in solution compared with the extended incubation times required in these assays. Other 2OG oxygenases, such as KDM2A and the KDM5s,[13,14] contain DNA binding domains and several, such as AlkB and TETs,[15,16] catalyse modification of DNA substrates. The targeting of histone demethylases to specific genomic targets is poorly understood, whereas crosstalk between histone methylation and DNA methylation status is well established.[17] Overall, these preliminary results indicate the possibility for a binding interaction between KDM6B and DNA, potentially indicating the presence of a DNA binding domain within the boundaries of the KDM6B construct.

Chapter 3 details optimisation of an immunofluorescence activity assay to assess the cellular histone demethylation activity of KDM6B against global H3K27Me3. The optimised immunofluorescence activity assay was employed to investigate the effect of oxygen availability on cellular KDM6B activity in HeLa cells. A graded response of KDM6B activity to oxygen concentrations between 0.1-21% oxygen was observed with both percentage demethylation and relative activity decreasing with decreasing oxygen

availability. The KDM6B immunofluorescence activity assay was also established in an alternative cell line, COS-7. Again, the cellular dependence of KDM6B on oxygen availability was evaluated as above. As in HeLa cells, both percentage demethylation by KDM6B and relative KDM6B activity decreased with decreasing oxygen concentration, indicating that the activity of KDM6B against H3K27Me3 in COS-7 cells is also reduced in an oxygen concentration dependent manner. These results indicate that KDM6B activity can be modulated by oxygen availability in a physiologically relevant manner.

The cellular oxygen dependence of KDM4A activity has been characterised in a study by Hancock et al.[6] The oxygen dependence of the DNA demethylase TET1 was also evaluated by also immunofluorescence in a preliminary (N=1) experiment undertaken by Dr Akane Kawamura and Dr Rebecca Hancock. Values for relative cellular activity of KDM4A and KDM6B determined at 0.1, 1.0 and 5.0% oxygen were within error of one another, indicating that the cellular oxygen sensitivity of these enzymes are similar. In contrast, the hypoxic reduction of relative TET1 activity was much greater than for KDM4A and KDM6B at each oxygen concentration tested, indicating that the oxygen sensitivity of TET1 is greater than that of KDM4A and KDM6B. The observation of oxygen sensitivity in overexpression models indicates that whilst upregulation may blunt the effect of hypoxic reduction of enzyme activity it may be insufficient to restore normal levels of demethylation in enzymes which display high oxygen sensitivity. Oxygen sensitivity of epigenetic modifiers such as KDM6B, KDM4A and TET1 is likely to lead to aberrant gene expression changes in hypoxia. Further, differential oxygen sensitivity could result in complex effects on gene regulation which will be dependent on the activity of epigenetic modifiers at the oxygen concentration in question.

Other factors, apart from oxygen availability alone, may influence the activity of 2OG oxygenase enzymes in hypoxic conditions. Hypoxia impacts cellular metabolism, and

leads to increased cellular concentration of succinate, fumarate and L-2HG.[18–22] 2OG, the co-substrate of 2OG oxygenase catalysis, is a TCA cycle intermediate (TCAI), and is structurally similar to many of the other TCAIs. Inhibition of various 2OG oxygenases by TCAI and related metabolites has been reported.[8,9,23] Biochemical studies were undertaken to assess the inhibition of KDM6B by TCAI. A panel of 17 TCAI were screened using an AlphaScreen inhibition assay. Many of these compounds inhibited KDM6B to some extent, of which the most potent were D-2HG, L-2HG, oxaloacetate and succinate, with IC_{50} values of 9.7, 15, 20 and 20 μM respectively. An orthogonal mass spectrometry based assay was used to further validate several of the most potent TCAI identified by the AlphaScreen including succinate, L-2HG and D-2HG. This confirmed that the inhibition observed in AlphaScreen was not due to interference with the assay. Inhibition of KDM6B by 2HG (both D-2HG and L-2HG with IC_{50} values of 203 μM and 328 μM respectively) was lower than that previously observed for KDM4A (IC_{50} values of 24 μM, 26 μM respectively),[24] but was on par with KDM5B (IC_{50} values of 203 μM, 150 μM respectively).[9] In addition to altered TCAI concentrations observed in hypoxia, loss-of-function and gain-of-function mutations in the IDH1/2, SDH and fumarate hydratase enzymes occur with a high prevalence in various cancers including glioma, renal cell carcinomas and acute myeloid leukaemia resulting in increased concentration of L-2HG, D-2HG, succinate and fumarate. As in hypoxia, differential inhibition of JmjC-KDMs may lead to complex outcomes for epigenetic gene regulation. As KDM6B has been identified as a tumour suppressor in some cancer types, inhibition of KDM6B by oncometabolites could potentially contribute to oncogenesis. KDM6A has been more widely identified as a tumour suppressor, and therefore evaluating the effect of TCAI on KDM6A activity would also be interesting. The effect of IOX1, TCAI inhibitors and 2OG, administered as cell-permeable esters, on cellular KDM6B activity was then

assessed using the KDM6B immunofluorescence activity assay. Inhibition of KDM6B on IOX1 dosing was observed as expected, but overall none of the TCAI tested showed strong cellular inhibition of KDM6B. Dosing of 2OG had no effect on cellular KDM6B activity, indicating 2OG conditions may be saturating. Crystal structures of KDM5B in complex with succinate and oxaloacetate, in addition to kinetic studies, indicate inhibition occurs in a 2OG competitive manner.[9] Therefore the lack of cellular KDM6B inhibition by TCAI may arise from saturating intracellular 2OG concentrations. Together these results show that KDM6B is inhibited by a number of TCAI *in vitro*, but that a deeper understanding of the cellular 2OG and TCAI concentrations present both in hypoxia and in cancer cells is required to determine the physiological relevance of this.

Epigenetic regulation by the histone demethylases has been shown to modulate gene expression changes associated with atherosclerosis and inflammation. The activity and expression of these enzymes is modulated in hypoxic conditions, and reduced oxygen availability has also been shown to contribute to the pathogenesis of atherosclerosis. Chapter 5 describes attempts to establish a cellular phenotypic assay of foam cell formation, in order to test the effect of inhibitors of epigenetic modulators, including the JmjC histone demethylases, and hypoxia on atherogenesis. Atherosclerosis is characterised by the formation of lipid-droplet filled macrophages, referred to as foam cells, which make up the expanding core of an atherosclerotic plaque. *In vivo*, these cells form due to receptor binding and phagocytosis of modified low density binding protein (LDL). Treatment of the murine macrophage cell line RAW 264.7 with both acLDL and oxLDL stimulated foam cell formation as demonstrated by the formation of lipid droplets, stained using the LipidTOX™ Red lipid stain and imaged using fluorescent confocal microscopy. Incubation of RAW 264.7 cells in hypoxia enhanced acLDL stimulated foam cell formation, as seen by an increased number of lipid droplets per cell mean per well.

Additionally, incubation of RAW 264.7 in hypoxia induced foam cell formation both at 0.1% and 1% oxygen. Chronic or intermittent hypoxia is often associated with diseases co-morbid with atherosclerosis, consistent with the hypoxic enhancement or stimulation of foam cell formation observed.[25,26] The effect of a panel of compounds including broad spectrum 2OG oxygenase inhibitors IOX1 and Octyl IOX1, KDM6B inhibitor GSK-J4 and MC3119, KDM5 inhibitor KDOAM25 and JNK2 inhibitor SP600125 on acLDL and hypoxia induced foam cell formation was evaluated. No reduction in the number of lipid droplets per cell mean per well was observed, even on treatment with SP600125, which is widely reported to inhibit oxLDL and acLDL stimulated foam cell formation.[27–31] Statistical Z' factor analysis, which is used to evaluate the dynamic range of phenotypic cellular assays, revealed that the dynamic range of the assay was low, potentially obscuring inhibitor effects. Despite the failure of these studies to demonstrate foam cell formation, the role of histone methylation status in regulation of inflammation and atherogenesis is increasingly recognised.[32,33] The apparent disparity between observed histone methylation changes and reduced histone demethylase activity in hypoxic atherosclerotic lesions might be rationalised by recent publications investigating the effect of intermittent hypoxia on atherosclerosis and epigenetic marks.[34,35]

Overall, the work described in this thesis demonstrates oxygen sensitivity of cellular KDM6B activity. Additionally, *in vitro* biochemical studies demonstrated inhibition of KDM6B by several TCAI whose concentration is known to be upregulated in hypoxia. It is possible that inhibition by TCAI contributes to hypoxic inhibition of KDM6B activity, though further work is needed to address this in a physiological context. Together these results reinforce the role of epigenetic modulators in facilitating alterations to gene expression in response to environmental changes. A greater understanding of the interplay between hypoxia, metabolism and epigenetic regulation will be useful in shedding light

on the mechanisms by which aberrant epigenetic regulation may contribute to disease pathogenesis.

6.1 References

1. Hong, S. *et al.* Identification of JmjC domain-containing UTX and JMJD3 as histone H3 lysine 27 demethylases. *Proc. Natl. Acad. Sci.* **104,** 18439–18444 (2007).
2. Agger, K. *et al.* UTX and JMJD3 are histone H3K27 demethylases involved in HOX gene regulation and development. *Nature* **449,** 731–734 (2007).
3. Walport, L. J. *et al.* Human UTY(KDM6C) is a male-specific Nϵ-methyl lysyl demethylase. *J. Biol. Chem.* **289,** 18302–13 (2014).
4. Burchfield, J. S., Li, Q., Wang, H. Y. & Wang, R.-F. JMJD3 as an epigenetic regulator in development and disease. *Int. J. Biochem. Cell Biol.* **67,** 148–157 (2015).
5. Van der Meulen, J., Speleman, F. & Van Vlierberghe, P. The H3K27me3 demethylase UTX in normal development and disease. *Epigenetics* **9,** 658–668 (2014).
6. Hancock, R. L., Masson, N., Dunne, K., Flashman, E. & Kawamura, A. The Activity of JmjC Histone Lysine Demethylase KDM4A is Highly Sensitive to Oxygen Concentrations. *ACS Chem. Biol.* **12,** 1011–1019 (2017).
7. Hancock, R. L., Dunne, K., Walport, L. J., Flashman, E. & Kawamura, A. Epigenetic regulation by histone demethylases in hypoxia. *Epigenomics* 1–21 (2015). doi:10.2217/epi.15.24
8. Chowdhury, R. *et al.* The oncometabolite 2-hydroxyglutarate inhibits histone lysine demethylases. *EMBO Rep.* **12,** 463–469 (2011).
9. Tarhonskaya, H. *et al.* Studies on the Interaction of the Histone Demethylase KDM5B with Tricarboxylic Acid Cycle Intermediates. *J. Mol. Biol.* **429,** 2895–2906 (2017).
10. Hultén, L. M. & Levin, M. The role of hypoxia in atherosclerosis. *Curr. Opin. Lipidol.* **20,** 409–14 (2009).
11. Biddlestone, J., Bandarra, D. & Rocha, S. The role of hypoxia in inflammatory disease (review). *Int. J. Mol. Med.* **35,** 859–69 (2015).
12. Sakurai, M. *et al.* A miniaturized screen for inhibitors of Jumonji histone

demethylases. *Mol. Biosyst.* **6,** 357–64 (2010).

13. Tu, S. *et al.* The ARID domain of the H3K4 demethylase RBP2 binds to a DNA CCGCCC motif. *Nat. Struct. Mol. Biol.* **15,** 419–421 (2008).

14. Dimitrova, E., Turberfield, A. H. & Klose, R. J. Histone demethylases in chromatin biology and beyond. *EMBO Rep.* **16,** 1620–39 (2015).

15. Tahiliani, M. *et al.* Conversion of 5-methylcytosine to 5-hydroxymethylcytosine in mammalian DNA by MLL partner TET1. *Science* **324,** 930–5 (2009).

16. Thalhammer, A. *et al.* Human AlkB homologue 5 is a nuclear 2-oxoglutarate dependent oxygenase and a direct target of hypoxia-inducible factor 1α (HIF-1α). *PLoS One* **6,** e16210 (2011).

17. Du, J., Johnson, L. M., Jacobsen, S. E. & Patel, D. J. DNA methylation pathways and their crosstalk with histone methylation. *Nat. Rev. Mol. Cell Biol.* **16,** 519–32 (2015).

18. Czibik, G., Steeples, V., Yavari, A. & Ashrafian, H. Citric acid cycle intermediates in cardioprotection. *Circ. Cardiovasc. Genet.* **7,** 711–9 (2014).

19. Cerebral metabolism in hypoxic hypoxia. II. Citric acid cycle intermediates and associated amino acids. *Brain Res.* **86,** 45–54 (1975).

20. Hochachka, P. W., Owen, T. G., Allen, J. F. & Whittow, G. C. Multiple end products of anaerobiosis in diving vertebrates. *Comp. Biochem. Physiol. B.* **50,** 17–22 (1975).

21. J.Folbergrova, B.Ljunggren, K.Norberg, B. K. S. Influence of complete ischemia on glycolytic metabolites, citric acid cycle intermediates, and associated amino acids in the rat cerebral cortex. *Brain Res.* **80,** 265–279 (1974).

22. Intlekofer, A. M. *et al.* Hypoxia Induces Production of L-2-Hydroxyglutarate. *Cell Metab.* **22,** 304–11 (2015).

23. Hewitson, K. S. *et al.* Structural and Mechanistic Studies on the Inhibition of the Hypoxia-inducible Transcription Factor Hydroxylases by Tricarboxylic Acid Cycle Intermediates. *J. Biol. Chem.* **282,** 3293–3301 (2007).

24. Chowdhury, R. *et al.* The oncometabolite 2-hydroxyglutarate inhibits histone lysine demethylases. *EMBO Rep* **12,** 463–469 (2011).

25. Lévy, P. *et al.* Obstructive Sleep Apnea and Atherosclerosis. *Prog. Cardiovasc. Dis.* **51,** 400–410 (2009).

26. Bäck, M. Atherosclerosis, COPD and chronic inflammation. *Respir. Med. COPD Updat.* **4,** 60–65 (2008).

27. Etzion, Y. *et al.* An unbiased chemical biology screen identifies agents that modulate uptake of oxidized LDL by macrophages. *Circ. Res.* **105,** 148–57 (2009).

28. Ricci, R. *et al.* Requirement of JNK2 for Scavenger Receptor A-Mediated Foam Cell Formation in Atherogenesis. *Science (80-.).* **306,** 1558–1561 (2004).

29. Oh, J. *et al.* 1,25(OH)2 vitamin d inhibits foam cell formation and suppresses macrophage cholesterol uptake in patients with type 2 diabetes mellitus. *Circulation* **120,** 687–98 (2009).

30. Rahaman, S. O. *et al.* A CD36-dependent signaling cascade is necessary for macrophage foam cell formation. *Cell Metab.* **4,** 211–21 (2006).

31. Lee, H. Y. *et al.* Serum amyloid A stimulates macrophage foam cell formation via lectin-like oxidized low-density lipoprotein receptor 1 upregulation. *Biochem. Biophys. Res. Commun.* **433,** 18–23 (2013).

32. Neele, A. E., Van den Bossche, J., Hoeksema, M. A. & de Winther, M. P. J. Epigenetic pathways in macrophages emerge as novel targets in atherosclerosis. *Eur. J. Pharmacol.* **763,** 79–89 (2015).

33. Bekkering, S., Joosten, L. A. B., van der Meer, J. W. M., Netea, M. G. & Riksen, N. P. The Epigenetic Memory of Monocytes and Macrophages as a Novel Drug Target in Atherosclerosis. *Clin. Ther.* **37,** 914–923 (2015).

34. Smith, S. & Watters, J. Role of JMJD3 and histone modifications in intermittent hypoxia-induced neuroinflammation (1120.6). *FASEB J* **28,** 1120.6- (2014).

35. Cortese, R. *et al.* Aorta macrophage inflammatory and epigenetic changes in a murine model of obstructive sleep apnea: Potential role of CD36. *Sci. Rep.* **7,** 43648 (2017).

Chapter 7: Materials and Methods

General methods

All chemicals, including buffer components, were acquired from Sigma Aldrich at the highest purity available unless otherwise stated. Water was purified using a Millipore Milli-Q system containing a 0.22 μm filter. Biological procedures were undertaken using sterile technique; equipment (pipette tips etc.) and solutions were sterilised using via autoclaving in at 121°C for 20 minutes. Other solutions were sterilised using a 0.22 μm filter.

pH measurement and adjustment

The pH of all solutions used was measured using Hanna Instruments HI 9321 microprocessor pH meter fitted with a 5 mm diameter electrode. Prior to each use, the pH meter was calibrated between pH 7 and pH 4 or between pH 7 and pH 10 using commercially sourced phthalate (pH 4), phosphate (pH 7) and borate (pH 10) buffer solutions (ThermoFisher Scientific). The electrode was stored in saturated KCl solution between uses. pH was adjusted to the desired value using solutions of NaOH or HCl.

Procedures relating to *in vitro* experiments

Plasmids for recombinant protein expression

Construct	Vector	Tag	Residues	Antibiotic resistance
KDM6A BR281	pET47b	*N*-His_6/*C*-S-tag	880-1401	Ampicillin
KDM6A BR242	pOPIN F	*N*-His_6	880-1401	Ampicillin
KDM6A BR71	pOPIN F	*N*-His_6	940-1401	Ampicillin
KDM6B JMJD3A-C031	pNH-TrxT	*N*-His_6	1141-1641	Kanamycin

Table 7.1 *Details of constructs of KDM6A and KDM6B used for E.coli expression*

Transformation

Competent Rosetta2(DE3) cells were acquired from New England Biolabs. For transformation, an aliquot of competent cells (30 µL) was transferred to a 1.5 mL sterile Eppendorf vial and the plasmid (1µL, 10 ng/µL DNA) was added with gentle mixing. The transformation mixture was chilled on ice for 15 minutes, followed by a heat shock for 30 seconds at 42 °C. Cells were incubated for 5 minutes on ice. Super Optimal broth with Catabolite Repression (SOC) medium (200 µL) was added and cells were incubated for 1 hour at 37 °C before being plated on LB-agar plates containing selection antibiotic. The plates were then incubated at 37 °C overnight (16 hours).

Bacterial growth medium

Component g/L	Tryptone	Yeast extract	NaCl	KCl	NaOH (1 M)	Agar
Lysogeny broth (LB)	10.0 g	5.0 g	10.00 g	/	/	/
2 Tryptone Yeast Extract (2 TY)	16.0 g	10.0 g	5.0 g	/	/	/
Super Optimal broth with Catabolite Repression (SOC)	0.2 g	0.05 g	0.0058 g	0.0019 g	0.04 mL	/
Agar	10.0 g	5.0 g	10.0 g	/	/	20.0 g

Table 7.2 *Bacterial growth components of growth media*

Terrific broth (TB) was prepared, according supplier instructions,[1] from Fisherbrand™ granulated modified TB containing: Casein Peptone 12 g/L, Yeast extract 24 g/L, Potassium Phosphate, Monobasic 2.2g/L, Potassium Phosphate, Dibasic 9.4 g/L, glycerol 4 mL/L.

Measurement of optical density (O.D) of bacterial cultures

Optical density is used as a measure of the cell density of a suspension and therefore can be used to monitor growth. Light is scattered as it travels through a cell suspension and the magnitude of this scattering, referred to as optical density, is dependent on the number

of cells in the solution. The optical density of 1 mL culture medium at λ = 600 nm ($O.D._{600}$) was measured using an Amersham Biosciences Novaspec III visible spectrophotometer; absorbance of the uninoculated growth medium was used as a blank.

Plasmid purification

Plasmid was transformed into *E. coli* XL10 Gold cells (Stratagene). A single colony from the transformation was used to inoculate 10 mL 2TY medium containing appropriate selection antibiotic and was incubated overnight (220 rpm shaking, 37 °C, 16 hours). The plasmid DNA was purified using a QIAGEN™ Miniprep or Maxiprep kit, according to the manufacturer's protocol.[2]

Bacterial expression of recombinant KDM6A (BR71, BR242, BR281)

Expression was undertaken in Rosetta2(DE3) pLysS or Rosetta2(DE3) *E.Coli*, Small and large expressions were carried out in 2TY LB growth media using IPTG induction in addition to selection antibiotic (ampicillin, 50 µg/mL). Growth medium was inoculated using a scrape from a glycerol stock of transformed cells, and incubated for 16 hours at 37 °C. Aliquots (10 mL) of the resulting overnight culture were used to inoculate each litre of large scale growth medium, which was then allowed to grow at 37 °C until reaching $O.D._{600}$ = 1.0. The culture temperature was then reduced to 18°C, and expression was induced using IPTG (1 mM). The culture was then incubated for 14-16 hours at 18 °C. Cell pellets were collected by centrifugation (5000 rpm, 15 minutes) and stored at -80°C.

Bacterial expression of recombinant KDM6B

Expression was undertaken in Rosetta2(DE3) pLysS or Rosetta2(DE3) *E.Coli*, Overnight growth of starter cultures was undertaken in 2TY growth media using IPTG induction in addition to selection antibiotic (kanamycin, 50 µg/mL, chloramphenicol 34 µg/mL),

inoculated using a single colony of transformed cells and incubated overnight at 37°C degrees. Aliquots (10 mL) of the resulting overnight culture were used to inoculate each litre of large scale growth media (terrific broth containing kanamycin, 50 μg/mL) which was then allowed to grow at 37 °C until reaching $O.D._{600}$ = 1.5. The culture temperature was then reduced to 18 °C, and expression was induced using IPTG (0.3 mM). The culture was then further incubated for 14-16 hours at 18°C. Cell pellets were collected by centrifugation (5000 rpm, 15 minutes) and stored at -80°C.

Purification of recombinant KDM6A (BR71, B281)

Cell pellets were resuspended in lysis buffer (50mM HEPES pH 7.5, 500 mM NaCl, 10 % glycerol, 0.1 mM PhenylMethylSulphonyl Fluoride (PMSF), 5 mg/ml DNAse), 25 mL/10 mg cell pellet, and stirred at 4 °C until homogenous. The cell lysate was sonicated on ice (45 seconds 60 % maximum amplitude, 45 seconds cool, six cycles), centrifuged (10,000 rpm, 10 minutes, 4 °C) and the resulting supernatant was filtered (0.45 μm, Minisart). The cell lysate was loaded on to a pre-packed nickel-sepharose affinity column (5 mL, HisTrap HP, GE Healthcare) in binding buffer (50mM HEPES pH 7.5, 500 mM NaCl, 10 % glycerol). The column was then washed with binding buffer until the UV absorbance (280 nm) plateaued to a minimum. Protein was eluted from the column using a gradient elution buffer (50 mM HEPES pH 7.5, 500 mM NaCl, 10 % glycerol) in binding buffer (0-100 %) Fractions were collected and selected fractions, corresponding to peaks within the UV trace, were analysed by SDS-PAGE. A sample of fraction (5 μL) was mixed with 2x protein loading buffer (5 μL, composition Table 7.3), heated at 100°C for 5 minutes and then loaded on to an SDS-PAGE gel (5 μL). Selected fractions were concentrated using an Amicron®Ultra centrifugal filter (4000 rpm, 4 °C, 15 minutes) and the buffer was exchanged to storage buffer (50 mM HEPES pH 7.5, 500 mM NaCl, 5% glycerol)

using a PD-10 desalting column (GE Healthcare). Aliquots of protein sample were snap frozen in liquid nitrogen and stored at -80 °C.

Purification of recombinant KDM6A (BR242)

Cell pellets were resuspended in lysis buffer (50 mM HEPES pH 8.1, 500 mM NaCl, 10 mM imidazole, 5 % glycerol, 0.1 mM PMSF, 5 mg/ml DNAse), 25 mL/10 mg cell pellet, and stirred at 4 °C until homogenous. Cell lysate was sonicated on ice (45 seconds 60% maximum amplitude, 45 seconds cool, six cycles), centrifuged (10,000 rpm, 10 minutes, 4 °C) and the resulting supernatant was filtered (0.45 µm, Minisart). Cell lysate was incubated directly with Protino Ni-TED resin (Machery Nagel) and was incubated for 30 minutes, stirring at 4 °C. The mixture was then centrifuged (100 rpm, 1 minute), and the supernatant was removed. The resin was washed with 10 volumes of lysis buffer. Protein was then eluted with 8 volumes of elution buffer (50 mM HEPES pH 8.1, 125 mM NaCl, 250 mM imidazole, 5 % glycerol). Eluate was concentrated using an Amicron®Ultra centrifugal filter (4000 rpm, 4 °C, 15 minutes) and the buffer was exchanged to loading buffer (50 mM HEPES pH 7.5, 150 mM NaCl, 5% glycerol) using PD-10 desalting column (GE Healthcare). Protein was loaded on to a HiTrap Heparin HP affinity column (GE Healthcare) and eluted using a gradient of 0-100% elution buffer (1 M NaCl, 50 mM HEPES, pH 7.5) in loading buffer (50 mM HEPES pH 7.5, 150 mM NaCl, 5% glycerol). Eluted fractions (final buffer composition 400 mM NaCl, 50 mM HEPES, pH 7.5), were analysed by SDS-PAGE and combined fractions were concentrated using an Amicron®Ultra centrifugal filter (4000 rpm, 4 °C, 15 minutes). Aliquots of protein sample were snap frozen in liquid nitrogen and stored at -80 °C.

Purification of recombinant N-His$_6$-TRX KDM6B

Cell pellets were resuspended in lysis buffer (50 mM HEPES pH 7.5, 500 mM NaCl, 10 mM imidazole, 5 % glycerol, 0.1 mM PMSF, 5 mg/ml DNAse, 1 mM MgCl2, 8 U/mL Bensonase (Merck Millipore), 1 protease inhibitor cocktail tablet/ 50mL (Santa Cruz), 20 mL/10 mg cell pellet, and stirred at 4°C until homogenous. Cell lysate was sonicated on ice (45 seconds 60 % maximum amplitude, 45 seconds cool, six cycles), centrifuged (10,000 rpm, 10 minutes, 4 °C) and the resulting supernatant was filtered (0.45 µm, Minisart). Cell lysate was loaded to a column pre-packed with Protino Ni-TED resin (Machery Nagel). Protein was then eluted with elution buffer (50 mM HEPES pH 7.5, 500 mM NaC, 250 mM imidazole, 5 % glycerol). Eluted fractions were analysed by SDS-PAGE and combined fractions were exchanged in to storage buffer (50 mM HEPES pH 7.5, 500 mM NaCl, 5 % glycerol) using PD-10 desalting column (GE Healthcare) and then concentrated using an Amicron®Ultra centrifugal filter (4000 rpm, 4 °C, 15 minutes). Aliquots of protein sample were snap frozen in liquid nitrogen and stored at -80 °C.

Purification of recombinant cleaved KDM6B

Cell pellets were resuspended in lysis buffer (50 mM HEPES pH 7.5, 500 mM NaCl, 10 mM imidazole, 5 % glycerol, 0.1 mM PMSF, 5 mg/ml DNAse, 1 mM $MgCl_2$, 8 U/mL Bensonase (Merck Millipore), 1 protease inhibitor cocktail tablet/ 50 mL (Santa Cruz)), 20 mL/10 mg cell pellet, and stirred at 4 °C until homogenous. Cell lysate was sonicated on ice (45 seconds 60% maximum amplitude, 45 seconds cool, six cycles), centrifuged (10,000 rpm, 10 minutes, 4 °C) and the resulting supernatant was filtered (0.45 µm, Minisart). Cell lysate was incubated directly with Protino Ni-TED resin (Machery Nagel) for 30 minutes, stirring at 4 °C. The mixture was then centrifuged, and the supernatant was removed. The resin was washed with 10 volumes of lysis buffer. Protein was then

eluted with elution buffer (50 mM HEPES pH 7.5, 500 mM NaCl, 250 mM imidazole, 5% glycerol). Eluted fractions were analysed by SDS-PAGE and combined fractions were exchanged to storage buffer (50 mM HEPES pH 7.5, 500 mM NaCl, 5% glycerol) using PD-10 desalting column (GE Healthcare) and then concentrated using an Amicron®Ultra centrifugal filter (30kDa, 4000 rpm, 4 °C, 15 minutes). Aliquots of KDM6B were snap frozen in liquid nitrogen and stored at -80 °C.

SDS-PAGE analysis

	SDS	Tris-HCl pH 8.8	Tris-HCl pH 6.8	glycine	glycerol	bromophenol blue	β-mercaptoethanol
separating gel buffer	0.2% (w/v)	750	---	---	---	---	---
stacking gel buffer	0.2% (w/v)	---	250 mM	---	---	---	---
1x running buffer	1.0% (w/v)	25 mM	---	192 mM	---	---	---
2x protein loading buffer	2.0% (w/v)	---	50 mM	---	12% (v/v)	0.2% (w/v)	5.0% (v/v)

Table 7.3. *Composition of SDS-PAGE buffers*

SDS-PAGE buffers were prepared according to Table 7.3. The separating gel and stacking gels were prepared according to Table 7.4. Tetramethylethylenediamine (TEMED) and Ammonium persulfate (APS, 25% in water) were added to combined gel components directly prior to gel casting, and gels were allowed to set for at least 1 hour at room temperature prior to use. The protein sample and 2x loading buffer were combined in a 1:1 ratio and then heated at 100°C for 5 minutes. Sample was loaded onto the gel (5µl/well), with one well containing PageRuler^{TM} Thermo-Scientific molecular eight marker (3µl/well). The gel was then run at 180 V for approximately 60 minutes using a Bio-Rad Mini-PROTEAN II system. Gels were stained for 15 minutes using

InstantBlue™ ultra-fast coomassie gel stain (Expedeon), before imaging using a ChemiDoc MP system (Bio-Rad).

	Stacking gel 15%	Seperating gel 15%
30% acrylamide	300 µL	2.5 mL
Milli-Q H_2O	700 µL	---
SDS-PAGE separating buffer	---	2.5 mL
SDS-PAGE stacking buffer	1 mL	---
Tetramethylethylenediamine (TEMED)	5 µL	1 µL
25% Ammonium persulfate (APS)	10 µL	25 µL

Table 7.4. *Composition of SDS-PAGE stacking and separating gels.*

Agarose Gel Electrophoresis

Agarose gels (2.5 %) were prepared using 1.25 g agarose in 50 mL of 1 x TAE buffer (40 mM Tris, 40 mM acetate, and 1 mM EDTA, pH 8.3). Agarose was dissolved by heating with intermittent stirring using a microwave. The gel was cooled briefly before addition of SYBR Safe™ DNA gel stain (5 µL, Invitrogen). Cast gels were cooled to room temperature protected from light. 6 x Loading Dye (New England Biolabs)(1 µl) was added to samples (5 µl) which were run against a 1 kb DNA ladder (New England Biolabs) and/or 100 bp DNA ladder (New England Biolabs) (5 µl loaded per lane). Gels were run in 1 x TAE buffer at 85 V for 50 minutes, protected from light, and visualised using a ChemiDock MP gel imager (BioRad).

UV-vis spectroscopy to assess protein and DNA solution concentration and purity

A NanoDrop ND-1000 spectrophotometer (ThermoFisher) was used to quantify UV-vis absorbance of protein and DNA solutions between 220 and 350 nm with a pathlength of 10 nm. Buffer solutions corresponding to the buffer composition of protein or DNA samples were used as a blank.

Whole Protein LC-MS

Purified recombinant protein (0.01 mg/mL) was analysed by LC-MS using a LCT Premier mass spectrometer/UPLC system (Waters), equipped with a ProSwift™ RP-4H 212 1 mm x 50 mm column (ThermoFisher Scientific). Samples were loaded onto the column (95 % 5 mM ammonium formate pH 7.0, 5% MeCN, buffer A) and eluted over a gradient of increasing buffer B (95% MeCN, 5% 5 mM ammonium formate pH 7.0) in buffer A. Eluted protein was applied directly into the electrospray ion source. Data was analysed in MassLynx 4.0 (Waters), with deconvolution using the MaxEnt1 algorithm.

Dynamic Light Scattering

DLS measurements were acquired using a Viscotek 802 instrument and analysed using OmniSIZE software. A minimum concentration of 0.1 mg/ml protein was used per measurement and a volume of 200 µl per measurement.

Solid Phase Peptide Synthesis

Peptides were synthesised using a LibertyBlue microwave peptide synthesiser (CEM). Synthesis proceeded from C to N using *N*-terminal Fmoc protection and side chain protection with acid-labile protecting groups if required. Peptides were synthesised on a rink amide-MBHA resin (AGTC Bioproducts). Peptide coupling was activated using diisopropylcarbodiimide (DIC) and hydroxybenzotriazole (HOBt) at a ratio of 1:1 in dimethyl formamide (DMF). Resin was treated with a solution of 92.5 % trifluoroacetic acid, 2.5 % triisopropylsilane, 2.5 % 1,3-dimethoxybenzene, 2.5% H_2O for 3 hours at 25 °C to achieve cleavage and side chain deprotection. Resin was removed via filtration and the filtrate was treated with cold diethylether to precipitate the peptide. Peptides were harvested by centrifugation and lyophilised prior to purification.

Peptide purification: Peptides were purified *via* High Performance Liquid Chromatography (HPLC) using a Dionex UltiMate 3000 system and a VYDAC© Protein and Peptide C18 silica column (Grace Division Discovery Sciences™). Purity of peptide fractions was assessed by UV trace (220 nm) and MALDI-MS analysis, and selected fractions were combined and lyophilised. Peptide purity was assessed using an HPLC/LC-MS system (Agilent Technologies 1200) attached to an Agilent Technologies 6120 quadrupole mass spectrometer. Peptides were analysed using a Grace Vydac 218TP 50 mm x 4.6 mm C^{18} column. Data was analysed using Agilent Chemstation software.

Determination of peptide concentration by ^{1}H NMR

^{1}H NMR spectra were recorded using a Bruker DPX400 (400 MHz) using deuterochloroform or DMSO-d6 as a reference for internal deuterium lock. Trimethylsilylpropanoic acid (TSP) was used as an NMR standard for peptide concentration determination. Peptide sample and trimethylsilylpropanoic acid standard (58.05 mM) were combined in a 1:1 volume:volume ratio, and diluted with D_2O to a total volume of 800 µL. Sample was transferred to an 2 mm NMR tube for spectra acquisition. Spectrum and quantification of H3K27Me3 21mer peptide stock shown in Appendix 1.

***In vitro* assays**

Ferrous ammonium sulphate hexahydrate, $(NH_4)_2SO_4$ $FeSO_4.6H_2O$, was used as the source of Fe^{2+} for all experiments. This was dissolved in 20 mM HCl at a concentration of 100 mM, before dilution in Milli-Q water to the desired concentration.

MALDI-MS activity assay

KDM6A and KDM6B MALDI-MS activity assays were conducted using the following conditions (Table 7.5), unless otherwise stated in the text. Assays were performed in 50 mM HEPES pH 7.5, 150 mM NaCl unless otherwise stated.

	Stock concentration/ mM	Final concentration/ µM
Enzyme	0.05	4
H3K27Me3 Peptide (21mer)	1.0	20
2OG	10	300
L-ascorbate	10	4000
Fe^{2+}	1.0	50

Table 7.5 *MALDI-MS assay conditions used in in vitro enzyme activity assays. At each time point 5 µl reaction mixture was quenched with an equal volume of methanol. As assays were conducted in triplicate, reaction volume was equal to 15 µl per time point, plus an additional volume (20%) to account for potential pipette error.*

A master mix containing buffer, peptide substrate, 2OG, L-ascorbate and Fe^{2+} were mixed and incubated at reaction temperature for 3 min. Reaction was initiated by the addition of enzyme and at each time point, 5 µl of reaction mixture was taken and quenched with an equal volume of methanol. Samples were stored at –20 °C until needed for MALDI analysis. All reactions were performed in triplicate unless otherwise stated. The reaction was initiated by the addition of enzyme and at each time point, reaction mixture (5 µL) was taken and quenched with an equal volume of methanol. Samples were stored at –20 °C until needed for MALDI analysis. All reactions were performed in triplicate unless otherwise stated.

KDM6B MALDI-MS Inhibition assay

KDM6B MALDI-MS Inhibition assays were conducted using the following conditions (Table 7.5), unless otherwise stated in the text. Assays were performed in 50 mM HEPES pH 7.5, 150 mM NaCl unless otherwise stated.

	Stock concentration/ mM	Final concentration/ µM
Enzyme	0.05	1
H3K27Me3 Peptide (21mer)	1.0	20
2OG	10	10
L-ascorbate	10	100
Fe^{2+}	1.0	10

Table 7.6 *MALDI-MS assay conditions used in in vitro KDM6B inhibition assays. 10 µl/well total volume.*

KDM6B was pre-incubated with compound (10 minutes, 22°C) prior to initiation of the reaction with the addition of a master mix of Fe2+ (ferrous ammonium sulphate), 2OG, ascorbate and H3K27Me3 21mer peptide (final concentrations indicated above) (Table 7.6). After 4 minutes, the reaction was quenched with 1:1 volume of methanol. Samples were stored at –20 °C until needed for MALDI analysis. All reactions were performed in triplicate unless otherwise stated.

MALDI-MS analysis

α-cyano-4-hydroxycinnamic acid (CHCA) MALDI matrix,(1 µL) and sample (1 µL) were mixed, applied to a 96-spot MALDI plate and allowed to dry. Samples were analysed in positive reflectron mode, flight tube voltage 12000 V, reflectron voltage 5200 V, 800 Da suppression. Spectra were processed using MASSLYNX 4.0 (Waters), and the following parameters: background subtraction polynomial order 3, below curve (10 %), tolerance 0.010; smooth window (channels) ±3, number of smooths 5, Savitzky Golay method. The percentage of demethylated peptide/ demethylation was calculated using the following formula, where control corresponds to no enzyme control:

$$\text{Percentage H3K27Me3 (\%)} = \frac{(I_{H3K27Me3})}{I_{H3K27Me3}+I_{H3K27Me2}+I_{H3K27Me1}I_{H3K27}}$$

$$\text{Demethylation (\%)} = \frac{Control\ Me3\ (\%) - Sample\ Me3\ (\%)}{Control\ Me3\ (\%)}$$

FDH assay

Production of formaldehyde as a by-product of demethylation was observed using the FDH/NADH coupled assay.[3] A 2X master mix (25 µl) containing H3K27Me3 Peptide (21mer) peptide substrate (100 µM), 2OG (400 µM), L-ascorbate (200 µM), Fe^{2+} (20 µM) and Nicotinamide adenine dissolved in assay buffer (50 mM HEPES (pH 7.5), 0.01% Tween), was incubated at 37 °C for 5 min. The reaction was initiated by the addition of 2X master mix (25 µl) of KDM6B (10 µM) and FDH (1U/mL) (Sigma) dissolved in assay buffer (50 mM HEPES (pH 7.5), 0.01% Tween), final assay conditions listed in Table 7.7. The reaction was incubated at 37 °C and production of NADH was fluorescently monitored using a PHERAstar FS plate reader (BMG Labtech). Reactions were conducted in 384 well plates (ThermoFisher) (50 µl per well). Readings were taken over 120 cycles with a cycle time of 30 seconds. Data was exported from Mars software (BMG Labtech).

	Final concentration/ µM
Peptide	50 µM
Fe(II)	10 µM
Asc	100 µM
NADH	500 µM
2OG	200 µM
Enzyme	5 µM
FDH	1U/mL

Table 7.7. *FDH assay conditions. Total volume 50 µl per well*

AlphaScreen inhibition assay

KDM6B was pre-incubated with compound (15 minutes, 22°C), prior to initiation of the reaction with Fe^{2+} (ferrous ammonium sulphate), 2OG, L-ascorbate and biotinylated H3K27Me3 peptide at the concentrations indicated (Table 7.8).

Component	Final concentration/ μM
KDM6B	0.1 nM
2OG	10 μM
Fe^{2+}	10 μM
L-ascorbate	100 μM
H3K27Me3 peptide	60 nM

Table 7.8. AlphaScreen assay conditions. *10 μl total volume per well.*

After incubation (10 minutes, 22 °C), the reaction was quenched using a solution of EDTA and NaCl (30 mM EDTA, 1600 mM NaCl). The amount of H3K27Me2 produced was detected using the AlphaScreen antibody-bead system (Sigma), according to the manufacturers protocol and previous studies conducted in the group.[4,5] Streptavidin Donor beads (0.08 mg/mL) and Protein-A conjugated acceptor beads (0.08 mg/mL) were pre-incubated for 1 hour with anti-H3-K27Me3 antibody (0.2 μg/mL, Abcam). The plate (384 well proxiplate, PerkinElmer) was then incubated at room temperature for 1 hour and the assay plates were read in a BMG Labtech Pherastar FS plate reader.

RapidFire mass spectrometry assay

Reactions were initiated by mixing equal volumes of a 2x substrate mix containing Fe^{2+} (20 μM), 2OG (20 μM), ascorbate (200 μM) and peptide (various) and a 2x KDM6B (various) solution. After incubation (22°C), Samples were quenched at each time point by addition of 0.5 volumes of trifluoracetic acid (0.5 %).

Reagent	Final concentration/ μM
KDM6B	100,150,250,500 nM
Fe^{2+}	50μM
L-ascorbate	50μM
2OG	10μM
H3K27Me3	30 μM

Table 7.9 RapidFire assay conditions *50 μl total volume per well.*

Mass spectra were acquired using a RapidFire200 integrated autosampler/solid phase extraction (SPE) system (Agilent Technologies) coupled to an API4000 triple quadrupole mass spectrometer (Applied Biosystems). Solvent A was water containing 0.01 % Trifluoroacetic Acid (TFA) and 0.09 % formic acid. Solvent B was acetonitrile/water (8:2) containing 0.01 % TFA and 0.09 % formic acid. Sample was loaded onto a C4 solid phase extraction cartridge to remove non-volatile buffer salts, using solvent. The retained analytes were eluted to the mass spectrometer by with solvent B. Data was analysed using RapidFire™ peak integration software.

Procedures relating to cellular experiments

Cell culture procedures were carried out using sterile technique in a laminar flowhood, with sterile culture grade pipette tips and growth flasks. All equipment and consumables were sprayed with 70% ethanol in water before being introduced into the flowhood. Phosphate buffered saline (PBS pH 7.2, Life Technologies) was used in all wash steps in cell culture experiments, unless otherwise stated. Mammalian cells were incubated at 5 % CO2, 37 °C and not grown above 70–80 % confluency. HeLa, COS-7, RAW 264.7 and THP-1 cells were obtained from ATCC. HeLa, COS-7, RAW 264.7 were maintained in DMEM supplemented with 10 % foetal bovine serum (FBS) and 2mM L-glutamine. THP-1 cells were maintained in Roswell Park Memorial institute medium (RPMI) supplemented with 10 % foetal bovine serum (FBS) and 2mM L-glutamine.

Plasmids used in cellular studies

Protein	Tag	Resistance
Full length *N*-Myc-KDM6A	Myc	Ampicillin
Full length *N*-FLAG-KDM6B	FLAG	Ampicillin
Full length *N*-FLAG-KDM6B MUT (H1390A)	FLAG	Ampicillin
Full length *N*-FLAG-KDM6C	FLAG	Ampicillin

Table 7.10 *Plasmids used in cellular experiments*

Passage of COS-7 and HeLa

Culture media was aspirated from the cells, which were then washed with PBS. Trypsin-EDTA (0.25 %) was applied to the cells, followed by incubation at 5 % CO_2, 37 °C for 3 minutes HeLa, 6 minutes COS-7. Cells were then gently resuspended in fresh growth media before transfer to fresh culture media a fresh culture flask.

Passage of RAW 264.7

Culture media was aspirated from the cells, which were then washed with PBS. A cell scraper was gently used to remove cells from culture flask. Cells were then resuspended in fresh growth media before transfer to fresh culture media a fresh culture flask.

Passage of THP-1

Cell suspensions were diluted in fresh growth media. Cell debris was removed by centrifugation of the cells, removal of 80% of the culture media, and addition of fresh media.

Seeding of cell culture plates

Adherent cells were released from culture flasks, as described above. To count cell number, Cell suspension (10 µL) was mixed with an equal volume of 0.4 % Trypan Blue (Life Technologies) (10 µL). The resulting mixture (10 µL) was immediately directly applied to the chamber of a dual chamber cell counting slide (Bio-Rad) and cells were

counted using a TC20™ Automated Cell Counter (Bio-Rad). Cells were then diluted with fresh medium to give the desired seeding density: HeLa 8 x 10^4 cells/mL, COS-7 5 x 10^4 cells/mL, RAW 264.7 5 x 10^4 cells/mL, THP-1 1 × 10^6 cells/mL. Cell suspensions were transferred to a 96-well Cell Carrier™, black, clear bottom TC treated plate (PerkinElmer) (100 µL/ well) and 100 µL PBS was added to surrounding wells. Cells were incubated overnight (5.0 % CO2, 37 °C, 16 h).

Transient transfection

Transient transfection was undertaken using GeneJuice (Novagen), FuGENE® (Promega), Lipofectamine2000 and Lipofectamine(Novagen) (Thermofisher) according to the manufacturers' instructions.[6-9] FuGENE®/GeneJuice: Plasmid DNA (100 ng) was combined with reagent and incubated for 5 minutes prior to addition (10 µL/well) to cell culture media (90µL). Lipofectamine2000, Lipofectamine3000: P3000 and DNA were incubated together for five minutes prior to addition of L3/2000 reagent, the resulting mixture was incubated for five minutes and then added (10 µL/well) to cell culture media (90µL). Ratio of DNA: reagent was optimised for each plasmid/ cell line. Cells were then incubated (5.0 % CO_2, 37 °C).

Hypoxic treatment of cells

Cells were incubated in Invivo$_2$ 400 hypoxic workstations set to 0.1 %, 1.0 % or 21 % O2, (5.0 % CO_2, 37 °C) for the durations indicated. Dissolved oxygen concentration in the medium above the cells was measured using an OxyLite Dissolved Oxygen Monitor with a bare fibre sensor (Oxford Optronix. See Appendix 2 for O_2 measurements).

COS-7 Compound dosing

COS-7 cells, were transiently transfected with full length, *N*-terminally FLAG tagged KDM6B, and the catalytically inactive mutant (H1390A). After 4 hours of transfection

with the KDM6B plasmid, the media was replaced, and 3-fold serial dilutions of the compounds were added. Compound stocks were prepared in dimethylsulphoxide (DMSO), unless otherwise indicated, with the final DMSO concentration being no higher than 1%. Cells were then incubated for a further 24 hours prior to fixing with 4% paraformaldehyde.

Antibody/fluorescence staining

Fixed cells were permeabilised (0.5% TritonX in phosphate buffered saline (PBS), 6 minute incubation) and washed three times (PBS, 100µL). Cells were then blocked with a solution of FBS (10% in PBS, 1 hour incubation) prior to primary antibody staining overnight (16 hours) against H3K27Me3 and FLAG at dilutions listed below. Cells were washed three times (PBS, 100µL) and underwent secondary antibody staining (1 hour incubation). Cells were again washed three times (PBS, 100µL) and then underwent nuclear staining with DAPI (10mg/mL, 1:10000 dilution in PBS, 5 minute incubation). Cells were finally washed three times (PBS, 100µL) and then were imaged using a Perkin Elmer Operetta instrument. Harmony® software (PerkinElmer) was used to quantify nuclear Flag and H3K27Me3 fluorescence intensity.

	Epitope	Conjugate	Host species	Source & catalogue no	Dilution
Primary antibodies	FLAG	---	Mouse M2	Sigma, F1804	1:1000
	H3K27me3	---	Rabbit	Millipore, 07-449	1:500
Secondary antibodies	Rabbit IgG (H+L)	Alexa Fluor® 488	Goat	Life Technologies, A11034	1:500
	Mouse IgG (H+L)	Alexa Fluor® 594	Goat	Life Technologies, A11032	1:500

Table 7.11 *Antibodies and dilutions used in cellular immunofluorescence experiments.*

Imaging and analysis of immunofluorescence experiments

Cells were imaged and analysed using an Operetta® High Content Imaging Microscope (PerkinElmer), using the Harmony software (Perkin Elmer). Nine fields per well were imaged at 20x magnification, and the average of 3 wells was calculated unless otherwise indicated. Transfected cell population was selected according to FLAG fluorescence as described in Chapter 3, and H3K27Me3 fluorescence intensity in the selected cells was calculated and averaged. Calculation of percentage demethylation of H3K27Me3 and KDM6 activity were performed as described in Chapter 3 (Figure 3.6, C).

RAW 264.7 foam cell formation assay

Foam cell assay were conducted according to the following protocol, unless otherwise indicated. RAW 264.7 were incubated in low serum media (DMEM supplemented with 2mM L-glutamine and 0.5 % FBS) for 24 hours. RAW 264.7 were then seeded in a 96 well microplate (CellCarrier™ Ultra, PerkinElmer, 5000 cells/well) in regular culture media (DMEM supplemented with 2mM L-Glutamine and 10% FBS) and incubated overnight for 16 hours at 37 °C in 5 % CO_2. Cell media was then replaced with regular culture media containing 50µg/mL acLDL. Cells were incubated for 24 hours at 37°C in 5 % CO_2. Cells were washed with PBS (100 µl/well) prior to fixation with 4 % paraformaldehyde (50 µl/well), nuclear staining using DAPI (10mg/mL, 1:10000 dilution in PBS, 5 minute incubation) and lipid staining using LipidTOX™ Red lipid stain (1:1000 dilution in PBS, 30 minute incubation). Widefield and confocal fluorescent microscopy images were captured using an Operetta® high content imaging system (PerkinElmer), and analysed using Harmony® image analysis software (Perkin Elmer).

RT-qPCR

All experiments with RNA used DEPC-treated water and RNAse-free certified plasticware. Work benches and equipment were cleaned using RNaseZap® (Ambion™),

and Distel High Level Laboratory Disinfectant (Tristel) to remove all traces of DNA and RNA. Isolation of mRNA: RAW 264.7 were harvested using RNA Cell Protect reagent (ThermoFisher). Total RNA was purified using a mirVana miRNA isolation kit (Life Technologies) according to the manufacturer's protocol, and DNA was removed using a Turbo DNA-free™ kit (Invitrogen). RNA purity and concentration was assessed using a NanoDrop ND-1000 UV/Vis spectrophotometer, measuring the absorbance between 220-350 nm. Samples with an A260:A280 ratio of 1.8–2.2 were deemed of sufficient purity for use in RT-qPCR analysis. Reverse transcription to produce cDNA libraries was carried out using High-Capacity cDNA Reverse Transcription kit (Applied Biosystems) according to the manufacturer's protocol. RT-qPCR primer sequences were derived from the primary literature or designed using NCBI PrimerTool, and sourced from Sigma Aldrich. Validation of primers was undertaken according to the Pfaffl method.[1] Evaluation of housekeeping genes, used for relative quantification of gene expression changes, was undertaken. Analysis of Cq values using BestKeeper software revealed GAPDH was the most appropriate housekeeping gene, maintaining consistent expression levels across the different treatments.[10] (However as both KDM6B and HIF mRNA levels were prohibitively low in all samples, reflected by Ct values >35 cycles, further experiments were not undertaken).

Target	Oligonucleotide Primer Sequence
HIF-1α	Rev: TGTTAGGCTGGGAAAAGTTAGGA
CD36	Fwd: TCCTCTGACATTTGCAGGTCTATC Rev: AAAGGCATTGGCTGGAAGAA
β-Actin	Fwd: GGCATTGTTACCAACTGGGACGAC REV: CCAGAGGCATACAGGGACAGCACAG
GAPDH	Fwd: TCAACGGCACAGTCAAGG Rev: ACTCCACGACATACTCAGC
G6PD	Fwd: CCTACCATCTGGTGGCTGTT Rev: CATTCATGTGGCTGTTGAGG
Cyclophillin A	Fwd: CAGACGCCACTGTCGCTTT Rev: TGTCTTTGGAACTTTGTCTGCAA
KDM6B	Fwd: CCTGTTTACCGCTTCGT Rev: TCACCTCGTTCCACTCATA

Table 7.12 *Primer sequences used in RT-qPCR studies*

References

1. FisherScientific. FisherBrand™ Terrific Broth : Documentation. (2018). Available at: https://www.fishersci.com/shop/products/fisher-bioreagents-terrific-broth-modified-granulated-3/p-4245455.
2. QIAGEN. QIAGEN Plasmid-prep kit User Manual. (2017). Available at: https://www.qiagen.com/qdm/aw/pla/maxiprep?cmpid=QVenGA3Maxiprep&kwid=%2Bminiprep.
3. Sakurai, M. *et al.* A miniaturized screen for inhibitors of Jumonji histone demethylases. *Mol. Biosyst.* **6,** 357–64 (2010).
4. AlphaScreen Assay Technology User Booklet. (2004). Available at: http://www.perkinelmer.com/Content/RelatedMaterials/Brochures/BRO_AlphaScreen2004.pdf.
5. Kawamura, A. *et al.* Development of homogeneous luminescence assays for histone demethylase catalysis and binding. *Anal. Biochem.* **404,** 86–93 (2010).
6. Novagen. GeneJuice ® Transfection Reagent User Protocol.
7. Promega Corporation. FuGENE ® HD Transfection Reagent Technical Manual. Available at: https://www.promega.com/-/media/files/resources/protocols/technical-manuals/101/fugene-hd-transfection-reagent.pdf.
8. Life Technologies. Lipofectamine ® 2000 Reagent Protocol Outline. (2013). Available at: https://tools.thermofisher.com/content/sfs/manuals/Lipofectamine_2000_Reag_protocol.pdf
9. Life Technologies, T. F. Lipofectamine ™ 3000 Reagent Protocol Outline. Available at: https://tools.thermofisher.com/content/sfs/manuals/lipofectamine3000_protocol.pdf.
10. Pfaffl, M. W., Tichopad, A., Prgomet, C. & Neuvians, T. P. Determination of stable housekeeping genes, differentially regulated target genes and sample integrity: BestKeeper – Excel-based tool using pair-wise correlations. *Biotechnol. Lett.* **26,** 509–515 (2004).

Appendix 1: HPLC-MS analysis of H3K27Me3 peptide for use in *in vitro* assays

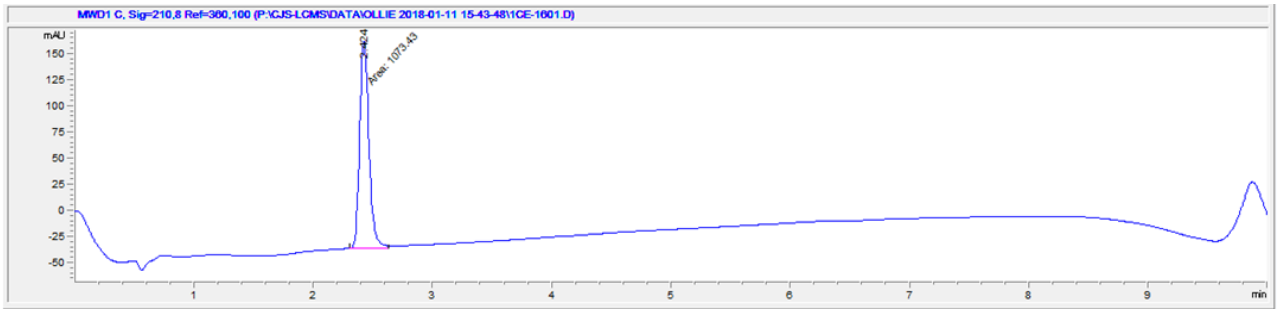


Figure A1. *UV chromatographs (absorption at 210 nm) from the High Performance Liquid Chromatography/ Liquid Chromatography-Mass Spectrometry (HPLC/LC-MS) analysis of H3K27Me3 21mer peptide (20 µM, 50 µL sample). Integration confirmed 100% purity of the peptide. Mass 2150.6 Da, expected peptide mass 2150.58 Da.*

Appendix 2: NMR analysis of H3K27Me3 peptide used for *in vitro* assays

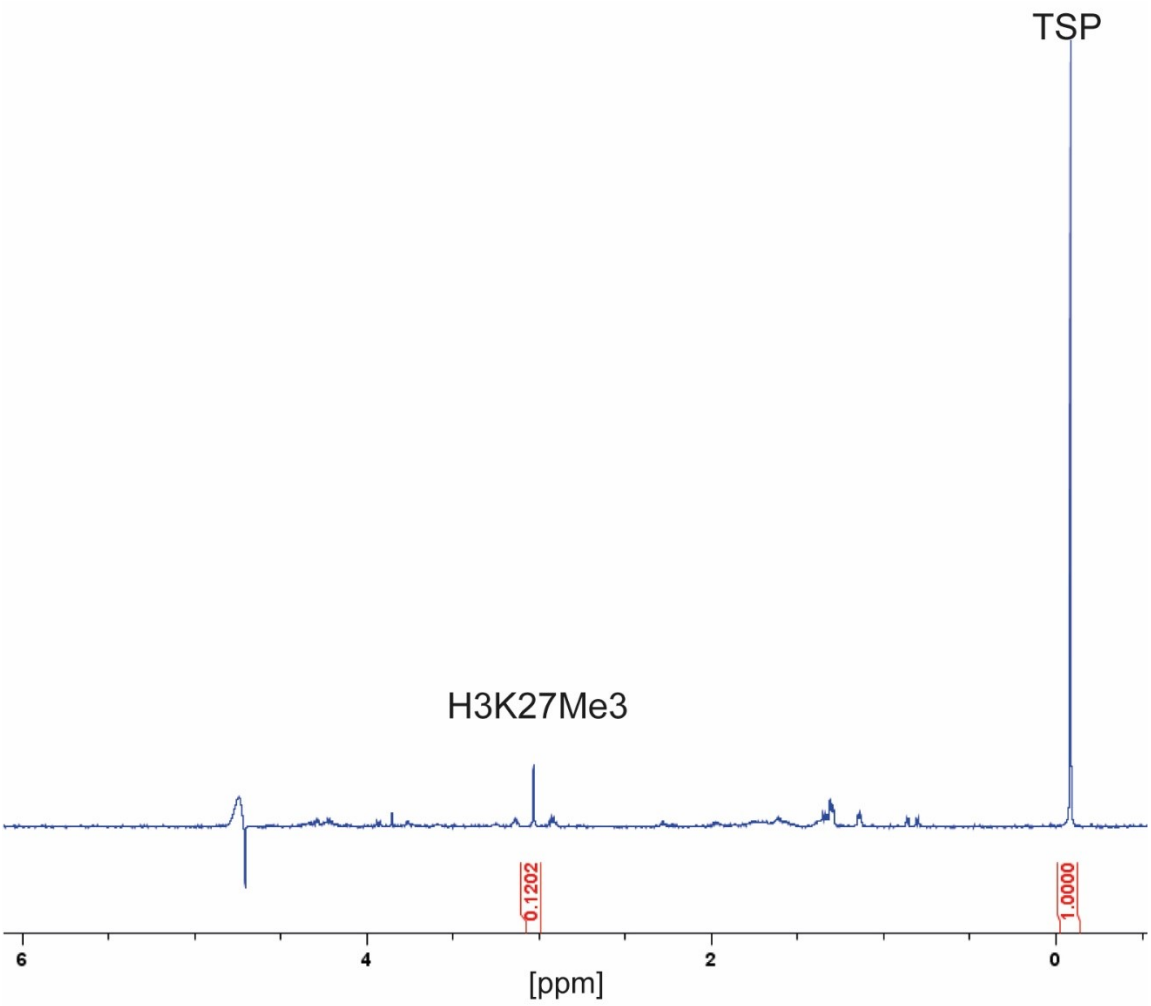


Figure A2. *^{1}H NMR spectra of H3K27Me3 21mer peptide solution in 50mM HEPES pH 7.5 buffer. Peptide sample and trimethylsilylpropanoic acid (TSP) standard (58.05 mM) were combined in a 1:1 volume:volume ratio, and diluted with D_2O to a total volume of 800 µL. Sample was transferred to an 2 mm NMR tube for spectra acquisition. Integration of H3K27Me3 (CH_3)$_3$ peak relative to TSP (CH_3)$_3$ peak indicates a (0.1202 : 1 = 1 : 8.3176) molar ratio of H3K27Me3 : TSP. Both species have an equal number of hydrogens at the integrated resonance. Concentration of TSP standard used 58.05 mM. Concentration of peptide solution calculated to be 6.9792 mM.*

Appendix 3: Recombinant KDM6B construct JMJC3A-C031

Tag	Sequence	MW (Da)
N-His_6-TRX-tagged $KDM6B_{1141-1641}$	MHHHHHHSSGMSDKIIHLTDDSFDTDVLKADGAILVD FWAEWCGPCKMIAPILDEIADEYQGKLTVAKLNIDQN PGTAPKYGIRGIPTLLLFKNGEVAATKVGALSKGQLKE FLDANLAGTENLYFQSMDVVRASRNAKVKGKFRESY LSPAQSVKPKINTEEKLPREKLNPPTPSIYLESKRDAF SPVLLQFCTDPRNPITVIRGLAGSLRLNLGLFSTKTLV EASGEHTVEVRTQVQQPSDENWDLTGTRQIWPCES SRSHTTIAKYAQYQASSFQESLQEEKESEDEESEEPD STTGTPPSSAPDPKNHHIIKFGTNIDLSDAKRWKPQL QELLKLPAFMRVTSTGNMLSHVGHTILGMNTVQLYM KVPGSRTPGHQENNNFCSVNINIGPGDCEWFAVHEH YWETISAFCDRHGVDYLTGSWWPILDDLYASNIPVYR FVQRPGDLVWINAGTVHWVQATGWCNNIAWNVGPL TAYQYQLALERYEWNEVKNVKSIVPMIHVSWNVART VKISDPDLFKMIKFCLLQSMKHCQVQRESLVRAGKKIA YQGRVKDEPAYYCNECDVEVFNILFVTSENGSRNTYL VHCEGCARRRSAGLQGVVVLEQYRTEELAQAYDAFT LVRARR	71135.60
Tobacco Etch Virus (TEV) protease cleaved $KDM6B_{1141-1641}$	SMDVVRASRNAKVKGKFRESYLSPAQSVKPKINTEEK LPREKLNPPTPSIYLESKRDAFSPVLLQFCTDPRNPIT VIRGLAGSLRLNLGLFSTKTLVEASGEHTVEVRTQVQ QPSDENWDLTGTRQIWPCESSRSHTTIAKYAQYQAS SFQESLQEEKESEDEESEEPDSTTGTPPSSAPDPKN HHIIKFGTNIDLSDAKRWKPQLQELLKLPAFMRVTSTG NMLSHVGHTILGMNTVQLYMKVPGSRTPGHQENNNF CSVNINIGPGDCEWFAVHEHYWETISAFCDRHGVDYL TGSWWPILDDLYASNIPVYRFVQRPGDLVWINAGTVH WVQATGWCNNIAWNVGPLTAYQYQLALERYEWNEV KNVKSIVPMIHVSWNVARTVKISDPDLFKMIKFCLLQS MKHCQVQRESLVRAGKKIAYQGRVKDEPAYYCNECD VEVFNILFVTSENGSRNTYLVHCEGCARRRSAGLQG VVVLEQYRTEELAQAYDAFTLVRARR	57208.73

Figure A3. *Protein sequence and expected molecular weight of JMJD3-C031 E.Coli expression construct encoding N-His_6-TRX-tagged $KDM6B_{1141-1641}$ and TEV protease cleaved $KDM6B_{1141-1641}$. Plasmid and sequence gifted by the Structural Genomics Consortium, University of Oxford.*

Appendix 4: Protein LC-MS analysis of His-tagged KDM6B JMJC3A-C031

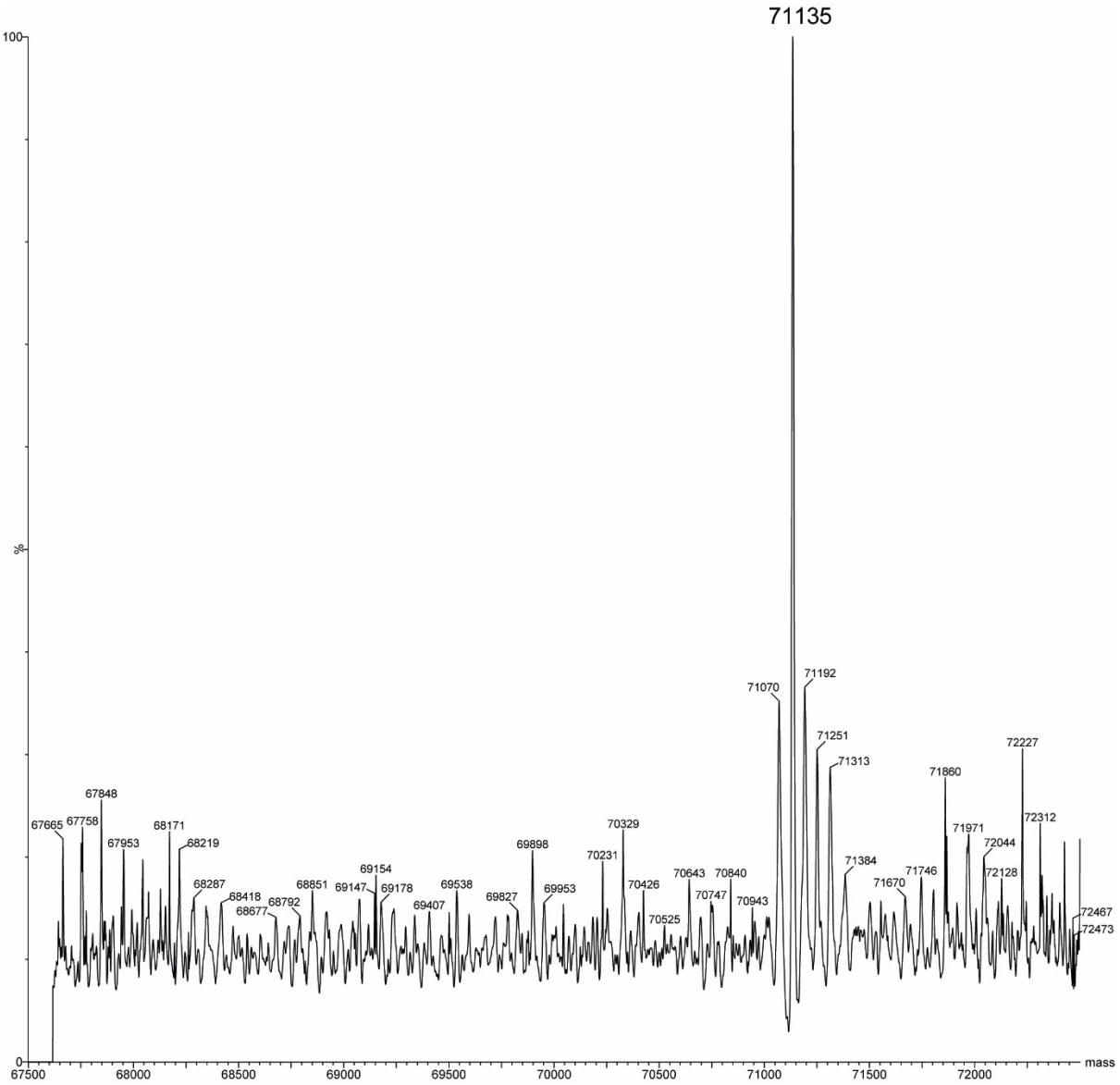


Figure A4. LC-MS analysis of purified N-His$_6$-TRX-tagged KDM6B$_{1141-1641}$ Expected mass 71135 Da, observed mass 71135 Da*. Purified recombinant N-His$_6$-TRX-tagged KDM6B$_{1141-1641}$ (10 µM, 20 µL sample) was analysed by LC-MS using a LCT Premier mass spectrometer/UPLC system (Waters), equipped with a ProSwift™ RP-4H 212 1 mm x 50 mm column (ThermoFisher Scientific). Samples were loaded onto the column (95 % 5 mM ammonium formate pH 7.0, 5% MeCN, buffer A) and eluted over a gradient of increasing buffer B (95% MeCN, 5% 5 mM ammonium formate pH 7.0) in buffer A. Eluted protein was applied directly into the electrospray ion source. Data was analysed in MassLynx 4.0 (Waters), with deconvolution using the MaxEnt1 algorithm.*

Appendix 5: Protein LC-MS analysis of cleaved KDM6B JMJC3A-C031

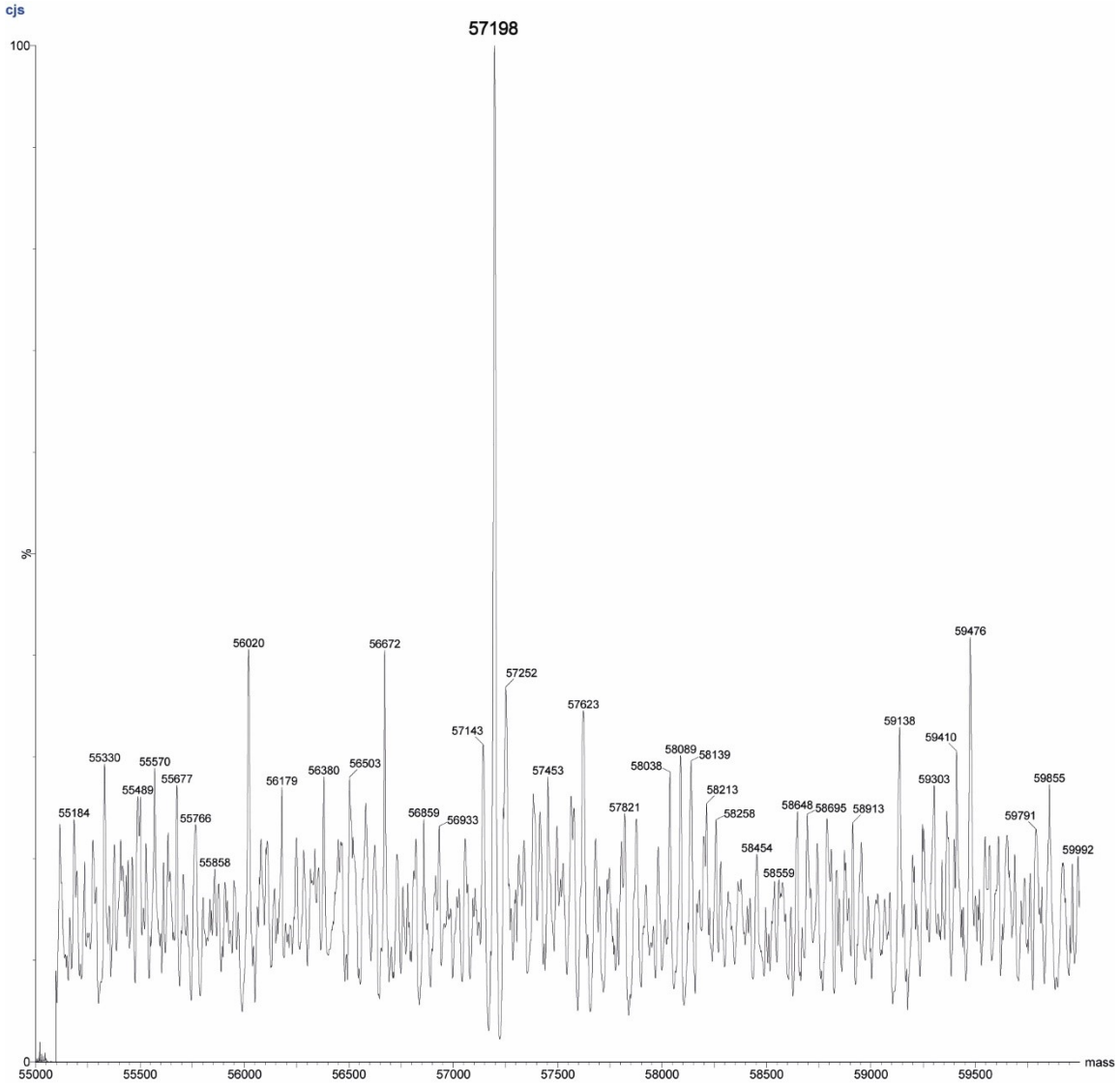


Figure A5. LC-MS analysis of TEV protease cleaved KDM6B$_{1141-1641}$. Expected mass 57208 Da, observed mass 57198 Da*. Purified TEV protease cleaved KDM6B$_{1141-1641}$ (10 µM, 20 µL sample) was analysed by LC-MS using a LCT Premier mass spectrometer/UPLC system (Waters), equipped with a ProSwift™ RP-4H 212 1 mm x 50 mm column (ThermoFisher Scientific). Samples were loaded onto the column (95 % 5 mM ammonium formate pH 7.0, 5% MeCN, buffer A) and eluted over a gradient of increasing buffer B (95% MeCN, 5% 5 mM ammonium formate pH 7.0) in buffer A. Eluted protein was applied directly into the electrospray ion source. Data was analysed in MassLynx 4.0 (Waters), with deconvolution using the MaxEnt1 algorithm.*

Appendix 6: Supplementary AlphaScreen IC_{50} curves

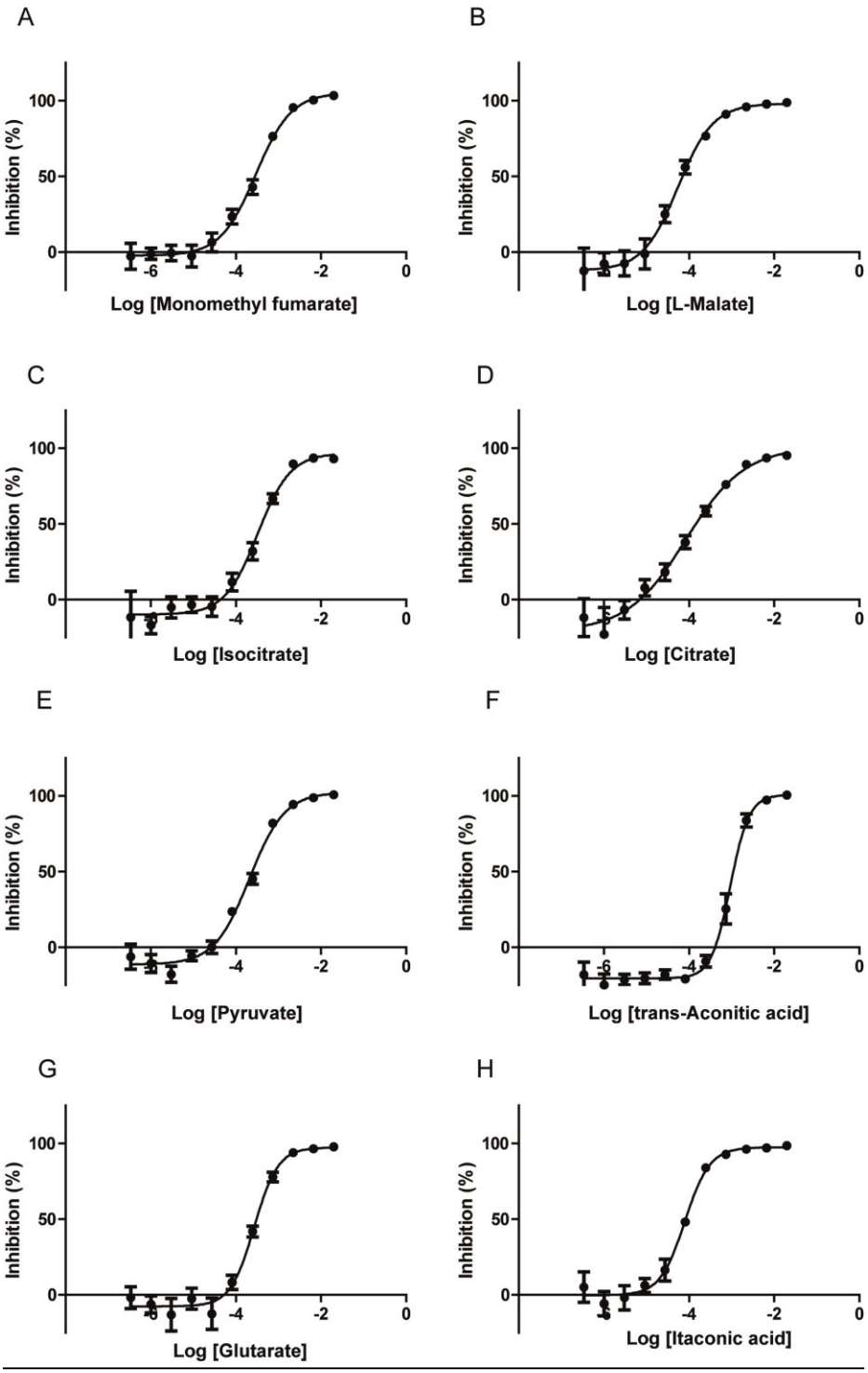


Figure A6 (I). *Inhibition of KDM6B by TCAI, determined by AlphaScreen assay. Assay conditions: 0.1 nM KDM6B, 60nM biotinylated H3K27Me3 peptide, 10 µM Fe^{2+}, 13 µM 2OG, 100 µM Ascorbate. KDM6B was pre-incubated with inhibitor (10 minutes, 22°C) prior to reaction (15 minutes, 22°C) IC_{50} values and 95% confidence intervals calculated using nonlinear regression with normalized dose–response fit on Prism GraphPad®. IC_{50} values calculated using N=6 data set. Data = mean Error bars represent STDERR. N=2 technical repeats, N=3 biological repeats.*

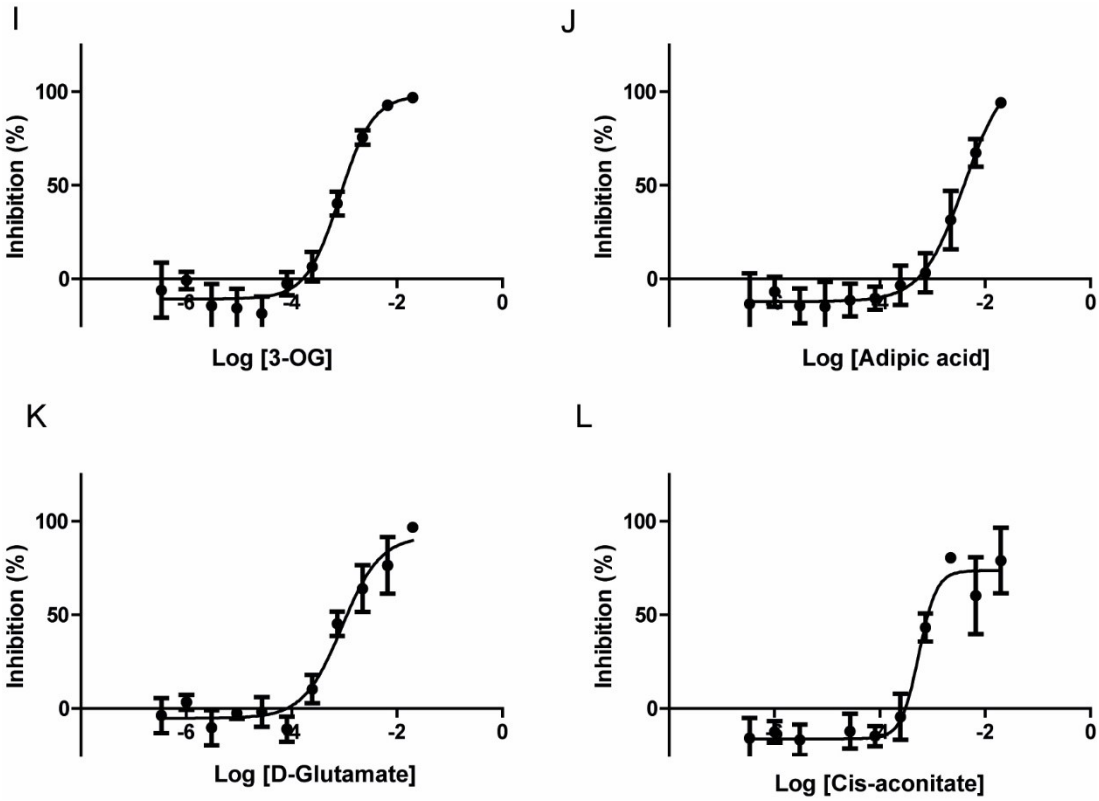


Figure A6 (II). *Inhibition of KDM6B by TCAI, determined by AlphaScreen assay. Assay conditions: 0.1 nM KDM6B, 60nM biotinylated H3K27Me3 peptide, 10µM Fe^{2+}, 13 µM 2OG, 100 µM Ascorbate. KDM6B was pre-incubated with inhibitor (10 minutes, 22°C) prior to reaction (15 minutes, 22°C) IC_{50} values and 95% confidence intervals calculated using nonlinear regression with normalized dose–response fit on Prism GraphPad®. IC_{50} values calculated using N=6 data set. Data = mean Error bars represent STDERR. N=2 technical repeats, N=3 biological repeats.*

Appendix 7: Dissolved oxygen calibration curve

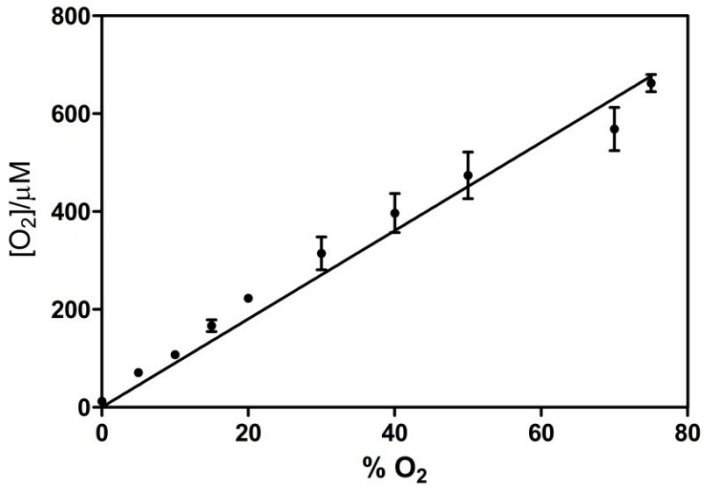


Figure A7. *Calibration curve used to calculate the concentration of O_2 (μM) in solutions equilibrated at a particular percentage O_2. 50mM HEPES buffer in sealed vials was incubated at the desired percentage O_2 using a mass flow controller (Brooks Instruments) for 10 min at 37°C. A FOXY electrode (Ocean Optics) was used to determine dissolved oxygen concentration in μM. GraphPad Prism was used to fit the curve to a linear regression model. N=3, error bars denote standard deviation. Adapted with permission from Hancock et al,[1] American Chemical Society.*

Appendix 8: Summary of human 2OG oxygenases and substrates

Reaction Type	Substrate/Residue	Enzymes (Substrates)
Protein Hydroxylation	Proline	PHD1-3 (HIFα)
		CP4H1-3 (Collagen)
		P3H (Collagen) OGFOD1 (RPS23)
	Asparagine	FIH (HIFα, Ankyrin Repeat Proteins)
	Aspartic acid	FIH (Ankyrin Repeat Proteins) ASPH1-2 (EGF Proteins)
	Histidine	FIH (Ankyrin Repeat Proteins) MINA53 (RPL27A) NO66 (RPL8)
	Lysine	JMJD4 (eRF1)
		JMJD6 (Splicing Regulatory Proteins) PLOD1-3 (Collagen)
Nucleic Acid Hydroxylation	5-Methylcytosine	TET1-3 (DNA)
	7-(α-amino-α-carboxypropyl)wyosine	TYW5 (tRNA)
	5-Methoxycarbonylmethyluridine	AlkBH8 (tRNA)
	N^{ϵ}-Trimethyllysine	TMLH
Small Molecule Hydroxylation	γ-Butyrobetaine	BBOX1
Lipid Hydroxylation	Phytanoyl-CoA	PAHX
Protein Demethylation	N^{ϵ}-tri/di/mono-methyllysine	KDM2A/B (H3K36me2/1) KDM3A/B (H3K9me2/1) KDM4A-C (H3K9me3/2/1, H3K36me3/2/1) KDM4D (H3K9me3/2/1) KDM5A-D (H3K4me3/2/1) KDM6A/B (H3K27me3/2/1) KDM7A (H3K27me2/1) PHF8 (H3K9me2/1)
	N^{ω}-di/mono-methylarginine	JMJD6 KDM3A KDM4A KDM5C KDM6B
Nucleic Acid Demethylation	3-Methyluracil	AlkBH2/3 (DNA/RNA) FTO (DNA)
	3-Methylthymine	AlkBH2/3 (DNA/RNA) FTO (DNA)
	3-Methylcytosine	AlkBH2/3 (DNA/RNA)
	1-Methylguanine	AlkBH2/3 (DNA/RNA)
	1-Methyladenine	AlkBH2/3 (DNA/RNA)
	6-Methyladenine	FTO (mRNA) AlkBH5 (mRNA)

Table A8. *Table of human 2OG oxygenases identified to date and their respective substrates. Adapted with permission from Islam et al, Annual Review of Biochemistry.*[2]

References

1. Hancock, R. L., Masson, N., Dunne, K., Flashman, E. & Kawamura, A. The Activity of JmjC Histone Lysine Demethylase KDM4A is Highly Sensitive to Oxygen Concentrations. *ACS Chem. Biol.* **12,** 1011–1019 (2017).
2. Islam, M. S., Leissing, T. M., Chowdhury, R., Hopkinson, R. J. & Schofield, C. J. 2-Oxoglutarate-Dependent Oxygenases. *Annu. Rev. Biochem.* **87,** annurev-biochem-061516-044724 (2018).